Durham E-Theses

Small Wind Turbine Starting Behaviour

WORASINCHAI, SUPAKIT

How to cite:

WORASINCHAI, SUPAKIT (2012) *Small Wind Turbine Starting Behaviour*, Durham theses, Durham University. Available at Durham E-Theses Online: http://etheses.dur.ac.uk/4436/

Use policy

The full-text may be used and/or reproduced, and given to third parties in any format or medium, without prior permission or charge, for personal research or study, educational, or not-for-profit purposes provided that:

- a full bibliographic reference is made to the original source
- a link is made to the metadata record in Durham E-Theses
- the full-text is not changed in any way

The full-text must not be sold in any format or medium without the formal permission of the copyright holders.

Please consult the full Durham E-Theses policy for further details.

Academic Support Office, Durham University, University Office, Old Elvet, Durham DH1 3HP
e-mail: e-theses.admin@dur.ac.uk Tel: +44 0191 334 6107
http://etheses.dur.ac.uk

Small Wind Turbine Starting Behaviour

Supakit Worasinchai

A Thesis presented for the degree of
Doctor of Philosophy

School of Engineering and Computing Sciences
University of Durham
England

June 2012

Dedicated to

All members of my family: Dad, Mum, Bank, Bua, and Bill

Small Wind Turbine Starting Behaviour

Supakit Worasinchai

Submitted for the degree of Doctor of Philosophy
June 2012

Abstract

Small wind turbines that operate in low-wind environments are prone to suffer performance degradation as they often fail to accelerate to a steady, power-producing condition. The behaviour during this process is called "starting behaviour" and it is the subject of this present work.

This thesis evaluates potential benefits that can be obtained from the improvement of starting behaviour, investigates, in particular, small wind turbine starting behaviour (both horizontal- and vertical-axis), and presents aerofoil performance characteristics (both steady and unsteady) needed for the analysis.

All of the investigations were conducted using a new set of aerodynamic performance data of six aerofoils (NACA0012, SG6043, SD7062, DU06-W-200, S1223, and S1223B). All of the data were obtained at flow conditions that small wind turbine blades have to operate with during the startup - low Reynolds number (from 65000 to 150000), high angle of attack (through 360°), and high reduced frequency (from 0.05 to 0.20). In order to obtain accurate aerodynamic data at high incidences, a series of CFD simulations were undertaken to illustrate effects of wall proximity and to determine test section sizes that offer minimum proximity effects.

A study was carried out on the entire horizontal-axis wind turbine generation system to understand its starting characteristics and to estimate potential benefits of improved starting. Comparisons of three different blade configurations reveal that the use of mixed-aerofoil blades leads to a significant increase in starting capability. The improved starting capability effectively reduces the time that the turbine takes to reach its power-extraction period and, hence, an increase in overall energy yield. The increase can be as high as 40%.

Investigations into H-Darriues turbine self-starting capability were made through the analogy between the aerofoil in Darrieus motion and flapping-wing flow mechanisms. The investigations reveal that the unsteadiness associated with the rotor is key to predicting its starting behaviour and the accurate prediction can be made when this transient aerofoil behaviour is correctly modelled. The investigations based upon the analogy also indicate that the unsteadiness can be exploited to promote the turbine ability to self-start. Aerodynamically, this exploitation is related to the rotor geometry itself.

Declaration

The work in this thesis is based on research carried out in the School of Engineering and Computing Sciences at University of Durham. No part of this thesis has been submitted elsewhere for any other degree or qualification and it all my own work unless referenced to the contrary in the text.

Copyright © 2012 by Supakit Worasinchai.
"The copyright of this thesis rests with the author. No quotations from it should be published without the author's prior written consent and information derived from it should be acknowledged".

Acknowledgements

The success of this thesis would not have been possible without the support and guidance of my supervisors: Dr Grant Ingram and Dr Robert Dominy. Their advice, suggestions, and expertise had shaped this thesis to be what it should be. My sincere thanks go to them both.

Many people had helped me along the way although they might not notice: Dr Nick Stannard, Dr Jim Bumby, Dr David Sims-Williams, Dr Richard Williams, Nicholas Oettle, Nick Cresswell, and Nathan Hill. I am extremely grateful to their help. Nicholas Oettle deserves special thanks for his willingness to help on calibration techniques.

I am indebted to the technical staff in the School of Engineering and Computing Sciences. Special thanks are due to: Collin Wintrip, Roger Little, and Anthony Collinson for their assistance in wind tunnel setup, Phillip Duffy for his excellent work on aerofoil rapid prototyping, Michael Wilson for computer support, and Ian Garrett for his assistance in the installation of motor and control system. This research work would be less fruitful without their contributions.

I wish to thank Professor David Wood from University of Newcastle, Australia (currently at the University of Calgary, Canada), for sending me information regarding to small turbine work. David Hail from NaREC (National Renewable Energy Centre) deserves thanks for providing me the wind data used in simulations.

The final thank you belongs to my family. They undoubtedly play a significant part in all aspects of my life. The most heartfelt appreciation is expressed to my mum for unfailing love, support, and always standing beside me whatever happens. I cannot come this far without you, mum.

Contents

List of Figures

List of Tables

Nomenclature

a	Speed of sound
A	Cross-sectional area
A_1	Indicial coefficient
A_2	Indicial coefficient
AEP	Annual Energy Production
AoA	Angle of attack
AR	Blade Aspect Ratio
$\vec{A}_n$	Unit normal vector
$\vec{A}_t$	Unit tangential vector
b_1	Indicial coefficient
b_2	Indicial coefficient
c	Scale factor
c	Aerofoil chord
C_C	Axial (or chordwise) coefficient
C_d	Drag coefficient
C_{d0}	Drag coefficient at zero angle of attack
C_l	Lift coefficient
C_N	Normal force coefficient
C_{N1}	Critical normal force coefficient
$C_{N\alpha}$	Slope of normal force coefficient
C_N^C	Circulatory load
C_N^f	Normal force coefficient due to separated flow
C_N^I	Impulsive load
C_N^P	Potential normal force coefficient
C_N^T	Total normal force coefficient
C_N^v	Normal force coefficient due to vortex formation
C_N'	Lagged Normal force coefficient
C_P	Power coefficient
C_P^*	Unsteady pressure coefficient
C_q	Torque coefficient
C_t	Thrust coefficient
C_T	Unsteady total coefficient
C_{WB}	Grid converter capacitance
D	Deficiency function for impulse load

D	Rotor diameter
f	Effective separation point
f''	Dynamic separation point
F	Weibull distribution
F_1	Prandtl's tip loss correction factor
F_2	Prandtl's tip loss correction factor
F_{eff}	Effective tip loss
F_i	Tangential force
H	Test section height
J	Rotor inertia
k	Reduced frequency
k	Shape factor
k_σ	Intensity factor
K	Generator constant
Ma	Mach number
MP	Mixed-aerofoil blade with pitch increment
MX	Mixed-aerofoil blade
n	Time step simulation
N	Number of blades
P	Power
PC	Percent of contribution
PC_D	Drag contribution
PC_L	Lift contribution
r	Radius
R	Radius
Re	Reynolds number
R_b	Battery resistance
R_d	Generator resistance
R_L	Load resistance
R_{over}	Overlap resistance
R_{phase}	Generator resistance per phase
s	Distance along the aerofoil surface
S	Blade span
S	Dimentionless time
SG	Single-aerofoil blade
St	Strouhal number
X	Deficiency function for attached flow
Y	Deficiency function for attached flow
T_a	Aerodynamic torque
T_f	Time constant for boundary-layer lag
T_i	Torque generated by each blade
T_P	Time constant for pressure lag
T_r	Resistive torque

T_v	Time constant for vortex
T_{vl}	Time that the vortex takes to reach trailing edge
U	Headwind velocity
V	Free-stream wind speed, Voltage
V_{batt}	Battery voltage
W	Resultant wind speed
$\vec{W}_n$	Resultant wind speed normal to aerofoil chord
$\vec{W}_t$	Resultant wind speed tangential to aerofoil chord
α	Rotor acceleration
α_0	Zero-lift angle of attack
α_A	Angle formed by lift and drag coefficients
α_D	Darrieus incidence angle
α_m	Mean incidence angle
α_{pitch}	Pitch component of Darrieus incidence angle
α_{plunge}	Plunge component of Darrieus incidence angle
β	Prandtl-Glauert compressibility factor
η_{WB}	Grid converter efficiency
λ	Tip speed ratio
ω	Rotational speed
ϕ	Angle on the aerofoil surface
ϕ_α^c	Indicial function for circulatory load
ϕ_α^I	Indicial function for impulsive load
ρ	Density
σ_r	Rotor solidity
θ	Azimuth angle
τ_v	Vortex time
μ	Air viscosity

Chapter 1

Introduction

The concern about global warming has initiated a renewed interest in renewable, emission-free energy sources. Wind energy is one of the sources that plays a major role in electricity production and the use of wind turbines to supply electricity has grown very rapidly in the last decade [1]. More than 1% of global electricity comes from wind power [2], UK capacity alone is now at 6.8GW [3].

Apart from large-scale production, it was estimated that small-scale wind turbines (less than 10 kW [4]) have a high potential to be part of the future electricity generation mix [5]. Their possible contributions to power generation can be in various forms: stand-alone, grid-connected, or building-integrated.

One of the challenges in employing these small devices is to make them more efficient when they operate in low-wind environments. Their energy-extraction performance under these conditions is often limited and unsatisfactory as they fail to accelerate to the point that power can be extracted. The period that the turbine takes to reach its power-extraction operation is called the "start-up period".

The study of starting behaviour of small-scale wind turbines during that period (both horizontal- and vertical-axis) is relatively immature and little useful information is available in the literature [6–10]. Attempts have been made to study and model their starting behaviour. Nevertheless, it appears that significant differences between the experimental results and numerical simulations are still seen. Hill [10] and Wood [11] suggested that better modelling cannot be carried out until more accurate aerofoil data is available.

The aerofoil aerodynamic data required must cover a suitable Reynolds number range for the full 360° range of incidence angle that is likely to be experienced including both unstalled and stalled conditions. This kind of information is scarce and most available aerofoil data covers only angles of attack up to or just past the stall point, e.g [12, 13]. Estimations were often made in order to extrapolate these data to higher angles of attack. Nevertheless, high-angle-of-attack tests on some real aerofoils has revealed that different aerofoils may demonstrate significantly different characteristics from each other even when fully stalled [14].

The motion of the turbine blade relative to the wind further complicates aerofoil-

data requirements, particularly for vertical-axis turbines where the blade moves in and away from the wind per revolution which leads to a periodic change in apparent wind velocity and incidence angle.

It is well-known that when an aerofoil is subjected to such motion, its performance characteristics will be "significantly" different from those of the steady case [15]. It introduces non-unique relations between aerodynamic coefficients and incidence angle, resulting in a hysteresis loop. One of the important features of this unsteady effect is the delay of stall and the increase in maximum lift coefficient when the incidence angle is increased. It is experimentally evident that the increase is large and can be as high as 200% [16]. Both steady and unsteady aerodynamic data are therefore required for small wind turbine start-up analysis. These data will help pave the way toward the better understanding of starting behaviour and the enhancement of starting capability.

The main purposes of this thesis are to:-

- assess and quantify the potential benefits gained from improved starting capability.
- present steady and unsteady wind-tunnel data for wind-turbine aerofoils at low Reynolds numbers and high incidence angles.
- model and investigate the turbine starting behaviour (both horizontal- and vertical-axis).

This series of work forms the main body of this thesis. It is divided into ten chapters:-

1. **Introduction** - this chapter
2. **Literature Review** - literature relevant to this research such as starting behaviour and aerofoil performance data is reviewed.
3. **Potential Benefits Gained through Starting Capability Improvement** - this chapter presents the impact of improved starting capability on energy yield so as to clearly show how important starting capability is. The horizontal-axis wind turbine is selected as a case study.
4. **The Physics of H-Darrieus Turbine Self-starting Capability** - due to the complexity of H-Darrieus turbine self-starting behaviour, a chapter is devoted to explore its behaviour in detail. The investigation is made through an analogy between the aerofoil in Darrieus motion and flapping-wing mechanism which is drawn in this chapter.
5. **Selection of Aerofoil Profiles** - due to a large number of potentially appropriate aerofoils, it is impractical to test all of them. Numerical modelling and a simulation-based selection are performed in this chapter to narrow down aerofoil choices.

6. **Experimental Configuration** - this chapter describes experimental facilities and techniques used in wind-tunnel testing.

7. **Experimental Results** - general discussions of experimental results are given here. Steady and unsteady results are presented and discussed separately.

8. **Aerodynamic Characteristics of Bird-like Aerofoils** - due to the analogy between the aerofoil in Darrieus motion and flapping-wing mechanism, an additional testing of a seagull-like aerofoil is conducted in order to seek a possibility to employ a special aerofoil for self-starting capability improvement.

9. **H-Darrieus Turbine Self-starting Capability** - H-Darrieus turbine starting behaviour is modelled and examined in this chapter using the aerofoil data and models developed.

10. **Conclusions and Recommendations**.

The work within this thesis has been the subject of a number of conference and journal publications:-

- Worasinchai, S., Ingram, G., and R. Dominy (2011), A Low-Reynolds-number, High-angle-of-attack Investigation of Wind Turbine Aerofoils, Proceedings of the Institution of Mechanical Engineers, Part A: Journal of Power and Energy, 225(6), pp 748-763.

- Worasinchai, S., Ingram, G., and R. Dominy (2011), The Effects of Improved Starting Capability on Energy Yield for Small HAWTs, GT2011-45674: ASME Turbo Expo 2011, June 6-10, 2011, Vancouver, Canada.

- Worasinchai, S., Ingram, G.L., and R.G. Dominy (2012), Effects of Wind Turbine Starting Capability on Energy Yield, ASME Journal of Engineering for Gas Turbines and Power, 134(4), 9 pages.

- Worasinchai, S., Ingram, G.L., and R.G. Dominy (2012), The Physics of H-Darrieus Turbine Self-starting Capability: Flapping-wing perspective, GT2012-69075: ASME Turbo Expo 2012, June 11-15, 2012, Copenhagen, Denmark.

The next chapter covers the review of the most recent literature that pertains to this research.

Chapter 2

Literature Review

This chapter reviews literature that is pertaining to this research. The main topics surveyed are small wind turbine starting behaviour, wind turbine aerofoils, aerofoil performance data, and dynamic stall. It also explains the motivations behind this research work and shows how this research is technically and socially significant.

2.1 Small-scale wind turbines and the benefits of improved efficiency

The impact of climate change, which is evident from observations of rising temperature, melting snow, and rising sea levels [17], has stressed the importance of low carbon-emission energy sources. Attempts have been made to address this concern and one of the clear attempts is the Kyoto agreement set by the United Nations [18]. The UK government itself has set the parallel target that 20% of CO_2 emission should be reduced and 20% of electricity should be generated by renewable sources by 2020 [5]. Much of this can be met by the use of wind power (both large- and small-scale). This thesis focuses on the latter.

Their contribution is directly related to their performance and, undoubtedly, their improved performance further promotes the contribution. Traditionally, wind turbine performance is defined in terms of power-extraction performance (expressed dimensionlessly as power coefficient (C_P)) and the turbine's ability to start is normally ignored. Nevertheless, if a turbine cannot accelerate through start-up, its power-extraction performance is severely limited.

The consideration of starting behaviour therefore offers another solution to improve the overall performance as the period that the turbine needs to start might be shortened and a longer power-production period might be achieved which might lead to a significant increase in energy yield.

The discussions above are the motivation behind this thesis which is to better understand and improve the starting behaviour of small wind turbines.

2.2 Small wind turbine starting behaviour

Different types of wind turbines behave differently during start-up. In this research, particular attention is paid to turbines that employ aerofoil-shaped blades for the purposes of torque generation: Darrieus- and propeller-type turbines

2.2.1 Straight-bladed Darrieus turbines

The Darrieus turbine was named after Georges Jean Marie Darrieus, a French engineer, who designed it in 1928 (it was patented in 1931) [19]. It is categorised as a lift-driven vertical-axis turbine as it employs lift forces to spin the rotor. Blade configurations of this turbine can be broadly categorized into curved- and straight-bladed types, each having its own advantages and disadvantages. The straight-bladed turbine is attractive for its simple blade design.

Most experimental testing of Darrieus turbines has been conducted in terms of power-extraction performance, eg. [20–23]. Very few tests have focussed upon their starting behaviour. To the best of the author's knowledge, there exist only two studies that provide starting behaviour in a time-varying format; tests conducted by Chua [8] and Hill et al [10].

In Chua's test, an H-rotor three-blade Darrieus turbine equipped with NACA0015 blades was tested using a set of three fans which provide an airflow to the turbine. Wind speed was measured at nine points upstream of the rotor using a handheld anemometer and then averaged. The shaft of the unloaded rotor was fitted with reflective tape which, together with a tachometer, was used to measure the turbine rotational speed. His results are reproduced and presented in Figure 2.1.

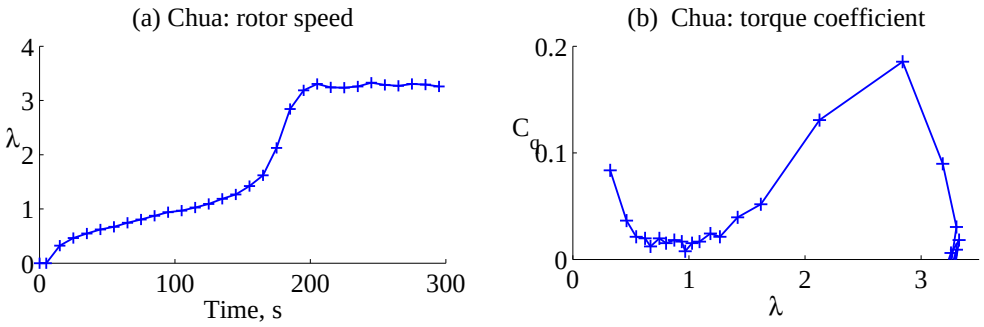

Figure 2.1: Chua's test performance [8].

It is observed from Chua's results that the rotor has a relatively high initial rate of acceleration but that the acceleration rate falls to a steady rate after about 30 seconds. The rotor continues spinning at that rate before accelerating again with a higher rate to its final tip speed which is reached after 200s. The corresponding torque coefficient curve shows that torque is relatively high at first but reduces with increasing tip speed ratio. The small torque between tip speed ratios from around 0.5 to 1.3 is consistent with the slower pace of acceleration observed in Figure 2.1a.

At tip speed ratios above 1.3 the rotor begins producing comparatively high torque and accelerates quickly to its operational tip speed ratio.

This process was further investigated by Hill et al. [10]. In their test, a straight-bladed Darrieus turbine equipped with NACA0018 aerofoils was tested in a 2m wind tunnel. The turbine was held stationary (It was noted that the orientation of the starting position does not affect the starting behaviour for this 3-bladed machine. Previous work by Dominy et al. [24] had shown that this was not true for 2-bladed rotors) before being released when the tunnel wind speed reached its set value of 6 m/s. Once the wind speed stabilised, the rotor was released and data acquisition process was triggered.

According to Hill et al, there are four main processes taking place during start-up (Fig. 2.2). The first process is a linear acceleration in which the turbine rotational speed linearly increases. The turbine then enters the period that the rotor speed is nearly constant (plateau). In this process, turbine rotational speed increases but only very slowly. After a long period of that idling, the rotor then accelerates rapidly to a tip speed ratio of around 3 and enters its steady operating state. It is observed that, although the tests of Chua [8] and Hill et al [10] are in qualitative agreement, there exist some differences in the rotor behaviour, especially in the plateau region at which Chua's rotor demonstrates a greater rate of acceleration. This difference implies that the rotor start-up behaviour might be significantly improved through design optimisation.

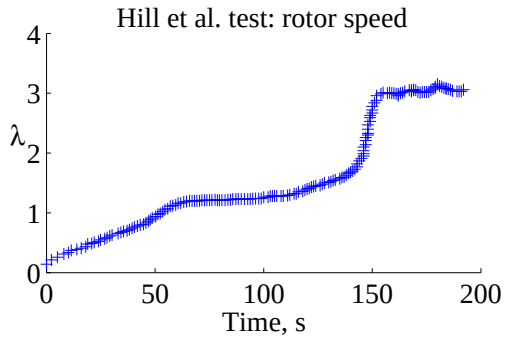

Figure 2.2: Hill's test performance [10].

A numerical model was also developed by Hill et al [10] to predict the rotor behaviour, based upon the approach of Dominy et al [24]. The predictions were made by using rare existing aerofoil data that cover high incidences (0° to 360°). He found that his prediction results qualitatively agreed with the measured behaviour for the first two regions i.e. the initial acceleration and plateau. Nevertheless, the model did not predict the escape of the rotor from the plateau into the second acceleration zone. He suggested that discrepancies were due to the quality of the aerofoil data.

All in all, the differences between experiments and predicted results confirm that further aerofoil testing and modelling are required in order to improve an un-

derstanding of this starting behaviour.

2.2.2 Horizontal-axis wind turbines

The starting behaviour of a small horizontal-axis wind turbine was first investigated by Ebert and Wood [6]. A two-bladed 5kW turbine was tested. The analysis of the experimental results showed that there are two main processes taking place in the starting sequence, namely periods of idling and rapid acceleration. During the idling period, the turbine blade rotates with slow acceleration and the angle of attack gradually decreases until the blade can generate a high lift-to-drag ratio. Here, the turbine enters its rapid acceleration phase with the blades continuing to accelerate more rapidly to the point at which useful power can be extracted. These two periods complete the whole starting sequence. It was also noted that the acceleration period is comparatively short and can be ignored in terms of designing a turbine for improved starting performance. This long idling period was a direct result of the high angle of attack that the blade was initially exposed to.

Effects of blade pitch angle (θ_P) on the idling period was experimentally conducted by Mayer et al. [7]. The investigation was made by varying the blade pitch angle from 0° to 35° with a 5° increment. They found that, with increased pitch angle, the idling period was shortened due to the lower angles of attack that the blade experienced.

Wright and Wood [9] further investigated the starting performance of a small HAWT. A three-bladed, 2m diameter turbine was experimentally investigated and the authors confirmed that the torque generated near the hub plays a particularly important role in spinning the rotor up to speed while torque at the tip plays a more significant role in power production. Numerical simulations were also performed by the authors. However, due to the lack of aerofoil data at high incidence (the analysis needs aerofoil data at incidence up to around 90°), three approximations were used. The first post-stall data set is predicted using a flat plate theory. The second set was a composite set in which the NACA4412 post-stall performance at a Reynolds number of 250,000 was directly combined with their aerofoil section (the SD7062). The third set was an average of the previous two. They found that the predictions greatly depend on the aerofoil data used.

It is seen from the survey that the starting behaviour of both types of turbines was not successfully modelled and noticeable differences are still observed. The disparity is highly sensitive to the aerofoil data employed. The sensitivity of the prediction model to aerofoil performance data demonstrates conclusively that reliable aerofoil performance data is needed.

2.3 Aerofoils for wind turbines and their performance data

2.3.1 Wind turbine operation: speed and torque control

Flow conditions that wind turbine blades experience are partly related to their modes of operation [25]. This review provides a brief summary of the operations and their influences on aerofoil design.

Modern wind turbines operate with two types of speed control: constant (or fixed) speed and variable speed [26]. In the constant-speed configuration, turbines operate with a nearly constant rotational speed (and frequency) to directly supply electricity to the grid. This constant rotor speed leads to a variation in the tip speed ratio when the wind speed changes (recall that $\lambda = \frac{\omega R}{V}$).

In the variable-speed configuration, turbines are designed to operate at a constant and optimal tip speed ratio. This is achieved by 'varying' the rotor speed in response to the change of wind speed. This turbine is typically connected to the grid through a power converter [27].

In addition to that, the turbines are also designed with a torque control feature in order to limit excessive power under strong winds. There are two types of torque control: passive (or stall-regulated) and active control (pitch-regulated). The pitch configuration allows more flexibility in power control and typically leads to constant power output above the rated speed (Fig. 2.3). The stalled-regulated turbine will produce less power above this rated speed as the blades become stalled.

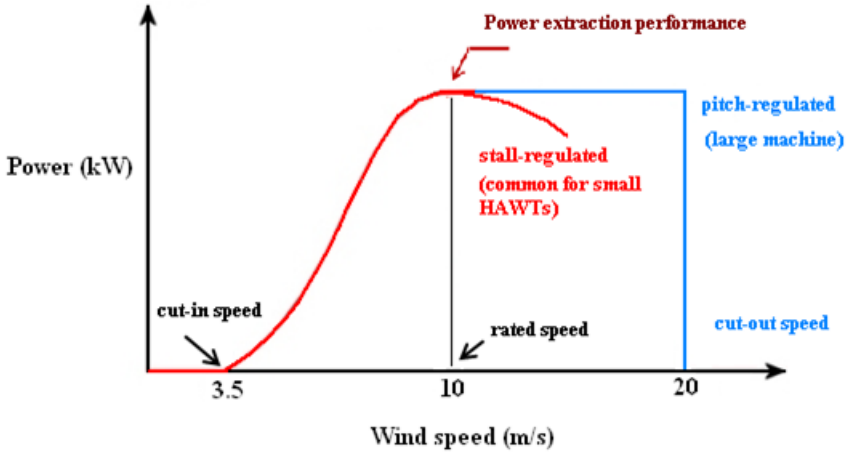

Figure 2.3: Typical power curves.

In terms of aerofoil design, the blades of stall-regulated turbines experience a wider range of flow conditions and have to exhibit a high lift-to-drag ratio over a wider range of incidence angle [28, 29]. The operating modes also pose a specific stall characteristic requirement. Generally, blades for stall-regulated turbines are required to exhibit gentle stall as they induce less stall vibration [28]. This is also

true for pitch-regulated turbines which their blades are pitched to stall.

2.3.2 Vertical-axis wind turbines

In the early development of Darrieus turbines in 1970s, symmetrical NACA 4-digit sections were commonly employed [20]. It was later realised that these aerofoils which were developed for aviation might not be suitable for VAWT applications and the use of specifically-tailored aerofoils could be more beneficial.

Migliore and Fritschen [30] examined ten different aerofoils and their effects on the aerodynamic performance of Darrieus turbines. They found that the use of NACA 6-series blades can produce a broader and flatter power curve whilst the peak power coefficient is comparable to the use of NACA 4-series. Their calculations showed that energy yield can be increased by 17% to 27% if a NACA $63_2 - 015$ was used.

An aerofoil series was proposed in 1990s by Sandia researchers [31, 32]. This series consists of three sections: SAND0015/47, SAND0018/50, and SAND0021/50. Its designation is similar to the NACA00xx that were used as a reference for the design of the SAND00xx/xx. A number had been added after a slash to indicate an aerofoil portion that supports laminar flow. They were designed to be Natural Laminar Flow (NLF) aerofoils due to a requirement that they should exhibit low drag at their operational speed. Although aerofoil geometries and some performance characteristics were presented in Berg's paper [32] (Fig. 2.4), no further information on their coordinates and performance characteristics are available from other sources.

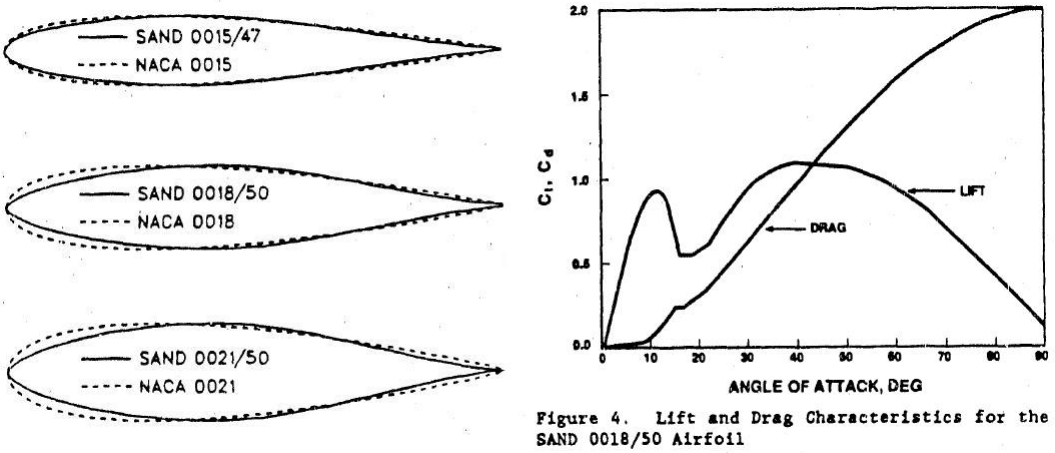

Figure 2.4: The SAND00xx/xx aerofoil sections and performance characteristics [32].

More recent aerofoil development has been made by Somers [16, 33], Claessens [34], and Islam et al. [35]. Nevertheless, useful information can be found for Claessens' aerofoil only since the Somers' aerofoil is proprietary and very little useful information is available in the open literature. Information about Islam's aerofoil such as

its geometry and performance data was not provided by the authors in their original work.

The aerofoil designed by Claessens is designated as DU06-W-200 to comply with the Delft aerofoil designation system. It is intended for small-scale application and the turby commercial Darrieus turbine was used as a reference for its design. The NACA0018 section which is commonly used on Darrieus turbine blades was used as a reference. Thickness and camber were added to improve strength and aerodynamic performance respectively and testing was performed at two Reynolds numbers of 300,000 and 500,000 up to incidence angles of 80° in the Delft University Low-speed wind tunnel.

2.3.3 Horizontal-axis wind turbines

Aerofoils utilised for horizontal-axis wind turbine blades in the early developments were directly employed from the aviation industry. However, as in the case of vertical axis wind turbines, researchers and wind turbine designers came to realise that those aircraft aerofoils such as NACA44xxx, NACA23xxx, and NACA63xxx, and NASA LS(1) series are not well-suited for wind turbine applications [25] and it became clear at that time that special aerofoils should be developed and utilised.

Since then, many organizations published specifically-tailored aerofoils such as S8xx series [25], Riso-A1-xxx series [36], and DUxx-W-xxx series [37]. It was evident that, with these specifically-designed aerofoils, the annual energy production of all types of HAWTs had been greatly improved [25, 38]. Most of them are intended for large turbine applications.

For small wind turbines, some existing low-Reynolds-number aerofoils which are designed for small aeroplanes such as E387 [39], FX63-137 [40] and SD2030 [41] etc. have been used and they are currently in use on some commercial small turbine blades [13].

Although the aerofoils are broadly applicable, specifically-tailored aerofoils potentially offer enhanced rotor performance. Somers designed the S822 and S823 aerofoils for small stall-regulated turbines sized from 2kW to 20kW [42]. The S822 was tested by Selig [13] at Reynolds numbers from 100,000 to 500,000 up to around the stall angle.

Giguere and Selig developed a family of aerofoils (denoted as SG640x) for small variable-pitch wind turbines having a rated power in the range of 1-5kW [29]. They were tested at a Reynolds number range of 100,000 to 500,000 up to the stall angle of around 14°.

2.3.4 Steady aerofoil performance data

For small wind turbine starting analysis, the aerofoil performance data required is significantly different from those of other applications. Since the turbine blade is comparatively small and has to operate with low apparent wind speed (a combina-

tion of free-stream and headwind velocity) before it reaches its normal operation, the Reynolds numbers that it experiences are comparatively low.

In addition, the incidence angle that the blades experience is far more extreme than any other applications. Whilst small horizontal-axis turbine blades experience an incidence range of 0° to 90°, Darrieus blades experience all possible incidences. At very low tip speed ratio the incidence range will be from 0° to 360° which reduces as tip speed ratio increases.

A review of aerofoil test conditions is conducted in this section. Special attention is paid to low-Reynolds-number and high-angle-of-attack test conditions.

Low-Reynolds-number tests:

One of the most extensive and reliable sources of low-speed aerofoil performance data is that provided by Selig and his colleagues at UIUC Applied Aerodynamics Group [43]. A bulk of aerofoils were tested at low Reynolds numbers comparable to those of small turbine blades experienced during start-up.

A series of low-Reynolds-number tests revealed that the flow over an aerofoil at this regime is associated with a laminar separation bubble. Its presence often leads to a degradation in aerofoil performance which is in the form of an increase in drag and nonlinear behaviour of lift [44].

The degradation depends greatly on both Reynolds number and the aerofoil geometry. Measurements conducted by Selig et al. [44] showed that the lift curve of most aerofoils will not follow the typical linear pattern and the slope is often lower than 2π (which means the increase of lift force with respect to incidence angle reduces) if Reynolds number is low enough (normally lower than 100,000). Hysteresis behaviour at around the stall angle is greatly influenced by the aerofoil shape. For instance, while the FX63-137 exhibited hysteresis behaviour, the NACA0009 and SD8020 did not [44]. High-lift sections such as the M06-13-128, which employs concave pressure distribution, exhibit a longer bubble in comparison to sections that employ convex pressure recovery. More severe degradation is expected for aerofoil sections with concave recovery type (Fig. 2.5).

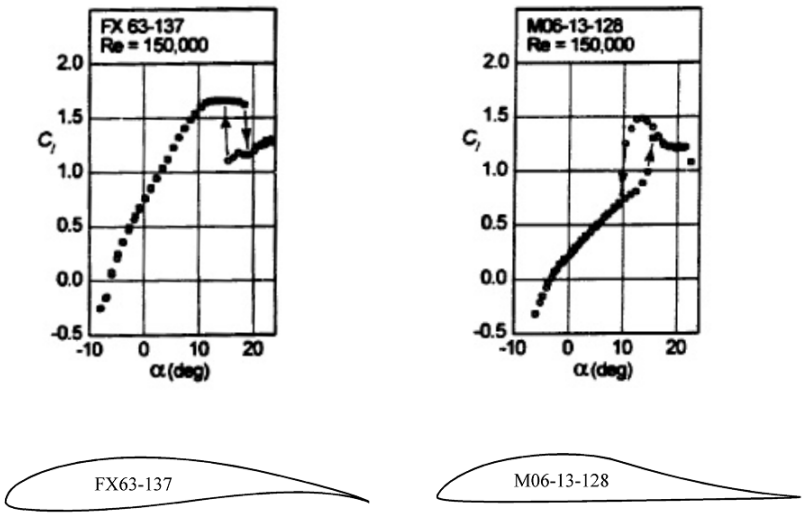

Figure 2.5: Effects of bubble on hysteresis behaviour of different aerofoils (adapted from [44]).

All tests conducted by the Group are in the incidence angle range from about $-10°$ to $25°$. Post- and deeper stall performance is not available. Some tested aerofoils that are often employed on wind turbine blades are presented in Table 2.1 together with their test conditions.

Table 2.1: Low-Reynolds-number tests.

Aerofoil	**Reynolds number**	**Incidence range**
E387 [113]	100,000 - 500,000	$-10°$ to $20°$
FX63-137 [46]	61,500 - 303,400	$-8°$ to $24°$
FX63-137 [47]	80,000 - 150,000	$-9°$ to $25°$
FX63-137 [113]	100,000 - 500,000	$-10°$ to $20°$
S1210 [44]	80,000 - 150,000	$-8°$ to $25°$
S822 [44]	102,500 - 408,700	$-8°$ to $20°$
S822 [113]	100,000 - 500,000	$-10°$ to $20°$
S823 [46]	102,500 - 409,200	$-8°$ to $21°$
S834 [113]	100,000 - 500,000	$-10°$ to $20°$
SD2030 [113]	100,000 - 500,000	$-10°$ to $20°$
SD7062 [48]	60,300 - 401,400	$-6°$ to $20°$
SG6040 [29]	100,000 - 500,000	$-10°$ to $20°$
SG6040 [48]	100,032 - 499,595	$-9°$ to $20°$
SG6041 [29]	100,000 - 500,000	$-10°$ to $20°$
SG6042 [29]	100,000 - 500,000	$-10°$ to $20°$
SG6043 [29]	100,000 - 500,000	$-10°$ to $20°$
SG6043 [48]	99,911 - 499,253	$-8°$ to $20°$
SH3055 [113]	100,000 - 500,000	$-10°$ to $20°$

High-incidence-angle tests:

The range of angle of attack perceived by small turbines during start-up is unusually wide. However, previous research has been mostly limited to around the stall angle, eg. [12]. There are some tests on NACA0012 section at very high Reynolds numbers (above 1,000,000) [49, 50].

After the energy crisis in the 1970s, an interest in renewable energy was initiated, particularly in wind power. Extensive researches were conducted toward the performance prediction of Darrieus turbines and some aerofoils were tested up to higher incidences [51–55]. Their Reynolds number test range is between 400,000 and 900,000 as was appropriate for large Darrieus turbines during normal operation.

In those tests, the lift curve normally exhibits a second-lift-peak behaviour at incidence angle of around 45°. The maximum drag peak of around 1.8 occurs at around 90° (Fig. 2.6).

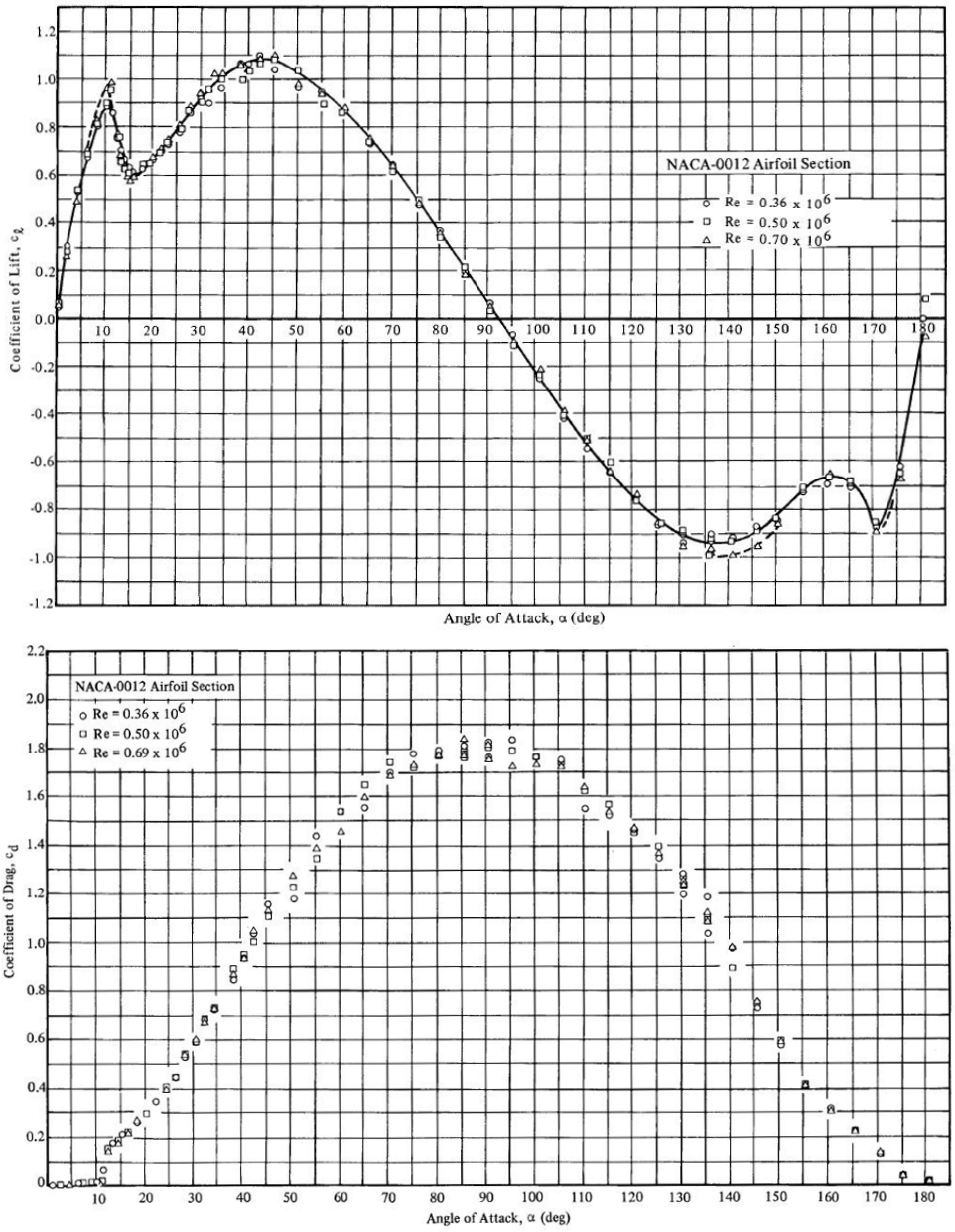

Figure 2.6: Lift and drag coefficients of a NACA0012 [51].

Two wind-turbine-dedicated aerofoils (the DU96-W-180 and the DU97-W-300) were tested for the full incidence range at Reynolds number of 700,000 by Timmer [64]. The measurements showed that different aerofoils exhibit different characteristics even fully stalled and a thicker aerofoil often generates higher lift (Fig. 2.7).

He also showed that, although aerofoils behave in a generic way in deep-stall, their characteristics are not exactly the same [56]. By comparing maximum drag coefficients of different aerofoils, he found that the maxima is related to aerofoil shape and is in a linear relation with the suction y/c value at x/c of 0.0125.

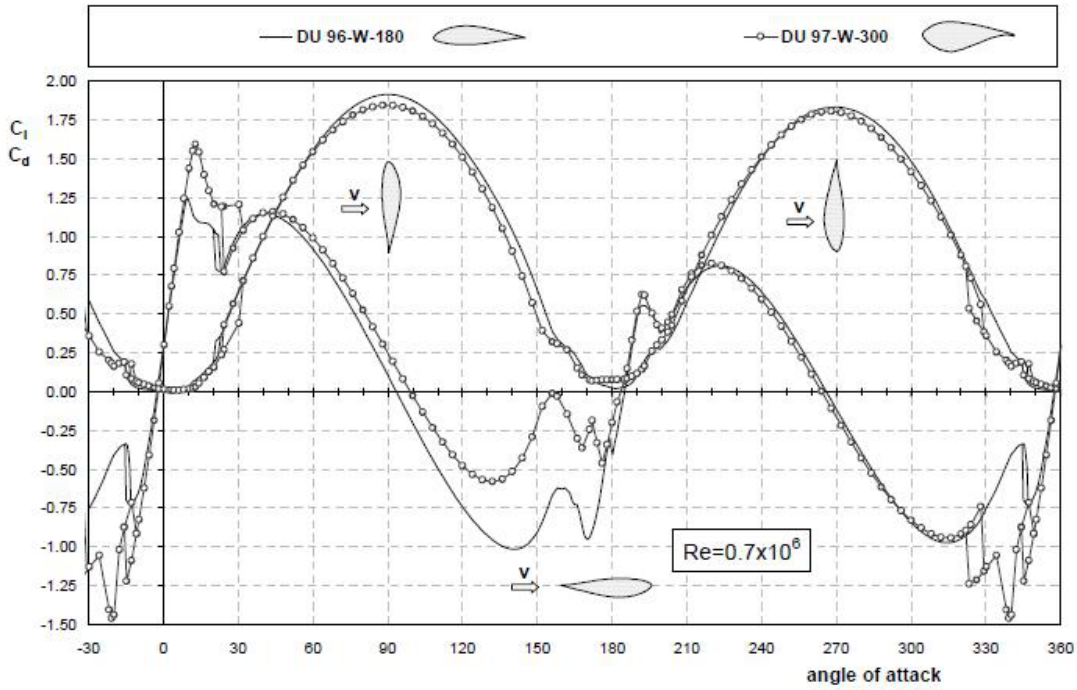

Figure 2.7: Lift and drag coefficients of two DU sections [64].

A series of high incidence measurements was also conducted at Durham University by Bickerdyke, Rainbird, and Crone [57–59]. Their experimental results did not exhibit the second-lift-peak behaviour as found by Sheldahl and Klimas [51]. Drag coefficients of their tests are nearly half of those tested by previous researchers.

Rainbird hypothesised that one of the possible causes of the difference is the effect of wind-tunnel wall proximity which was supported by experimental tests for both closed and open test sections on the same aerofoil. Figure 2.8 compares lift and drag coefficients from closed and open test sections.

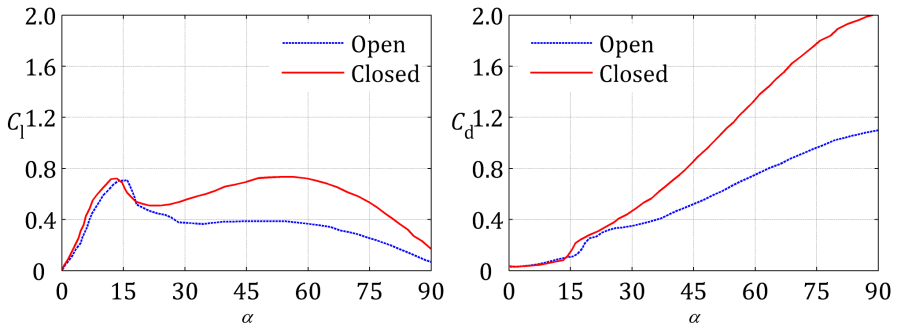

Figure 2.8: Closed and open test section aerodynamic data of a NACA0015 (from Rainbird [58]).

The results clearly indicate the influence of the wind tunnel upper and lower walls on the aerodynamic coefficients when tested at high incidences. The effect of wall proximity should be investigated in detail before conducting further high-

angle-of-attack testing. This investigation was conducted by the author and it is presented in section 6.1.

Table 2.2 summarises aerofoils that have undergone high-angle-of-attack tests together with their test conditions.

Table 2.2: High-angle-of-attack tests.

Aerofoil	Incidence range	H/C ratio[1]	Reynolds number
NACA0012 [49]	0° - 360°	n/a	2,000,000
NACA0012 [50]	0° - 180°	n/a	1,600,000
NACA0009 [51]	0° - 180°	14	360,000, 500,000, and 690,000
NACA0012 [51]	0° - 180°	14	360,000, 500,000, and 700,000
NACA0012H [51]	0° - 180°	14	360,000, 490,000, and 700,000
NACA0015 [51]	0° - 180°	14	360,000, 500,000, and 700,000
NACA0015 [51]	0° - 360°	14	1,000,000
NACA0018-64 [55]	0° - 360°	n/a	140,000 to 300,000
NACA4415 [64]	0° - 360°	7.2	1,000,000
DU96-W-180 [64]	0° - 360°	7.2	1,000,000
DU97-W-300 [64]	0° - 360°	7.2	1,000,000
NACA0018 [34]	0° - 80°	7.2	300,000 and 500,000
DU06-W-200 [34]	0° - 80°	7.2	300,000 and 500,000
NACA0012 [57]	0° - 360°	∞[2]	165,000
NACA0018 [57]	0° - 360°	∞	165,000
NACA4412 [57]	0° - 360°	∞	165,000
NACA0015 [58]	0° - 360°	∞	209,000
NACA0018 [58]	0° - 360°	∞	218,000
NACA4412 [58]	0° - 360°	∞	189,000
Flat plate [58]	0° - 360°	∞	217,000
Gottingen 407 [58]	0° - 360°	∞	208,000
NACA0018 [59]	0° - 180°	∞	194,000
S1210 [59]	0° - 180°	∞	110,000 and 190,000

2.3.5 Estimation of aerofoil data at high angles of attack

Since the data required by wind turbine analysis must cover a suitable Reynolds number range for the full 360° range of angle of incidence, estimation often has to be used in order to extrapolate these data to higher angles of attack. The estimation is normally done through the application of flat plate theory or empirical correlations [60–63].

In flat plate theory, all aerofoils are assumed to behave like a flat plate and, hence, their post-stall characteristics are independent of their shape and Reynolds number. Nevertheless, high-angle-of attack tests on some real aerofoils has revealed that different aerofoils may demonstrate significantly different characteristics from each other even when fully stalled [52–54, 64], thus casting doubt on the validity of the flat plate assumption.

[1] Or width-to-chord ratio if aerofoils are installed vertically.
[2] Half-open test section.

Wind tunnel based correlations have also been developed to predict aerodynamic coefficients at high incidence angles, including the empirical correlations developed by Spera (AERODAS) [63]. In his correlation process, selected aerofoils data at high angle of attack in a Reynolds number range from 250,000 to 2,000,000 were analysed and modelled in order to obtain expressions for aerodynamic coefficient prediction. Although the correlations provide useful information for wind turbine analysis, it is questionable whether it is possible to apply this to other aerofoils or to conditions outside this Reynolds number range, especially lower Reynolds number.

This shows that although a large amount of wind-tunnel data is available, none of them meet the required range of test conditions to fully investigate small wind turbine starting. The lowest Reynolds number tested is comparable to the Reynolds number that small wind turbine blades experience during start-up but it is limited to incidence angles only up to or slightly beyond stall angle. High incidence tests were found on some specific aerofoils such as NACA sections but their performance greatly varies from test to test. Further wind-tunnel investigations on wind turbine aerofoils at suitable conditions have to be made.

2.4 Aerofoils in Darrieus motion

Any aerofoil on a Darrieus rotor moves in a cyclical motion and experiences highly varying flow conditions when it moves along its rotational path. Such a motion introduces a periodic change in both apparent wind speed and incidence angle. In effect, dynamic stall is a common event for any aerofoil moving in Darrieus motion. Previous research showed that this is particularly the case for the Darrieus rotor operating at tip speed ratios lower than 5 [65–72]. The presence of dynamic stall at low tip speed ratios is mainly due to the fact that the incidence angle is large and the aerofoil will move across the stall angle when it rotates. The incidence variation reduces with increasing tip speed ratio and the aerofoil will eventually operate within unstalled region at sufficiently high tip speed ratios (or normal operational operation at which the flow remains attached). The effect of dynamic stall is then small at high tip speed ratios.

Apart from that, other flow features are also associated with this kind of motion such as curvilinear flow [73] and blade/wake interaction.

The earliest attempts to investigate airloads on aerofoils in Darrieus motion were made by Webster [65] and Graham [66]. Webster measured forces acting on the blade moving in cycloidal motion and visualised the flow structure. Blade loadings were measured using strain gages. Visualisation techniques used were dye injection and solid particle markers to study vortex trajectory and velocity defect in the wake, respectively. The test rotor had NACA0012 blades having a chord length of 9.14 cm and had a radius of 1.22m. It was tested at three tip speed ratios (2.5, 5.0, and 7.5). Normal and tangential forces were measured.

It was found that the delay of aerodynamic stall was observed at tip speed ratios

as high as 5.0 and became more prevalent at lower tip speed ratios. The observed delay in stall onset indicated that the dynamic stall phenomenon should be included in the analytical model.

Force measurements on Darrieus rotor blades were also conducted by Laneville and Vittecoq [67]. In this test, a Darrieus rotor equipped with NACA0018 blades was tested at tip speed ratios ranging from 2 to 5. Their results indicated that dynamic stall phenomena is prevalent when the rotor tip speed ratio is lower than 3.5.

Fujisawa et al [68–70] conducted flow visualisation and PIV measurements on a small Darrieus rotor in a water tunnel to study dynamic stall development. Their turbine is a small Darrieus rotor with NACA0018 blades having a chord of 10mm and a radius of 30mm. The tests were run at the very low Reynolds number of 3000 at tip speed ratios of 1, 2, and 3. It was found that the dynamic stall structure is independent of the tip speed ratio but its development is greatly influenced by tip speed ratios that cause different incidence angles perceived by the blade.

PIV studies were also conducted by Ferreira et al. [71, 72]. Their tests were run at a Reynolds number of around 10^5 at three tip speed ratios (2, 3, and 4). The tested rotor has one blade having a NACA0015 section. It has a blade chord length of 0.05m and a radius of 0.2m. It was tested at Reynolds number of 50,000 and 70,000. The clearest effects of dynamic stall was observed at the lowest tip speed ratio of 2.

All the research conducted on aerofoils in Darrieus motion show consistently that dynamic stall is evident. Its effect seems to be more dominant at low tip speed ratios, suggesting that it might be of significance for turbines during their start-up period; a period at which tip speed ratio is relatively low.

2.5 Unsteady aerofoil performance data

The interest of unsteady data (or dynamic stall) had its origin in the compressor and helicopter industries. In such applications, the blade is forced to travel in a cyclic motion and the blade experiences a periodic change of incidence angle. Since it had been shown that this flow phenomena is similar to the flow around a pitching aerofoil [74], many unsteady experiments were conducted with sinusoidal pitching aerofoils and dynamic stall has been extensively tested with this type of oscillation, eg. [75–77] etc.

A series of experiments were conducted on many helicopter aerofoils at very high Reynolds numbers [75–78]. Their aerofoil types and operating conditions are significantly different from those relating to small wind turbine starting behaviour and cannot be directly employed. Examples of aerofoils and test conditions are listed in Table 2.3.

Table 2.3: Helicopter aerofoils and test conditions.

Aerofoil	**Re**	**k**[1]	α_m[2]	$\Delta\alpha$[3]
Ames A-01 [75]	490,000 - 4,200,000	0.01 - 0.20	10°, 15°	2°, 5°, 10°
Wortmann FX-098 [75]	490,000 - 4,200,000	0.01 - 0.20	10°, 15°	2°, 5°, 10°
Sikorsky SC-1095 [75]	490,000 - 4,200,000	0.01 - 0.20	10°, 15°	2°, 5°, 10°
Hughes HH-02 [75]	490,000 - 4,200,000	0.01 - 0.20	10°, 15°	2°, 5°, 10°
Vertol VR-7 [75]	490,000 - 4,200,000	0.01 - 0.20	10°, 15°	2°, 5°, 10°
NLR-1 [75]	490,000 - 4,200,000	0.01 - 0.20	10°, 15°	2°, 5°, 10°
NLR-7301 [75]	490,000 - 4,200,000	0.01 - 0.20	10°, 15°	2°, 5°, 10°
NACA0012 [76]	2,500,000	0.05 - 0.25	6° - 20°	6° - 14°
NACA23012 [78]	1,500,000	0.01 - 0.20	6° - 20°	2°, 6°, 10°

Aerofoils dedicated to wind turbines were also tested by many researchers at Ohio State University [16, 79–89] and at Riso [90–95].

The S8xx aerofoil series were mainly tested at Ohio State University. Most of the tests were conducted at conditions experienced by large-scale wind turbines. The Reynolds numbers tested were in the range of 750,000 to 1,400,000. Incidence angle ranged from $-20°$ to $40°$ at two oscillation amplitudes of $\pm 5°$ and $\pm 10°$. Under the same test conditions, the unsteady effects vary and the increase in maximum lift coefficient due to unsteady effects seems to be dependent on aerofoil geometry. For example, while the lift increase is in the range from 7% to 53% for the S815, the increase is as large as 200% for the S824. One clear implication from the results is that unsteady effects are of great significance and cannot be neglected.

Numerous tests were also conducted at Riso Laboratory at small oscillation amplitudes ($\approx 2°$). Dynamic effects were clearly seen even with this small oscillation (Fig. 2.9)

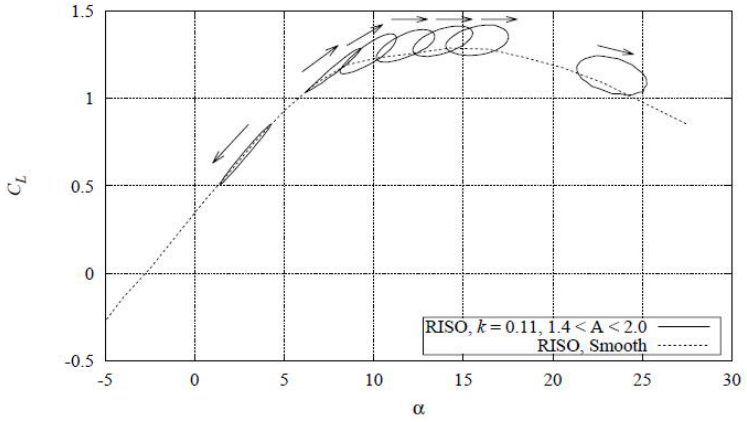

Figure 2.9: Dynamic lift behaviour of the Riso-1 aerofoil at Reynolds number of 1,600,000 and at a reduced frequency of 0.11 [90].

[1]Reduced frequency which is defined as $\frac{\omega c}{2V}$.
[2]Mean angle of attack.
[3]Oscillation amplitude.

The aerofoils and test conditions are summarised in Table 2.4.

Table 2.4: Wind turbine aerofoils and unsteady test conditions.

Aerofoil	**Re**	**k**	α_m	$\Delta\alpha$
LS(1)-0421MOD [79]	750,000 - 1,500,000	0.077, 0.11	8°, 14°, 20°	5°, 10°
LS(1)-0417MOD [80]	750,000 - 1,500,000	0.077, 0.11	8°, 14°, 20°	5°, 10°
NACA4415 [81]	750,000 - 1,500,000	0.077, 0.11	8°, 14°, 20°	5°, 10°
S801 [82]	750,000 - 1,500,000	0.077, 0.11	8°, 14°, 20°	5°, 10°
S809 [83]	750,000 - 1,500,000	0.077, 0.11	8°, 14°, 20°	5°, 10°
S810 [84]	750,000 - 1,500,000	0.077, 0.11	8°, 14°, 20°	5°, 10°
S812 [85]	750,000 - 1,500,000	0.077, 0.11	8°, 14°, 20°	5°, 10°
S813 [86]	750,000 - 1,500,000	0.077, 0.11	8°, 14°, 20°	5°, 10°
S814 [87]	750,000 - 1,500,000	0.077, 0.11	8°, 14°, 20°	5°, 10°
S815 [88]	750,000 - 1,500,000	0.077, 0.11	8°, 14°, 20°	5°, 10°
S824 [16]	750,000 - 1,500,000	0.077, 0.11	8°, 14°, 20°	5°, 10°
S825 [83]	750,000 - 1,500,000	0.077, 0.11	8°, 14°, 20°	5°, 10°
Riso-1 [90]	1,600,000	0.077, 0.11	2.8° to 23.3°	2°
FFA-W3-241 [91]	1,600,000	0.070, 0.093	2.° to 25°	1.4° to 2.0°
FFA-W3-301 [91]	1,600,000	0.09	3° to 25°	1.7° to 2.6°
NACA63-430 [91]	1,600,000	0.09	2° to 24°	1.3° to 2.1°
NACA63-415 [92]	1,600,000	0.092	1.5° to 22.8°	1.3° to 2.1°
NACA63-215 [93]	1,300,000	0.022, 0.044	−0.6° to 27.4°	2.5° to 3.0°
Riso-A1-18 [94]	1,600,000	0.09	4.3° to 28.9°	1.7° to 2.6°
Riso-A1-21 [94]	1,600,000	0.09	4.3° to 26.3°	1.3° to 2.1°
Riso-A1-24 [94]	1,600,000	0.093	4.3° to 26.3°	1.3° to 2.1°
Riso-B1-18 [95]	1,600,000	0.09	4.3° to 28.9°	1.7° to 2.6°
Riso-B1-24 [95]	1,600,000	0.09	4.3° to 26.3°	1.3° to 2.1°

It is seen from Table 2.4 that dynamic stall tests have been conducted at relatively high Reynolds numbers of around million as they were intended for large-scale machines. The maxima of mean angle of attack is around 30° and oscillation amplitudes are generally quite small. These aerofoil data are not directly applicable to small turbine starting analysis.

Unsteady tests at lower Reynolds number were conducted by Gerontakos [96]. In his test, a NACA0012 section undergoing harmonic pitching was investigated at a Reynolds number of 135,000. Unsteady parameters were set in such a way that different stall cases, namely attached flow, light-stall, and deep-stall, can be studied. He found that the unsteady behaviour is highly affected by the reduced frequency. A stall in lift was observed when the leading-edge vortex reach 90% of the chord.

This review has clearly shown that unsteady data necessary for small wind turbine starting analysis is not readily available. Dynamic stall information at low Reynolds numbers at high incidence angles is needed.

2.6 Dynamic-stall models

There exist various dynamic-stall models for unsteady airload predictions [97–102]. Some of the models rely solely on the reduction and synthesis of unsteady aero-

dynamic data [97, 99, 101] while the others try to model some important unsteady features [100, 102].

It is noted, however, that the models are in part based on wind tunnel data and some parameters have to be deduced from wind-tunnel tests of the selected aerofoil. The models are not general and they are limited to a particular aerofoil and operating conditions.

Amongst the models developed, the Leishman-Beddoes (LB) model [102] is probably the most widely used model in both helicopter and wind turbine applications. It provides a good description of the flow physics, good computational efficiency and does not require too many empirically deduced constants.

The LB model consists of three modules; namely attached, separated, and induced-vortex flows. In the attached flow module, the model is an approximation of unsteady thin-aerofoil theory which is obtained through the use of indicial response. The latter two modules account for dynamic stall behaviour which is related to flow separation and vortex formation. They model unsteady loads as a resulting effect of lags in separated flow. Vortex lift accumulation is considered as a difference between linear and nonlinear lifts.

2.7 Modifications of the Leishman-Beddoes model

Following great success in helicopter blade load predictions, the LB model has been adopted for wind turbine applications. However, some concerns about the applicability arise because the typical aerofoil used and operating conditions in wind turbine applications are different from those of helicopter applications.

One of the modifications is an extension of incidence angle. In helicopter operations, the rotor blade normally experiences angle of attack in a range of $-10°$ to $30°$ while wind turbine blades experience much larger incidence range. Wind turbine performance analysis codes require the entire range of incidence angle ($-180°$ to $180°$). One way of extending the method is to use a modified angle of attack by assuming that aerodynamic coefficients are symmetrical [103, 104]. It is noted that this assumption seems to be justified for symmetrical and low camber aerofoils that possess symmetric aerodynamic properties. The accuracy of this model is not known because of unavailability of unsteady data at high incidence angles.

Gupta and Leishman [105] had modified the LB model for wind turbine application. Dynamic stall behaviour of the S809 was modelled and validated against unsteady wind-tunnel data. They found that the S809 has stall characteristic that is different from those of helicopter aerofoil sections. It had been shown that the LB model has the ability to model unsteady airloads on the aerofoil typical for wind turbines if the static stall characteristic is satisfactorily modelled.

The LB model was also modified by Sheng et al. [106,107] for low Mach numbers. Modifications such as stall onset, reattachment from stall, a revised chordwise force, and dynamic vortex had been added to the model. The model was later used to

predict airloads on the NREL aerofoils [108].

Although the modified LB method has been proposed, it is intended for large-scale wind turbines. In order to accurately predict unsteady airloads on small turbine blades, unsteady tests of oscillating aerofoils at low Reynolds numbers with unsteady conditions normally encountered by small turbines are needed.

2.8 Conclusions

Literature pertaining to small Darrieus- and horizontal-type wind turbine for starting behaviour had been explored in this chapter. It was found that, albeit their configurations are different, the starting analysis of both machines basically requires the same source of information; low-Reynolds-number and high-angle-of-attack aerofoil performance data.

Nevertheless, a review on wind-turbine-dedicated aerofoils and their performance data reveals that almost all of the tests were conducted at relatively high Reynolds numbers at incidences up to stall or just pass the stall angle. Inconsistency in aerofoil performance data was also observed from these tests, in particular in the post-stall regimes.

Experimental investigations of aerofoils in Darrieus motion revealed that dynamic stall effects are in evidence, especially at low tip speed ratios. This leads to a further review of unsteady aerofoil performance data and dynamic-stall model. It was found that none of the existing data can be directly employed in small wind turbine starting analysis. Model modifications are also needed if one wants to apply the dynamic-stall model to the starting analysis.

To sum up, our present knowledge of small wind turbine starting behaviour is still limited and this is largely due to the lack of suitable and reliable aerofoil performance data which is not sufficiently provided by previous wind-tunnel tests.

Chapter 3

Potential Benefits Gained through Starting Capability Improvement

This chapter assesses and quantifies benefits gained through starting capability improvement. A horizontal-axis turbine is selected as a study case but it is important to note that the potential benefits gained are equally applicable to vertical-axis types as the improved starting capability *always* leads to a shorter start-up period and a longer energy-production period for both types of machines. For the case study presented here, the entire system including wind, turbine, and loads are considered. Three different blades are defined, simulated, and compared. The benefits gained are justified in terms of time-varying behaviour and Annual Energy Production.

The contents of this chapter were presented in ASME Turbo Expo 2011 in Vancouver, Canada. It has also been published in ASME Journal of Engineering for Gas Turbines and Power [109].

3.1 Modelling assumptions

3.1.1 Rotors

The starting capability of a turbine (or rotor acceleration, α) can be mathematically expressed as

$$\alpha = \frac{T_a - T_r}{J} \tag{3.1}$$

where T_a is aerodynamic torque generated by the rotor, T_r is resistive torque generated by other components, and J is the rotor inertia. It can be seen that, with constant resistive torque, the acceleration can be improved by increasing aerodynamic torque and decreasing rotor moment of inertia.

Aerodynamic torque generated by the rotor depends on many factors such as the aerofoil used and the pitch angle. There are a number of ways of generating higher starting torque. Increasing the the number of blades is one option but the disadvantage is that it also introduces additional inertia to the rotor. A further

disadvantage is that the higher number of blades (or solidity) produces a narrow power curve with a sharp peak resulting in a turbine which is very sensitive to changes in tip speed ratio [110], a configuration that is clearly not suitable for small turbines operating in turbulent areas.

It was also shown by Mayer et al. [7] that, by increasing the pitch angle, the blade would generate more torque as the blade experiences a smaller angle of attack. This also reduces the idling as the blade produces a higher lift-to-drag ratio. However, with the increase in pitch angle the turbine performance curve is shifted towards a lower tip speed ratio and so the turbine will stall earlier resulting in unsatisfactory performance at higher wind.

The second factor involved in starting is rotor inertia which is related to the blade geometry and material used as follows:

$$J = \rho \sum_{i}^{n} A_i r_i^2 \Delta r_i \tag{3.2}$$

where ρ is density of material used, r is radius, and A is cross-sectional area of blade at the radius r. It can be seen that, apart from the material used, the inertia is directly related to the blade size. The size of the rotor is determined by the chord distribution and aerofoil shape. The chord distribution is normally designed using established design procedures from the aerofoil chosen [110]. It is, therefore, reasonable to conclude that obtaining an inertia reduction is dependent on the aerofoil employed.

From these considerations, the starting capability can be improved through a careful selection of an aerofoil that exhibits high lift-to-drag ratio and has a small cross-sectional area. However, an aerofoil with a small cross-section (or thin aerofoil) is unlikely to be suitable for the root section that experiences a high bending moment. It is therefore common to employ an aerofoil with an acceptable compromise between optimal structural and aerodynamic requirements in which the same section will be employed all along the blade albeit with changing twist and chord (a "single-aerofoil" blade) [111, 112].

This raises the question as to whether it is beneficial to employ a "mixed-aerofoil" blade in which the blade profile changes along its span. Suitable aerofoils would be selected to generate high torque without introducing additional inertia or sacrificing the power-extraction performance at high wind speeds.

It should be noted that the use of mixed-aerofoil blades is not new and various series of aerofoil profiles (also called aerofoil families) have been designed for different blade sections e.g. [25, 29]. However, their impact on self-starting had not been investigated to date. An accurate estimation of their self-starting performance can only be completed if aerodynamic data is available at suitable Reynolds numbers and high angles of attack. This aerodynamic data is scarce and not readily available in the literature.

In this present work, numerical investigations of aerofoil performance using an

unsteady two dimensional Reynolds Averaged Navier Stokes (RANS) solver were performed to select promising aerofoils. The key requirement was that aerofoils should exhibit a high lift-to-drag ratio at low Reynolds number. Two promising aerofoils emerged, the SG6043 [113] and SD7062 [47], proposed by Selig. Detail of these aerofoils and their performance characteristics can be found in chapter 5 and 6.

Based upon these aerofoil data, three alternative simulated blades have been defined and their relative performance is presented here. The first simulated blade was a single-aerofoil design based upon the SD7062 aerofoil over the full span and was designed to produce 1kW at a rotational speed of 700RPM and a wind speed of 10 m/s. The blade was designed using the method described by Burton et al [110]. This blade was set at a pitch angle of 5° and is referred to as the SG blade in this study.

The second simulated blade was a mixed-aerofoil blade which was obtained by replacing the outer two-thirds of the span with the SG6043 aerofoil. The intent was to produce a high aerodynamic torque with a smaller cross-sectional area contributing to a lower inertia whilst retaining the SD7062 profile at the blade root. This blade is referred to as the MX blade in this study (Fig. 3.1).

The third blade was designed to further improve starting performance of the mixed-aerofoil blade by increasing the pitch angle to 6° to reduce high angles of attack at start-up. This design is labelled as MP in this study.

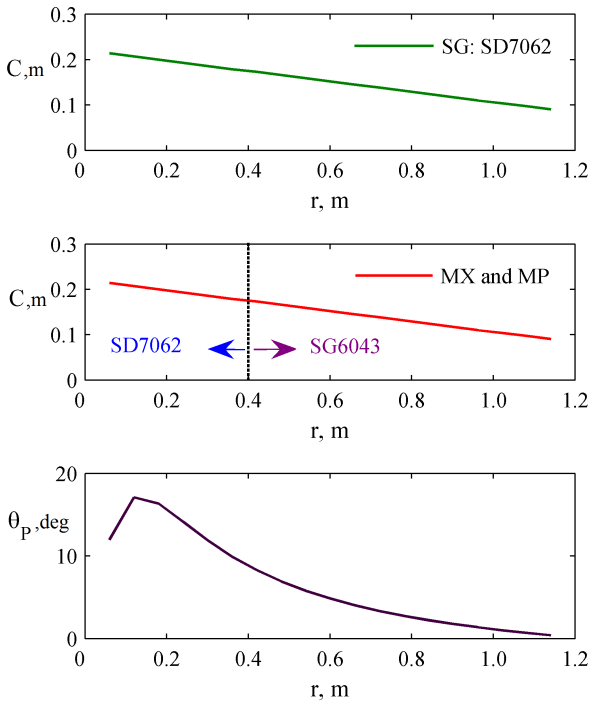

Figure 3.1: Blade geometries.

Rotor inertias were calculated using equation 3.2 and it was found that the mixed-aerofoil rotor exhibited a 21-percent reduction in moment of inertia relative to the SD7062-based single-aerofoil design (see Table 3.1).

Table 3.1: Design parameters.

Parameter	SG	MX	MP
Rated power (W)	1,000	1,000	1,000
Rated speed (RPM)	700	700	700
Rated wind (m/s)	10	10	10
Radius (m)	1.2	1.2	1.2
Aerofoil	SD7062	SD7062 + SG6043	SD7062 + SG6043
Inertia ($kg - m^2$)	2.5668	2.0287	2.0287
Pitch angle (degree)	5°	5°	6°

3.1.2 Generators and load types

Small wind turbines are most commonly coupled to permanent magnet generators [4, 114] and this study assumes the use of such generators although the analysis is easily extended to include other generator characteristics if required.

One of the inherent properties of these generators is their cogging torque that has to be overcome by the turbine. Even though recent research has shown that permanent magnet generators can be designed with no cogging torque [4], it seems reasonable to consider this cogging torque in this analysis as it remains relevant to many currently used systems.

The cogging torque created by permanent magnet generators depends on many factors such as rated size and configuration [114] and methods of calculating this cogging torque are available [115, 116]. However, detailed analysis is beyond the scope of this study and a simple estimation has been used. It has been reported that typical cogging torques of permanent magnet generators rated from 500W to 1.5kW are 0.3 to 0.6 Nm, respectively [117]. Since the turbine considered here is a 1kW device, a cogging torque of 0.45 Nm is assumed.

In addition to the cogging torque that acts when starting from rest, the generator also adds a resistive torque when rotating. In the Wright and Wood experiment [9] in which a 600W rated generator was considered, a constant resistive torque of 0.24 Nm was applied when the generator was moving. Since a larger generator is considered here, a resistive torque of 0.3 Nm was used in this study. Table 3.2 summarises all resistive torques used in this calculation.

Table 3.2: Resistive torques.

Resistive torque	Value (Nm)
Cogging torque (stationary)	0.45
Cogging torque (rotating)	0.30
Load resistive torque	load-dependent

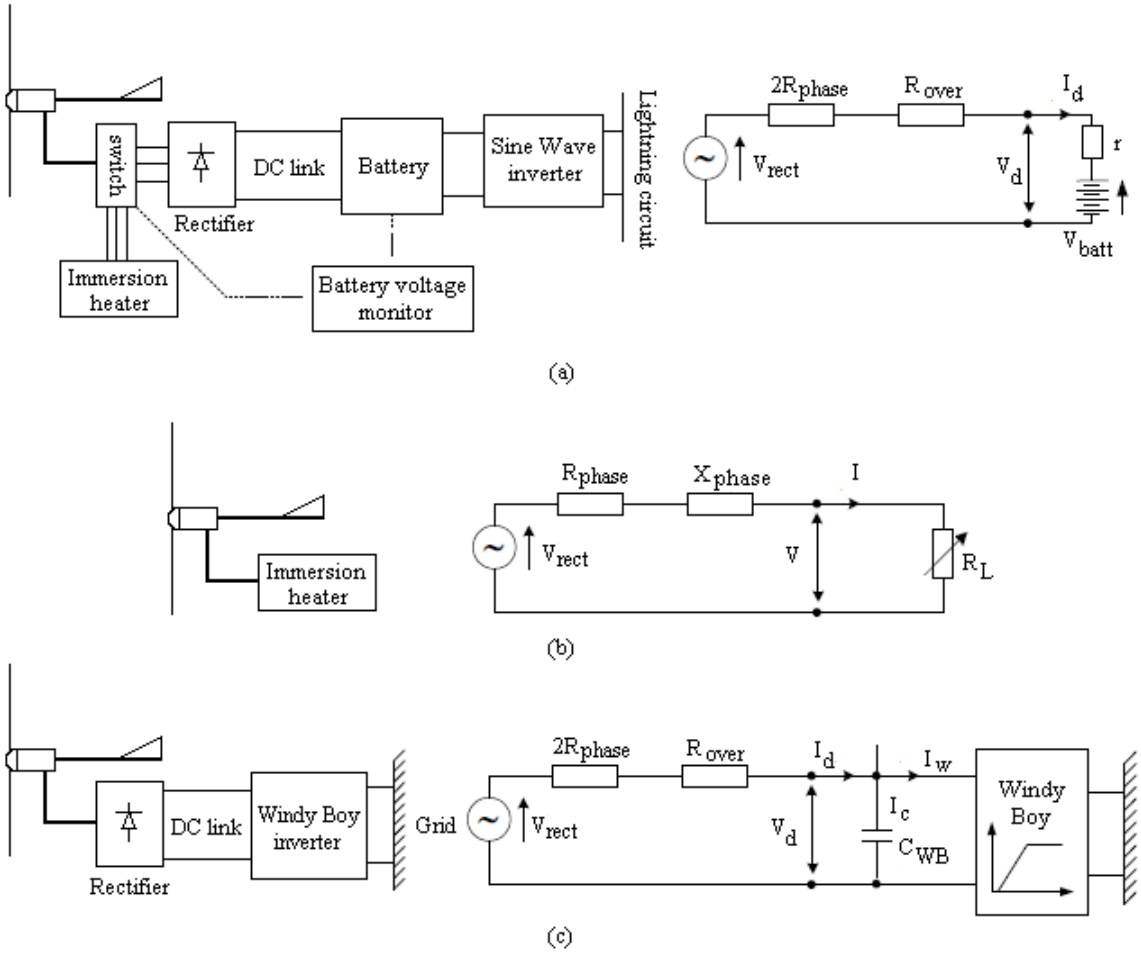

Figure 3.2: Schematic diagrams and equivalent circuits: (a) Battery charging (b) Resistive heating (c) Grid connection.

Small turbines are usually used for stand-alone applications including battery charging and resistive heating. Nevertheless, it is also possible to employ these small turbines to generate power to the grid through a grid-tie converter [118]. Load types considered in this paper are battery charging, resistive heating, and grid connection, each having different characteristics. Mathematical descriptions of these loads were obtained through the analysis of equivalent circuits. Detailed derivations and validations of these equations can be found in Stannard [118]. Figure 3.2 presents a schematic diagram of these three different loads together with their corresponding equivalent circuits.

3.1.3 Wind models

Both real and simulated wind data are used in this study. The wind data used was measured in East Kilbride, Glasgow by NaREC (National Renewable Energy Centre) covering the period from 15 May 2008 to 2 July 2009 [119]. The wind data were averaged over a five-minute interval. One-minute data is also available from

15 May 2008 to 15 June 2008. It is important to note that the real wind data has a temporal resolution of minutes but that the starting behaviour of a turbine occurs over a much smaller time scale, typically seconds. In addition the real wind data is site-specific.

A turbulent wind model simulator which was developed by Stannard [118] was employed in this simulation in addition to the real wind data as it provides the temporal resolution required (in a scale of seconds) and allows estimation of site variations.

3.2 MATLAB/Simulink implementation

The aforementioned models (rotors, loads, and turbulent wind) were individually modelled using the MATLAB/Simulink environment. Blade Element Momentum (BEM) theory was employed to estimate aerodynamic torque. Load models (battery, resistive heating, and the grid) were modelled using subsystem blocks provided by SIMULINK. The implementation of this model was based on the assumption that the system can be considered quasi-steady.

In essence, starting behavior of the turbine is modelled using a time-stepping approach. The rotational speed of the rotor at the next time step can be mathematically expressed as:

$$\omega_{n+1} = \omega_n + (\frac{T_{a,n} - T_{r,n}}{J})\Delta t_n \tag{3.3}$$

where ω is turbine rotational speed and Δt is time step used in the simulation. A variable-step was used to adjust the time as the speed changed.

The resistive torque caused by different loads is computed using the following equations:

Resistive load:

$$T_{r,n} = \frac{3K^2\omega_n}{R_L} \tag{3.4}$$

Battery load:

$$T_{r,n} = \frac{K^2\omega_n}{R_d + R_b} - \frac{V_{batt}K}{R_d + R_b} \tag{3.5}$$

Grid load:

$$T_{r,n} = (2.34K) \times \frac{2.34K\omega_n - V_d}{2R_{phase} + R_{over}} \tag{3.6}$$

$$V_d = \frac{1}{C_{WB}} \int \frac{V_{d0} - V_d}{2R_{phase} + R_{over}} - \frac{P}{\eta_{WB}V_d} \tag{3.7}$$

where K is generator constant, R_L is load resistance, V_{batt} is battery voltage, R_d is generator resistance, R_b is battery resistance, R_{phase} is generator resistance per phase, R_{over} is overlap resistance, C_{WB} is grid converter capacitance, and η_{WB} is grid converter efficiency.

A validation of the MATLAB/SIMULINK model was performed by simulating the turbine tested by Wright and Wood [9]. In their experiment, a three-bladed, 2m diameter horizontal axis wind turbine was tested under turbulent wind. The turbine was designed to produce 600W at a rotor speed of 700RPM and a wind speed of 10 m/s. Figure 3.3 compares the measured data of Wright and Wood [9] with predicted rotational speed during start-up under the same turbulent wind conditions. It can be seen that they agree satisfactorily and provide confidence that the model captures the measured starting performance correctly.

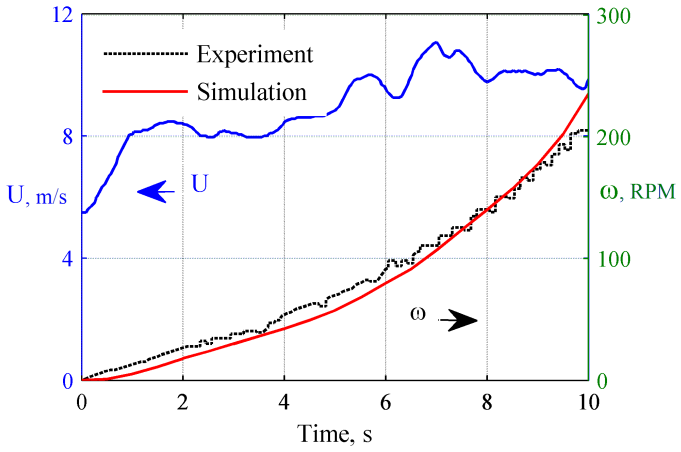

Figure 3.3: Measured and predicted rotational speed during start-up.

3.3 Results

3.3.1 Rotor performance

Power coefficients of the three rotors used in this study (calculated from Blade Element Momentum theory (BEM)) and their starting sequences under a steady wind speed of 4 m/s calculated using the model described above are presented in Figure 3.4.

For the datum, single-aerofoil case, it may be seen that a peak power coefficient occurred at a tip speed ratio of approximately six. The power coefficient curve of the mixed-aerofoil blade is higher than that of single-blade for most tip speed ratios with a maximum of a twenty-percent increase in peak power coefficient at the same tip speed ratio. With the additional increment in pitch angle provided by the *MP* blade compared to the *SG* case there is a small increase in power coefficient at low tip speed ratios but a reduced peak power coefficient at higher tip speed ratios. The start-up curves demonstrate that the mixed-aerofoil blades have a better starting performance under steady wind, roughly halving the starting time.

It is noted that the exploitation of the mixed-aerofoil blade does not lead to a faster stall and the rotor performance at high tip speed ratios is nearly identical

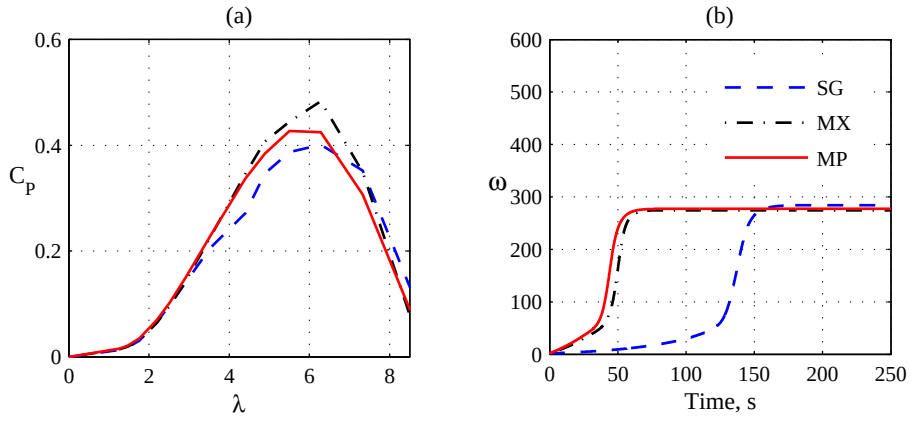

Figure 3.4: Rotor performance: (a) Power coefficients and (b) Start-up sequences under steady wind conditions.

to the single-aerofoil blade. The increase in pitch angle however affects the rotor performance at high tip speed ratios as the C_P curve is shifted to lower tip speed ratios but it is also seen that the degradation in rotor performance is offset by the higher maximum C_P (0.427 to 0.401) and better performance at low tip speeds.

In order to clearly see the effect, the integration of the C_P curves over the full tip speed ratio range, which basically represents energy capture, was made and the following values were obtained: 1.821, 1.876, and 1.984 for the *SG*, *MP*, and *MX* blades, respectively. The values indicates that the starting capability can be improved without a degradation in the overall performance if the selection of aerofoils and the increase in pitch angle are carefully made.

Figure 3.5 shows how this uplift in starting performance is achieved. Improvement of the blade aerodynamics leads to a reduced idling period. A further reduction of inertia will increase the rotor acceleration and hence shorten the acceleration period. Increase of pitch angle also further shortens the idling period but does not significantly affect the rotor acceleration.

Figure 3.6 presents time-dependent contributions of these effects (in percent) on the improved starting capability. These contributions were obtained by calculation of the change of rotational speed in Figure 3.5. The total change in rotational speeds between the datum and *MP* was first calculated then contribution of each factor was estimated. The latter calculation was performed by, for example, keeping pitch angle and moment of inertia constant whilst adding the mixed-aerofoil blade. Any difference would therefore solely be the effect of aerodynamics. Percent contributions of aerodynamic, inertia, and pitch angle were calculated by dividing the change of rotational speed caused by each factor by the total change. This calculation can be conceptually expressed as:

$$\Delta\omega_T = \Delta\omega_A + \Delta\omega_I + \Delta\omega_P \tag{3.8}$$

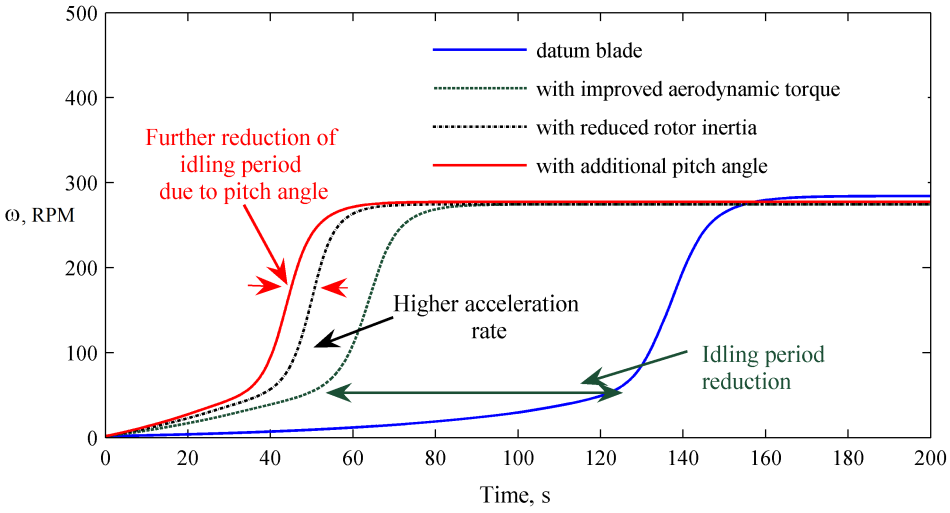

Figure 3.5: Factors contributing to the improved self-starting.

where $\Delta\omega_T$ is the total rotational speed improvement, $\Delta\omega_A$ is the rotational speed change due to aerodynamics, $\Delta\omega_I$ is the rotational speed change due to inertia, and $\Delta\omega_P$ is the rotational speed change due to pitch angle.

A percent of contribution (PC) of any improvement is then

$$PC_i = \frac{\Delta\omega_i}{\Delta\omega_T} \times 100 \tag{3.9}$$

where i denotes the appropriate abbreviation for A, I, and P (aerodynamics, inertia, and pitch improvements respectively).

It is apparent that the contribution of improved aerodynamics is low at the beginning and the main contributors for starting are the reduction of inertia and the increment in pitch angle that reduces the incidence angle experienced by the blade. After the rotor has spin, half of the improvement is provided by aerodynamic performance. The effects of pitch angle increment and reduced inertia appear again in the acceleration period and it appears that the reduction in inertia is the primary contributor in this region. The effects of inertia and pitch angle disappear when the rotor enters steady state (power-extraction performance under steady wind).

Although the *MP* blade had a lower peak power coefficient it gave the best starting characteristics. Since this was the main focus of the work, only comparisons between the *SG* and the *MP* are presented from here onwards.

3.3.2 System performance

The effects of improved self-starting capability on the system performance are evaluated in two ways; time-varying behaviour (starting sequence) and Annual Energy Production (AEP). Starting sequences will be presented under real and simulated wind conditions. Predictions of AEPs are presented to evaluate the greater energy

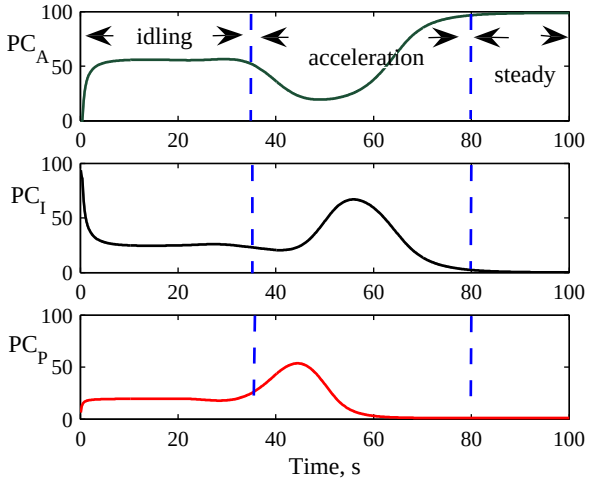

Figure 3.6: Percent of contributions.

yield that can be obtained through the improvement of self-starting.

Real turbulent wind variations In order to investigate the system performance in some detail for a reasonably long period of time, single day wind variations and turbine characteristics are shown in Figure 3.7. To illustrate turbine performance under low wind speed conditions, a day with relatively low wind speed was chosen from the measured data. For this day, the wind speed is lowest at the beginning of the day (1 m/s) but increases to around 6 m/s which is maintained with some fluctuations to the end of the day. The average wind speed is 5.135 m/s. Figure 3.7 also presents the corresponding rotor speeds for each of the three different load types and for the *SG* and *MP* cases.

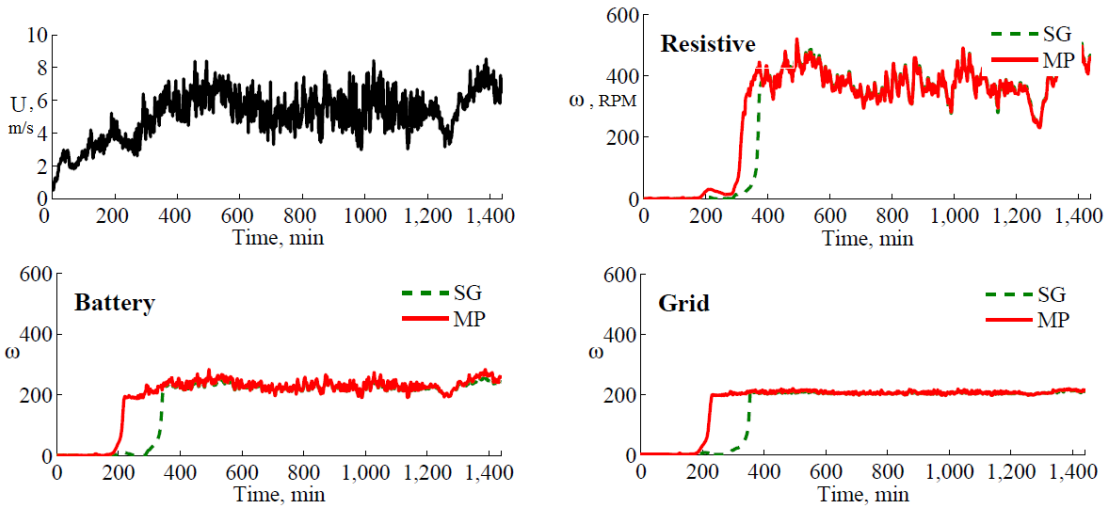

Figure 3.7: One day wind variation and turbine rotational speed for different loads.

For resistive heating, the difference between the *SG* and *MP* blades is narrower

than those of battery and grid connection cases. This is because this type of load imposes resistive torque on the turbine as soon as the turbine spins. High fluctuation can also be seen in the energy-production period.

By way of contrast improvements in self-starting can be clearly seen for the battery-charging case. For the battery, resistive torque is not imposed on the turbine until the voltage generated by the turbine exceeds the battery voltage. With more torque generated by the modified blade and no resistive torque imposed by the battery, the modified turbine manages to rotate and reach the energy-production period more quickly than the original one, resulting in a shorter starting period and longer power-extraction period. In the power-extraction period, both turbines operate with nearly constant rotational speed of around 200rpm. The corresponding tip speed ratio under the average wind speed is approximately 5.0. At this tip speed ratio, it can be seen from the C_P curve (Fig. 3.4) that the *MP* turbine has a better performance and this is reflected in a higher rotational speed during the power-extraction period. The same characteristics are seen in the grid connection case.

Simulated turbulent wind model In order to see the effect of improved self-starting at different sites simulated turbulent winds were used. These simulations provided two advantages over the real wind data: a more finely resolved time scale and the opportunity to explore different site characteristics. Two average wind speeds are explored (4 and 7 m/s) for a city center terrain which is expected to have higher turbulence level. The turbulence level is normally expressed in terms of turbulent intensity factor (k_σ) and for this city center terrain, this factor was approximated to be 0.434 [118]. It should be noted that the much smaller time interval between wind data samples required the use of a smaller overall simulation period in order to keep the output size manageable. Figures 3.8 and 3.9 present simulation results for twenty-minute periods.

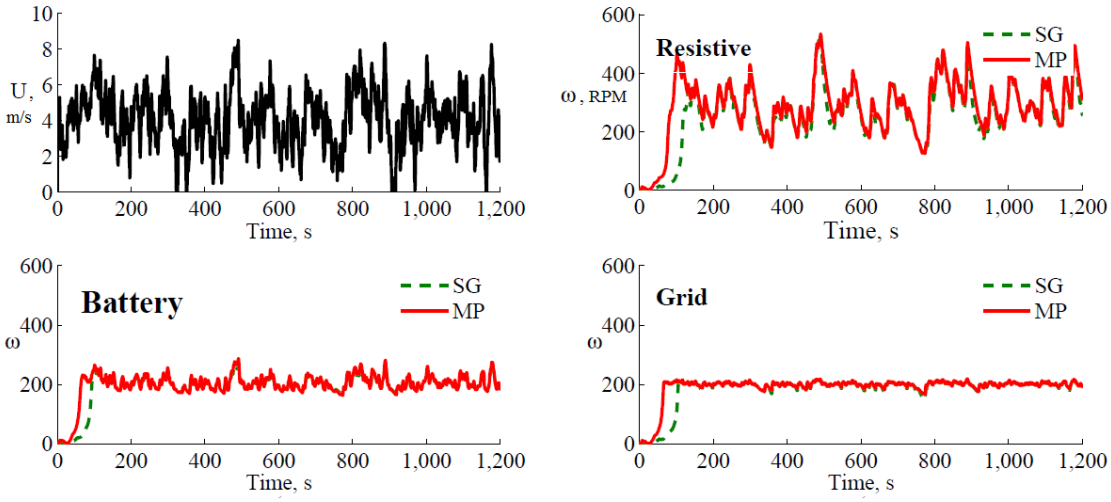

Figure 3.8: Turbine rotational speed at an average wind speed of 4 m/s.

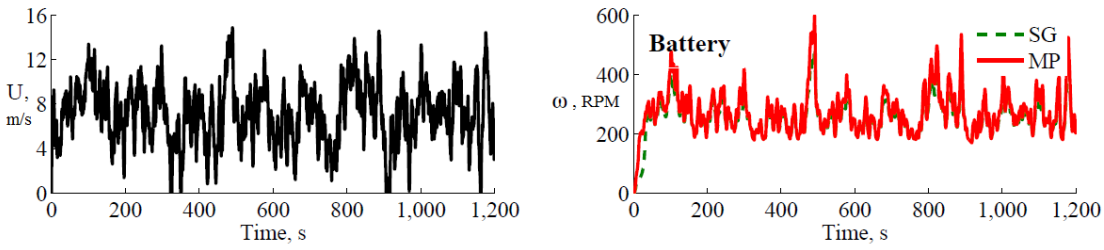

Figure 3.9: Turbine rotational speed at an average wind speed of 7 m/s.

Generally, it can be seen that the turbine behavior is comparable to the real turbulent wind simulations. In the low wind simulations, the turbines begin to spin when there is a sudden increase in wind speed (or gust) from around two to five m/s that occurs at around 50 seconds into the simulation (Fig. 3.8). The modified blades manage to quickly capture the wind and accelerate themselves while the single blade suffers a longer idling period. Some useful energy is also produced in this region by the modified blades. After both blades have gone through the acceleration phase, it appears that they have comparable energy-production performance. The difference in starting behavior between the two turbines is reduced when the average wind speed is higher as can be seen in Figure 3.9 (only battery case is presented).

Effects of loads on the turbine operating condition In order to compare and show deviations in turbine behaviour when connected to different loads, a normalised rotational speed is plotted and presented in Figure 3.10.

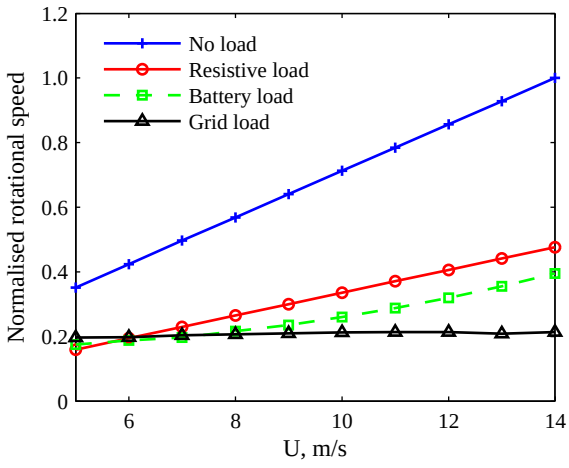

Figure 3.10: Load effects on turbine rotational speed.

The figure clearly shows that the loads have a significant influence on the system operational speed and if these loads are not considered, the operational speed will not reflect the real behavior.

It is also observed that the system characteristic varies from load to load. For

the resistive case, the operational speed increases linearly with wind speed and this often leads to a high fluctuation in rotational speed under turbulent wind, see Figure 3.7 for example. While the turbine connected to a battery exhibits a moderate increase in rotational speed, the turbine connected to the grid exhibits a nearly constant rotational speed. The load characteristics, namely the voltage of the battery and the current control features of the grid converter [120] make them operate with a nearly constant rotational speed (Fig. 3.7). One clear implication from this consideration is that if the load is not considered, estimations of rotor speed and energy production will be misleading. Such estimations do not reflect the real improvement gained from the blade design.

3.4 Annual Energy Production (AEP)

In order to quantify the potential benefits of improved self-starting, energy production of the turbines was estimated using both the measured and simulated wind data (Weibull distribution method).

It is important to note that the benefits of starting improvement can be best evaluated by simulating the turbine for a whole year. It is however computationally expensive. The AEP method used in this evaluation is a steady-state method in which transient effects are not included. This is due to the fact that the Weibull function is obtained by 'binning' the wind variation and basically shows how 'frequent' the wind speed occurs (not how fast the wind has changed, for example, from 4 to 5 m/s). With this characteristic, the improved starting which is closely related to how fast the turbine responds to the wind change is not included and the two turbines are assumed to have the same idling and energy-production periods.

It is fortunate however that the turbine with improved starting always has a longer energy-production period which leads to an additional power generation which is not included in this steady-state evaluation. Any increase obtained by this steady-state prediction is therefore sufficient to quantify the benefits of improved starting.

Due to the lack of one-minute data over a year, energy production was calculated over one-month in order to evaluate the effect of different time intervals of measured wind data on the evaluation of improved starting on energy production.

One-minute and five-minute measured wind data have been processed to obtain probability distributions (Fig. 3.11). One-month energy productions for both data sets are listed in Table 3.3. Scale and shape factors (calculated by the maximum likelihood method [121]) are as follows: $c = 5.55$ and $k = 2.46$ for one-minute data and $c = 5.53$ and $k = 2.56$ for five-minute data. It appears that the two time intervals give nearly identical probabilities and energy productions indicating that they can be used interchangeably to evaluate effects on improved starting performance on energy yield prediction.

Further estimations on Annual Energy Production were performed using Weibull distribution functions. The AEP can be calculated from:

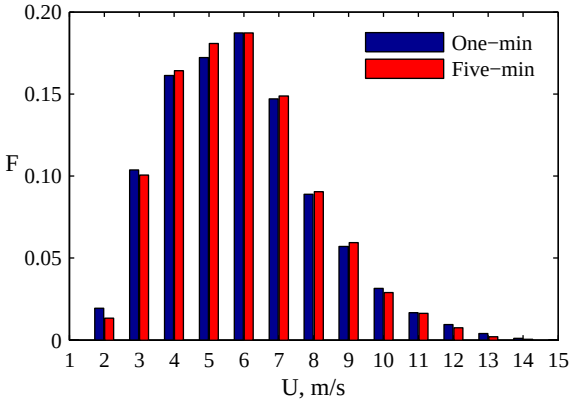

Figure 3.11: Wind data probabilities.

Table 3.3: Energy production (kWh) and net energy changes (%).

Data set	Battery			Resistive			Grid		
	SG	*MP*	%	*SG*	*MP*	%	*SG*	*MP*	%
One-min	78	91	17	35	37	5	152	201	32
Five-min	76	89	17	34	36	6	150	200	33

$$AEP = 8760 \sum_{V_{start}}^{V_{stop}} P(v_i)F(v_i) \tag{3.10}$$

where V_{start} is the cut-in wind speed, V_{stop} is the cut-out wind speed, P is power produced by the turbine at a specific wind speed, and F is Weibull distribution function. The Weibull distribution of any wind variation at a site can be expressed in the form

$$F = (\frac{k}{c})(\frac{v}{c})^{k-1} \exp[-(\frac{v}{c})^k] \tag{3.11}$$

where v is wind speed, c is a scale factor, and k is a shape factor. The scale and shape factors are site-specific and are related to each other as follows:

$$v = c\Gamma(1 + \frac{1}{k}) \tag{3.12}$$

where Γ is the gamma function. It can be seen that the value of c is proportional to the average wind speed and it can be interpreted as a characteristic speed of the site while the k factor defines the uniformity of the wind and, hence, the shape of distribution. The site parameters used in this estimation are defined and tabulated in Table 3.4.

The first two Weibull distributions are defined to represent low wind speeds (4 m/s) at different sites having different wind distribution ($k = 1.2$ and $k = 2.0$). The others are defined to represent higher wind speed (10 m/s) at the same sites.

Table 3.4: Site parameters.

Sites	c	k
Low wind with low uniformity (LWL)	4.25	1.2
Low wind with high uniformity (LWH)	4.51	2.0
High wind with low uniformity (HWL)	10.62	1.2
High wind with high uniformity (HWH)	11.28	2.0

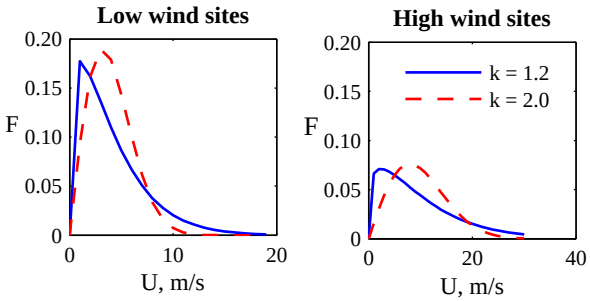

Figure 3.12: Weibull distributions.

The cut-out wind speed is assumed to be 20 m/s for all turbines. The Weibull distributions are presented in Figure 3.12. Power curves of the turbines connected to different loads are shown in Figure 3.13. From the wind distributions and the power curves, the energy captured over a year was evaluated assuming that there would be no outages for planned or unplanned maintenance. Table 3.5 lists AEPs and net energy changes of all cases.

Table 3.5: Annual energy production (kWh) and net energy changes (%).

Case	Battery			Resistive			Grid		
	SG	*MP*	%	*SG*	*MP*	%	*SG*	*MP*	%
LWL	846	993	17	404	412	2	1403	1807	29
LWH	630	727	15	264	294	12	1181	1657	40
HWL	245	280	14	1261	1219	-3	2988	3657	22
HWH	351	405	16	1822	1751	-4	4393	5287	20

For resistive heating, the two curves are nearly the same. An improvement from the modification of the blade from single to mixed-blade design is only seen at the low wind speed of 4 m/s and is very small. The power generated by the modified blade is very slightly lower than the original at higher wind speeds. This is mainly because of the resistive torque that is exerted on the turbine by the load. In resistive heating, this resistive torque will act on the turbine as soon as the turbine spins and continuously increases with rotational speed. At high rotational speed, the modified blade will not produce as high a torque as the original because the blade at the root will stall and this results in a smaller net torque and a modest reduction in energy production.

For the battery case, both blades begin to produce useful power at 4 m/s but

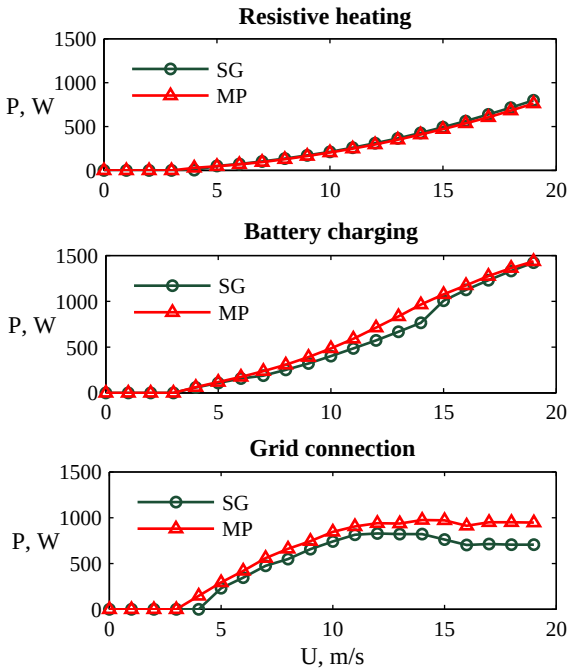

Figure 3.13: Power curves.

the modified blade produces higher power for all wind speeds. The most significant improvement is found in the grid connection case. The modified version outperforms the original one for all wind speeds.

Generally, it can be seen that increases are found for most cases using the modified blade geometry except the resistive load at high wind speed. Comparisons of net changes in energy production using measured wind data and simulated Weibull distributions show that they are in the same order. Though of course the high temporal resolution model provides a means of actually physically realizing changes in power curves via aerodynamic designs.

3.5 Conclusions

The effects of improved starting capability on energy production of small HAWTs had been evaluated in this chapter. The evaluation has clearly demonstrated that starting performance of the wind turbine is significant on the overall energy yield and improved starting capability can increase energy yield by up to 40%. This result explains why the subsequent research in this thesis is significant and the consideration of the turbine starting behaviour will lead to a useful contribution to wind energy research.

However, the improvement of starting capability cannot be successfully made until its fundamental starting characteristic is well-understood. The next chapter focuses on the complex starting behaviour of H-Darrieus turbines.

Chapter 4

The Physics of H-Darrieus Turbine Self-starting Capability

This chapter examines self-starting behaviour of the H-Darrieus turbine. It presents an analysis of the aerofoil that undergoes Darrieus motion with particular attention to the decomposition of the Darrieus incidence angle into two separate angles, introducing the analogy between the aerofoil in Darrieus motion and flapping-wing mechanism. Based upon the analogy, the understanding of the flow physics and its influences on torque development can be explored.

The contents of this chapter were presented in ASME Turbo Expo 2012 in Copenhagen, Denmark [122].

4.1 Kinematics

In order to understand the starting behaviour, it is useful to consider flow conditions experienced by the Darrieus blade when it rotates around its vertical axis. The consideration presented herein is based upon the sign convention defined in Figure 4.1. Discussions are made in terms of apparent wind, incidence angle, and reduced frequency.

From the sign convention, the relative wind speed and incidence angle that the blade experiences can be calculated from the following equations.

$$W = V \times \sqrt{\lambda^2 - 2\lambda\cos\theta + 1} \tag{4.1}$$

$$\alpha_D = \arctan\left[\frac{\sin\theta}{\lambda - \cos\theta}\right] \tag{4.2}$$

where V is free-stream velocity, θ is azimuth angle, and λ is tip speed ratio. Figure 4.2 presents variations of apparent wind speed and incidence angle.

Figure 4.2a shows that the variations of the apparent wind is periodic and has a maximum at the azimuth angle of 180° when the blade moves windward. One

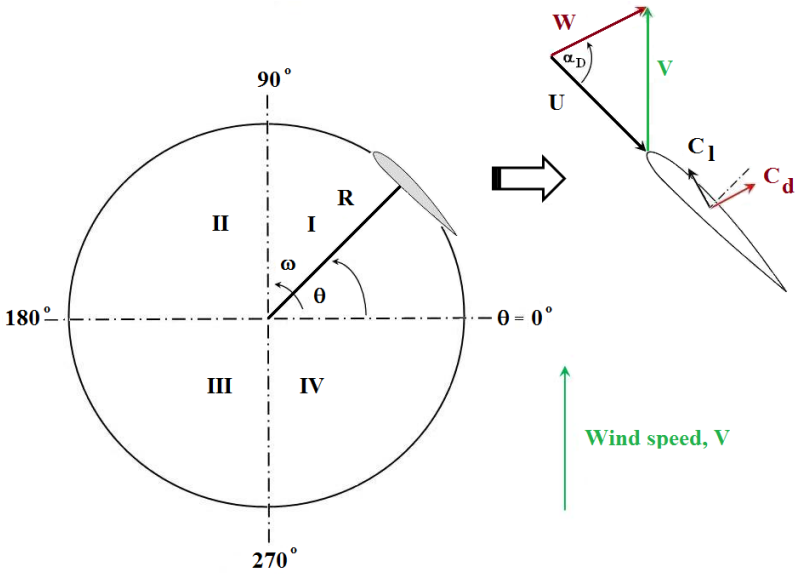

Figure 4.1: Sign convention.

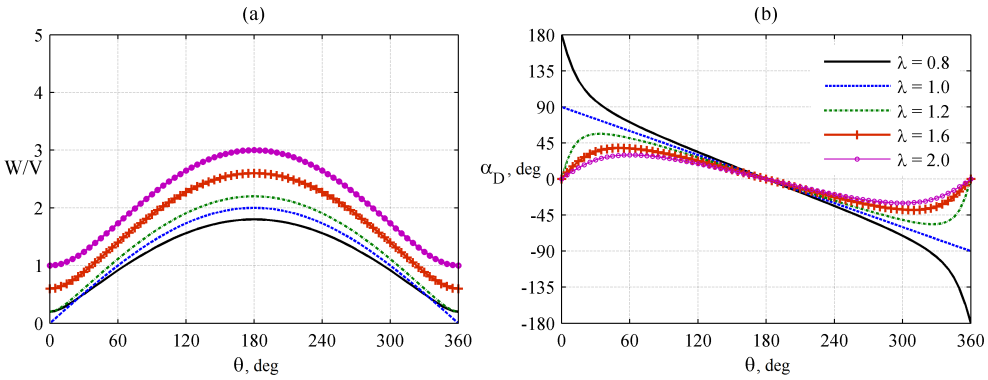

Figure 4.2: Flow conditions (a) Ratio of apparent wind speed to free stream wind speed and (b) incidence angle variation.

special case occurs at a tip speed ratio of one when the relative wind speed becomes zero at an azimuth angle of 0°.

In terms of incidence angle, it can be seen that the incidence variation is large and strongly dependent on the tip speed ratio. Figure 4.2b also shows that the incidence change roughly follows a cotangent curve when the tip speed ratio is between 0 and 1. Beyond the unity-tip-speed ratio, the variation follows a sine-like curve but it is not perfectly sinusoidal suggesting that the motion can be decomposed into further components; not only pitch.

Further analysis shows that the deviation is due to the change of translational speed that the aerofoil experiences when moving along its rotational path ($U - V\cos\theta$) (Fig. 4.3). This change in translational speed effectively induces an additional velocity normal to the aerofoil and the aerofoil apparently experiences heave (or plunge) movement, effectively making the Darrieus blades operate with a 'combined' pitch and plunge motion. This kind of motion is typically referred as 'flapping

foil' which is analogous to the mechanism that fish and birds employ to generate propulsion (see [123], for example).

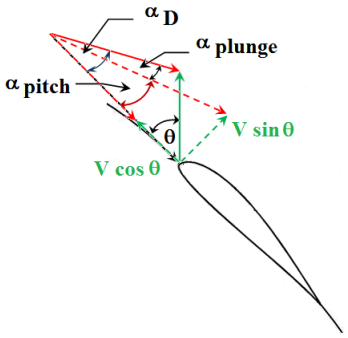

Figure 4.3: Pitch and plunge components in Darrieus motion.

With this information, the incidence angle for each component can be broken down. The following equations are applied to calculate pitch and plunge components.

$$\alpha_{pitch} = \arctan\left(\frac{\sin\theta}{\lambda}\right) \tag{4.3}$$

$$\alpha_{plunge} = \arctan\left(\frac{\sin\theta\cos\theta}{\lambda^2 - \lambda\cos\theta + \sin^2\theta}\right) \tag{4.4}$$

where α_D is incidence angle of the Darrieus motion, α_{pitch} is the pitch component, and α_{plunge} is the plunge component. Figure 4.4 presents an example of pitch and plunge components.

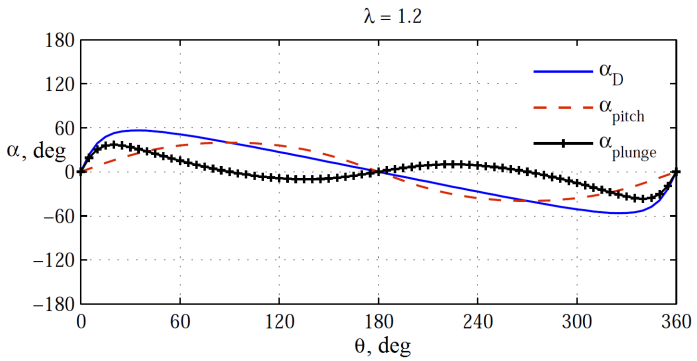

Figure 4.4: Pitch and plunge components in Darrieus motion at a tip speed ratio of 1.2.

It can be observed from Figure 4.4 that the pitch component always follows the sine curve. The two components reach their peaks at different azimuth angles (for $\lambda = 1.2$, at azimuth angles of 20° and 90°, respectively). This difference is typically termed the 'phase shift' in the study of fish propulsion and flapping wings [124]. It is one of the important parameters that governs the generation of thrust.

The reduced frequency (level of unsteadiness) can be expressed in terms of tip speed ratio as

$$k = \left[\frac{c}{D}\right] \times \left[\frac{\lambda}{\sqrt{\lambda^2 - 2\lambda\cos\theta + 1}}\right] \tag{4.5}$$

where c is aerofoil chord, and D is diameter.

The expression indicates that the level of unsteadiness at a specific tip speed ratio is dependent on rotor geometry c/D and the blade position relative to the wind. Figure 4.5 presents variations of reduced frequency at tip speed ratios of 1 and 1.2 and c/D ratios of 0.05, 0.10, and 0.15 (only up to the azimuth angle of 180° because of its symmetry). The unsteadiness is small and can be treated as quasi-steady when the reduced frequency is lower that 0.05 [15].

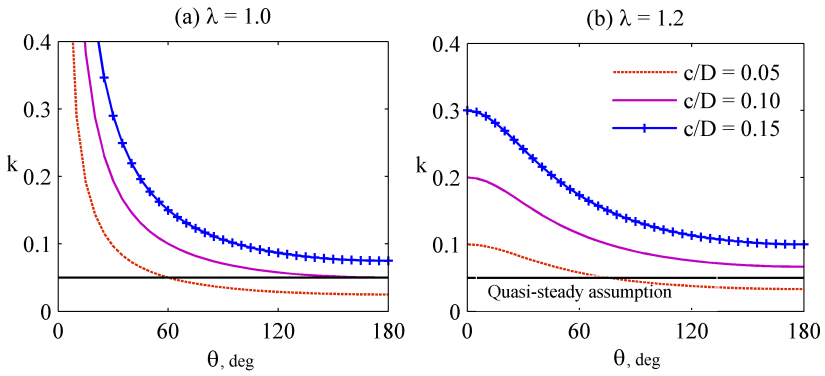

Figure 4.5: Reduced frequency as a function of λ and c/D.

4.2 Analogy to flapping-wing mechanism

4.2.1 Flapping wing aerodynamics

Basically, the flapping-wing mechanism involves two stages: the down and upstrokes. During each stroke, the angle of attack changes (Fig. 4.6). If an aerofoil is used to represent the tail, it can be seen that the aerofoil pitches and moves up and down at the same time. Previous studies have shown that thrust force generated by each stroke is different and majority of the thrust is generated during down-stroke (Fig. 4.6) [125–127].

With the continuously changing incidence angle, the flow cannot establish itself immediately to the new equilibrium because of its viscosity, causing unsteady flow. According to Dickinson et al [123], the unsteady flow phenomena associated with flapping wings are the formation of a leading-edge vortex, rotational circulation, and wake capture.

The formation of leading-edge vortex occurs when the aerofoil suddenly moves to a higher incidence angle. Such motion increases the relative velocity which induces

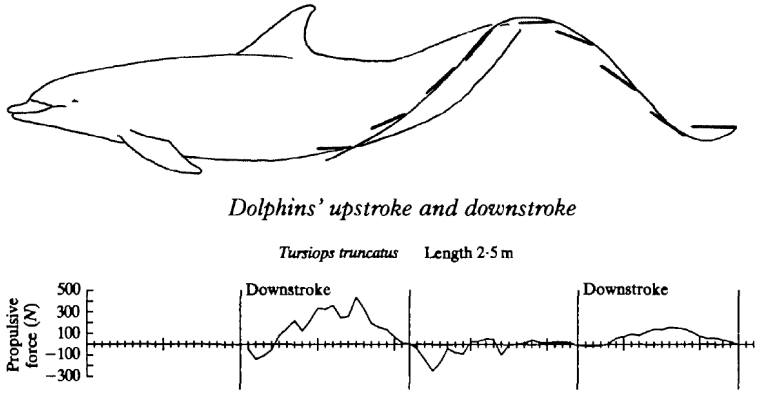

Figure 4.6: Dolphins dynamics during up- and down-stroke (adopted from [128] and [126])

more negative pressure on the suction side (leading-edge vortex) and the stall is delayed, resulting in the continuous generation of lift. This flow phenomena is the so-called 'dynamic stall' which occurs not only in nature but also in mechanical aerodynamic systems such as helicopter rotors [15]. Although this vortex occurs on both the up and downstrokes, it was found that the formation is stronger during down-stroke as it stays attached to the wing for a greater part of the stroke [129].

While dynamic stall takes place during the stroke, the rotational circulation occurs when the wing reaches the end of the stroke. At the end of the stroke, the angle of attack of the wing suddenly changes in order to perform the next stroke and this sudden change adds rotation to the wing, causing the air to flow suddenly to the suction side and additional lift is produced. Dickinson et al [123] said that this is similar to the Magnus effect on a spinning ball where a circulation is generated by rotation. It is then called 'rotational circulation'.

Apart from these two phenomena, Dickinson et al also pointed out that there is an interaction between the wing and the wake. The wake from the previous stroke meets the wing during the current stroke and effectively changes the flow that the wing sees at a particular time.

Another important flow feature associated with flapping wing is wake formation and a 'reverse' von Karman vortex street [124, 130, 131]. Experiments by Lau et al. [130] and Godoy-diana [131] have shown that this phenomenon depends on Strouhal number. At low frequency (Strouhal number is less than 0.2), the flow produces a 'classical' von Karman vortex street as found in bluff body flow [132], resulting in drag instead of propulsion. With increasing Strouhal number, the wake will enter transition and then propulsion zones. In the propulsion zone, the vortex street forms a 'reverse' von Karman vortex street and effectively produces propulsion.

The reverse von Karman vortex street consists of two row of vortices just as the classical one but of different sign and these rotating vortices produce a jet-like wake downstream. Observations of flying and swimming animals consistently show that they operate within a narrow optimal range of Strouhal number around 0.25 to 0.35

(i.e. [124, 133]).

The ability of flapping wings to generate propulsion also depends on their angle of attack. A parametric study by Anderson et al. [124] shows a good summary of these parameters (Fig. 4.7). The figure was divided into six regions, denoted from A to F. The most effective region for generating thrust force lies within region C. In this region two vortices form at the leading edge and the trailing edge. The two vortices then merge and introduce a large negative pressure on the suction side. This condition occurs when the aerofoil flaps at sufficiently large angle of attack and at sufficiently high frequency.

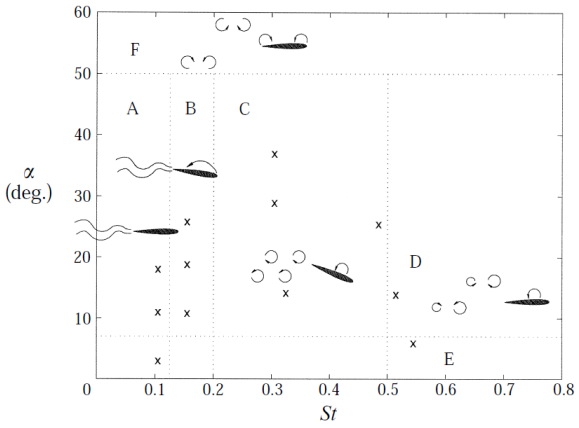

Figure 4.7: Wake patterns (from [124]).

The magnitude of wake is not constant over the wingbeat cycle. Wake measurements on bird's flying at low and high speeds revealed that birds employ different strategies when flying at different speeds, leading to different wake structures (Fig. 4.8).

The first wake to be shown (Fig. 4.8A) is called vortex-ring gait which is caused by a discrete thrust. The wake structure changes to continuous vortex when birds fly at a sufficiently high speed. Here, wings are active in both down- and up-stroke and wake is continuously generated (continuous vortex gait).

In summary, the wingbeat cycle of flapping wings consists of up- and downstroke where flow structures are different as characterised by different wake structures. These characteristics will be used in the next section to understand the flow physics associated with Darrieus blade.

4.2.2 Darrieus flight path and flow physics

In order to clearly demonstrate the analogy and to apply this knowledge to Darrieus rotor analysis, the Darrieus flight path is divided into equivalent up- and downstrokes (Fig. 4.9). The movement of the blade from quadrant 4 to quadrant 1 can be interpreted as the up-stroke and the movement from quadrant 2 to 3 can be interpreted as the down-stroke. The end of each stroke occurs at around the azimuth angle of around 90° and 270°; the magnitude is dependent on tip speed

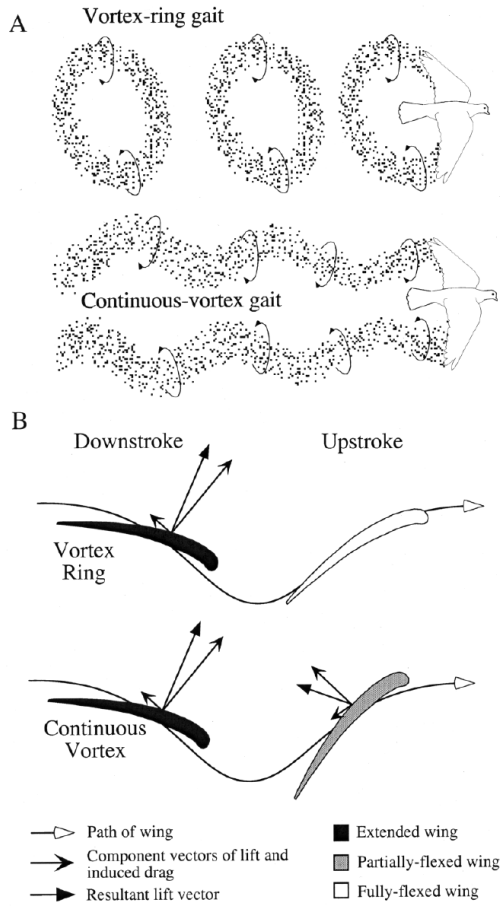

Figure 4.8: Bird gait change [136].

ratio. A detailed sketch of an aerofoil in flapping motion by using pitch and plunge components calculated from Eqs. 4.3 and 4.4 at a tip speed ratio of 1.6 is presented in Figures 4.10 and 4.11. This tip speed ratio is specifically selected because thrust measurements are available at this condition. It can be easily seen that the aerofoil in Darrieus motion effectively operates with flapping motion.

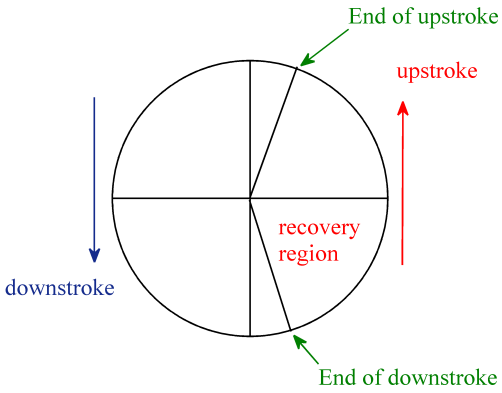

Figure 4.9: Darrieus flight path and its analogy to flapping wings.

Azimuth angle	Pitch	Plunge	Flow features	Aerofoil motion
$\theta = 90^\circ$	Maximum (positive)	Neutral	· Vortex convection · $\alpha_D = 32^\circ$	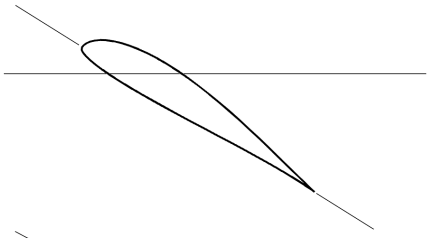
$90^\circ < \theta < 115^\circ$	Decreasing	Decreasing	· Vortex convection · $32^\circ < \alpha_D < 24^\circ$	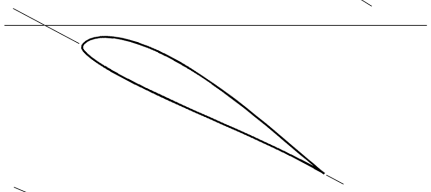
$\theta = 135^\circ$	Decreasing	Maximum (negative)	· Begin entering unstalled regime · $\alpha_D = 17^\circ$	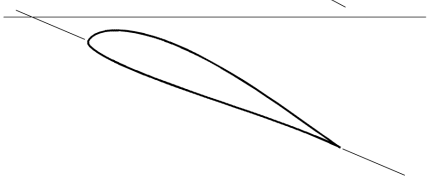
$135^\circ < \theta < 180^\circ$	Decreasing	Increasing	· Unstalled · $0^\circ < \alpha_D < 17^\circ$	
$\theta = 180^\circ$	Neutral	Neutral	· Unstalled flow · $\alpha_D = 0^\circ$	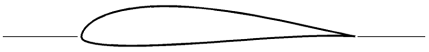
$180^\circ < \theta < 225^\circ$	Decreasing	Increasing	· LE formation (pressure side) · Delayed stall · $-17^\circ < \alpha_D < 0^\circ$	
$\theta = 225^\circ$	Decreasing	Maximum (positive)	· LE formation (pressure side) · Delayed stall · $\alpha_D = -17^\circ$	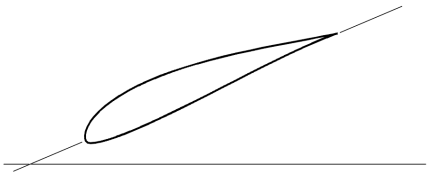
$225^\circ < \theta < 270^\circ$	Decreasing	Decreasing	· LE formation (pressure side) · Delayed stall · $-32^\circ < \alpha_D < -17^\circ$	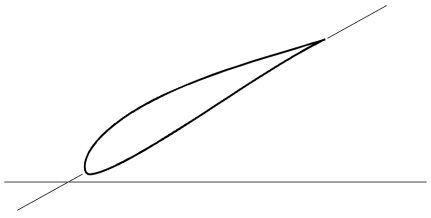

Figure 4.10: Summary of aerofoil motion and flow associated at a tip speed ratio of 1.6: downstroke.

Azimuth angle	Pitch	Plunge	Flow features	Aerofoil motion
$\theta = 270^{\circ}$	Maximum (negative)	Neutral	· LE formation (pressure side) · Delayed stall · $\alpha_D = -32^{\circ}$	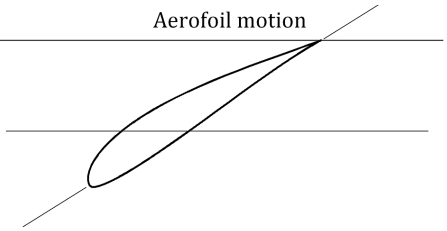
$270^{\circ} < \theta < 330^{\circ}$	Increasing	Decreasing	· Vortex shedding · Rotational circulation · $\alpha_{D,\,max} = -38^{\circ}$	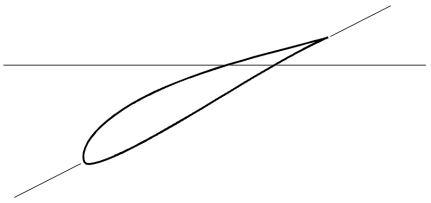
$\theta = 330^{\circ}$	Increasing	Maximum (negative)	· Completely stall · $\alpha_D = -34^{\circ}$	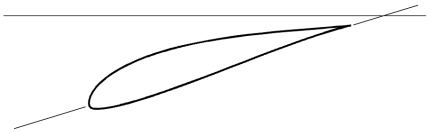
$330^{\circ} < \theta < 360^{\circ}$	Increasing	Increasing	· Completely stall · $-34^{\circ} < \alpha_D < 0^{\circ}$	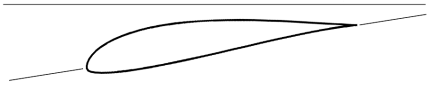
$\theta = 0^{\circ}$	Neutral	Neutral	· Unstalled flow · $\alpha_D = 0^{\circ}$	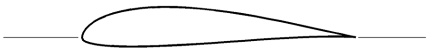
$0^{\circ} < \theta < 30^{\circ}$	Increasing	Increasing	· LE formation · Delayed stall · $0^{\circ} < \alpha_D < 34^{\circ}$	
$\theta = 30^{\circ}$	Increasing	Maximum (positive)	· LE formation · Delayed stall · $\alpha_D = 34^{\circ}$	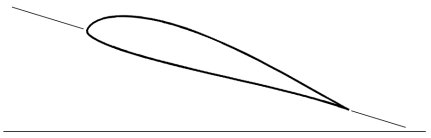
$30^{\circ} < \theta < 90^{\circ}$	Increasing	Decreasing	· Vortex convection · $\alpha_{D,\,max} = 38^{\circ}$	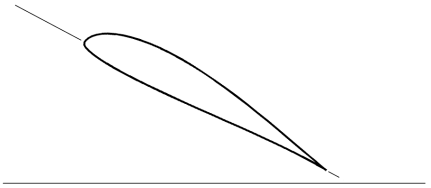

Figure 4.11: Summary of aerofoil motion and flow associated at a tip speed ratio of 1.6: upstroke.

The insights into the analogy can be used to explain the driving torque characteristics of a vertical axis wind turbine. The Darrieus flight path and the thrust force measurements of Tullis et al [134] and Hsieh [135] have been divided into effective up-stroke and down-stroke phases (Fig. 4.12). Their rotors are equipped with NACA0015 blades with c/D ratios of 0.075 and 0.16, respectively.

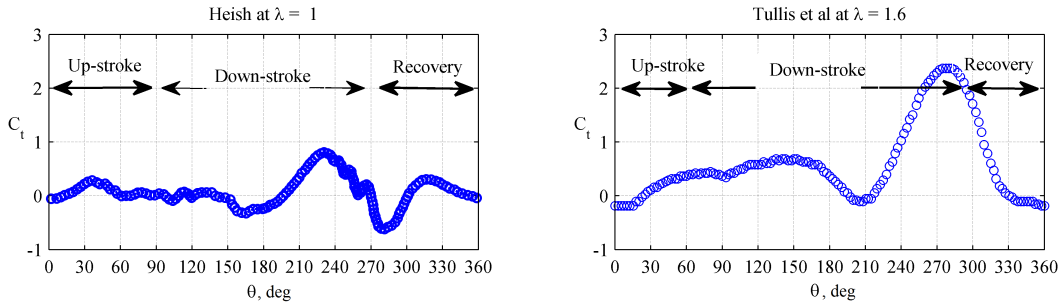

Figure 4.12: Thrust development by Darrieus blades at tip speed ratios of 1 and 1.6.

It can be seen from Figure 4.11 that the aerofoil is flapping up and the incidence increases (azimuth angles between 0° and 60° of quadrant 1). Although the flow is attached in the first region of the quadrant, the thrust force is small. This small force is due to the fact that the incidence angle is low and the lift force generated is nearly perpendicular to the aerofoil. The aerofoil continues to move and the incidence angle increases and finally exceeds the stall angle. However, the formation of a leading edge vortex delays the stall and promotes more negative pressure on the suction side and, hence, more lift and thrust. This process continues until the aerofoil reaches the end of upstroke. The measurement of Tullis et al shows higher thrust coefficient than that of Hsieh's measurement and this is because of a higher c/D ratio ($c/D = 0.16$ and 0.075 for Tullis et al and Hsieh, respectively). In addition, the blade also operates at a higher tip speed ratio at which incidence angle range is smaller.

The downstroke takes place when the aerofoil begins flapping down. The driving force generated in this region depends on the strength of the vortex and incidence angle that the blade experiences in the up-stroke. At a low tip speed ratio, the up-stroke will end with a large angle of attack (for example, 56° at a tip speed ratio of 1.2) and the vortex that forms during the up-stroke will be shed during up-stroke. This motion stalls the blade and leads to a small thrust (between 90° to 180° in Heish's measurement). In contrast, at the tip speed ratio of 1.6, the incidence angle range is smaller (around 38°) and the vortex will stay attached on the aerofoil surface until the blade enters its down-stroke and flaps down. This causes the vortex to convect along the aerofoil surface and this effectively induces more negative pressure on the suction side and hence a continuous production of thrust.

After the blade reaches the azimuth angle of 180° (or the neutral position), the blade continues flapping down and enters quadrant 3. When the aerofoil enters this

quadrant, thrust generated is mirrored (symmetrical aerofoils exhibit symmetrical properties). This generation of thrust, however, differs from the normal curve when the incidence angle is high and leading-edge vortex forms on the pressure side. This formation promotes the aerofoil to continuously generate thrust (as seen from the increase in thrust (from 180° to 270° in Fig. 4.12). This process continues until the aerofoil reaches the end of the stroke. At this point, the aerofoil suddenly rotates and lift from rotation is created [123], leading to a significant amount of thrust. The maximum of driving torque always takes place around this region.

After the aerofoil reaches the end of the stroke, all vortices are shed and the aerofoil is completely stalled. The aerofoil then recovers to the neutral state at the azimuth angle of zero before flapping up again. Thrust generation is not expected in this recovery region.

It is worth noting that the change of thrust pattern are comparable to the way that birds change their flying strategy from low to high speeds [136]. The change of flying strategy is basically take-off capability.

In addition to the physical description of thrust, the analogy also suggests that:-

1. The unsteadiness associated with the Darrieus rotor can be exploited to generate unsteady, additional thrust as is done by fish and birds.

2. The understanding of birds' take-off capability will give an insight why some Darrieus turbines can self-start.

The next section explores this in detail.

4.3 Exploitation of unsteadiness

Since much research reveals that flapping creatures cruise in a narrow optimal range of Strouhal number (St) in order to produce unsteady thrust efficiently, it is reasonable to expect that there should be an optimal range for Darrieus blade. However the Strouhal number cannot be directly applied to Darrieus rotor analysis as it is defined in terms of wake which is not generally known. The reduced frequency which is closely related to Strouhal number will be used in this discussion (Eq. 5).

Equation 5 indicates that, at a specific tip speed ratio, the value of reduced frequency depends on rotor geometry (c/D) and if one wants to design a Darrieus rotor to generate thrust force efficiently, the only parameter that can be modified is c/D ratio.

This finding raises the question of whether the difference between blade geometries that have been reported to self-start and those that have not can be explained by this pitch-heave concept. A critical review has therefore been undertaken to collect and analyse alternative blade configurations. Figure 4.13 compares blade configuration employed in early developments with that recently tested by Hill et al [10]. Table 4.1 lists examples of the blade configurations found.

Table 4.1: Darrieus rotor blade configuration.

Blade configurations	Profile	N	c, m	D, m	c/D	AR
Curved (Muraca and Guiliotte [137])	NACA0012	2	0.0142	4.267	0.00333	300.49
Curved (Chasteau [138])	NACA0012	2 and 3	0.286	4.72	0.061	15.98
Curved (Sheldahl et al [139, 140])	NACA0012	2	0.190	5.0	0.038	26.84
Curved (Sheldahl [141])	NACA0012	2 and 3	0.0587	2.0	0.029	34.48
Curved (Worstell [20])	NACA0012	2 and 3	0.600	17.0	0.035	28.57
Curved (Templin and Rangi [142])	NACA0015	2	0.365	11.2	0.033	46.03
Curved (Bergeles et al [143])	NACA0012	2 and 3	0.065	1.68	0.039	25.38
Curved (Ashwill [144])	NACA0021, SNL0018/50	2	0.91, 1.07, 1.22	34.0	0.026, 0.031, 0.036	54.94, 46.73, 40.98
Straight (Moran [145])	NACA0018	3	0.213	2.13	0.100	7.14
Straight (Chua [8])	NACA0015	3	0.070	0.50	0.140	7.14
Straight (Price [146])	NACA0015	2	1.250	25.0	0.050	14.4
Straight (Hill et al [10])	NACA0018	3	0.083	0.75	0.110	7.23
Straight (Tullis et al [134])	NACA0015	3	0.400	2.50	0.160	7.5
Straight (Hsieh [135])	NACA0015	3	0.090	1.20	0.075	13.33
Straight (Bulow [147])	NACA0021	3	0.250	3.00	0.0417	20.0

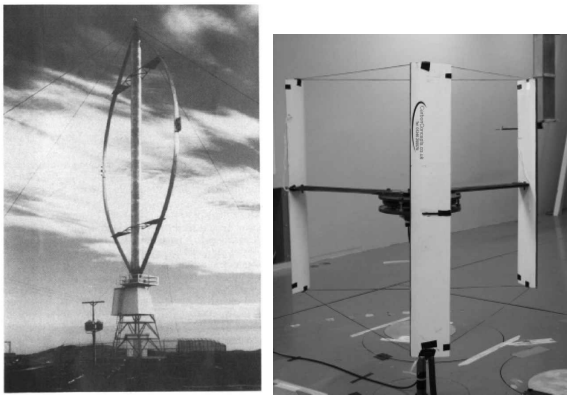

Figure 4.13: Darrieus blade configurations (from left to right): Templin and Rangi [142] and Hill et al [10].

The review shows that, regardless of the difference between curved and straight-bladed (curved blades are typically designed to minimise centrifugal stress and they are less effective in the generation of torque), the blade configurations used in the early developments have very small c/D ratios, ranging from around 0.03 to 0.06 (it can be seen from Figure 4.5 that the effect of unsteadiness is small with these c/D values). In addition, most of them also employed two-bladed configuration and it has been shown by Dominy et al [24] that its ability to self-start might be problematic. Rotor configurations used by Chua [8] and Hill et al [10], having the c/D ratios of 0.14 and 0.11, respectively, have been reported to be self-starting.

It is also observed that previously-employed blades have very high aspect ratios (larger than 25) while Chua and Hill et al rotors have aspect ratios of around 7.

Studies on bird locomotion reveal that different birds have different wing aspect ratios (ranging from 1.8 to 18) and this is directly related to their main capabilities. In general, high aspect ratio wings generate less induced drag and are very efficient in non-flapping flight (gliding and soaring). The wandering albatross, for example, which is an expert glider has an aspect ratio of around 15 [148]. This type of bird typically has a difficulty in taking off from ground level and has to increase wind speed that the wing perceives by running or jumping from elevated levels. Once it becomes airborne, it can fly effortlessly. The way that this type of bird takes off is comparable to the early large Darrieus turbines having small c/D ratios and high aspect ratio wings that need external assistance to increase wind speed that the blade experiences and once the relative wind is high and the incidence angle is low enough the turbine will catch the wind.

Aerial predators such as hawks and falcons have lower aspect ratio wings as they require great maneuverability (take-off and turning capabilities) in order to capture prey. Their wing aspect ratio ranges from 5.57 to 8.36 [149]. Lower aspect ratio wings mean lower wing inertia and the wings are easier to flap.

In the Darrieus context, the ability of the blade to flap is related to c/D ratio, AR ratio, and number of blades (N). At a specific chord length, the diameter determines

distance that the blade has to move to complete the stroke (Fig. 4.14). Too small c/D ratio then means the blade will not be effective in generating unsteady force and this small force is also not sufficient to bring the blade back to the region that it can generate force again, particularly if the blade has a high AR ratio. Multi-bladed rotors decrease the distance that the blade has to move to begin a new stroke and effectively increase the number of flapping per revolution.

This is particularly true during take-off. In order to take off successfully, birds typically spread their wings as much as possible to increase effective c/D and flap their wings as fast as possible (increasing ω, it is noted that birds having smaller aspect ratio wings can flap their wings at a faster rate). All of these lead to an increase in reduced frequency.

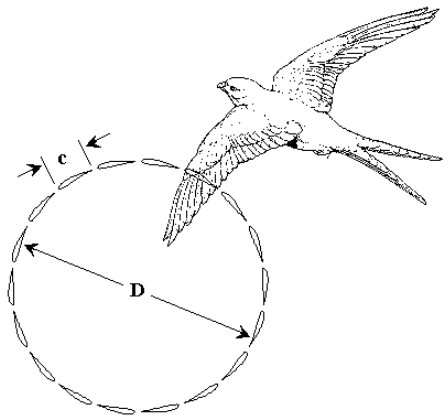

Figure 4.14: A comparison between Darrieus blade and bird's wings.

One implication from these is that the rotor geometry strongly affects the turbine ability to self-start and it should be in a suitable range in order that the unsteadiness can be exploited.

The next section examines thrust development over the startup period and applies this knowledge to understand the turbine's ability to self-start.

4.4 Thrust-producing state

The examination using the widely adopted steady-state approximation is first presented; followed by the addition of unsteadiness in order to investigate how the additional, unsteady force contributes to the thrust development and to determine thrust-producing state.

Figures 4.15 presents a qualitative analysis of the driving force generated by the blade when it is in quadrant 1. The driving force generated when the aerofoil operates within other quadrants can be obtained in a similar way.

It can be seen that the force that drives the turbine in a counterclockwise direction is generated by the drag force at low rotational speed (the angle of attack perceived by the blade is 'larger' than 90°). This angle of attack will continuously

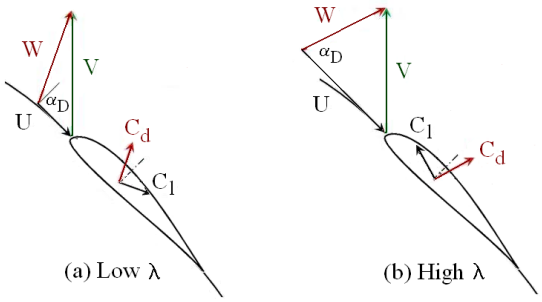

Figure 4.15: Driving force generated by the blade at different tip speed ratios.

decrease with increasing tip speed ratio until at a sufficiently high tip speed ratio the angle of attack will be smaller than 90°. Here, the turbine changes its state from a 'drag-driven' to 'lift-driven' machine.

It appears from this qualitative analysis that, although the Darrieus turbine is categorised as lift-driven machine, it operates as a 'combined lift- and drag-driven' machine at low tip speed ratios and it will shift to 'full' lift-driven only if it spins at a sufficiently high tip speed ratio ($\lambda \geq 1$).

Under unsteady conditions, the magnitudes of lift and drag are altered. The effect of unsteadiness is in the form of leading-edge and trailing-edge vortex formations and these formations induce greater negative pressure on the suction side and extra force is generated. This extra force is difficult to evaluate as it is strongly related to complex flow phenomena and the best way of getting this information is to conduct experimental testing. However, it is possible to estimate how this extra force contributes to the torque development.

As noted earlier, the Darrieus rotor has two operating modes in the starting period: combined lift- and drag-driven and fully lift-driven. In the first mode, both forces are equally important in driving the machine, but as soon as the tip speed ratio is larger than one and the turbine is fully driven by the lift force, the drag will always act against the rotor movement (Fig. 4.15). Since, it is not difficult to reach the tip speed ratio of one, the analysis described below is specific to the full lift driven state. With reference to Figure 4.16, the lift and drag force due to this extra force and their contributions to thrust can be expressed as

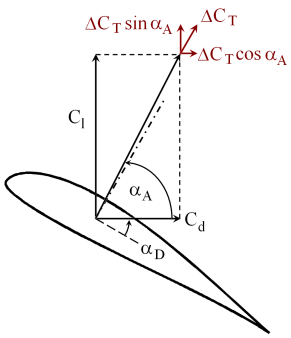

Figure 4.16: Increment of normal force due to unsteadiness.

$$\Delta C_L = \Delta C_T \sin\alpha_A \quad \text{and} \quad \Delta C_D = \Delta C_T \cos\alpha_A \tag{4.6}$$

$$PC_L = \sin\alpha_A \quad \text{and} \quad PC_D = \cos\alpha_A \tag{4.7}$$

where ΔC_T is the extra force due to unsteadiness and α_A is an angle formed by lift and drag coefficients which is defined as $\alpha_A = \arctan C_l/C_d$.

It is noted that the angle α_A depends on the magnitude of lift and drag which is in turn a function of incidence angle. Calculations of this angle using experimental data of four aerofoils show that this angle varies inversely with incidence angle [150] (Fig. 4.17). All of them are roughly in the form of $\alpha_A \approx 90° - \alpha_D$.

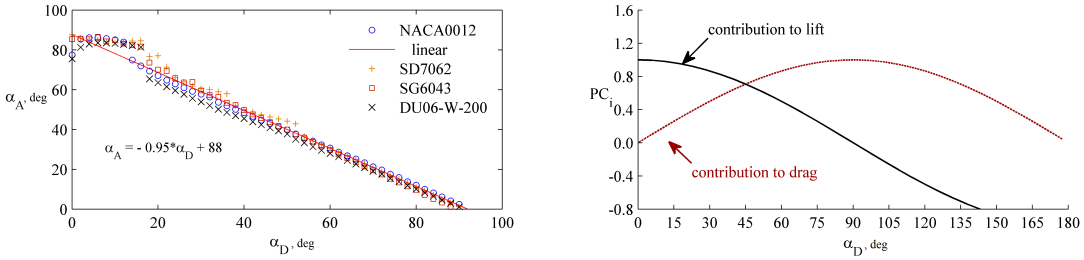

Figure 4.17: Contribution to lift and drag forces.

With this information, the percent contributions of the extra force to lift and drag components become

$$PC_L = \cos\alpha_D \quad \text{and} \quad PC_D = \sin\alpha_D \tag{4.8}$$

The equations indicate that the extra lift and drag forces depend on the incidence angle that the blade experiences at a particular time. The unsteady effects will contribute to lift increment and, hence, driving torque when the incidence angle is less than 45°.

Figure 4.18 shows incidence angle variations that the blade experiences at different tip speed ratios. The shaded area represents a region where the incidence angle is larger than 45° and the presence of the unsteadiness will not effectively drive the rotor. It can be seen from Figures 4.18a and 4.18b that the shaded area covers nearly half of the circle. Torque then increases very slowly at these tip speed ratios. The shaded area reduces with increasing tip speed ratio (4.18c and d).

The shaded area will disappear completely at a tip speed ratio of 1.5 as the incidence angle that the blade perceives at any azimuth angle is lower than 45°. It is noted however that the area in quadrant 4 is still shaded since the blade is in the recovery region. It is also noted that, although there is a shaded area in quadrant 1 at tip speed ratio of 1.4, it covers only a small region and the rotor should produce a significant amount of thrust force at this tip speed ratio and begin accelerating. At a tip speed ratio of 1.5, the quadrant 1 becomes fully effective in creating thrust, leading to a continuous generation of thrust for nearly the entire Darrieus path.

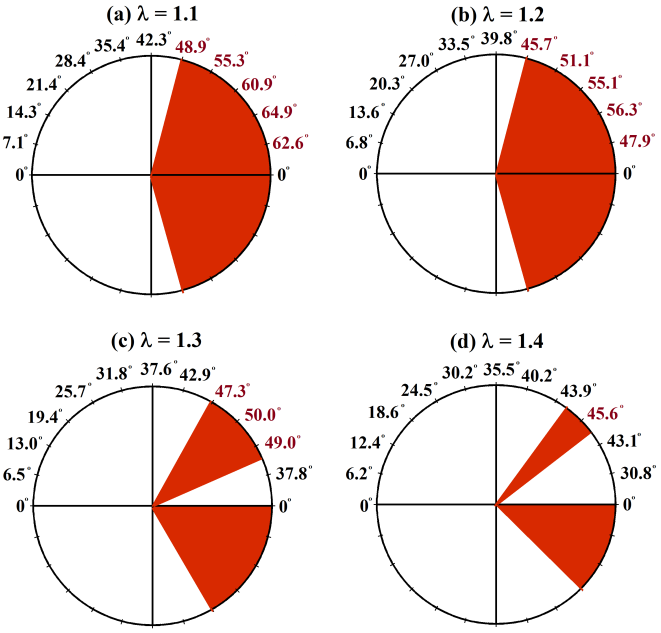

Figure 4.18: Contributions of unsteadiness.

The contribution of quadrant 1 to thrust generation is comparable to the way that birds change their flying strategies from low to high speeds. This also coincides with the rotor behaviour tested by Chua [8] and Hill et al [10] (Fig. 2.1 and Fig. 2.2). Both rotors change their acceleration rates and finally take-off to their final speeds when they reach this tip speed ratio. This characteristic clearly suggests that the full lift-driven state can be subdivided into 'discrete' and 'continuous' thrust-producing modes and the shift takes place when the rotor reaches a tip speed ratio of 1.5 (Fig. 4.19).

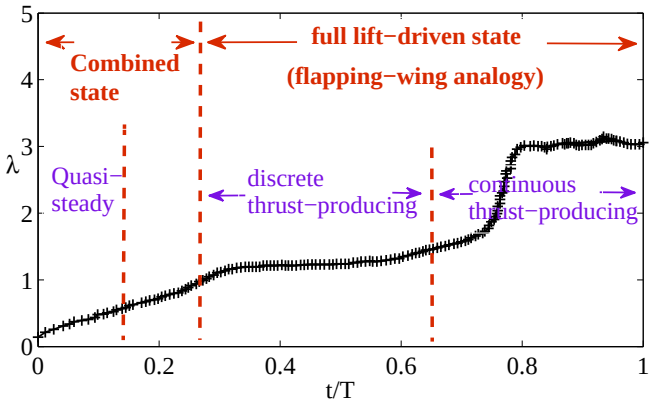

Figure 4.19: Thrust-producing state over the starting process.

The total torque that the blade generates at any tip speed ratio can be obtained by integrating C_t over the azimuth angle ($C_q = \int C_t \times R d\theta$). Figure 4.20 compares quasi-steady C_q with that was deduced from Hill's experiment. It is seen that they are in good agreement up to λ of around 0.5. Calculation of reduced frequency indi-

cates that the reduced frequency is high and the quasi-steady assumption becomes invalid. While the C_q becomes negative in quasi-steady prediction, the experimental C_q is positive but comparatively small in the deadband due to the fact that thrust is discrete. The discrepancy confirms that the unsteadiness can be exploited to produce 'positive' C_q in the deadband region. This positive C_q can be obtained by increasing c/D ratio (Fig. 4.5), just like birds that spread their wings during downstroke to maximise the thrust production.

In order to get through the deadband, the rotor must be able to accelerate to the continuous thrust-producing region with this comparatively small C_q (for a specific material, this can be obtained by reducing AR). It is then clear that the means to escape from the deadband is to promote unsteady thrust and to reduce rotor inertia. This can be achieved by 'properly' sizing the rotor configuration.

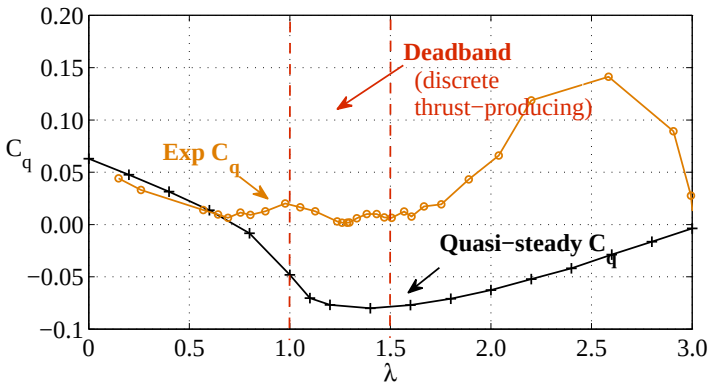

Figure 4.20: Effect of unsteadiness on torque coefficient.

4.5 Conclusions

A physical description of Darrieus turbine starting capability has been investigated in this paper through a simple pitch-heave concept. The investigation and observations of flapping animals lead to the following conclusions:

1. The aerofoil in Darrieus motion is analogous to a flapping wing mechanism; a mechanism that involves the exploitation of unsteadiness to generate lift and thrust.

2. The Darrieus turbine operates with two distinct modes during start-up: 'combined' lift- and drag-driven and 'full' lift-driven. The shift to full lift-driven state takes place when the tip speed ratio is higher than one.

3. There are two modes of thrust generation in the full lift-driven state: discrete and continuous thrust-producing. In the discrete mode, thrust is generated mainly during downstroke. The continuous thrust production occurs when the

incidence angle in the upstroke part becomes lower that 45°. The shift of the modes takes place when the turbine reaches a tip speed ratio of 1.5.

4. The shift from combined to full lift-driven state is not a guarantee of further acceleration and it is possible the rotor will be locked in the deadband due to a large area of high incidence angle and discrete thrust production ($1 \leq \lambda \leq 1.5$).

5. The ability to escape from the deadband is directly related to rotor configurations: number of blades, chord-to-diameter ratio, and blade aspect ratio. Exploitation of the unsteadiness to promote self-starting can be achieved through a proper combination of these parameters.

However, detailed investigation of this starting behaviour requires aerofoil performance data - both steady and unsteady. They are presented in subsequent chapters.

Chapter 5

Selection of Aerofoil Profiles

Due to the myriad of available aerofoil profiles, wind-tunnel testing of even a small set of seemingly appropriate aerofoils for wind turbine applications is prohibitive and impractical. The CFD approach offers another solution to the problem as it can be used to study the flow over an aerofoil and to obtain its aerodynamic performance for a wide range of conditions with relative ease and reasonable computing expense. CFD modelling and simulation-based selection of aerofoils is described in this chapter so as to select promising aerofoils for further wind-tunnel testing.

5.1 Low-Reynolds-number aerofoils

Aerofoils at low Reynolds numbers do not behave like aerofoils at high Reynolds numbers. At high Reynolds number (typically above one million), transition to turbulence occurs very quickly and the laminar and transitional zones normally cover only a very small region of the aerofoil surface. That rapid transition does not have a profound effect on aerofoil performance. In effect, the flow separation process starts near the trailing edge and progresses upstream as incidence is increased.

In contrast, the flow at low Reynolds numbers is prone to separate even when the adverse pressure gradient is not severe due to its low kinetic energy [151]. The flow normally separates and forms a transition in the free air before reattaching to the aerofoil surface as a turbulent layer, forming a laminar separation bubble (the main distinguishing feature of low-Re flow over an aerofoil). The length of the bubble depends on many factors such as Reynolds number, angle of attack, and aerofoil shape. The effects of the bubble can be mild if it is sufficiently small. In the worst case, the flow will not reattach and the flow fully separates, leading to a severe degradation in aerofoil performance (Fig. 5.1).

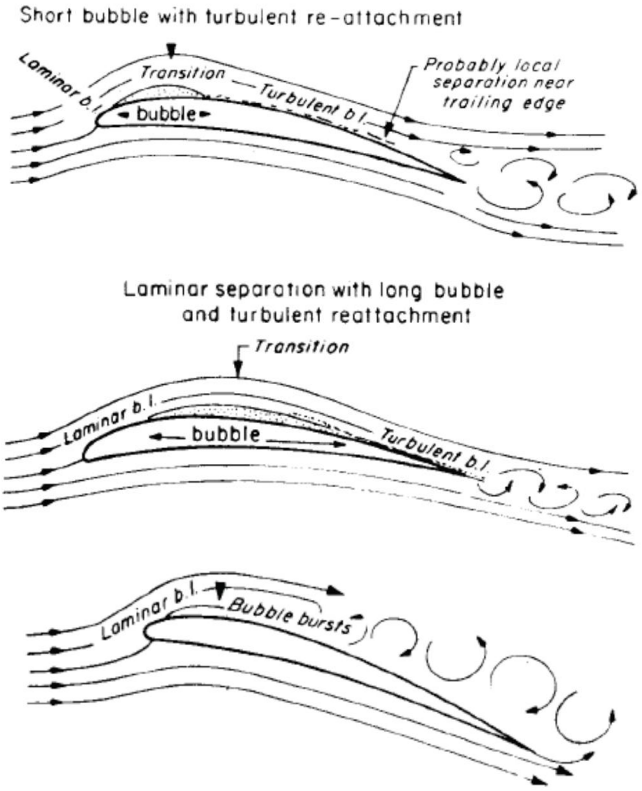

Figure 5.1: Laminar separation bubbles [152].

It is critical that low-Re aerofoils should be designed in such a way that the presence of the bubble can be identified and minimised. A 'transition ramp' concept is often adopted to accomplish the task (eg. [42,113]) (Fig. 5.2). The transition ramp is basically a small region of a shallow, adverse pressure gradient intended to stabilise and promote an effective transition from laminar to turbulent flow. This will lead to a smaller bubble and softer stall since the flow has become turbulent and normally can better withstand an adverse pressure gradient at the back of the aerofoil. A separation ramp is also used to further control trailing edge separation [42].

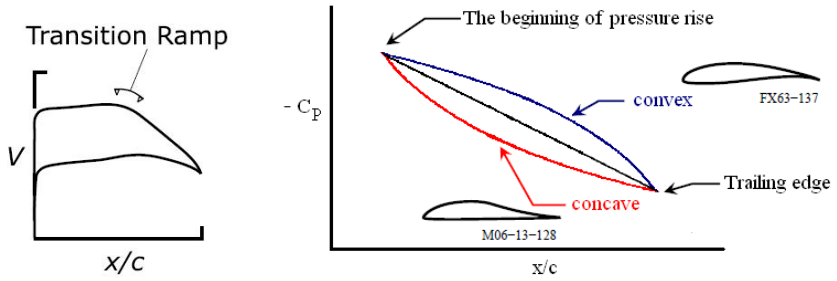

Figure 5.2: Transition ramp concept [113] and pressure recovery types.

Apart from that, how the pressure recoveries aft of that ramp is also of importance. Generally, the recovery can be classified into three types: linear, concave, and

convex types, each leading to different separation and stalling behaviour (Fig. 5.2).

For the concave type, as the name implies, the C_p of the aerofoil with this recovery type curves inwards. One of the well-known concave pressure recovery type is the stratford-type which is usually used on high-lift sections [153]. The underlying concept of this pressure recovery is to apply a suitable pressure distribution that promotes negative pressure without separating the boundary layer. It is evident that, by applying this pressure recovery type in which the boundary layer is just on the verge of separation, high lift can be obtained. One example of this is the Liebeck high-lift aerofoil (Fig. 5.2).

Although this kind of aerofoil can generate high lift, they exhibit abrupt trailing-edge stall [154]. They also suffer severe performance degradation when operating at low Reynolds numbers [44] (see Fig. 2.4). This aerofoil characteristic does not seem to be well-suited for small wind turbine blade during start-up that operates with low Reynolds numbers for a wide range of incidence angle.

Conversely, the aerofoil with convex pressure recovery exhibits milder stall than the others and most low-Re aerofoils are designed to be of this type in order to avoid large separation and bubbles. The FX63-137 aerofoil is a good example for this recovery type (it is well-known for its gradual progress of trailing-edge separation to the leading edge and soft stall characteristics). Characteristics of aerofoils with a linear pressure recovery fall between those explained above.

With these characteristics in mind, aerofoil choices can be narrowed down. Aerofoils having the convex pressure-recovery type seems to be suitable for small turbine blades during start-up as they exhibit gradual stall and have good aerodynamic characteristics for a wide range of operation, particularly at low Reynolds numbers and high angles of attack.

Nevertheless, it should be noted that, although existing aerofoils are generally well-designed, they are almost all intended for use up to around stall point and at higher Reynolds numbers than those relevant to small wind turbines. Their performance at lower Reynolds numbers and higher incidence angles is generally not known and needs further investigations.

5.2 Aerofoils for Darrieus turbines

Aerodynamically, aerofoils for Darrieus turbines experience extreme conditions which do not occur in horizontal-axis types. The flow experienced by the the profile is always transient even when the turbine operates with steady wind due to the cyclic change of incidence angle as the turbine rotates. In addition, it also experiences a repeated reversal of the suction and pressure sides as it rotates upwind and downwind. The optimum aerofoil shape for this type of turbine seems to be complex.

Until now, there have been very few aerofoils designed specifically for Darrieus-type turbines [16,31,33,34] and the NACA sections such as NACA0012, NACA0015, and NACA0018 are still the most popular choices, though they were designed ex-

clusively for aircraft applications.

5.2.1 The SAND00xx

The first dedicated VAWT aerofoils were developed by Klimas of the Sandia Laboratory [31]. NACA sections having a thickness from 15% to 21% had been modified to promote more laminar flow at the leading edge by gradually applying a favourable pressure gradient. They were designated as SAND0015/47, SAND0018/50, and SAND0021/50 (modified from the NACA0015, NACA0018, and NACA0021, respectively). The numbers after the slash indicate percent of chord that supports laminar flow. They were designed for a Reynolds number range from 1 to 3 million and are therefore appropriate only for large machines.

5.2.2 The S824

Another aerofoil intended for vertical-axis turbine application is the S824 aerofoil designed by Somers [16, 33]. This aerofoil is proprietary and very little useful information is available in the open literature although it is known to be a laminar and symmetrical aerofoil.

5.2.3 The DU06-W-200

The most recent aerofoil section for Darrieus turbines is the DU06-W-200 [34]. It was intended specifically for small-scale Darrieus turbines (the 2.5kW Turby [155] was used as a design case). Contrary to the previous sections, this is a cambered aerofoil. The NACA0018 section was used as a reference for the design. It is a laminar aerofoil with a thickness of 20% and a camber of 0.8% and it is intended for an operational Reynolds number range from 150,000 to 700,000.

In the absence of any better alternative aerofoil sections, the 'NACA0012' and the 'DU06-W-200' profiles were selected for further investigation during the course of the current work.

5.3 Aerofoils for small horizontal-axis turbines

Unlike VAWTs, a large number of aerofoils have been designed for horizontal-axis machines. The first wind turbine-dedicated aerofoils were the aerofoil families developed by the joint cooperation of the National Renewable Energy Laboratory (NREL) and Airfoils Incorporated. [25]. A number of dedicated aerofoils were also developed at Delft University [37] and by Riso [36]. Most of them were intended for large-scale machines.

5.3.1 The S8xx

Aerofoils that are of interest here are the S823 and the S822 (for root and tip, respectively) which were designed for small stall-regulated wind turbines ranging from 2 to 20 kW. Their design Reynolds numbers are 400,000 and 600,000 for root and tip sections, respectively. To comply with the stall-regulated type, they were designed to produce restrained lift to limit excessive torque. Their thicknesses are 0.21c and 0.16c. They were experimentally investigated by Selig and McGranahan [13] over a Reynolds number range from 100,000 to 500,000 up to the stall angle.

5.3.2 The SG604x

This aerofoil series was developed specifically for small variable-speed wind turbines sized from 1- to 50 kW [29]. For this type of operation, the turbine blade is controlled to operate within a smaller incidence angle range than that of stall-regulated type. The design, therefore, focussed primarily on a narrower incidence range than those of stall-regulated types. The series consists of four aerofoils: SG6040, SG6041, SG6042, and SG6043 with a design Reynolds number of 300,000. Two aerofoils are selected here to be representative for root and tip sections: the SG6040 and the SG6043.

5.3.3 The FX63-137

Apart from the specifically tailored sections, some alternative low-Re aerofoils exhibit good characteristics and are attractive for small wind turbine applications. One of them is the FX63-137 aerofoil section which was designed by Wortman for human-powered aircraft [13]. It is well-known for its good performance and soft-stall characteristics.

5.3.4 The SD7062

Another aerofoil that is of interest here is the SD7062 which started its life as an aerofoil for model gliders. It was reported to possess high lift and low drag at low Reynolds number. It has a thickness ratio and a camber of 14% and 4%, respectively.

The aerofoils discussed above are depicted in Figure 5.3 and their design conditions are summarised in Table 5.1.

5.4 CFD- and simulation-based selection

5.4.1 CFD modelling

In order to compare aerofoil performance, 2D CFD modelling was carried out using FLUENT 6.3.26. The computational domain used in this modelling is shown in Figure 5.4. The domain is extended 10 chords upstream, above, and below the aerofoil. It is also extended 20 chords downstream in order to make the pressure

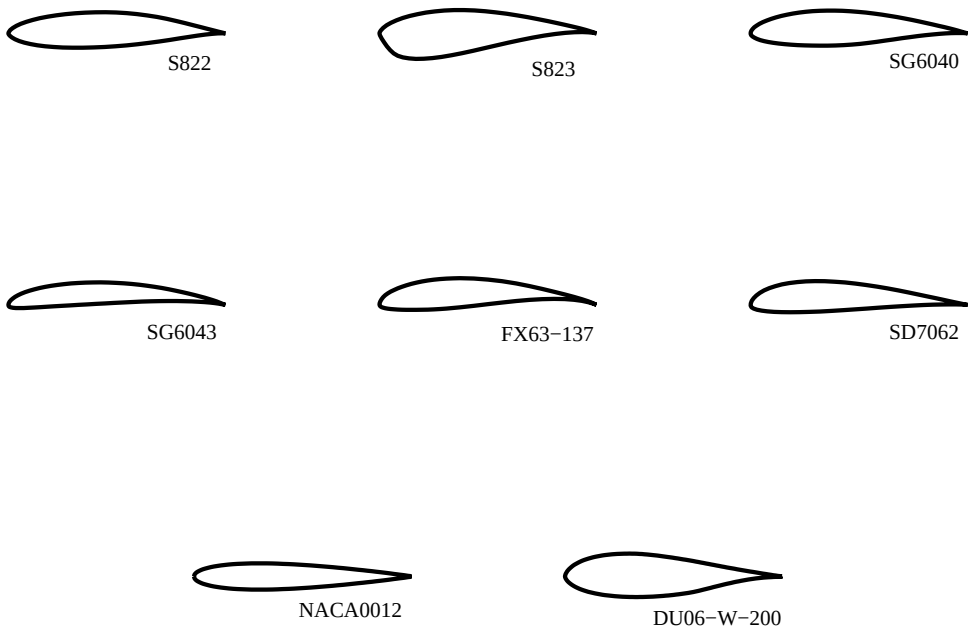

Figure 5.3: Aerofoils subjected to numerical investigation.

Table 5.1: Profile parameters.

Profile	**Thickness (%)**	**Camber (%)**	**Design Re**
NACA0012	12.0	0.0	$\geq$ 1,000,000
DU06-W-200	20.0	0.8	150,000 - 700,000
S822	16.0	1.89	600,000
S823	21.0	n/a	400,000
SG6040	16.0	2.5	200,000
SG6043	10.0	5.5	300,000
FX63-137	13.7	6.0	n/a
SD7062	14.0	4.0	n/a

outlet as close to a uniform atmospheric pressure as possible. Unstructured meshes are used because of their simplicity. Pressure far field boundary conditions were set at the upper, lower, and downstream boundaries. At the upstream boundary of the inlet, a uniform velocity was prescribed.

Flow models used are the laminar model and realizable $k-\epsilon$ model with enhanced wall treatment, which were appropriate according to the Reynolds number regime of the simulation. Parameters for the simulation are summarised in Table 5.2. An investigation of y^+ value shows that this modelling gives the maximum value of y^+ less than 10 all over the aerofoil surface, providing confidence that the flow near the wall region is properly captured (Fig. 5.5).

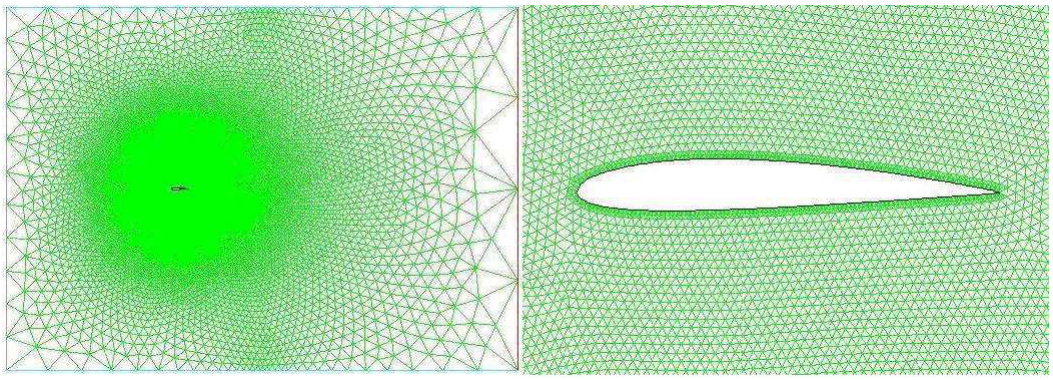

Figure 5.4: Computational domain and close-up.

Table 5.2: Simulation parameters.

Number of cells	$\approx$ 60,000
Model solvers	steady (0° - 15°) and unsteady (20° - 90°)
Flow model: Re $> 200,000$	Realizable $k-\epsilon$ model with enhanced wall treatment
: Re $\leq 200,000$	laminar model

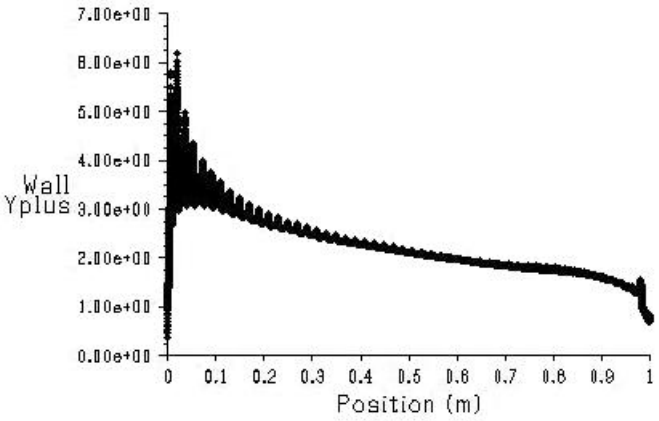

Figure 5.5: Distribution of y^+ values over the aerofoil surface.

Convergence treatments

As a general rule, residuals are monitored and the simulation is said to be convergent when the maximum residual is less than specified tolerance (10^5 in this thesis). However, at high incidence, the flow around the aerofoil becomes unstable as a result of vortex shedding in its wake leading to fluctuating results. In order to obtain the result from this situation, the unsteady model is used and C_l and C_d are monitored. The simulations are said to be convergent when they reach certain values and if some fluctuation is still seen, an average is taken to represent average properties. Figure 5.6 and 5.7 present examples of the monitoring.

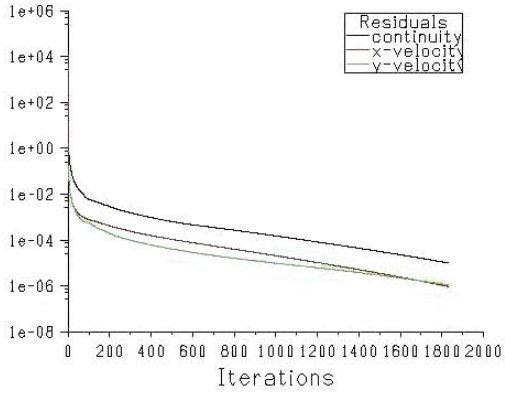

Figure 5.6: Residual monitoring.

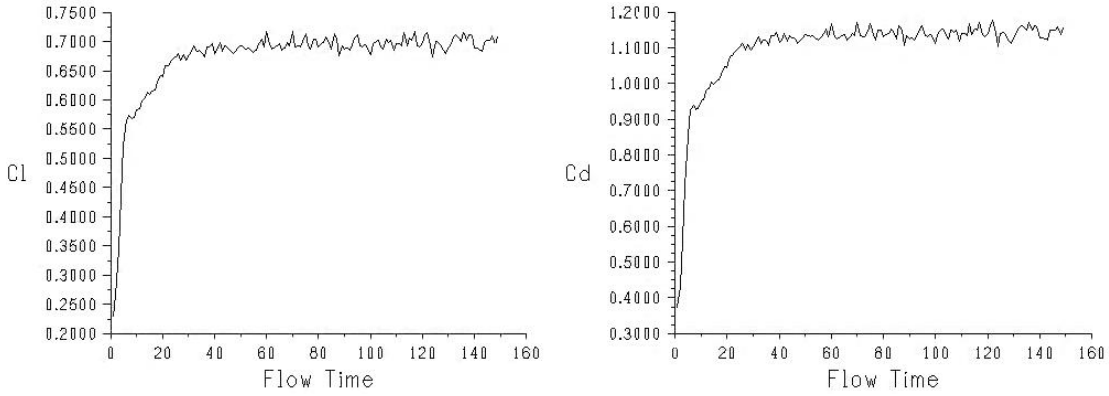

Figure 5.7: Force monitoring.

Validation

Very little rigorous experimental data are available to validate these CFD predictions as most of the tests have been conducted at relatively high Reynolds numbers up to incidence angle of around the stall angle. The most useful experimental data are the tests conducted by Crone [59] and Rainbird [58] at Durham University. Their tests on NACA0018 and NACA4412 aerofoils cover an incidence range from 0° to 180° at Reynolds numbers of 194,000 and 208,000, respectively. Figure 5.8 presents comparisons of lift and drag coefficients up to 90°. The lift coefficient at a Reynolds number of 150,000 conducted by Heffley and Van Treuren [156] is also plotted.

Overall, good agreement is seen from the comparison. Excellent agreement is found in the NACA0018 case except in post-stall regime where the CFD over-predicts lift coefficients.

For the NACA4412, a comparison between C_l and C_d shows a good agreement in the pre-stall region. It should be noted that Rainbird's data is not in good agreement even in this flow regime due to inaccuracies of the manufacturing process used for his blades [58]. However, his data is still qualitatively beneficial as it shows that general trends of the C_l and C_d are well captured. An over-prediction of C_l in post-stall regime is also observed from this comparison.

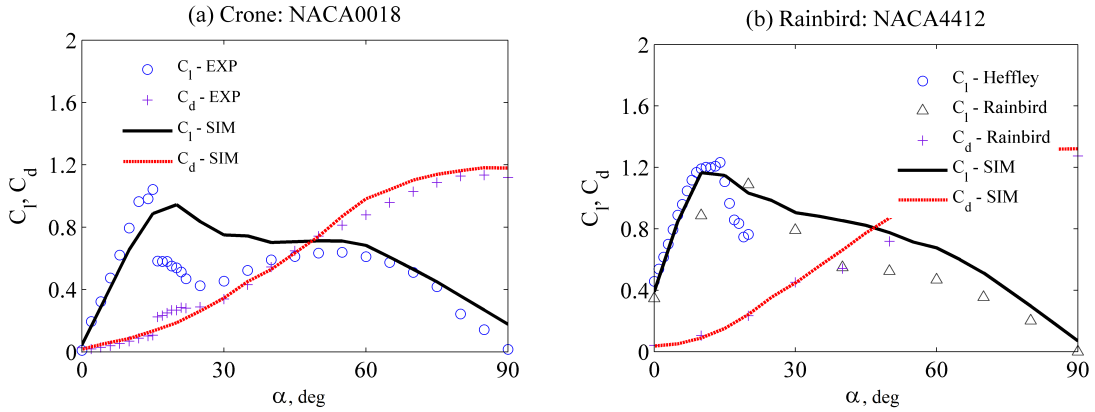

Figure 5.8: C_l and C_d comparisons: (a) NACA0018 at a Reynolds number of 194,000 (b) NACA4412 at a Reynolds number of 208,000.

The discrepancies between measured and predicted lifts in the post-stall region are further investigated by comparisons of surface pressure coefficients at incidence angles from 10° to 17° (Fig. 5.9).

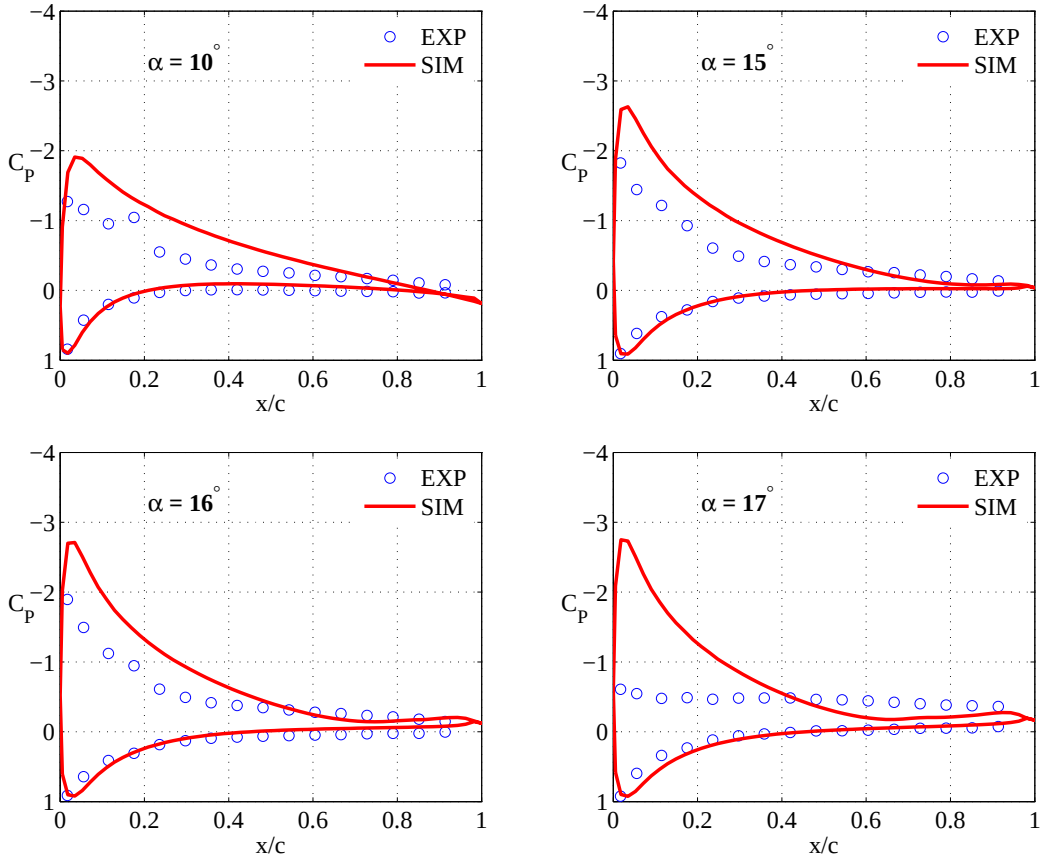

Figure 5.9: Pressure coefficient comparisons [58].

The comparisons show that there is a significant error between measured and predicted pressure coefficients for all incidences, especially on the suction surface of the aerofoil. The integration of the measured C_P over the aerofoil surface shows that lift coefficient from the integration is significantly lower than that of force readings, indicating that there might be an error associated with his pressure measurements. Despite that, the results are still revealing as they show how the C_P qualitatively changes and what causes the over-prediction when the incidence angle is increased.

The figures clearly show that stall behaviour is not properly captured by the CFD. While the CFD always predicts a gradual stall that is caused by the progression of the trailing to the leading edge, experiment shows a sudden stall behaviour which seems to be related to the presence of laminar separation bubble [150].

To sum up, it can be said that lift and drag coefficients are well predicted by the CFD in pre- and deep-stall regimes. The shortcoming of the CFD exists in the near post-stall regime at which separation occurs. Despite this, the CFD result is still useful for comparison as the over-prediction of lift in post-stall regime is present for all simulated cases.

5.4.2 General requirements

The key requirement of this simulation study is:-

The aerofoil should exhibit high C_l/C_d ratio with respect to its cross-sectional area at low Reynolds numbers so that it can be used on the rotor blade to enhance starting performance.

An additional requirement is that one thick and one thin aerofoil should be selected for the inboard and outboard sections of mixed-aerofoil HAWT blades.

Aerofoil performance predictions

A Reynolds number of 90,000 was chosen as representative in this simulation. Since this lies within the Reynolds number range of 50,000 to 200,000 in which the flow is reported to be extensively laminar [157]. A laminar model is adopted for all simulations. Predicted lift and drag coefficients of all of the investigated aerofoils are plotted in Figure 5.10.

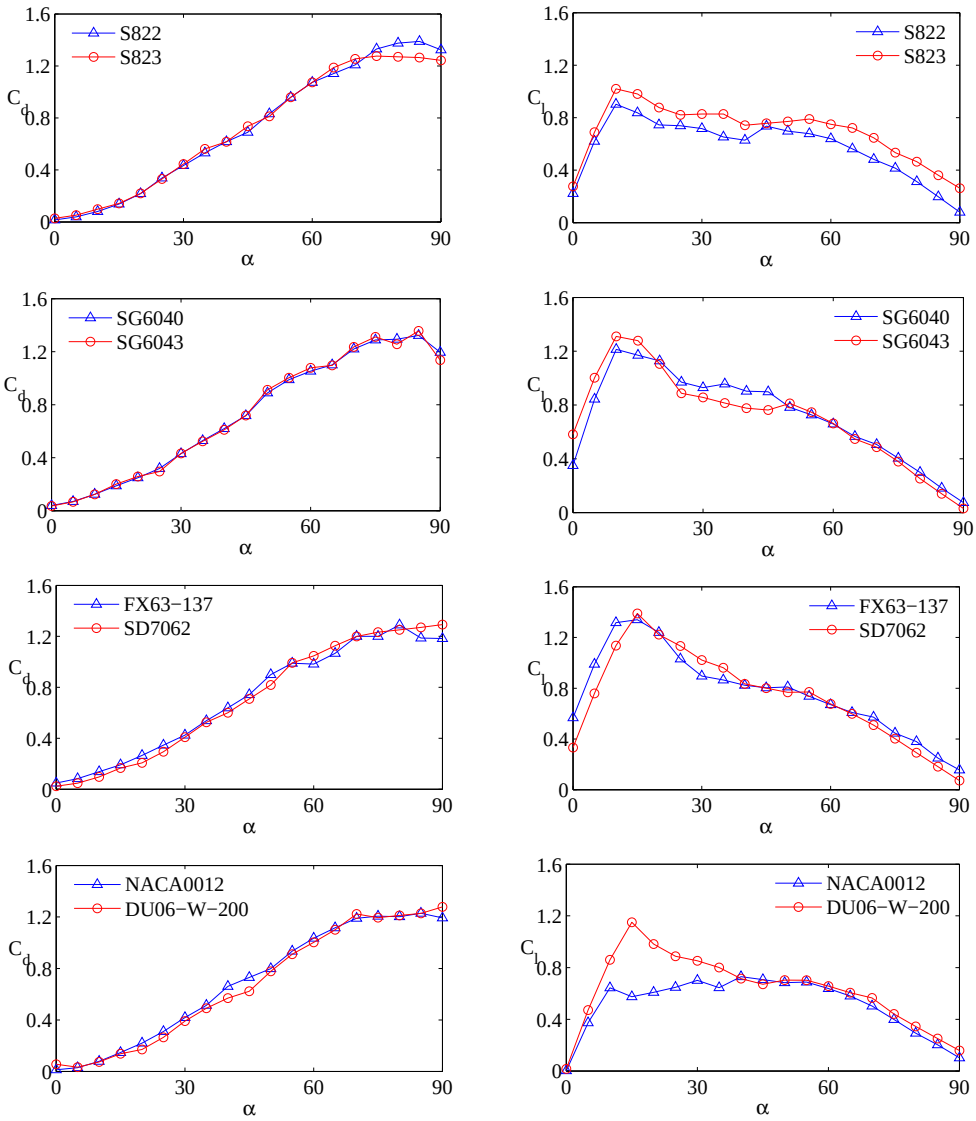

Figure 5.10: CFD prediction of lift and drag coefficients at a Reynolds number of 90,000 at an incidence range from 0° to 90°.

To facilitate the comparison, the aerofoil lift-to-drag ratios with respect to their cross-sectional areas are plotted in Figure 5.11. Main emphasis is given on the post-stall region.

In general, it can be seen from Figure 5.11a that the $\frac{C_l/C_d}{A}$ values increase exponentially with decreasing angle of attack, at different rate though. The aerofoils that exhibit fast increasing rate are the SG6043, the SD7062, and the FX63-137 aerofoils. Most of them exhibit a reduction in $\frac{C_l/C_d}{A}$ when the aerofoil enters the pre-stall region. This ratio reduced to around zero for the DU06-W-200 and the NACA0012.

In light of this, the SG604x series, the FX63-137, and the SD7062 seem to operate well for a wide incidence range.

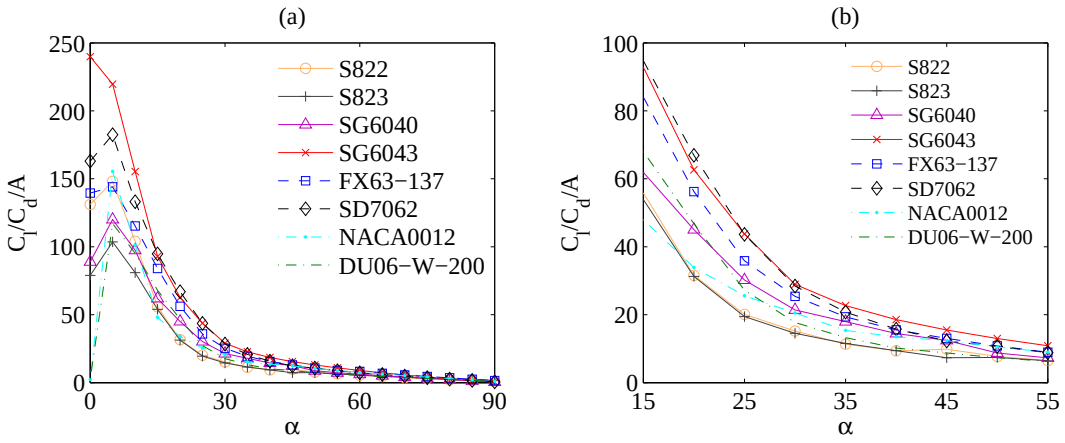

Figure 5.11: Predicted lift-to-drag ratios per the aerofoil cross-sectional area.

5.4.3 Rotor performance simulation

In order to take the effect of rotor inertia into consideration, a numerical turbine performance simulation was made using a MATLAB/SIMULINK model by creating a 1kW horizontal axis turbine blade to investigate their performance during start-up [109, 158] using the method described in Chapter 3. Three-dimensional effects such as dynamic stall, tip and hub losses were switched off so that the difference in rotor performance can be established solely as a result of the different 2D aerofoil sections. All blades were assumed to be made of the same material. Rotor inertias are presented in Table 5.3. Figure 5.12 presents simulation results in terms of time history of the rotational speed during startup.

Table 5.3: Inertia of rotors made of different aerofoils.

NACA0012	DU06-W-200	S822	S823	SG6040	SG6043	FX63-137	SD7062
2.3767	3.5799	3.1610	3.7209	2.9302	1.9939	2.4187	2.5568

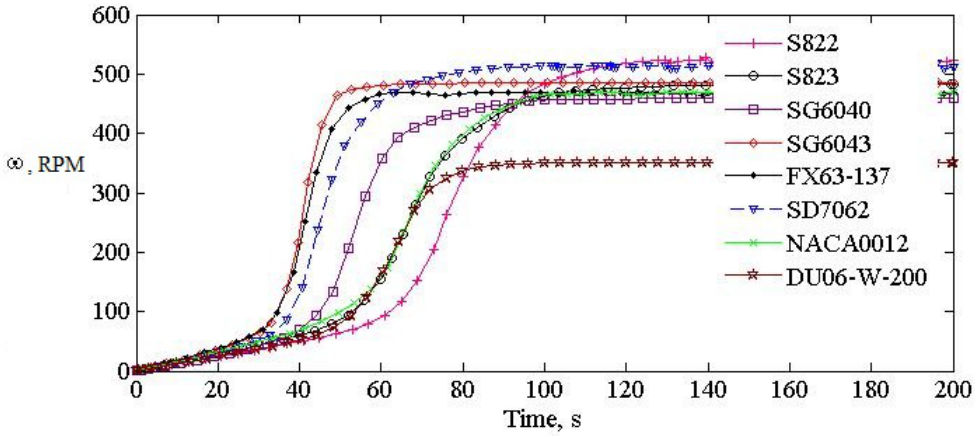

Figure 5.12: Start-up sequences of rotors made of different aerofoils.

It is observed that blades that can accelerate swiftly from standstill are the blades based upon the SG6043, the FX63-137 and the SD7062 profiles. It is further seen that these three blades reach different, steady-state rotational speeds. Of these three blade sections, the lowest rotational speed is produced by the FX63-137-based rotor. One of the reasons for this is that this aerofoil is highly cambered and exhibits a larger drag at low incidences and it is low incidence performance that dominates once the rotor has accelerated to its steady-state TSR. It appears that the aerofoils performing best during start-up are 'the SG6043' and 'the SD7062'. They also satisfy the requirement that one thin and one thick aerofoil should be selected as the SD7062 is thick enough to be used on the root section. It is noted that, although the NACA0012 and the DU06-W-200 sections did not perform well in this simulation, they are still selected for wind-tunnel testing as they had been specifically recommended for use in VAWTs.

5.5 Conclusions

This chapter has outlined the reasons behind the selection of aerofoils for experimental testing. It basically consists of two steps:-

- CFD calculations of lift and drag coefficients of candidate aerofoils at low Reynolds numbers and high incidences.
- MATLAB simulations of rotor start-up characteristics by using the CFD-derived lift and drag coefficients.

Based upon simulations, two promising aerofoils for HAWTs emerge; the SD7062 and the SG6043. These and two other aerofoils that were intentionally selected for VAWT applications (the NACA0012 and the DU06-W-200) are subjected to further experimental investigations.

The next chapter details wind-tunnel configuration used in this work.

Chapter 6

Experimental Configuration

Although the CFD approach can be used to compare aerofoil aerodynamic performance, wind-tunnel testing remains essential to understand the flow physics and to get real aerodynamic characteristics. This chapter provides a detailed description of the wind tunnel configuration used during this study. It details the effects of wall proximity and the concept of employing a "half-open" test section. It also explains how the tests were conducted. All test conditions are summarised at the end of the chapter.

6.1 Effects of wall proximity

Previous research by Rainbird [58] has shown that the presence of wall has a significant influence on aerofoil performance when tested at high incidences. He suggested that, in order to avoid any possible wall effects, an open test section must be used.

In order to clearly demonstrate the effect of the test section configuration when testing at high angles of incidence and to confirm Rainbird's finding [58], CFD calculations of flow around a NACA0012 aerofoil in closed and half-open test sections at different height-to-chord ratios were performed.

The CFD modelling was performed using FLUENT 6.3.26. Two computational domains were created to simulate the wind tunnel test section having different height-to-chord ratio (Fig. 6.1). Both domains were extended 7.5 chord upstream and downstream. Different height-to-chord ratios were obtained by extending the domain above and below the aerofoil in such a way that the aerofoil was located at the centre of the airstream. This configuration resulted in the computational domain extending 2.5 and 7.5 chords above and below the aerofoil for height-to-chord ratios of 5 and 15, respectively, which led to 2-D, unstructured mesh size of 0.0011 m^2 for both domains. The resulting number of cells were approximately 27,000 and 73,000, respectively.

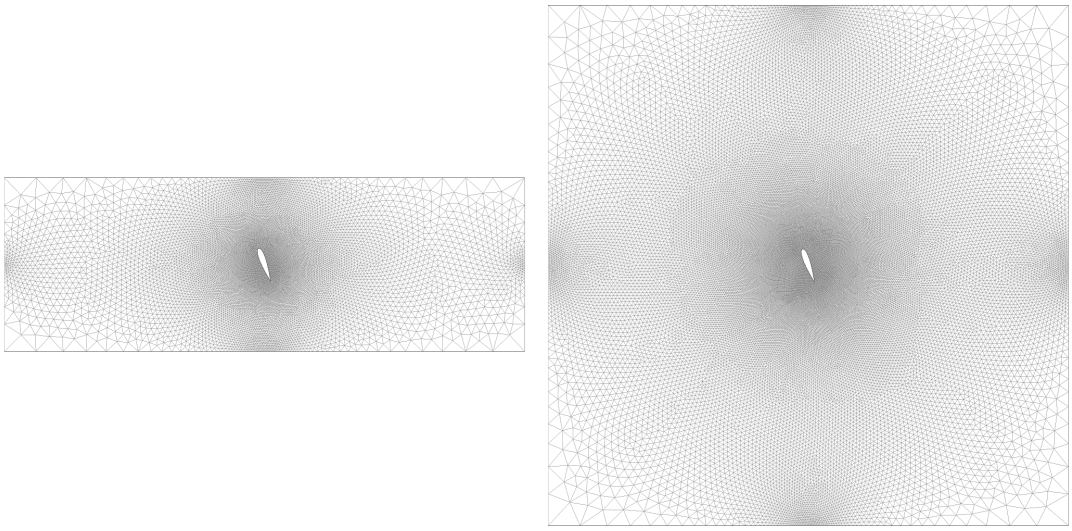

(a) H/C ratio of 5 (a) H/C ratio of 15

Figure 6.1: Computational domains for different height-to-chord ratios.

The effects of wall proximity were investigated by changing boundary conditions at the upper and lower domain boundaries which were defined as walls and pressure outlets for the closed and half-open test section. A laminar flow model was adopted for all simulations since it has been reported that the flow with a Reynolds number lower than 200,000 is extensively laminar [157].

Static pressure distributions and velocity distributions for a NACA0012 section in a closed test section are presented with different height-to-chord ratios (Fig. 6.2 and 6.3).

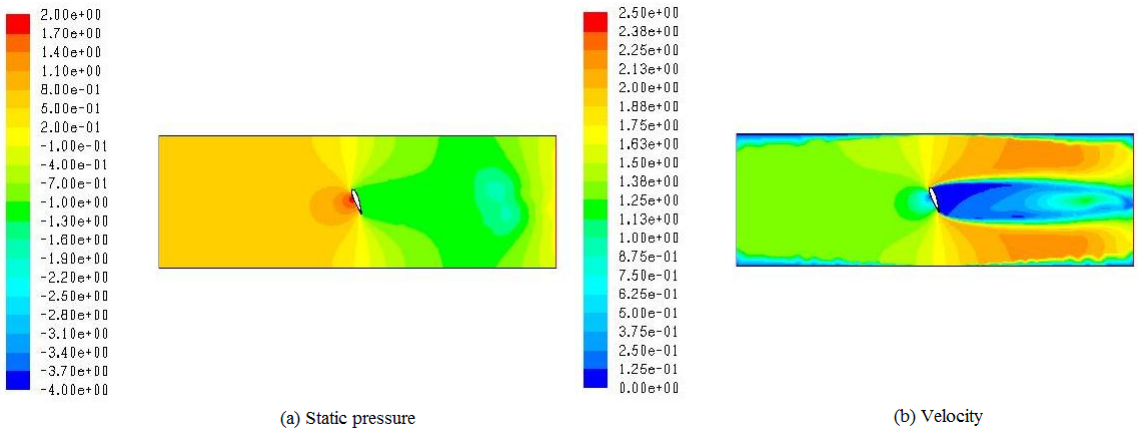

Figure 6.2: Flow around a NACA section at $H/C = 5$ and AoA of 70° (closed).

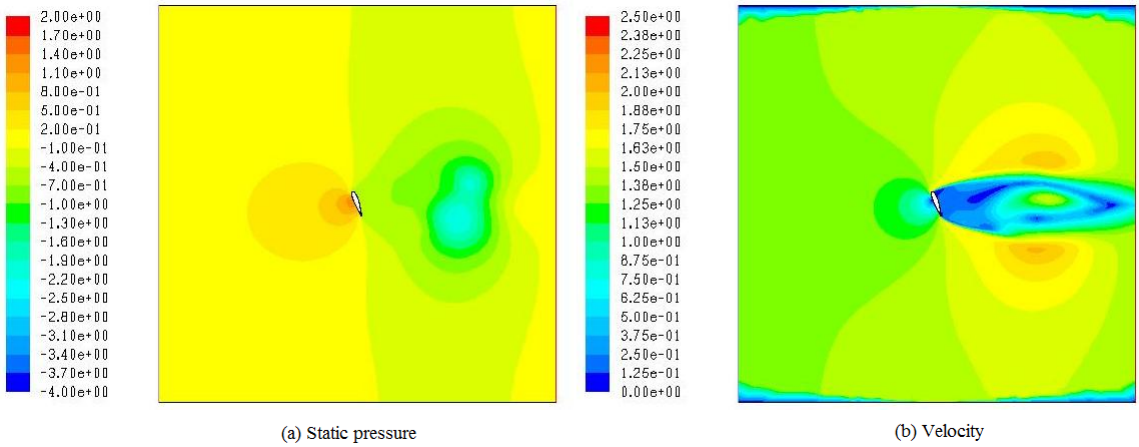

Figure 6.3: Flow around a NACA section at $H/C = 15$ and AoA of 70° (closed).

Comparisons between the two test cases clearly demonstrates the effect of changing the test section height-to-chord ratio from $H/C = 5$ (Fig. 6.1) to $H/C = 15$ (Fig 6.2) where, in particular, the development of the blade's wake structure is inhibited at the lower H/C ratio by the proximity of the upper and lower walls. For most wind tunnels, significant changes of their working section aspect ratio to accommodate high incidence aerofoil testing are not a viable option.

Similar improvement can be achieved by removing the top and the bottom walls and results for this "half-open" configuration for the same jet aspect ratios are shown in Figures 6.4 and 6.5.

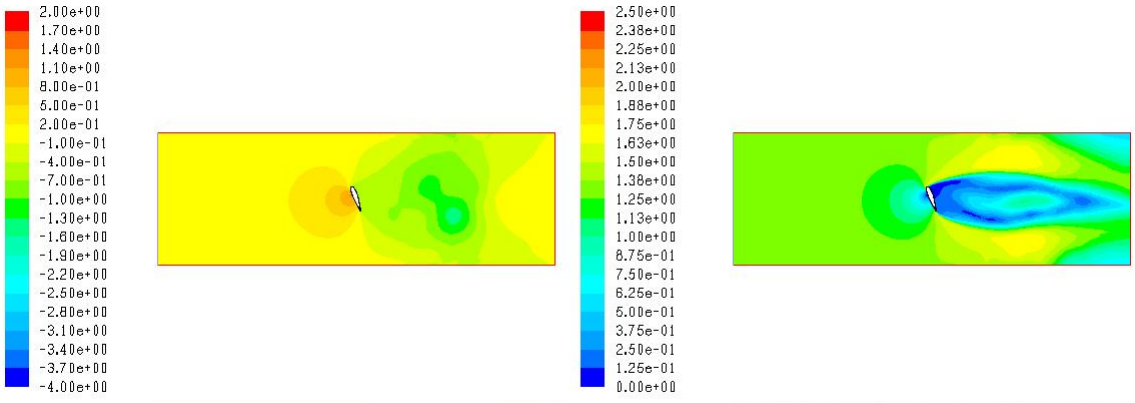

Figure 6.4: Flow around a NACA section at $H/C = 5$ and AoA of 70° (open).

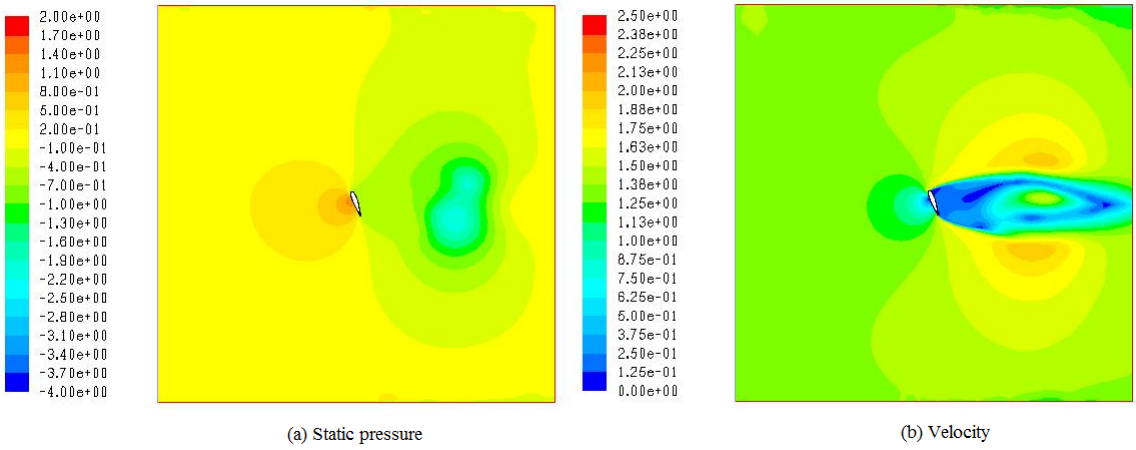

Figure 6.5: Flow around a NACA section at $H/C = 15$ and AoA of 70° (open).

For the larger jet area the results are almost identical to those of the closed section but for the smaller jet the flow is dramatically improved by the adoption of the half-open configuration. CFD derived surface static pressure coefficients around the aerofoil inclined at 70° for both the closed and half-open test sections at the different height-to-chord ratios are presented in Figure 6.6 together with pressure coefficients in an infinite jet ($H/C = \infty$).

It is clear that at this high angle of attack there is very little difference on either surface of the aerofoil between the high H/C closed test section and the corresponding half-open section. However, at the lower H/C ratio very substantial errors are observed in the closed section pressures, particularly on the downstream suction side of the blade. On the pressure surface all three cases demonstrate an almost constant static pressure over most of the surface but the magnitude of this negative pressure coefficient is almost doubled as a consequence of wall interaction in the closed section, low H/C case. The clear implication of these results is that wind tunnel testing must be performed either in half-open test sections or in closed

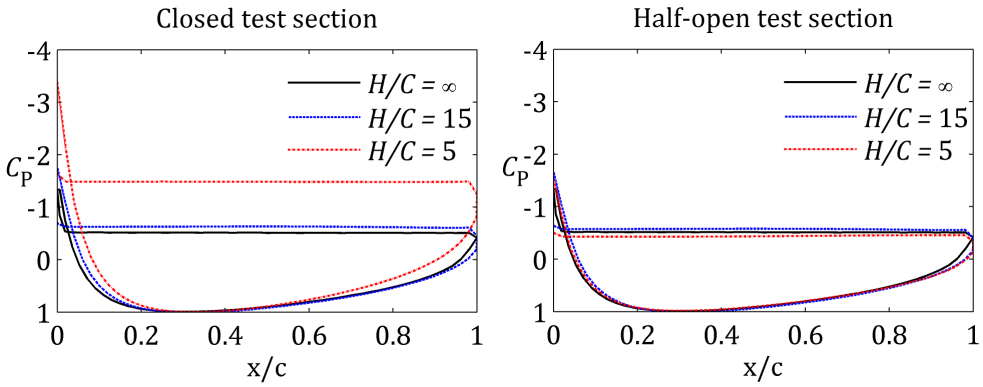

Figure 6.6: Pressure coefficients.

sections with very high H/C ratio. For the study described here a half-open test section was adopted.

6.2 Experimental set-up and measurements

6.2.1 Wind tunnel and test section

The wind tunnel used for the experiments presented here was the 0.5m Plint wind tunnel at Durham University; an open circuit design which discharges directly to the atmosphere. For this investigation the wind tunnel working section was configured to have a square cross-section (457mm x 457mm) with solid sides but open top and bottom (Fig. 6.7) as recommended by Rainbird [58].

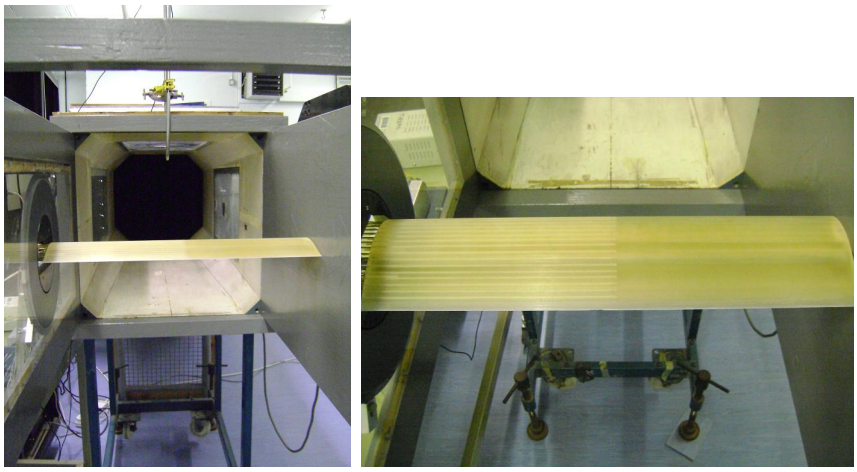

Figure 6.7: Test section.

6.2.2 Oscillating system

Although the unsteady data required for Darrieus start-up analysis is the combined pitch and plunge motion, the motion considered in this preliminary investigation

is a harmonically sinusoidal motion. This is mainly because the pitch motion is the main component and is relatively easy to perform in wind tunnel environments. It is noted the pure pitch motion is less effective in generating vortex formation than the combined motion and it generally requires a higher reduced frequency to produce a vortex of comparable size. Despite that, the data obtained from this testing should be sufficient to allow an investigation of how the unsteadiness affects thrust generation during start-up process.

The motion is generated by the use of crank mechanism which is powered by a 250W DC. motor (Fig. 6.8). The crank mechanism consists of a controller, a motor, a spinning disc, a crank, a connector, and a linear potentiometer.

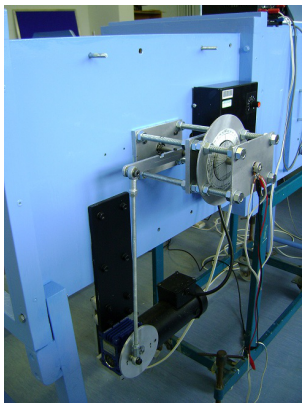

Figure 6.8: Photograph of the pitch oscillating system.

The spinning disc has four connecting points for oscillation amplitude adjustment. The connector is connected directly to the aerofoil pitching axis. The potentiometer is connected to the end of the shaft to track incidence angle. The oscillation frequency is controlled through the control system.

6.2.3 Aerofoil models

To suit the test section, the aerofoils were designed to have a span of 0.450 m and a chord of 0.11 m resulting in both section H/C ratio and the aerofoil aspect ratio having a value of 4.1 (Fig. 6.9). Initial CFD evaluation confirmed that this test configuration resulted in 2D flow over much of the aerofoil's span whilst retaining a large enough cross section to contain the required internal instrumentation. The aerofoils were produced by rapid prototyping from Fullcure 720 material giving a high surface precision ($\pm$ 0.1mm). Two sets of aerofoil models were manufactured for steady and unsteady tests.

Pressure tappings were located at midspan to measure the nominally two dimensional pressure coefficient. Each aerofoil had different pressure tapping locations depending on the shape and local thickness of the aerofoil. The number of pressure tappings were 24, 22, 30 and 32 for NACA0012, SG6043, SD7062, and DU06-W-200, respectively. Aerofoils for unsteady tests are physically the same as those of the

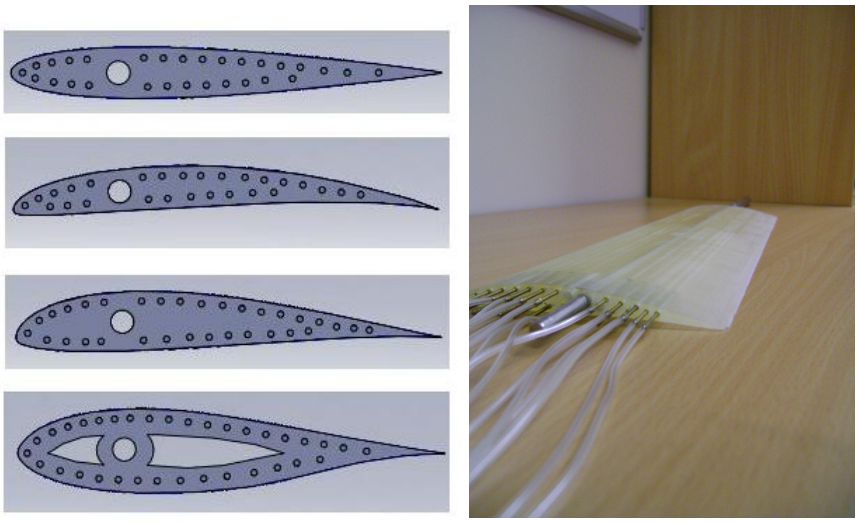

Figure 6.9: Tested aerofoil models.

steady tests except that the pitching axis that was located at quarter chord. Pressure tapping coordinates are provided in Appendix A. All tappings were connected to a 48-channel Scanivalve. The models were cantilevered from a Plint electronic force balance that was mounted on one side of the test section and which had been modified to provide an analogue output signal for each force component.

6.2.4 Data acquisition system

A computer-based system was used to record all pressure and force signals via an NI USB-6218 ADC consisting of 16 channels with a resolution of 16 bits. This device has a sample rate of up to 250 kS/s.

6.2.5 Calibration

Steady cases: The calibration of the force balance was made by applying known mass (or forces) to the balance for each component and recording the load cell output. From these data, a calibration matrix for the balance was created.

Unsteady cases: In addition to the steady-state calibration of the pressure transducers, the system dynamic response is needed for unsteady tests due to damping effect of the system. The system frequency response is taken into consideration using transfer function correction [159].

The measuring system (consisting of part of an aerofoil section, tubing, the scannivalve, and a transducer) was connected to an unsteady calibration apparatus (Fig. 6.10). The apparatus consists of a signal generator, a loud speaker, and a reference pressure transducer.

In the calibration process, the loud speaker, which is sinusoidally activated by a signal generator, inputs a fluctuating pressure to the system. Pressures from the

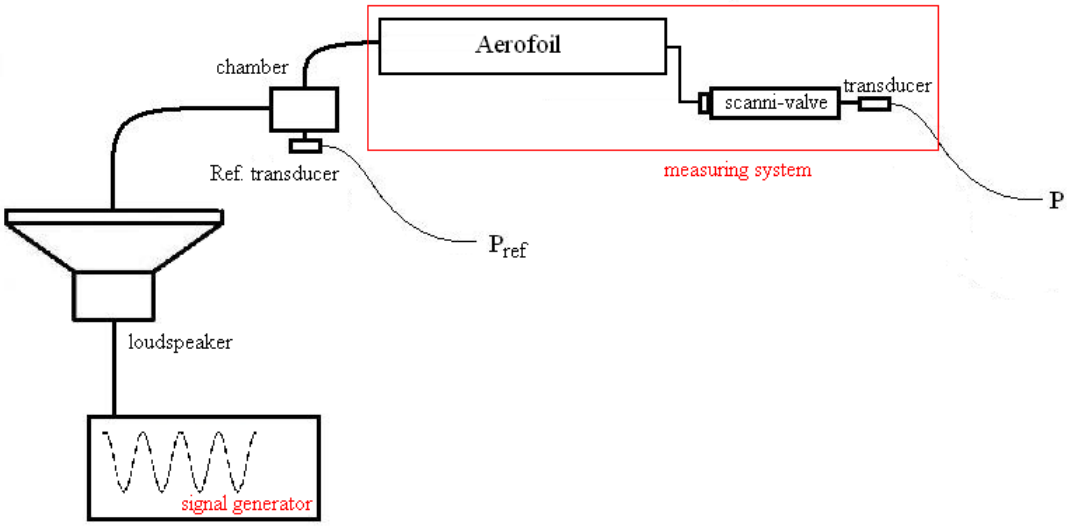

Figure 6.10: Schematic of unsteady calibration.

reference transducer and from the output of the measurement system are logged simultaneously over the sweep frequency. The relation between both pressures is then processed to obtain a pressure-frequency curve.

The potentiometer was calibrated by varying the aerofoil incidence and recording the voltages produced. The calibration produces a linear angle-voltage curve which can the be used to track the change in angle of attack.

6.2.6 Data acquisition methods

Force and pressure data of both static and dynamic tests were recorded using the Durham software suite.

Steady cases: Both forces and pressures are measured for steady tests. The models were cantilevered from a Plint electronic force balance that was mounted on one side of the test section and which had been modified to provide an analogue output signal for each force component. All pressure tappings were connected to a 48-channel scanivalve.

All forces were measured at a rate of 800Hz and averaged over a period of 2.5 seconds. Forces were measured for the full 360° incidence range in 2° increments (except for the symmetric NACA0012 which was measured over 180°). The static pressure measurements on each aerofoil were obtained through the computer controlled Scanivalve using the same sampling rate and frequency. Measurements on the aerofoils were obtained at three Reynolds numbers (nominally 65,000, 90,000, and 150,000).

Unsteady tests: Unsteady surface pressures were also measured using a scanivalve at a same sampling rate used in the steady tests. The measurement is carried

out port by port. The tests were conducted at the same nominal Reynolds numbers, namely 65,000, 90,000, and 150,000.

Unsteady data recorded was in the form of instantaneous pressure and aerofoil incidence angle. In all cases, 2048 data were sampled at an even time interval at a sample frequency of 800Hz. This sample frequency was selected in order that a sufficient amount of data is collected for the highest frequency tests (50Hz). The mean incidence angle and oscillation amplitude were set manually prior to the start of the tests.

6.2.7 Data reduction

In order to obtain unsteady surface pressure at specific incidence angles, time-series measurement of pressure and incidence angle at each port are combined and divided into up- and down-strokes. The data in each stroke is then binned and averaged. An example of this data (at two ports on suction and pressure side) is presented in Fig 6.11.

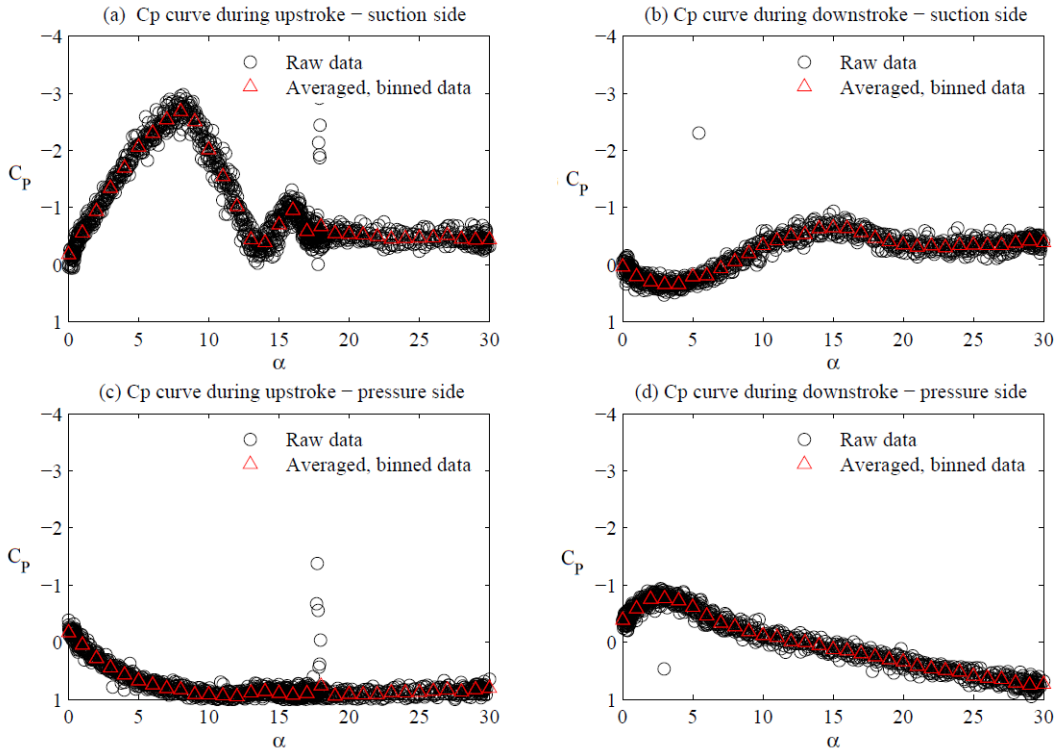

Figure 6.11: An example of representative surface pressure coefficients.

Port-by-port data reduction leads to a contour of pressure coefficients with respect to chordwise position and incidence angle.

It is noticeable that, the pressure on the suction side is significantly changed by the unsteadiness as it involves a vortex formation (Fig. 6.11a). The pressure variation on the pressure side is less complicated and mainly involves the movement of the stagnation point (Fig. 6.11c and 6.11d). The process is repeated for all ports to

produce unsteady surface pressure as a function of chordwise position and incidence angle during each stroke.

The C_P variations are then integrated to obtain normal and axial force coefficients by using the following equation.

$$C_n = \int_0^1 (C_P^L - C_P^U) \times \cos\phi \; d(s) \tag{6.1}$$

$$C_c = \int_0^1 (C_P^L - C_P^U) \times \sin\phi \; d(s) \tag{6.2}$$

where s is distance along the aerofoil surface and ϕ is the angle on the aerofoil surface.

Unsteady lift and drag are computed from the following equations.

$$C_l = C_n \cos\alpha - C_c \sin\alpha \tag{6.3}$$

$$C_d = C_n \sin\alpha + C_c \cos\alpha + C_{d0} \tag{6.4}$$

6.2.8 Measurement error

Multiple measurements had been taken to estimate error and repeatability of the results. In steady tests, force and pressure measurements were conducted three and four times, respectively. The results were then averaged to obtain representative values. All measurements were found to be repeatable with standard deviation of ± 0.014, ± 0.011, and ± 0.017, for lift, drag, and pressure coefficients, respectively.

In unsteady tests, the setting of mean incidence angle was found to be the largest source of error and was within $\pm 2.5°$. The incidence angle measurements using the potentiometer were found to be $\pm 1°$. Unsteady pressure measurements were conducted for 2048 data points which led to a certain number of cycles, depending on the aerofoil oscillation frequency (6 to 16 cycles for the lowest and highest oscillation frequencies, respectively). Repeatability of results was found to be good with standard deviation of ± 0.16. Figure 6.12 shows an example of error bars associated with unsteady pressure measurement.

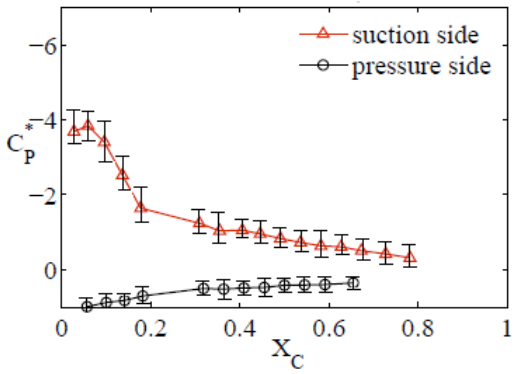

Figure 6.12: An example of pressure coefficient and error bars.

6.3 Test matrix

The testing is extensive. It includes steady and unsteady testing of six aerofoils (four from the previous chapter and other two which will be presented later). In steady tests, pressure and force measurements were conducted at three Reynolds numbers through 360° (2° increment).

Unsteady testing of the aerofoils were conducted in terms of unsteady pressure coefficients at three Reynolds numbers, four reduced frequencies, and over a wide range of mean incidence angles. All of these results in almost 950 tests in total. Table 6.1 summarises all test conditions conducted.

6.4 Conclusions

Effects of wall proximity and the reason for using an 'half-open' test section had been presented in this chapter together with experimental techniques. A series of numerical modelling on different test sections had clearly shown that the size (or height) of the wind-tunnel test section is critical for high incidence testing. The simulation results had been used to determine an aerofoil size for high incidence testing. In order to measure the aerofoil transient performance, a transfer function technique to account damping effect of the measuring system had also been presented.

Experimental results of the four aerofoils under static and dynamic conditions are presented in the next chapter.

Table 6.1: Test conditions.

Aerofoil	Steady	Unsteady		
	Re	k	α_m	$\Delta\alpha$
NACA0012	65,000	0.08, 0.10, 0.15, 0.20	5°, 15°, 30°, 45°, 60°, 90°, 120°, 240°, 270°, 300°, 315°, 330°, 345°	30°
	90,000	0.08, 0.10, 0.15, 0.20	5°, 15°, 30°, 45°, 60°, 90°, 120°, 240°, 270°, 300°, 315°, 330°, 345°	30°
	150,000	0.07, 0.10, 0.15, 0.20	5°, 15°, 30°, 45°, 60°, 90°, 120°, 240°, 270°, 300°, 315°, 330°, 345°	30°
SG6043	65,000	0.08, 0.10, 0.15, 0.20	5°, 15°, 30°, 45°, 60°, 90°, 120°, 240°, 270°, 300°, 315°, 330°, 345°	30°
	90,000	0.08, 0.10, 0.15, 0.20	5°, 15°, 30°, 45°, 60°, 90°, 120°, 240°, 270°, 300°, 315°, 330°, 345°	30°
	150,000	0.07, 0.10, 0.15, 0.20	5°, 15°, 30°, 45°, 60°, 90°, 120°, 240°, 270°, 300°, 315°, 330°, 345°	30°
SD7062	65,000	0.08, 0.10, 0.15, 0.20	5°, 15°, 30°, 45°, 60°, 90°, 120°, 240°, 270°, 300°, 315°, 330°, 345°	30°
	90,000	0.08, 0.10, 0.15, 0.20	5°, 15°, 30°, 45°, 60°, 90°, 120°, 240°, 270°, 300°, 315°, 330°, 345°	30°
	150,000	0.07, 0.10, 0.15, 0.20	5°, 15°, 30°, 45°, 60°, 90°, 120°, 240°, 270°, 300°, 315°, 330°, 345°	30°
DU06-W-200	65,000	0.08, 0.10, 0.15, 0.20	5°, 15°, 30°, 45°, 60°, 90°, 120°, 240°, 270°, 300°, 315°, 330°, 345°	30°
	90,000	0.08, 0.10, 0.15, 0.20	5°, 15°, 30°, 45°, 60°, 90°, 120°, 240°, 270°, 300°, 315°, 330°, 345°	30°
	150,000	0.07, 0.10, 0.15, 0.20	5°, 15°, 30°, 45°, 60°, 90°, 120°, 240°, 270°, 300°, 315°, 330°, 345°	30°
S1223	65,000	0.08, 0.10, 0.15, 0.20	5°, 15°, 30°, 45°, 60°, 90°, 120°, 240°, 270°, 300°, 315°, 330°, 345°	30°
	90,000	0.08, 0.10, 0.15, 0.20	5°, 15°, 30°, 45°, 60°, 90°, 120°, 240°, 270°, 300°, 315°, 330°, 345°	30°
	150,000	0.07, 0.10, 0.15, 0.20	5°, 15°, 30°, 45°, 60°, 90°, 120°, 240°, 270°, 300°, 315°, 330°, 345°	30°
S1223B	65,000	0.08, 0.10, 0.15, 0.20	5°, 15°, 30°, 45°, 60°, 90°, 120°, 240°, 270°, 300°, 315°, 330°, 345°	30°
	90,000	0.08, 0.10, 0.15, 0.20	5°, 15°, 30°, 45°, 60°, 90°, 120°, 240°, 270°, 300°, 315°, 330°, 345°	30°
	150,000	0.07, 0.10, 0.15, 0.20	5°, 15°, 30°, 45°, 60°, 90°, 120°, 240°, 270°, 300°, 315°, 330°, 345°	30°

Chapter 7

Experimental Results

This large chapter presents and discusses general performance characteristics of the four aerofoils. Steady and unsteady results are discussed separately.

7.1 Static performance

A series of lift, drag, and pressure coefficients are presented in this section. The measured pressure coefficients are presented alongside numerical predictions generated by FLUENT 6.3.26.

7.1.1 NACA0012 aerofoil

Figure 7.1 and 7.2 show the lift and drag coefficient curves for the NACA0012 section at three tested Reynolds numbers and, as expected, it can be seen that the lift curves in pre-stall are not significantly affected by Reynolds number. The maximum lift coefficients occur at 12° angle of attack for all Reynolds numbers but the peak lift coefficient is seen to increase with Reynolds number to maxima of 0.778, 0.781, and 0.816 for the three tested Reynolds numbers. This maximum lift is comparable to the value of 0.853 measured by Shedahl and Klimas [51] at the higher Reynolds number of 160,000.

With a further small incidence increase, the flow separates over the entire aerofoil surface and the lift drops rapidly to a value of approximately 0.64 at 14° before gradually increasing again to 0.8 at around 45°. There is a further sudden drop in lift at 54° followed by further gradual reduction to zero at 90°. Static pressure measurements either side of 54° degrees reveal that the fall in lift corresponds to a sudden change of flow behaviour, particularly on the suction side. Figure 7.3 shows the variation of pressure coefficient with distance from the leading edge.

As expected in this stalled flow the suction side pressure remains almost constant over the entire surface but there is a very significant change in the magnitude of that pressure coefficient between 50° and 60° incidence. When the AoA is lower than 54° the flow remains attached over the first few millimeters of the leading edge

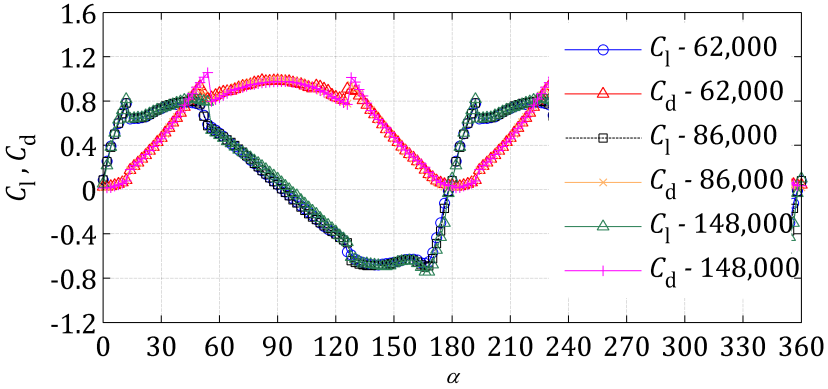

Figure 7.1: Lift and drag coefficients: NACA0012.

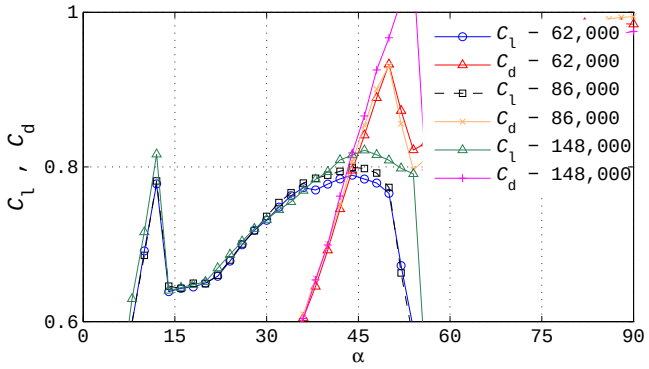

Figure 7.2: Lift and drag coefficients: NACA0012 (close-up).

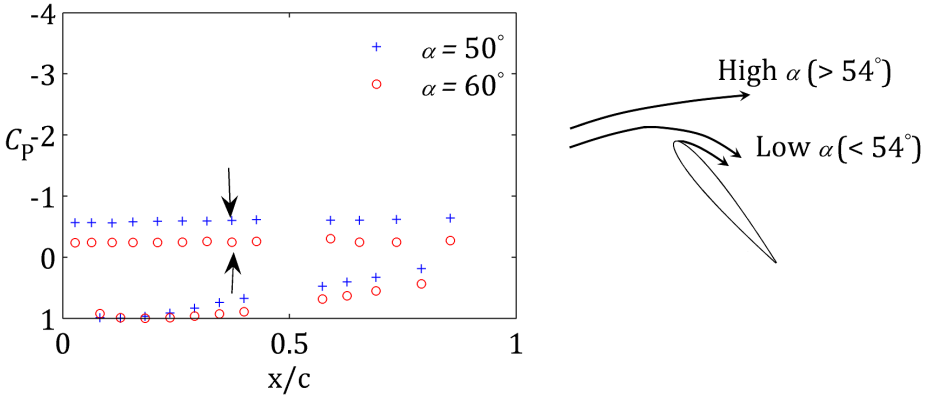

Figure 7.3: Surface static pressure coefficients and flow schematic.

which is sufficient to cause substantial turning of the flow before separation occurs. Above 54° incidence the flow separates immediately as though over a flat plate, resulting in deflection of the opposite sign (shown schematically in Fig. 7.3). The latter flow regime induces lower air movement (lower velocity) on the suction surface and, hence, higher (or less negative) pressure coefficient.

These trends, including the pressure coefficient discontinuities, are reversed as

the *AoA* passes 90° and the aerofoil is, in effect, travelling backwards.

In terms of drag, the usual pre-stall trend is followed as the angle of attack increases (Fig. 7.1 and 7.2). It is also seen that drag coefficients decrease from 0.0242 to 0.0136 with Reynolds number increases from 62,000 to 148,000. Drag then increases sharply at the stall point, corresponding to the observed reduction in lift, and continues to increase rapidly to a peak at approximately 54°. Further incidence increase results in a rapid fall in drag, again corresponding to an observed discontinuity in the lift curve at that incidence. Although the peak drag magnitude appears to be Reynolds number sensitive, all three tests show a fall to about the same value of drag coefficient (0.8). The drag then increases again reaching a second peak at 90°. Above 90°, the trend is reversed.

Figure 7.4 presents CFD-derived and experimental pressure coefficients for the NACA0012 and it is seen that at modest incidences (e.g. 5°) the CFD captures the experimental results well as might be expected.

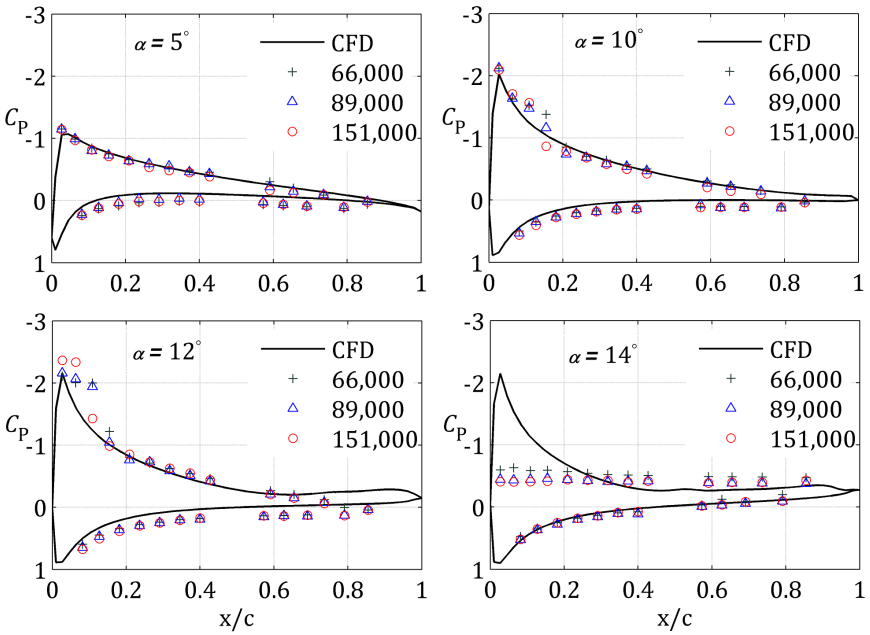

Figure 7.4: Pressure coefficients: NACA0012.

However, as stall is approached, the wind tunnel data revealed a suction surface separation bubble in the diffusing zone immediately downstream from the suction peak which is not captured by the CFD (*AoA* 10° and 12°). At 14° incidence, the aerofoil is completely stalled. Reynolds number does not have a profound effect on the C_P characteristics except in the formation of the laminar separation bubbles. In each case, the laminar separation occurs in the rapidly diffusing flow at around 5-percent chord, moving slightly upstream with increasing angle of attack. Turbulent reattachment occurs at around 20% chord. By 14° incidence, full stall has occurred which is thought to be caused when the flow that is separated by the bubble can no longer sustain turbulent reattachment due to low energy in the flow; a process known

as bubble bursting [151]. This results in a sudden stall with relatively sharp lift peak (as can be seen from the force measurements (Fig. 7.2)). This is not captured by the CFD prediction in which formation of the bubble is not predicted and stalling is a result of a gradual separation that is initiated at the trailing edge. In this experiments, the stalling angle of attack is 14° for all three of the tested Reynolds numbers. A summary of the positions of separation, reattachment, and bubble size for the NACA0012 is presented in Figure 7.5. There is no significant difference in the laminar separation point for different Reynolds numbers but the reattachment process takes place more rapidly at higher Reynolds number.

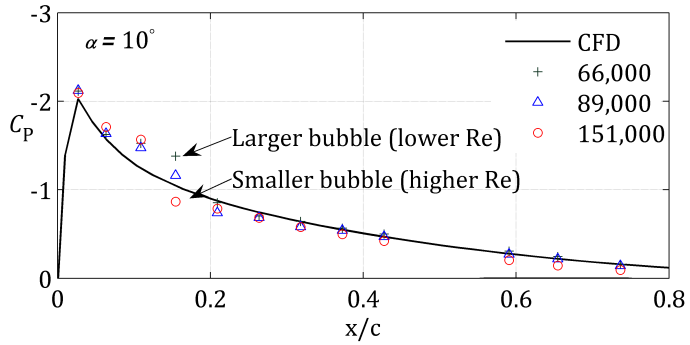

Figure 7.5: Separation and reattachment: NACA0012 suction surface.

In addition to the figures presented, pressure coefficients measured up to the incidence of 90° are also provided on the CD-ROM which accompanies this thesis.

7.1.2 SG6043 aerofoil

The SG6043 aerofoil exhibits both a higher peak lift and a slightly more progressive and delayed stall relative to the NACA0012 (Fig. 7.6).

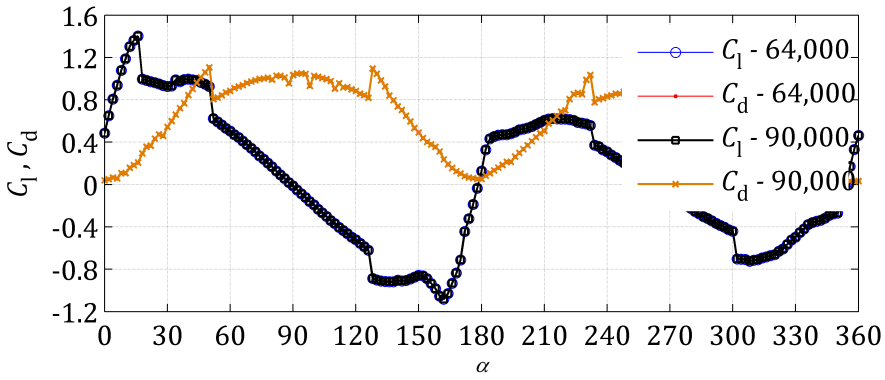

Figure 7.6: Lift and drag coefficients: SG6043.

In this case the stall characteristic is a combination of trailing-edge stall and leading-edge stall. A trailing-edge separation advances progressively upstream with

increasing incidence as can be seen from the static pressure distributions (Fig. 7.7). It should be noted that although measurements were not possible very close to the trailing edge because of insufficient blade thickness to accommodate the instrumentation, the agreement between the measurements and CFD over the blade surfaces approaching the trailing edge give confidence in the use of CFD predictions in this zone. In addition to the trailing edge separation a separation bubble is also seen which moves towards the leading edge with increasing AoA. The surface static pressure distribution at 16° incidence angle shows that trailing-edge separation covers around 30% of the blade's suction surface when the bubble reaches the leading edge. Further incidence increase leads to bubble bursting. The consequence of these two different simultaneous stall mechanisms is an initially progressive stall as the trailing edge stall develops, followed by an abrupt loss of lift when the leading edge bubble bursts. The maximum values of lift for this aerofoil at the three increasing test Reynolds numbers are 1.358, 1.403, and 1.431 at respective incidence angles of 16°, 16°, and 18°. After the stall point, the lift drops to a value of around 0.97. A comparison of the surface static pressure distributions of the NACA0012 and the SG6043 (Fig. 7.4 and 7.7) shows that the SG6043 produces a consistently larger pressure difference between the suction and pressure surfaces even when fully stalled. This is mostly due to the effect of camber that leads to an increased lift contribution from the pressure surface.

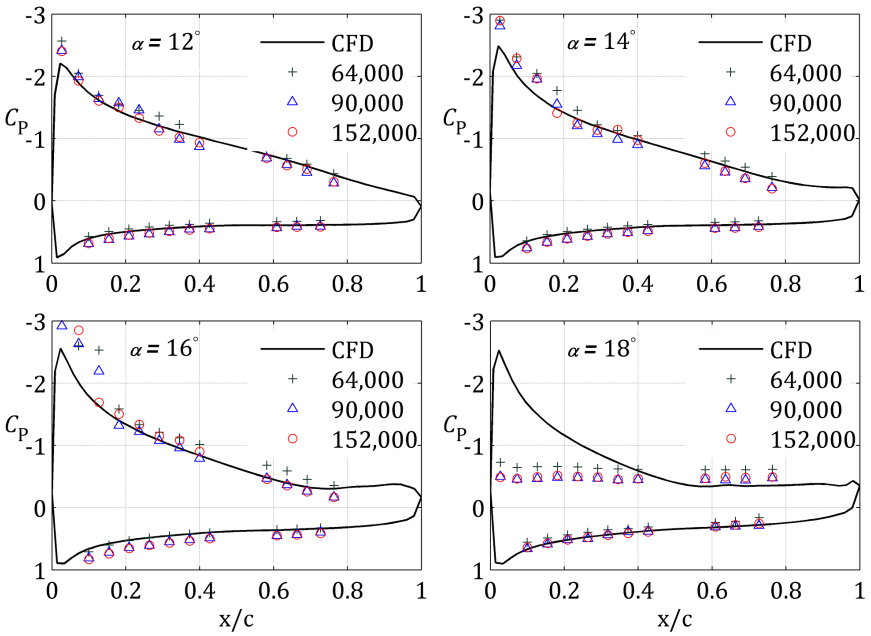

Figure 7.7: Pressure coefficients: SG6043.

Like the NACA0012, the lift coefficient remains relatively constant with further increase in angle of attack up to approximately 50°, where a second rapid fall in lift occurs followed by a further, almost linear fall to zero lift at the 90° incidence point. A similar but reversed characteristic is mirrored beyond 90°, but it should

be noted that unlike the symmetrical NACA0012, the lift characteristic on either side of 90° incidence is no longer perfectly symmetrical. The drag characteristic is almost identical to that of the previously described NACA0012.

Further analysis of the static surface pressure distributions for this aerofoil show that relative to the NACA section, the bubble is first detected at a higher angle of attack (12°). Trailing edge separation is first seen at 14° incidence as indicated by a nearly constant pressure and full stall is observed at an angle of attack of 18° when the bubble reaches the leading edge and bursts.

7.1.3 SD7062 aerofoil

The lift characteristics of the SD7062 aerofoil are shown in Figure 7.8 and it can be seen that it closely resembles that of the SG6043 profile. As the Reynolds number is increased, the maximum lift coefficients of 1.163, 1.354, and 1.397 occur at the respective angle of attack of 14°, 16°, and 18°. The post-stall values of lift coefficient for this aerofoil are around 0.8 which is a little bit lower than for the SG6043. The drag coefficients are again similar to both of the previously presented cases.

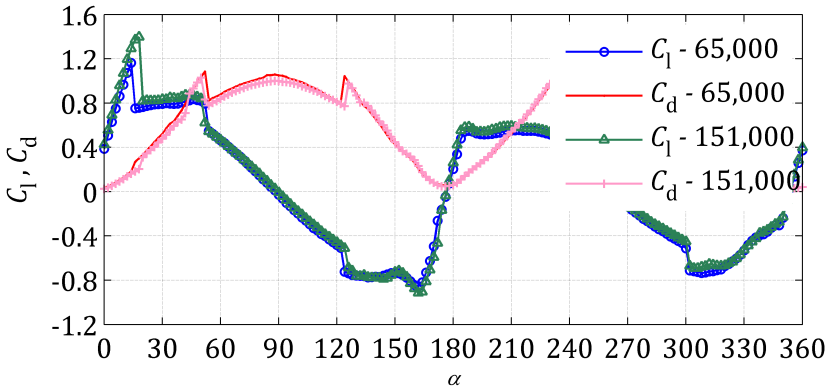

Figure 7.8: Lift and drag coefficients: SD7062.

The SD7062 aerofoil section also demonstrates the presence of a laminar separation bubble which is first seen at 12° angle of attack (Fig. 7.9). However, the separation bubble differs from the previous two cases in that it occurs further downstream at about 20% chord and that the length of the bubble seems to be much more sensitive to Reynolds number. At the highest tested Reynolds number the layer reattaches almost immediately but for the lowest Reynolds number, reattachment does not occur until around 40% chord. The bubble's separation point moves forward to the leading edge with further increase in AoA. Full stall is first observed at 16° incidence at the lowest Reynolds number (68,000), whereas at the highest Reynolds number stall is delayed to 20° incidence.

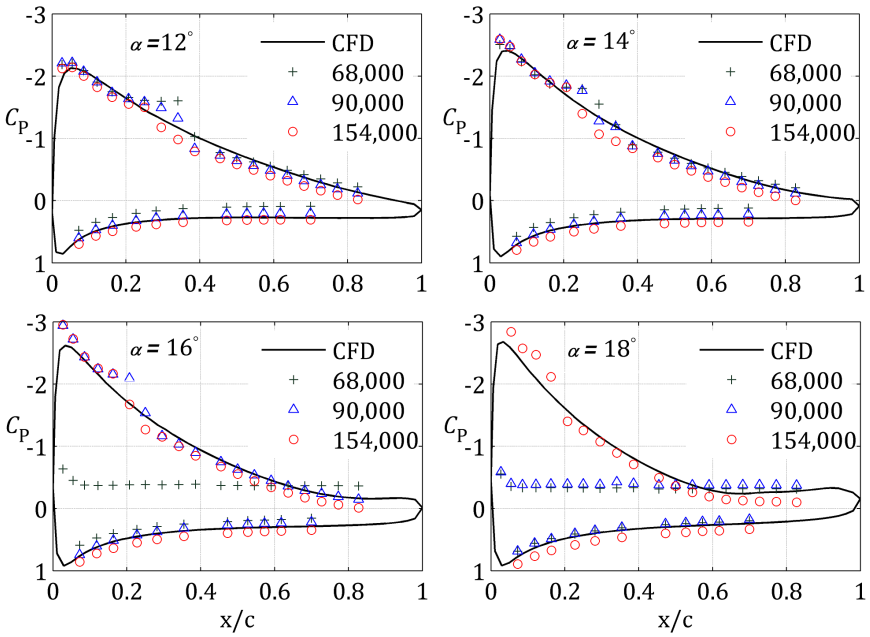

Figure 7.9: Pressure coefficients: SD7062.

7.1.4 DU06-W-200 aerofoil

Figure 7.10 presents the lift characteristics of the DU06-W-200. The maximum pre-stalled lift coefficients with progressively increasing Reynolds number are 0.804, 1.067, and 1.136, but it can be seen that the lift production of this aerofoil is more sensitive to the Reynolds number than the previous three aerofoils. For instance, when the Reynolds number is reduced from 151,000 to 68,000, a lift coefficient reduction of almost 0.33 is seen. Lift generation at higher angles of attack is similar to that of the NACA0012.

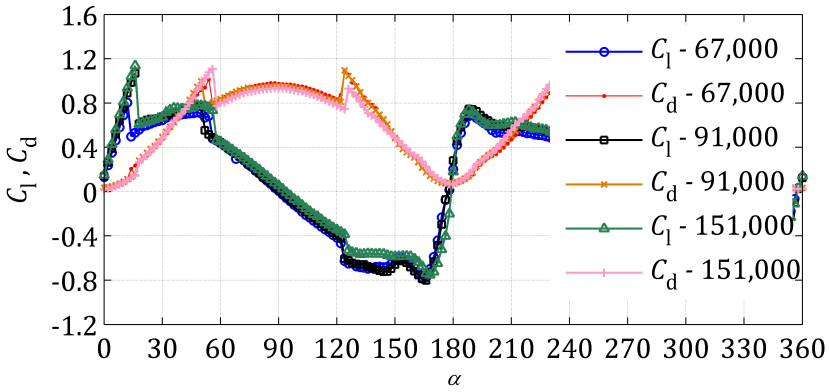

Figure 7.10: Lift and drag coefficients: DU06-W-200.

The surface pressure distributions (Fig. 7.11) again reveal the formation of separation bubble which is observed to form at moderate *AoA* and which moves forward towards the leading edge and reduces in length as the angle of attack increases. At

the lowest Reynolds number, the aerofoil stalls at 14°.

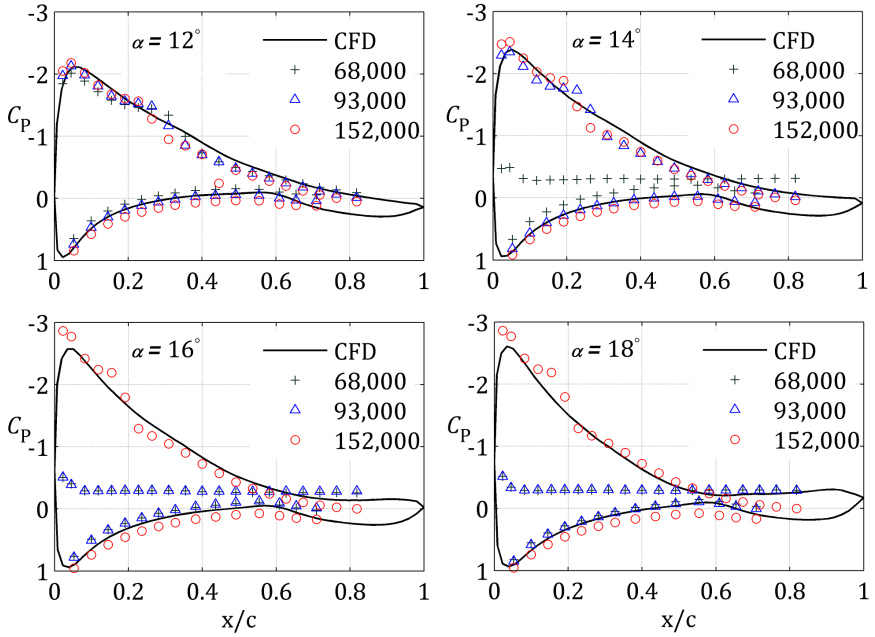

Figure 7.11: Pressure coefficients: DU06-W-200.

7.1.5 Performance comparison

In the light of these experimental results, it can be seen that the SG6043 and the SD7062 exhibit relatively higher pre-stall lift coefficient peaks (around 1.4) and outperform the others at all incidence angles from 0° to 90°. Significantly, for wind turbine applications their higher lift characteristics in the post-stall region make them well suited for horizontal-axis applications for which incidence angles experienced by the turbine blades are frequently in this range.

Performance comparisons between the NACA0012 and the DU06-W-200 show that the latter can produce a higher lift peak at the highest tested Reynolds number but suffers from performance degradation with decreasing Reynolds number. This, combined with its comparatively high thickness ratio which contributes to a higher moment of inertia, suggests that the DU06-W-200 is less suitable for a turbine operating predominantly in a relatively low-wind environment in which the self-starting problem is of concern.

It is also observed that, although the SG6043 and the SD7062 lose their performance advantage at very high incidence (180° to 360°), their degraded performances remain comparable to those of the NACA0012 and the DU06-W-200 (Fig. 7.12), suggesting that these high camber aerofoils might be used with vertical-axis applications to improve rotor performance.

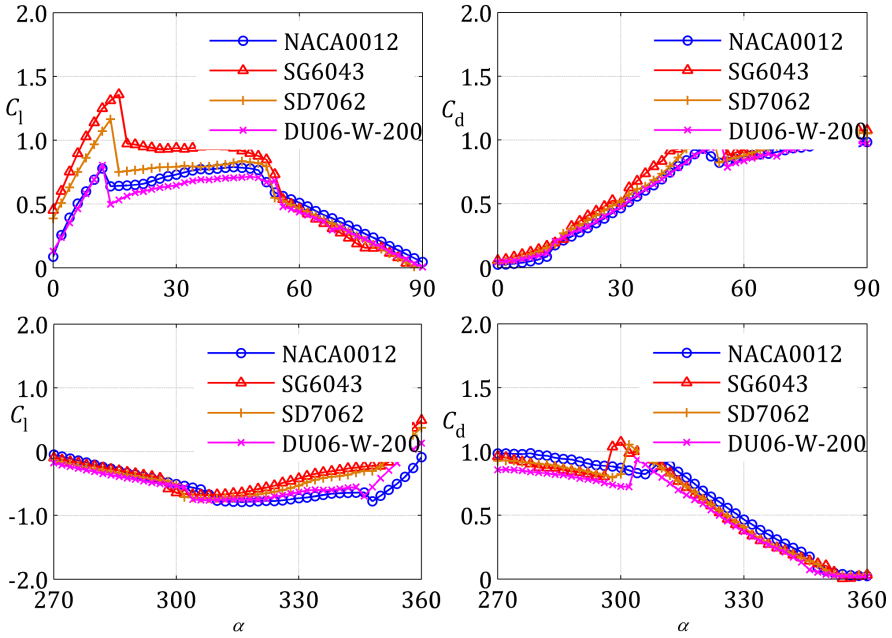

Figure 7.12: Performance comparison.

7.1.6 Comparison with previous work: The NACA0012 case

Probably, the most well-documented and widely adopted data for high incidence wind turbine applications is that of Sheldahl and Klimas [51]. In this section, the measured lift and drag coefficients from this study at the highest tested Reynolds number (148 000) are compared to their data at the relatively similar Reynolds number of 160 000. Despite the widespread use of this particular set, it must be noted that Sheldahl and Klimas conducted measurements at only three Reynolds numbers (360 000, 500 000, and 700 000) and consequently the results that they published for other Reynolds numbers were obtained through extrapolations. It is also noted that their tests were conducted in a closed test section wind tunnel with height-to-chord ratio of 14. Figure 7.13 and 7.14 show the comparison.

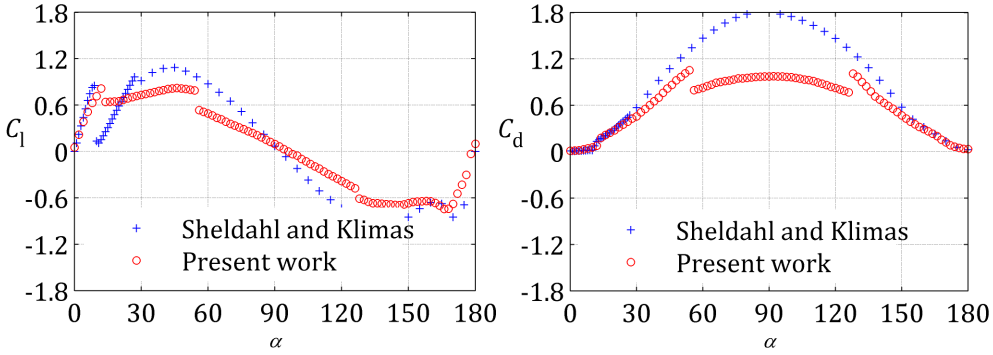

Figure 7.13: Lift and drag comparisons.

In terms of lift coefficient, relatively good agreement is seen between the two

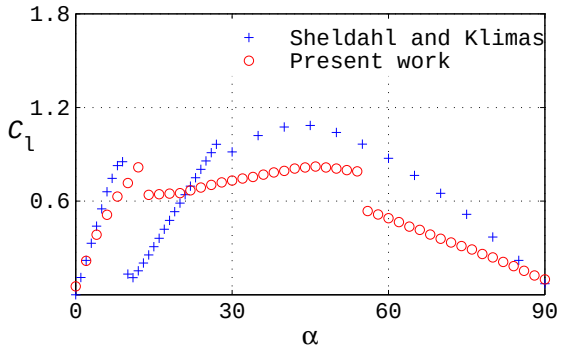

Figure 7.14: Lift comparison (close-up).

sets of data in the pre-stall regime. Both give almost identical lift coefficient peak values, although the Sheldahl and Klimas data show a very slightly earlier stall. Immediately after the stall, the lift coefficient from the current study falls to a value of around 0.6, maintaining and gradually increasing that value with increasing *AoA* to 54°. The Sheldahl lift curve shows a quite different post-stall characteristic in which the lift coefficient suddenly drops to almost zero before sharply rising to the second peak of around 1.1 C_l. It is not clear what physical flow mechanism could result in such a dramatic lift loss and recovery in the immediate poststall zone and this feature was not discussed by Sheldahl and Klimas in their original work. Examination of static pressure coefficients of this present work at the stall angle (Fig. 7.4) reveals that when the *AoA* changes from 12° to 14°, although there is a loss of pressure on the suction side, the static pressure coefficients on the pressure side do not change dramatically and there still exists a pressure difference. It seems improbable that such a low value of lift (0.1) will occur at the stall angle.

Lift from both tests then gradually reduces to around zero at 90° *AoA*, although the Sheldahl data does not exhibit the discontinuity at 54° that has been observed in this study.

In terms of drag, good agreement is again seen in the pre-stall region and, perhaps surprisingly, the drag results are similar too in the post-stall zone up to almost 60°, despite the significant differences in the observed lift characteristics.

Another important difference between the two data-sets is the second lift peak behaviour (i.e. the peak of lift coefficient that occurs close to 45° incidence). Here, the results of Sheldahl and Klimas [51] show a very clear peak that even exceeds the measured maximum pre-stall lift, while only a slight increase in lift is seen in this work.

A similar discrepancy was first examined by Rainbird [58] who undertook a broad review of published aerofoil performance data and found it to be inconsistent, especially post-stall. The data can be categorized into two clear groups: those that display a distinct, high second lift peak and those that do not. He hypothesized that it might be an effect of the test section configuration used in the experiments and by conducting his own tests using both closed and open test sections, he found that

he could replicate both of the alternative lift characteristics simply by changing the test section configuration. Figure 7.15 illustrates his results.

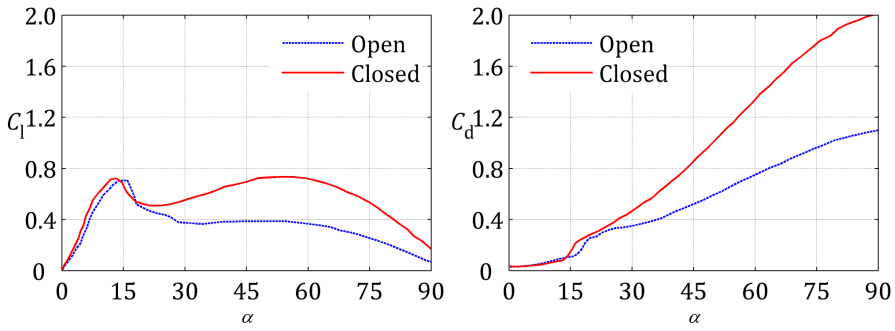

Figure 7.15: Closed and open test section aerodynamic data of a NACA0015 (from Rainbird [58]).

It can be seen from the results that the test with a closed, high blockage test section managed to replicate the Sheldahl trend for both lift and drag coefficients. While the lift coefficient of the open test section is nearly constant in the post-stall region, the lift coefficient from the closed test section rises to the second peak. For drag coefficient, it appears that drag from the closed test section is higher than that of an open test section in the post-stall region. The difference is more pronounced with increasing *AoA* and at 90° where the drag coefficient from the closed test section is nearly double that of the open test result. Generally, the percent of deviation increases with increasing angle of attack and can be as high as 100% (Fig. 7.16). In light of this information, the data of Sheldahl and Klimas and others who performed their high-incidence measurements at low H/C ratio must be viewed with some caution.

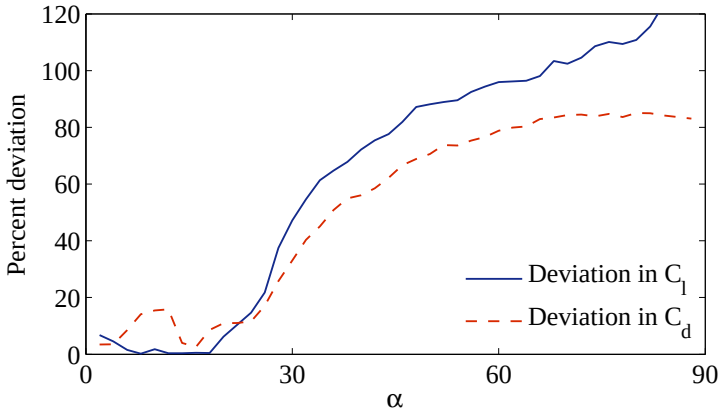

Figure 7.16: Percent deviation in lift and drag coefficients.

Rainbird's [58] force measurements are consistent with the CFD simulation results that were presented in Fig. 7.3, which show that there is a substantial reduction

of pressure on the suction side of the aerofoil at high incidence which leads to a significant increase in the pressure difference contributing to higher lift and drag. It appears that the closed test section confines and significantly alters the flow around the aerofoil leading to increased acceleration and high velocity in the vicinity of the leading and trailing edges. This leads to lower pressure on the suction side and, hence, to the second lift peak characteristics.

It is worth noting that the observed change in lift and drag at around 50° angle of attack that has been reported in this study was not seen in Rainbird's tests which is thought to be a consequence of the higher Reynolds numbers that were investigated by Rainbird (Re ≈ 200,000).

7.1.7 Post-stall comparison with the AERODAS model

Post-stall comparisons between this wind tunnel data and the lift and drag prediction from the most recent stall model developed by Spera [63] (it was named AERODAS and a summary of the model is provided in Appendix C) have been made to check the ability of that model to predict aerodynamic data under these conditions. The comparisons are made for one Reynolds number (90,000). Since aerodynamic coefficients in the pre-stall region are almost linear and normally well predicted, only post-stall data (from 20° to 90°) are presented here (Fig. 7.17).

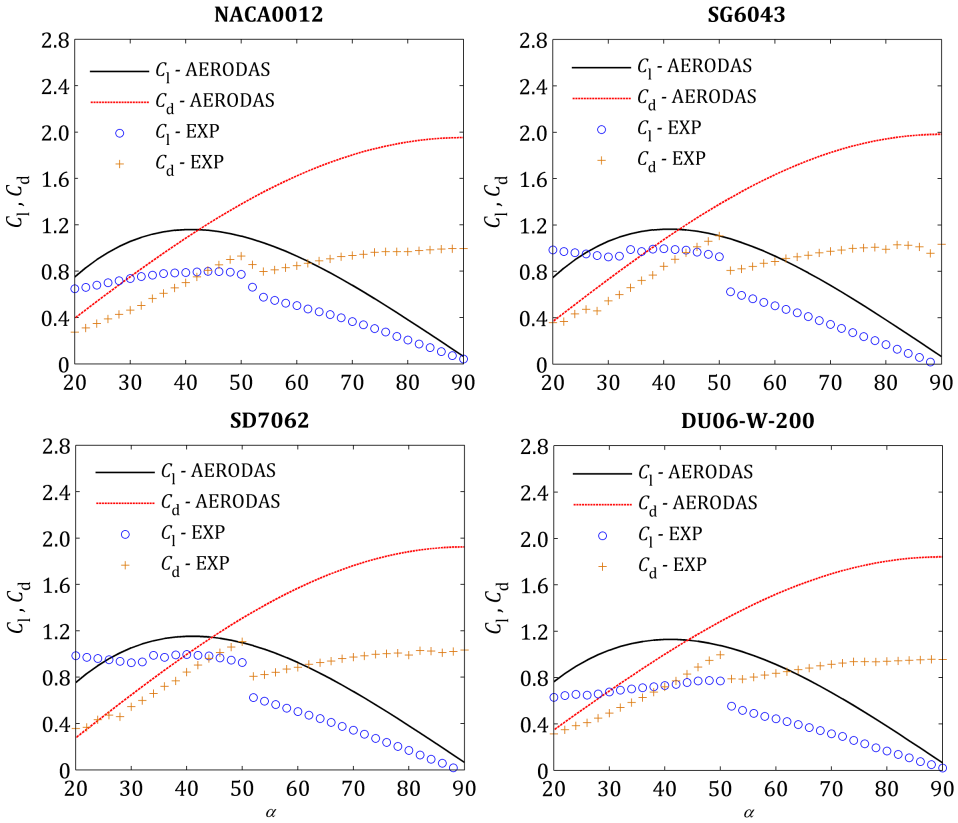

Figure 7.17: Post-stall comparisons between measurements and the AERODAS model.

The comparisons demonstrate significant differences between predictions by the AERODAS model and experimental results. Lift predicted by the model always increases to a second peak at around 40° (note that the first peak is not seen on this incidence scale) and then gradually reduces to around zero at 90°, while post-stall measured lifts behave differently (nearly constant post-stall lift up to 50° before falling to zero at 90°). Discrepancies between predicted and measured drag coefficients are seen for all angles of attack and they are more pronounced with increasing incidence angle. The maximum predicted drag is about two at 90°.

The discrepancies are mainly due to the source of high-incidence-angle aerofoil data used in the AERODAS correlation that were obtained from Ostowari and Naik [53, 54]. Their measurements were made in a closed test section wind tunnel having a height-to-chord ratio of only 10; a ratio that is inadequate according to Rainbird's hypothesis.

7.2 Dynamic performance

The dynamic performance characteristics of the aerofoils are discussed in terms of unsteady chordwise pressure distributions (C_P^*) and unsteady normal force coefficients (C_N).

Discussion of the C_P^* distributions over a series of incidence ranges will be first presented to show how unsteady flow phenomena such as vortex formation and shedding affect the C_P^* variations. The overall effect of these flows on aerodynamic loadings is illustrated in the form of unsteady C_N (obtained by integrating the unsteady C_P^* over the aerofoil chord) over the incidence range.

Initial observations of the C_P have shown that the effect of Reynolds number was less significant than dynamic parameters such as reduced frequency and incidence range. The change in Reynolds number generally alters the magnitude of the airloads while the behaviour of surface pressure variations along the aerofoil chord are qualitatively the same. The detailed discussion of the results is therefore restricted to one Reynolds number of 90,000.

It is also noted that the C_P^*s at specific angles of attack are obtained by varying mean incidence angle (α_m) (Fig. 7.18). For example, with an oscillation amplitude of 15°, setting the mean angle of attack of $-15°$ and 15° will give C_P^* variation over the incidence range of $-30°$ to 30°. Almost all of the C_P^*s presented this chapter were obtained from this setting as it is the range that the transient effects is most significant. The negative mean incidence is also referred to as 'reversed camber' mode of operation in this work as the suction surface has now operated as a pressure side and the formation of vortex will take place on its pressure side (Fig. 7.19).

Since each motion is associated with different flow phenomena, the presentation of unsteady surface pressure distributions are divided into four cases (Fig. 7.19):-

(a) Normal mode with increasing incidence angle The incidence angle is positive and increasing in this motion. Flow characteristics associated with this

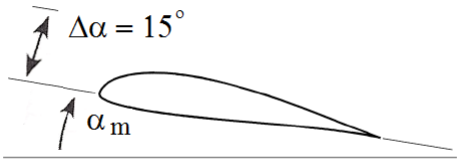

Figure 7.18: Mean incidence angle and oscillation amplitude.

(a) Normal mode with increasing AoA

(b) Normal mode with decreasing AoA

(c) Reversed mode with decreasing AoA

(d) Reversed mode with increasing AoA

Figure 7.19: Normal and reversed cambered modes of operation.

motion are vortex formation and convection which can be observed by higher-than-normal suction peak at the leading edge and a wave-like pressure variation along the aerofoil chord, respectively.

(b) Normal mode with decreasing incidence angle In this motion, the incidence range is still positive but decreasing (pitch-down motion). The primary flow feature associated with this motion is flow reattachment. The reattachment typically occurs at the leading edge and can be observed from the C_P variation that begins to follow the aerofoil nose shape.

(c) Reversed cambered mode with decreasing incidence angle In this mode, the incidence is negative and decreasing. This motion is mirrored of the first mode and the formation and convection of dynamic-stall vortex take place on the pressure side.

(d) Reversed cambered mode with increasing incidence angle The incidence angle increases back to the neutral position in this motion. The flow will reattach and regain its suction peak as the aerofoil returns to the normal mode.

The presentation that follows will be presented aerofoil by aerofoil (NACA0012, SG6043, SD7062, and DU06-W-200) and mode by mode. Two reduced frequencies

are shown in each mode to show how the flow is changed by the level of unsteadiness (Fig. 7.20).

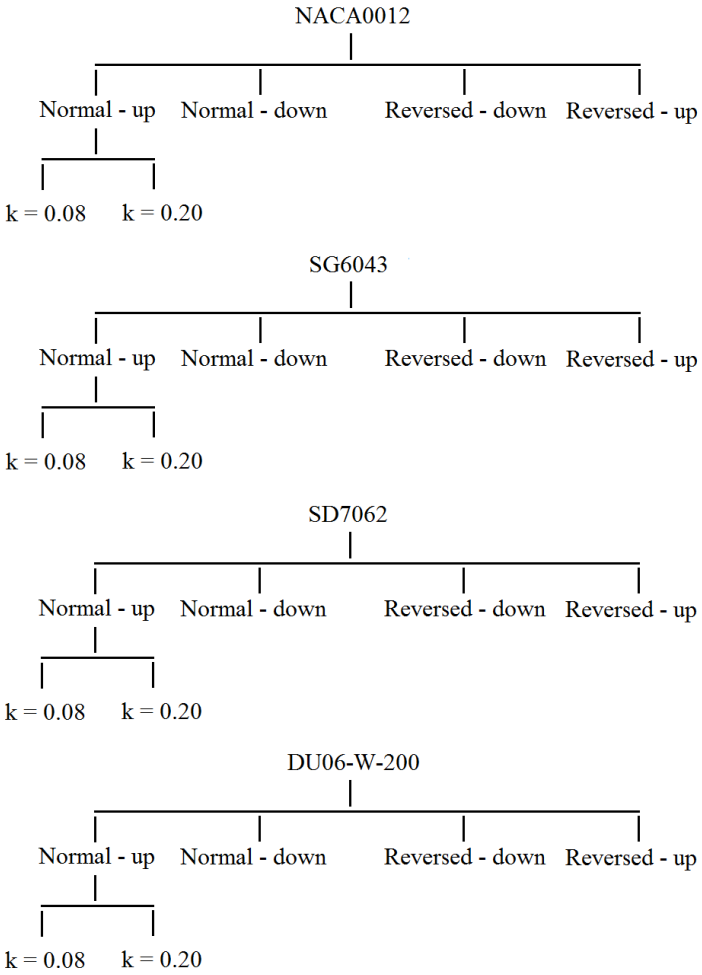

Figure 7.20: Order of presentation.

Each plot consists of unsteady C_P^* at some selected incidences (normally at six incidences, Fig. 7.21). The instantaneous incidence can be ascending or descending, depending on mode of operation (compare Fig. 7.21 and Fig. 7.22). The C_P^* on the suction and pressure sides are represented by solid line with *triangles* and *circles*, respectively. Under reversed camber operation the formation of vortex will be observed by the solid line with circles (Fig. 7.22). At the end, the overall transient effect will be presented in the form of unsteady normal load (C_N) together with its static counterpart. Figure 7.23 is an example of the presentation.

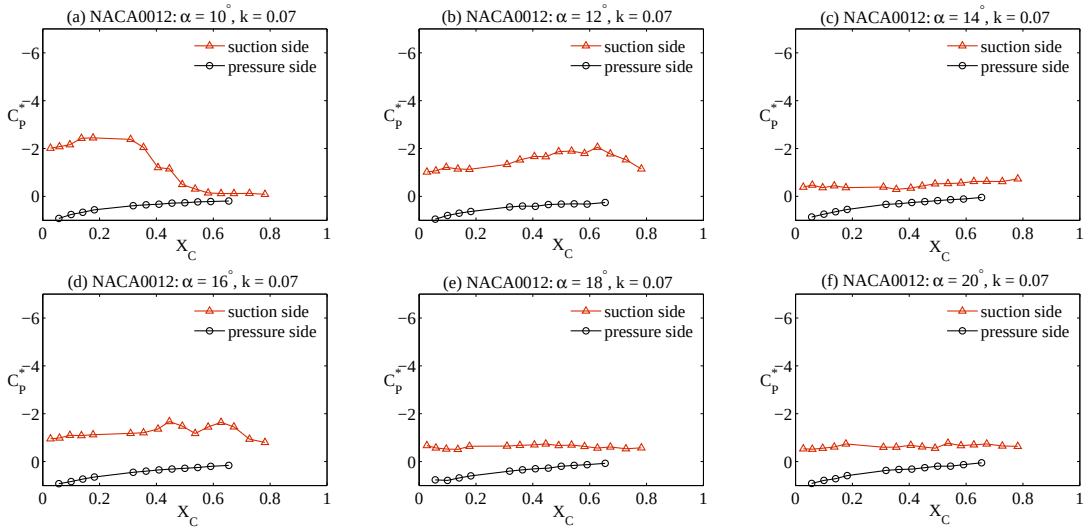

Figure 7.21: Example of presentation: Normal mode with increasing incidence angle.

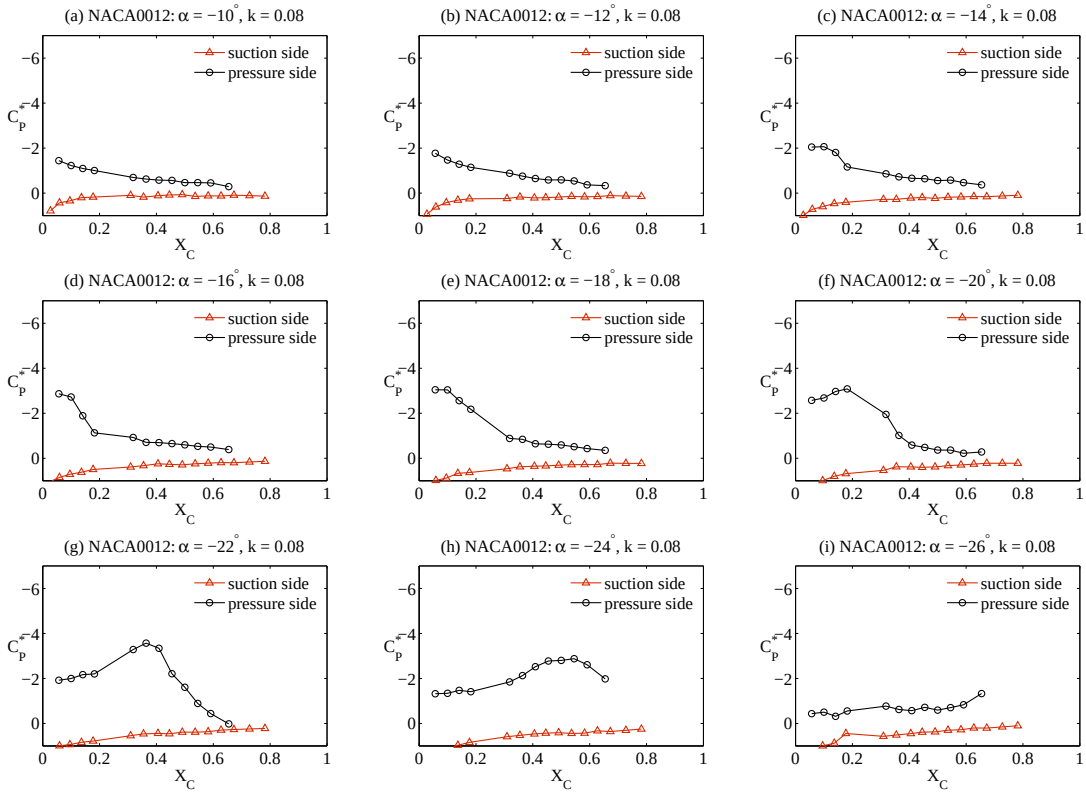

Figure 7.22: Example of presentation: Reversed camber mode with decreasing incidence angle.

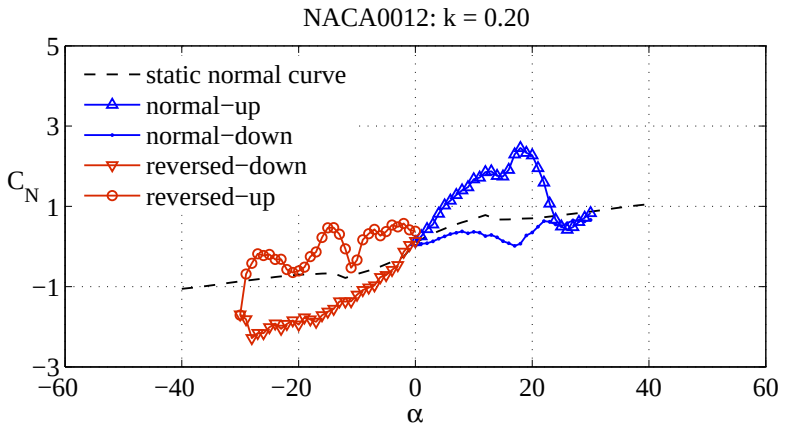

Figure 7.23: Example of presentation: Normal force coefficient.

As seen from the Figure, different lines are used to present different modes. They are:-

- **Static C_N curve** - *dotted* line.
- **Unsteady C_N during normal mode with increasing incidence angle** - solid line with *triangles*.
- **Unsteady C_N during normal mode with decreasing incidence angle** - solid line with *points*.
- **Unsteady C_N during reversed cambered mode with decreasing incidence angle** - solid line with *upside down triangles*.
- **Unsteady C_N during reversed cambered mode with increasing incidence angle** - solid line with *open* circles.

7.2.1 NACA0012 aerofoil

Normal mode with increasing incidence angle

Figure 7.24 presents unsteady surface pressure coefficients for the NACA0012 at ascending incidence angles of 10° to 20° with a 2° increment (7.24a to 7.24f). This incidence change is associated with a vortex formation process. Figure 7.25 presents basically the same information except at a higher reduced frequency of 0.20.

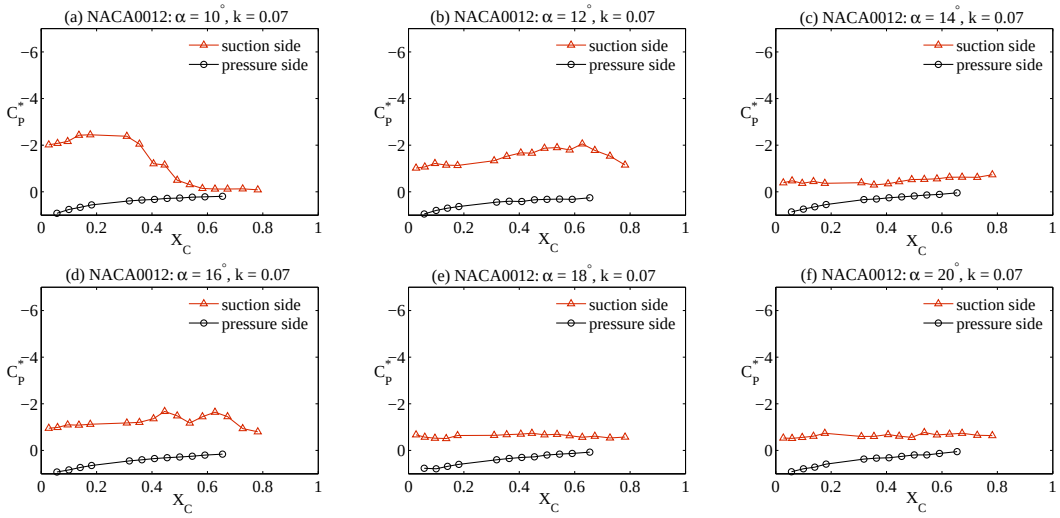

Figure 7.24: Unsteady C_P^* at a reduced frequency of 0.07: NACA0012 - normal-up.

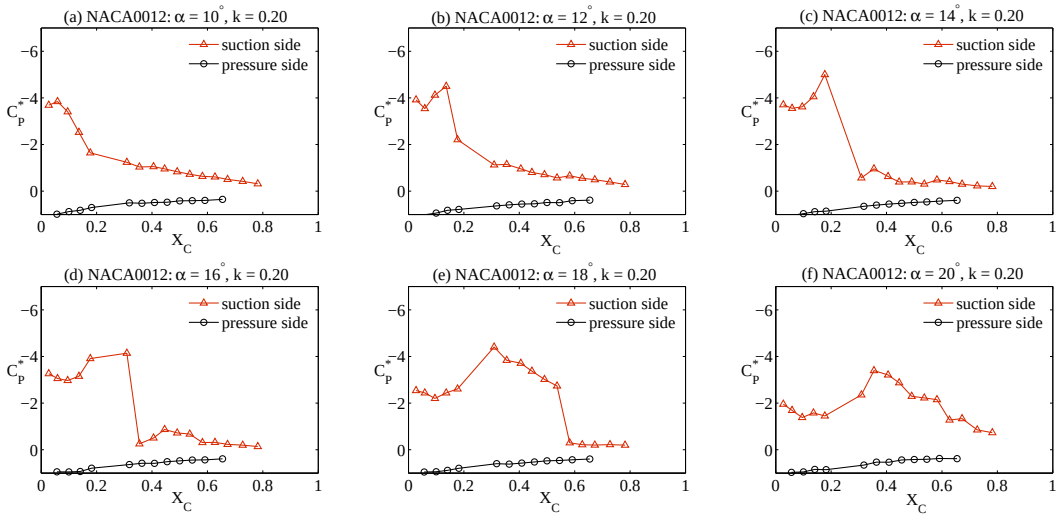

Figure 7.25: Unsteady C_P^* at a reduced frequency of 0.20: NACA0012 - normal-up.

It can be observed that the C_P^*s are different from those was found statically where the suction peak is always around the leading edge of the aerofoil (compare Fig. 7.4 and 7.24). The peak suction, under dynamic conditions, the peak pressure (or dynamic-stall vortex) will transverse along the aerofoil, causing a wave-like C_P^* curves.

It is seen from Figure 7.24a that dynamic-stall vortex has formed and, not long after the formation, the vortex convects along the aerofoil surface as incidence increases (Fig. 7.24b) and is finally shed into the wake (Fig. 7.24c), causing full stall at an incidence angle of 14° at a reduced frequency of 0.07 (not significantly different from that of static case).

The strength of the vortex increases with increasing reduced frequency (Fig. 7.25). The higher strength results in a lower rate of convection (compare Fig. 7.24b and Fig. 7.25b) and the stall is postponed to a higher incidence angle. The state of full stall occurs at 14° and 24° at reduced frequencies of 0.07 and 0.20, respectively. The presence of the vortex creates a suction peak C_P^* of around -4 at the reduced frequency of 0.20 (double of that was found statically). It is worth noting that, although the presence of dynamic stall vortex can delay stall to a higher incidence, its movement to the trailing edge causes a change of centre of pressure (from 0.25c to 0.41c, Fig. 7.26), leading to a more negative (nose-down) pitching moment (torsional damping) on the rotor structure. This unsteady effect is insignificant when the aerofoil is fully stalled (Fig. 7.27).

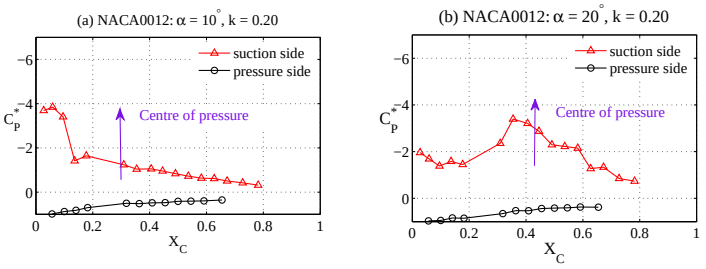

Figure 7.26: Movement of vortex and a change in centre of pressure.

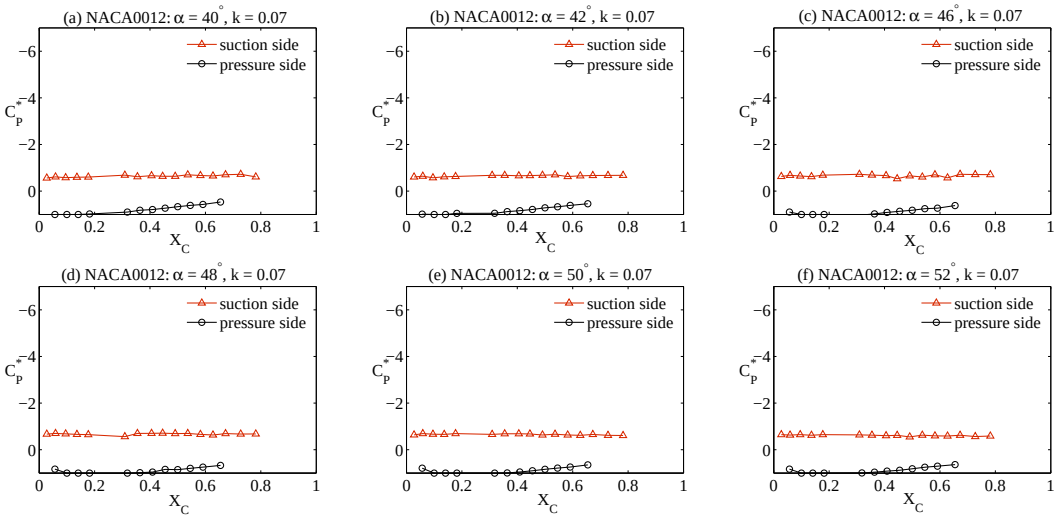

Figure 7.27: Unsteady C_P* at high incidence angles: NACA0012.

Presentation of unsteady C_P^*s after this point is then limited within ±30°.

Normal mode with decreasing incidence angle

In this normal mode where the incidence decreases (pitch-down motion), the flow is typically stalled and will try to reattach from the leading edge when the incidence angle is sufficiently low. Figures 7.28 and 7.29 show unsteady C_P^*s at selected incidences of 30°, 28°, 26°, 20°, 10°, and 5° (a to f).

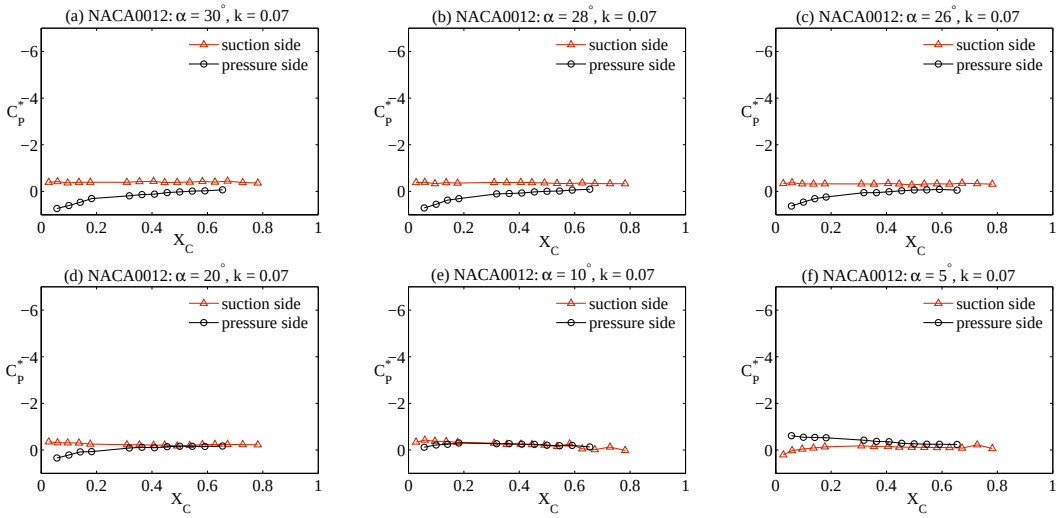

Figure 7.28: Unsteady C_P^* at a reduced frequency of 0.08: NACA0012 - normal-down.

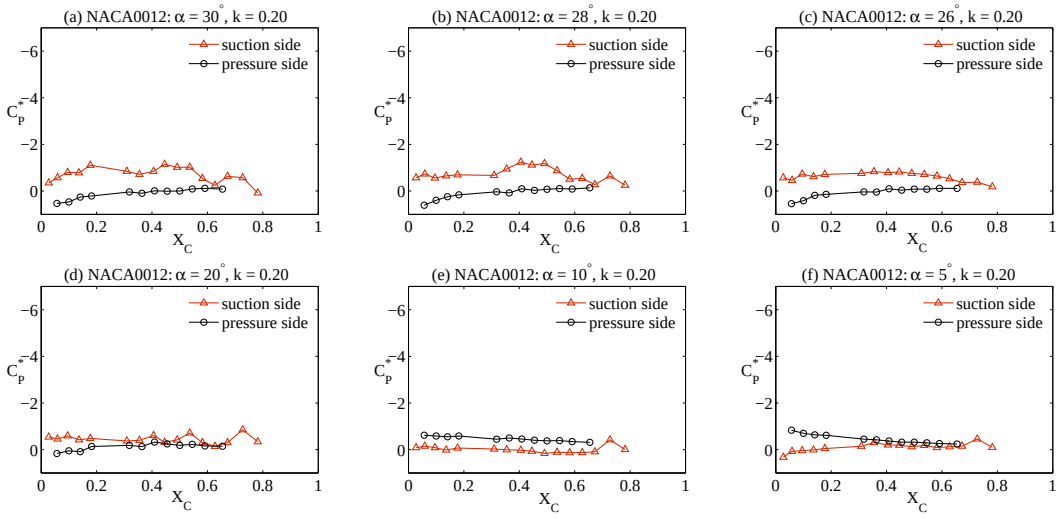

Figure 7.29: Unsteady C_P^* at a reduced frequency of 0.20: NACA0012 - normal-up.

It can be seen that the flow separation (as indicated by the flat C_P^* curve (Fig. 7.28a to 7.28d)) persists until the incidence angle is around 10°. This delay in flow reattachment, together with the delay of stall during the pitch-up motion, causing a hysteresis in dynamic loads over the incidence range (will be presented later).

Reversed camber mode with decreasing incidence angle

In this reversed camber operation, the suction and pressure sides are reversed. The suction peak and formation of dynamic-stall vortex will take place on the pressure side (solid line with circles). Figures 7.30 and 7.31 present unsteady C_P^*s at selected incidence angles of $-10°$ to $-30°$ with a $2°$ decrement at reduced frequencies of 0.07 and 0.20, respectively.

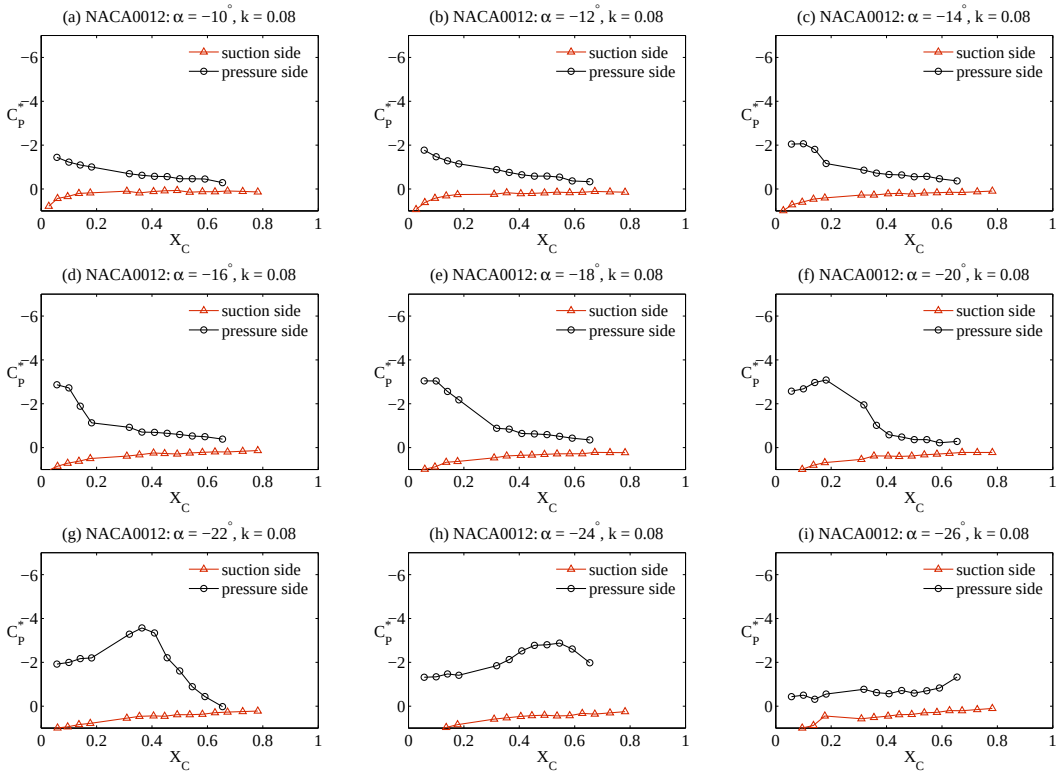

Figure 7.30: Unsteady C_P^* at a reduced frequency of 0.07: NACA0012 - reversed-down.

It is observed that the maximum suction peak is approximate -3 at a reduced frequency of 0.07, taking place at an incidence angle of $-18°$ (Fig. 7.30e). Not long after that, the vortex transverses over the aerofoil chord before detaching at an incidence angle of $-26°$ (Fig. 7.30i). It is noted that, although the maximum suction peak is comparable to that was found in the normal mode, the vortex stays attached longer and convects along the chord at a slower rate. This effect is more pronounced with increasing reduced frequency (Fig. 7.31). At the reduced frequency of 0.2, the maximum suction peak is increased to around -5 (Fig. 7.31f) and the vortex convects along the aerofoil at a significantly slower rate (Fig. 7.31f to 7.31k), causing the full stall to occur at $-30°$. This slower rate of convection suggests that the vortex experiences flow conditions that are different from that of the normal mode.

The difference between these two modes is though to be a result of the incoming flow. In the normal mode, the vortex seems to be more diffuse and can be swept away by the incoming flow (Fig. 7.32). In the reversed cambered mode the vortex is

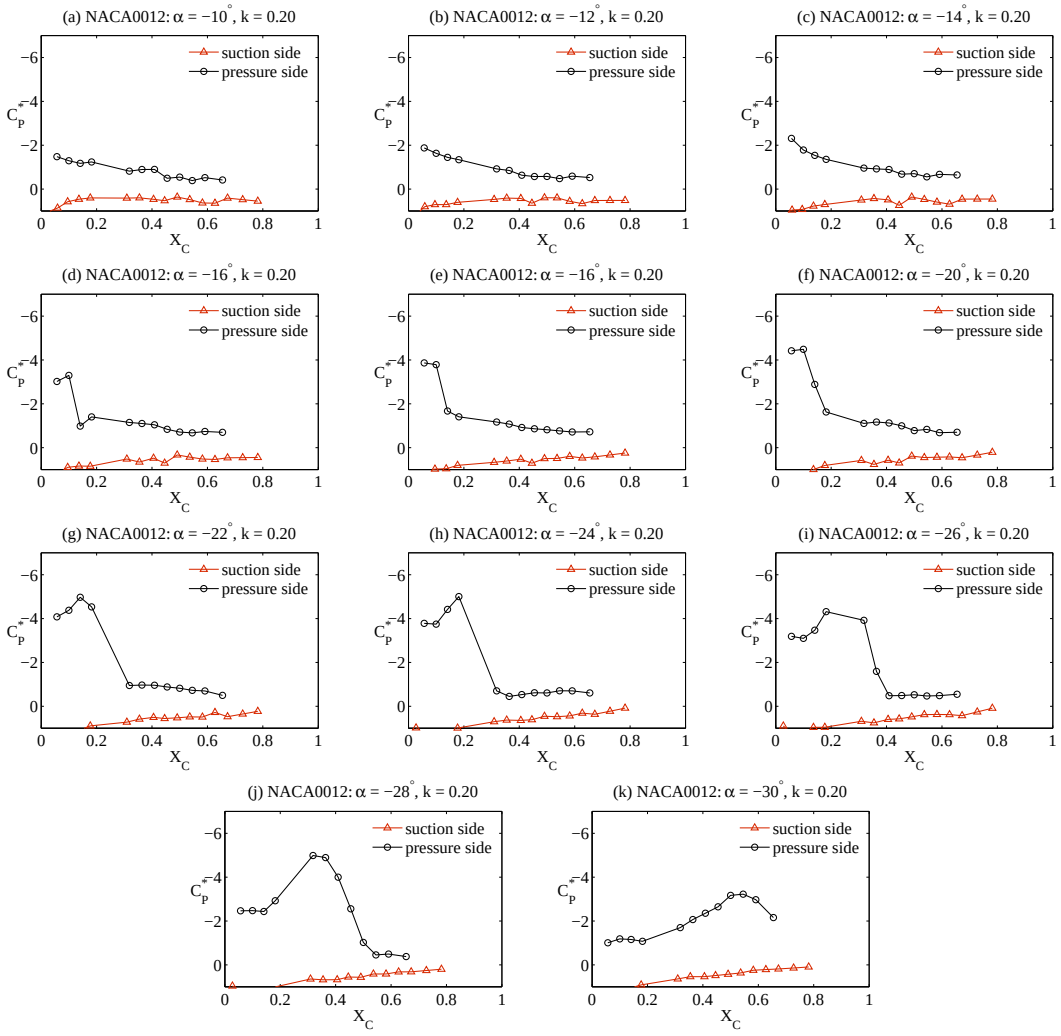

Figure 7.31: Unsteady C_P^* at a reduced frequency of 0.20: NACA0012 - reversed-down.

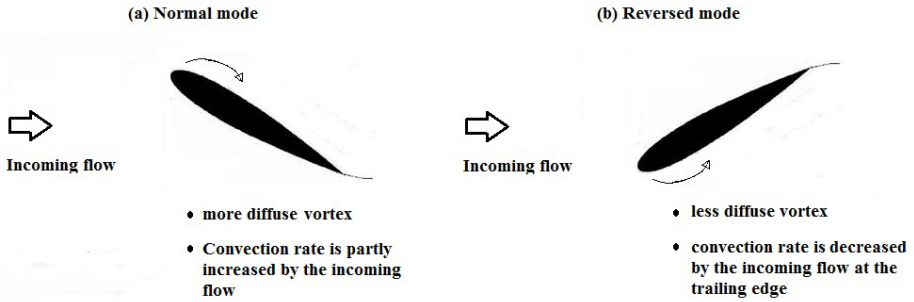

Figure 7.32: Flow schematics of normal and reversed modes of operation.

not significantly affected by the flow and the vortex strength is nearly constant when travelling along the aerofoil chord. Moreover, the incoming flow over the trailing edge seems to force the vortex to convect at a slower rate, resulting in an imbalance flow behaviour on this symmetrical section.

Reversed mode with increasing incidence angle

During pitch-up motion of the reversed camber mode, the flow recovers and the suction and pressure sides will return to their normal mode of operation. Figures 7.33 and 7.34 shows C_P^* variations at selected incidence angles from $-20°$ to $-10°$.

The flow on the pressure side, as expected, is fully stalled at the beginning of the pitch-up motion. The regain of suction peak on the suction side increase with increasing reduced frequency (compare Fig. 7.33c and 7.34c).

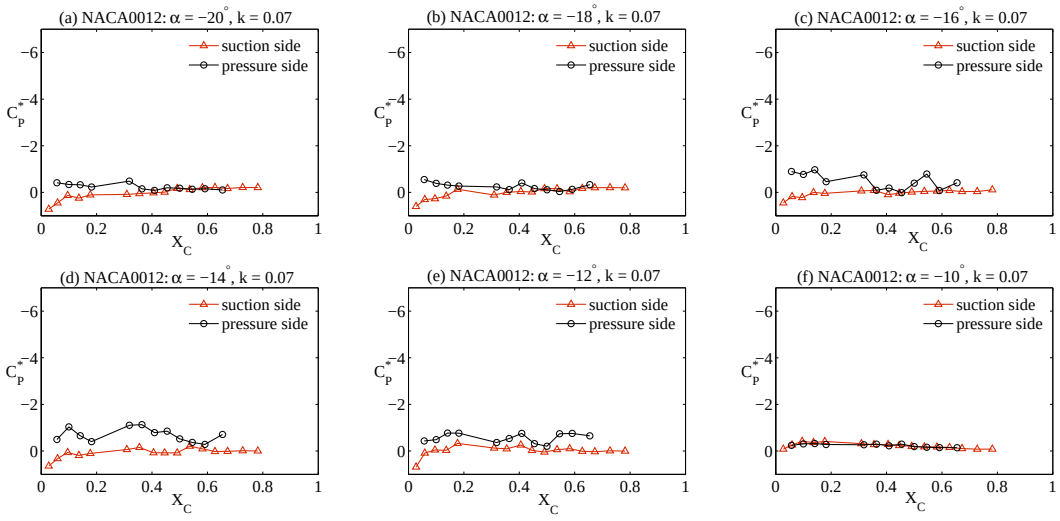

Figure 7.33: Unsteady C_P^* at a reduced frequency of 0.07: NACA0012 - reversed-up.

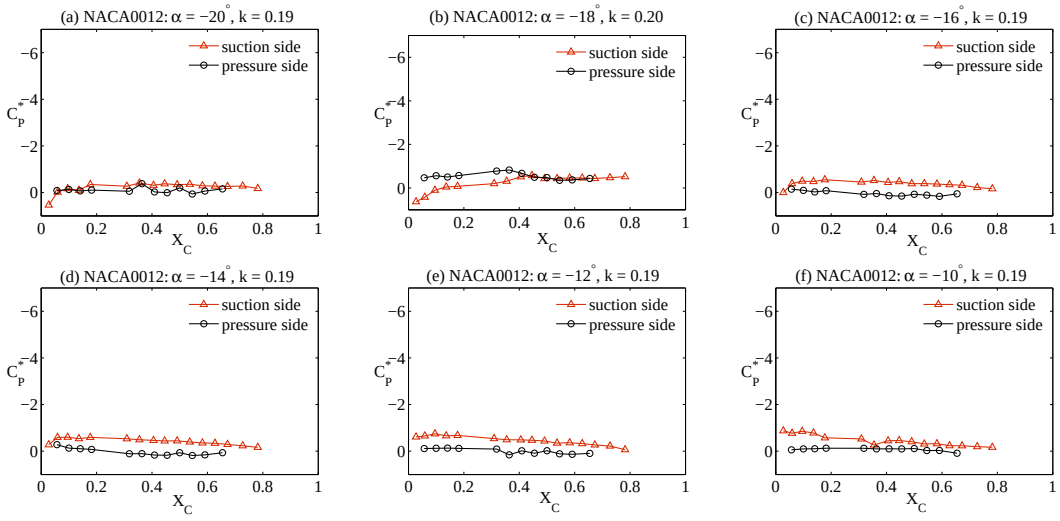

Figure 7.34: Unsteady C_P^* at a reduced frequency of 0.20: NACA0012 - reversed-up.

Normal force coefficient

The transient flow behaviour in the four different modes leads to an hysteresis in aerodynamic airload. Figures 7.35 and 7.36 present unsteady normal force coefficients of the NACA0012 section together with its static counterpart (dotted line).

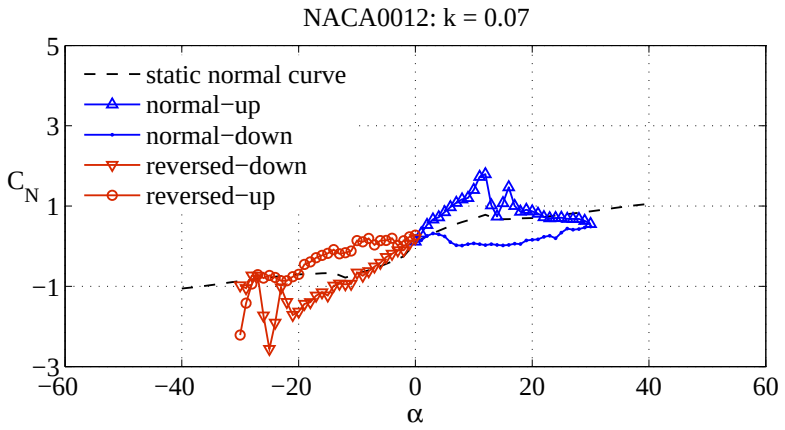

Figure 7.35: Unsteady C_N at a reduced frequency of 0.07: NACA0012.

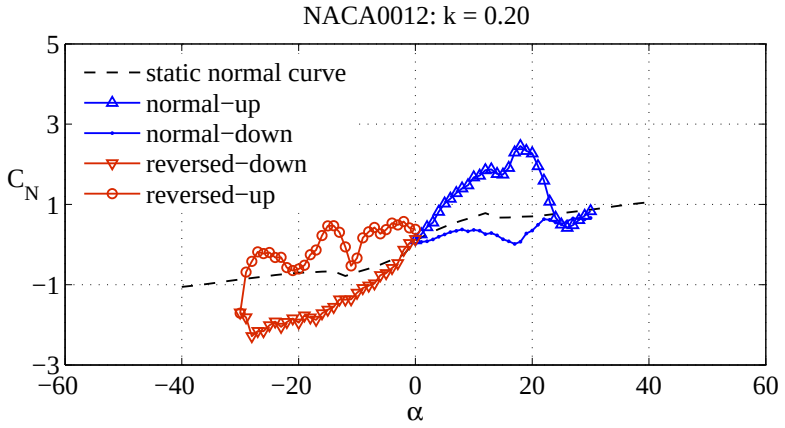

Figure 7.36: Unsteady C_N at a reduced frequency of 0.20: NACA0012.

It is apparent that, in the normal mode, dynamic-stall formation generated by the aerofoil motion overshoots the C_N to around 2 (solid line with triangles). After the vortex shedding, the C_N drops to around its static value which continuously decreases during pitch-down motion (solid line with points). The hysteresis loop widens with increasing reduced frequency as the transient effect is more pronounced (Fig. 7.35 and 7.36).

In reversed camber operation, the imbalance flow feature promotes an overshoot of the C_N to around -2.5 at an incidence angle of 28° and 30° at reduced frequencies of 0.07 and 0.20, respectively. It is noted that the asymmetry in the airload is also subjected to an error due to incidence accuracy (±2.5°).

7.2.2 SG6043 aerofoil

Normal mode with increasing incidence angle

Figures 7.37 and 7.38 show unsteady C_P^* variations of the SG6043 aerofoil at selected incidences from 10° to 20°.

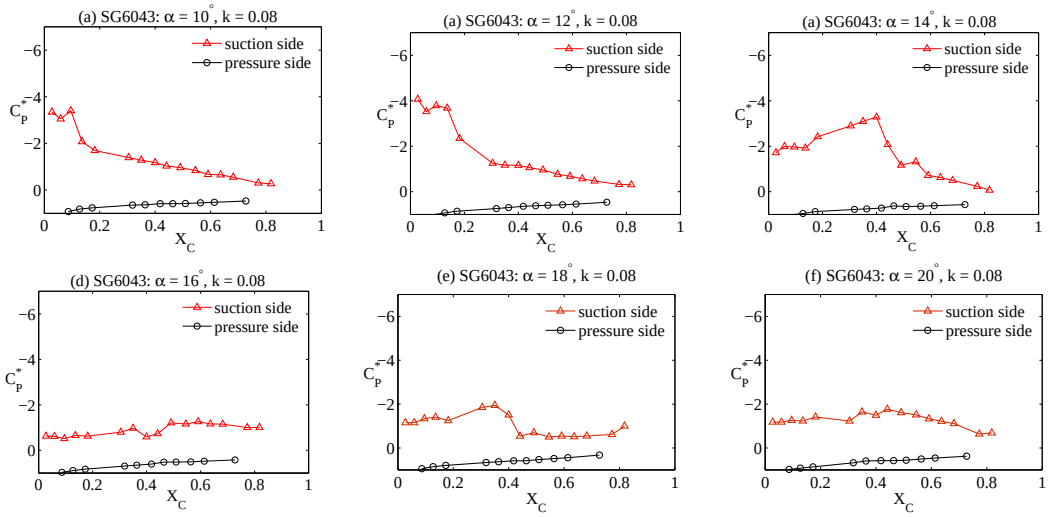

Figure 7.37: Unsteady C_P^* at a reduced frequency of 0.08: SG6043 - normal-up.

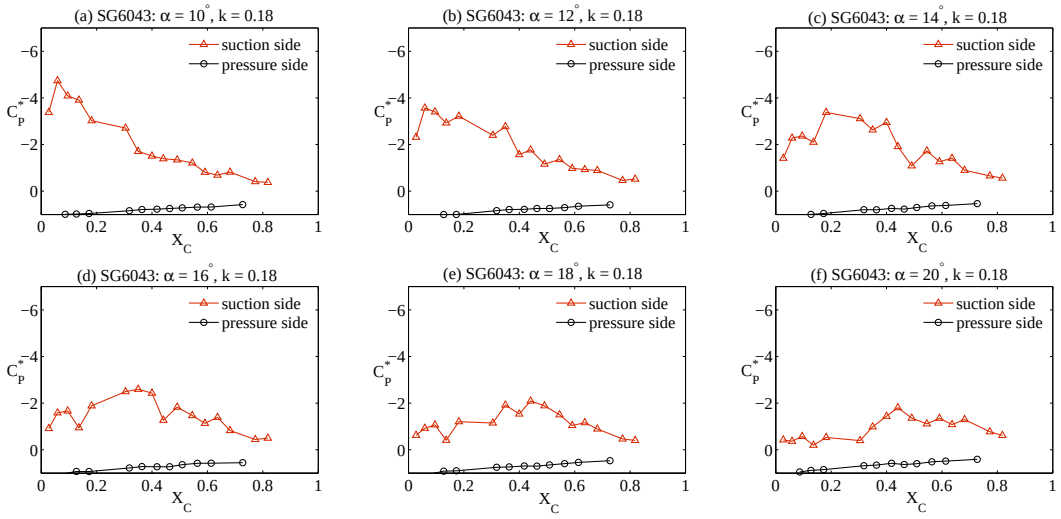

Figure 7.38: Unsteady C_P^* at a reduced frequency of 0.20: SG6043 - normal-up.

It is seen that the presence of dynamic-stall vortex has increased the suction peak to around -4 at a reduced frequency of 0.07 (Fig. 7.37b). Not long after the formation, the vortex transverses along the aerofoil chord and eventually shed (Fig. 7.37c to 7.37e). Again, the vortex grows in strength with increasing reduced frequency (Fig. 7.38a). However, the stall angle is not significantly change for this aerofoil section and is comparable to that was found statically (approximate 18°).

Normal mode with decreasing incidence angle

Figures 7.39 and 7.40 show unsteady C_P^* at discrete incidences from 30° to 5°. The measurement results indicate that the reattachment process, as expected, will not take place until the incidence angle becomes low (approximate 10° as the pressure curve begins to follow the aerofoil nose shape (Fig. 7.39e and 7.40e). It is also observed that the reattachment process is faster with increasing reduced frequency.

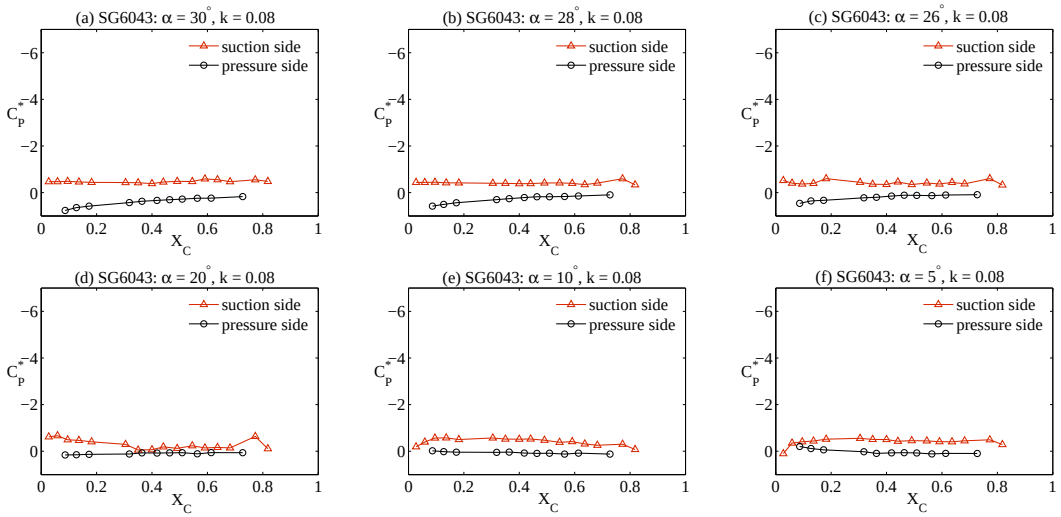

Figure 7.39: Unsteady C_P^* at a reduced frequency of 0.08: SG6043 - normal-down.

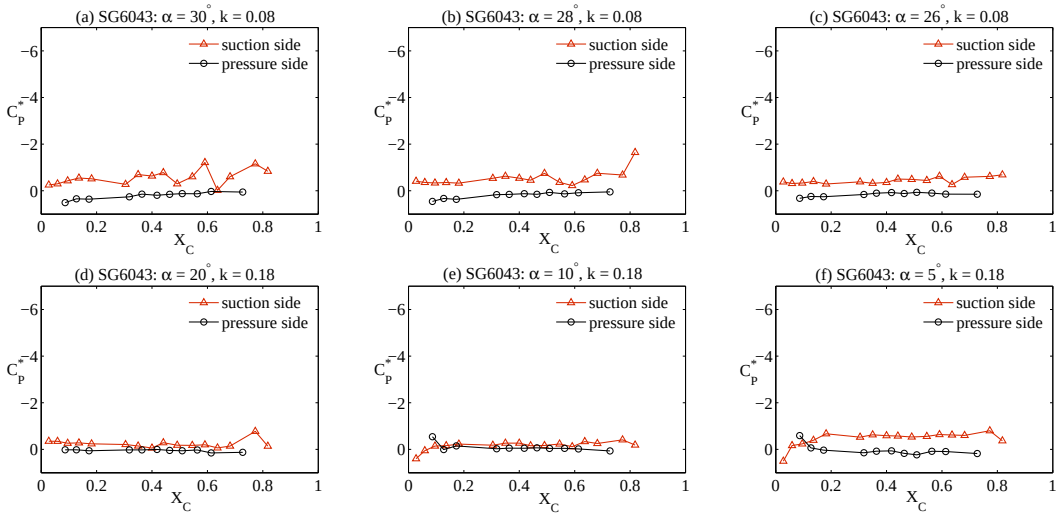

Figure 7.40: Unsteady C_P^* at a reduced frequency of 0.18: SG6043 - normal-down.

Reversed camber mode with decreasing incidence angle

Figures 7.41 and 7.42 present unsteady C_P^* variations for the SG6043 section and it can be seen that the vortex formation is comparatively low in strength. The peak is around -2 at the reduced frequency of 0.07. Higher reduced frequency results in higher dynamic-stall vortex and, hence, higher pressure peak (Fig. 7.41e and Fig. 7.42e). One clear implication from these results is that high cambered section tend to be less effective in promoting unsteady suction peak than that of symmetrical section.

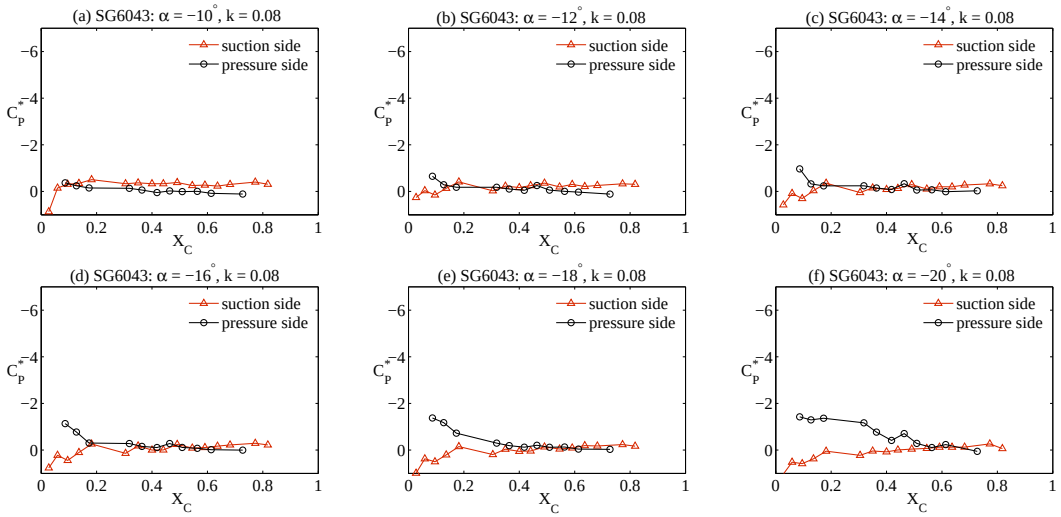

Figure 7.41: Unsteady C_P^* at a reduced frequency of 0.08: SG6043 - reversed-down.

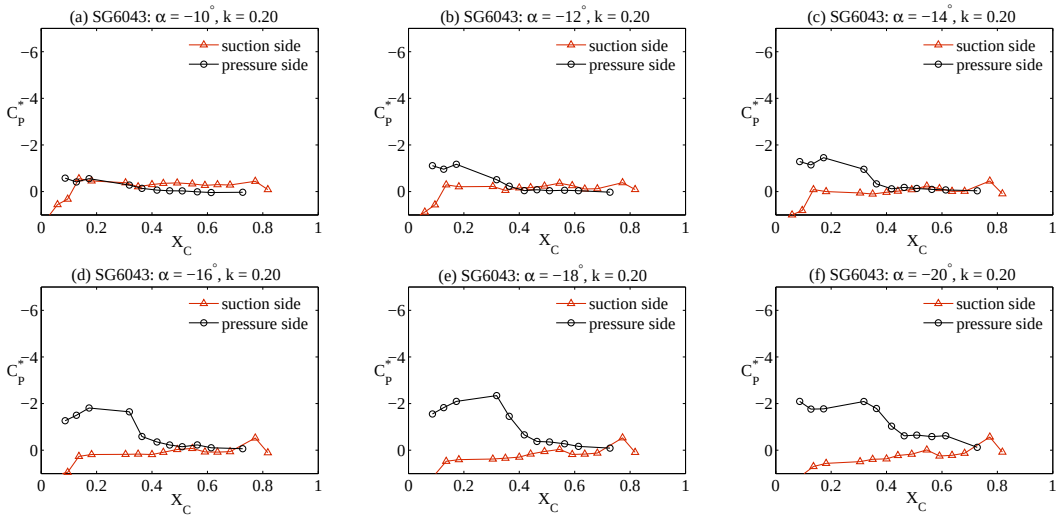

Figure 7.42: Unsteady C_P^* at a reduced frequency of 0.20: SG6043 - reversed-down.

Reversed camber mode with increasing incidence angle

Figures 7.43 and 7.44 show unsteady C_P^* variation of the SG6043 aerofoil when it turns back to its normal mode of operation. It can be seen that the pressure on suction side (solid line with triangles) regains its suction peak at a comparatively higher rate than the symmetrical section (see Fig. 7.43d).

A comparison of the C_P^* shows that the return rate increases with increasing reduced frequency (see Fig. 7.43d and Fig. 7.44d, for example)

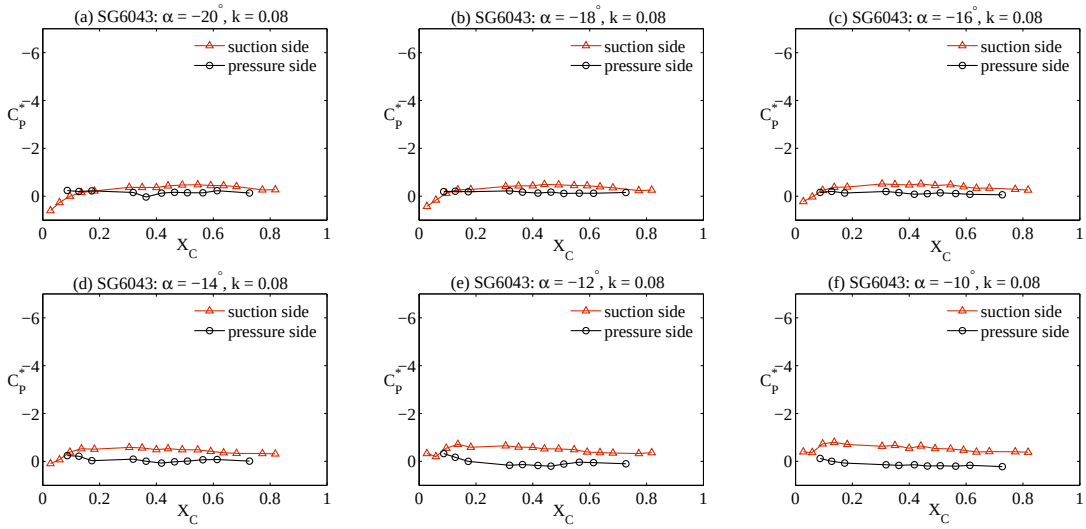

Figure 7.43: Unsteady C_P^* at a reduced frequency of 0.08: SG6043 - reversed-up.

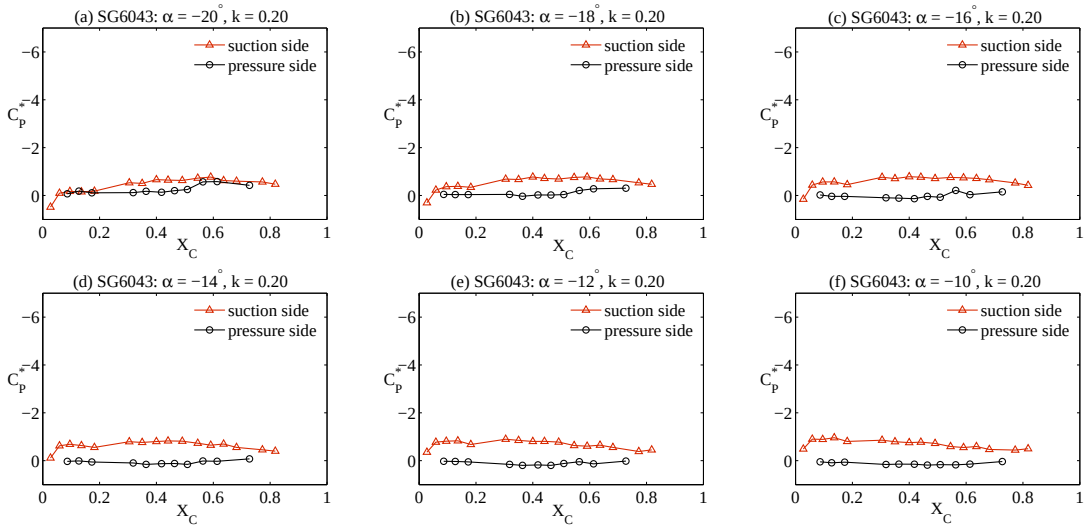

Figure 7.44: Unsteady C_P^* at a reduced frequency of 0.20: SG6043 - reversed-up.

Normal force coefficient

The transient effects on aerodynamic airload are presented in Figures 7.45 and 7.46. Generally, it can be seen that the change of airload is comparable to that of the NACA0012.

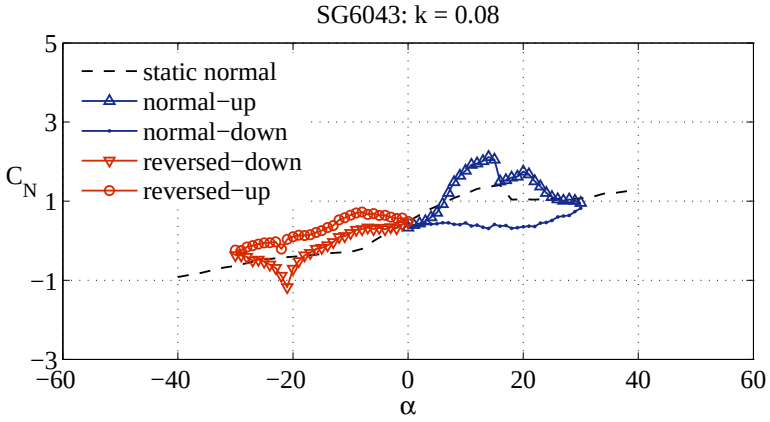

Figure 7.45: Unsteady C_N at a reduced frequency of 0.08: SG6043.

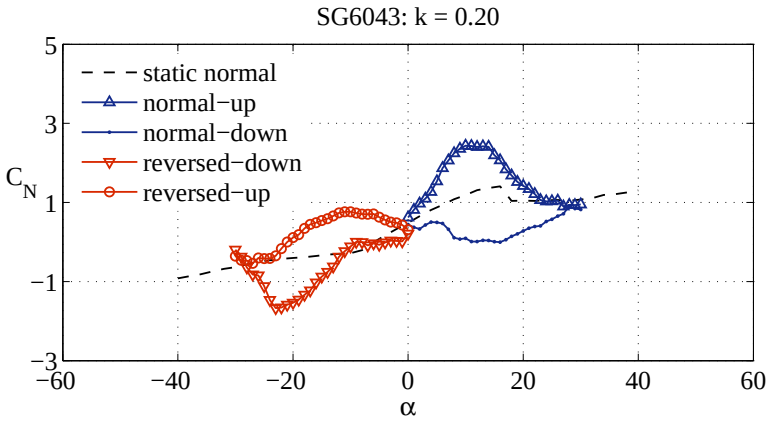

Figure 7.46: Unsteady C_N at a reduced frequency of 0.20: SG6043.

It is apparent that the C_N is increased beyond its static value as found in the NACA case in the normal mode of operation. The hysteresis loop is relatively wide as flow reattachment process is slow for this thin aerofoil section. The overshoot of normal force is less pronounced in the reversed camber operation and is strongly affected by reduced frequency which is a direct result of the leading edge shape of this section. The overshoot however does occur when the aerofoil pitches down at a higher rate (k = 0.2).

Performance comparison between the SG6043 and the NACA0012 indicates that the addition of camber might lead to a performance degradation in the reversed mode, particularly if the aerofoil is thin.

7.2.3 SD7062 aerofoil

Normal mode with increasing incidence angle

Figure 7.47 and 7.48 present unsteady C_P^* variations of the SD7062 aerofoil at reduced frequencies of 0.08 and 0.20, respectively. Figure 7.47 contains incidence angles from 10° to 28° (Fig. 7.47a to 7.47h).

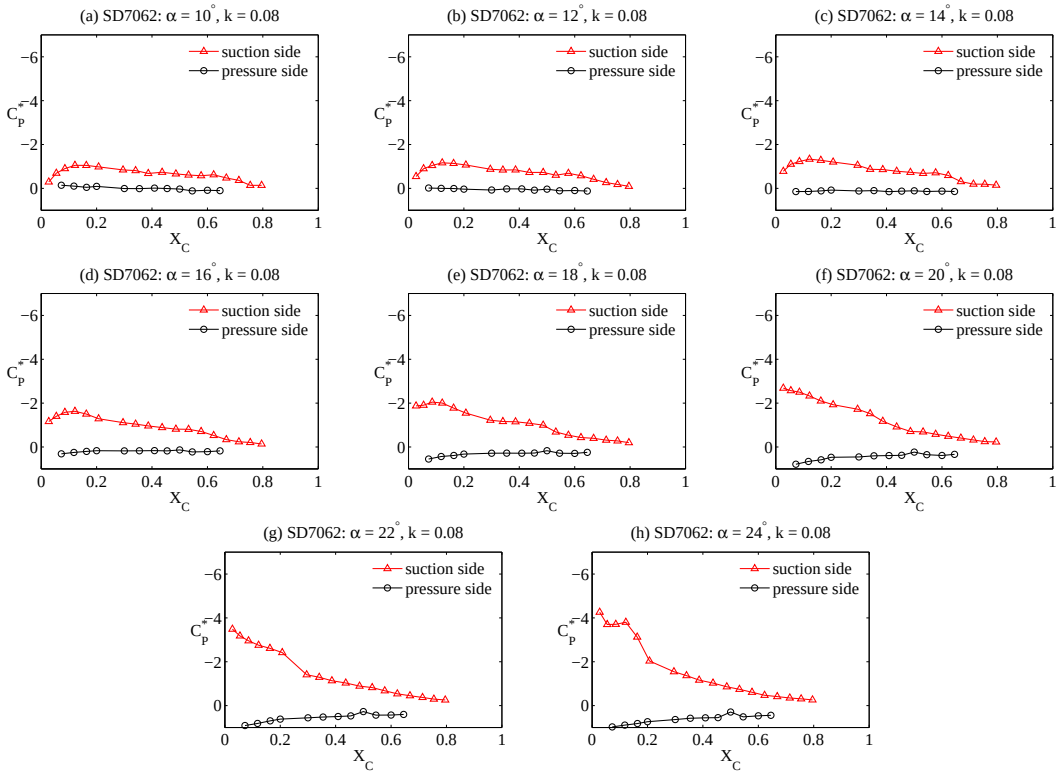

Figure 7.47: Unsteady C_P^* at a reduced frequency of 0.08: SD7062 - normal-up.

It can be seen that the C_P^* continues to develop as the incidence increases beyond static stall angle (18°) (Fig. 7.47e). Although the development is similar to that was found statically, it is observed that the dynamic C_P^* is smaller than that of static case (For example, Fig. 7.9 and Fig. 7.47b), indicating there exists a delay in flow development.

At the incidence angle beyond 18°, the suction peak continues to develop as a vortical flow structure (dynamic-stall vortex) has developed and grown in strength. Consideration of the C_P^* curve also indicates that trailing-edge separation which is expected to occur has been suppressed by the dynamic-stall formation, as indicated by the C_P^* curve that is not flat at the trailing edge. The maximum suction C_P^* is -4 in comparison to -3 in the static case (compare Figures 7.47g and 7.9).

It is also observed that there exists the presence of laminar separation bubble that moves progressively upstream (this is not seen in the previous sections). The stall is initiated by the bubble as in the static case but the stall angle is postponed up to a higher incidence angle of 30°.

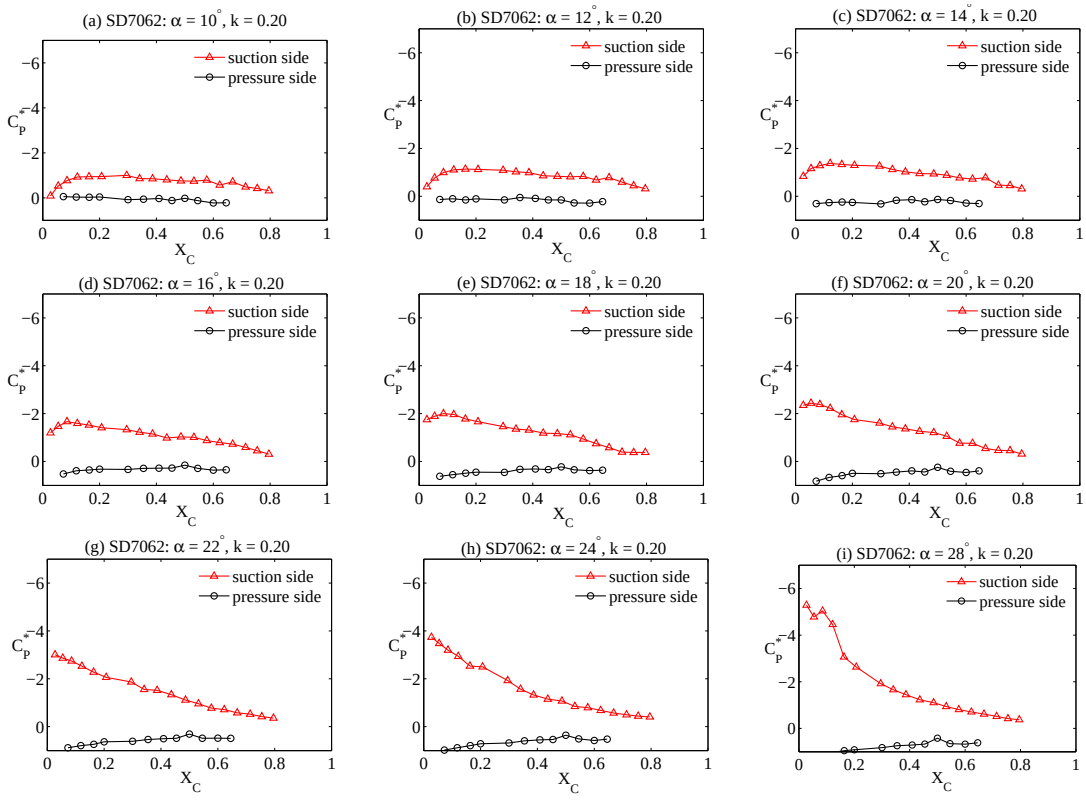

Figure 7.48: Unsteady C_P^* at a reduced frequency of 0.20: SD7062 - normal-up.

Surface pressure variations at a higher reduced frequency of 0.20 are shown in Figure 7.48. It can be seen that, at this higher reduced frequency, the maximum suction peak is increased to approximate -6 (Fig. 7.48i), the bubble size is smaller, and the stall is delayed up to 30°.

Normal mode with decreasing incidence angle

Figures 7.49 and 7.50 show unsteady C_P^* of this section at discrete incidence angles of 30°, 28°, 26°, 20°, 10°, and 5° which are intended to show the process of reattachment.

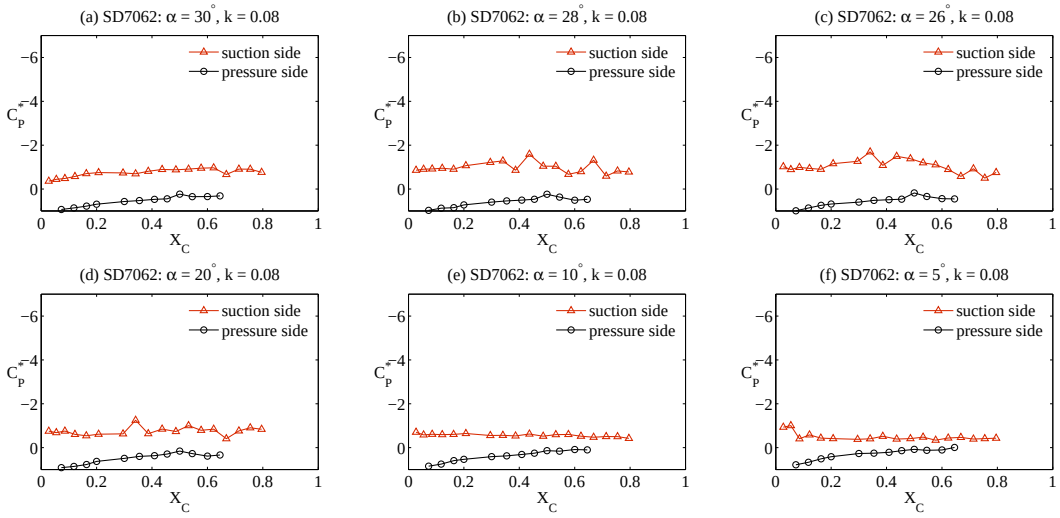

Figure 7.49: Unsteady C_P^* at a reduced frequency of 0.08: SD7062 - normal-down.

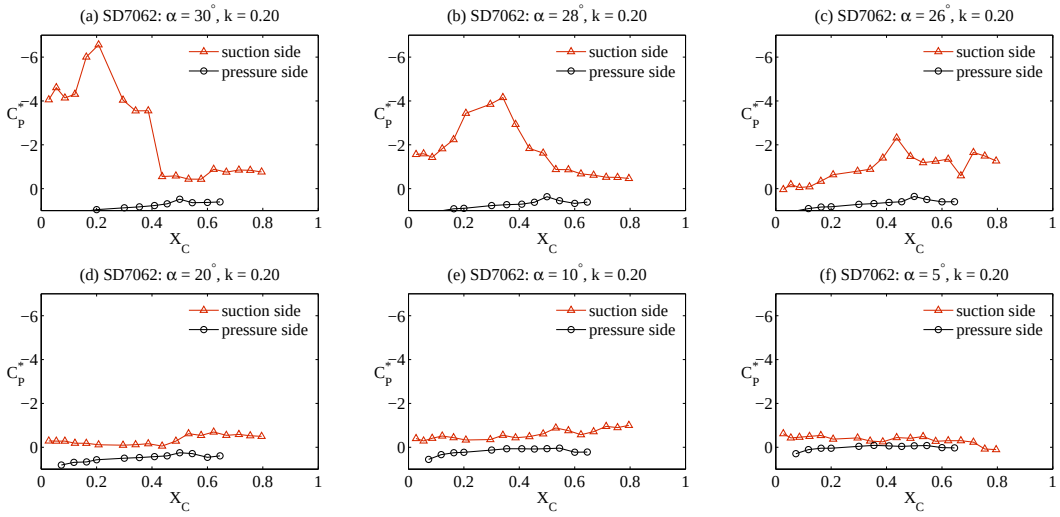

Figure 7.50: Unsteady C_P^* at a reduced frequency of 0.20: SD7062 - normal-down.

It is observed that the aerofoil is completely stalled at the low reduced frequency of 0.08. This state of stall persists with decreasing incidence angle. Flow reattachment is not clearly seen from the measurements.

At the higher reduced frequency of 0.20, it is seen that the aerofoil is not stalled yet and the suction peak seems to continuously develop at the end of pitch-up motion. Convection and detachment process is therefore present at the beginning of the motion, implying that the stall is postponed beyond 30°. Again, flow reattachment is not clearly seen from the measurements.

Reversed camber mode with decreasing incidence angle

Dynamic performance characteristics of the SD7062 aerofoil section when operating in reversed camber operation are presented in Figures 7.51 and 7.52.

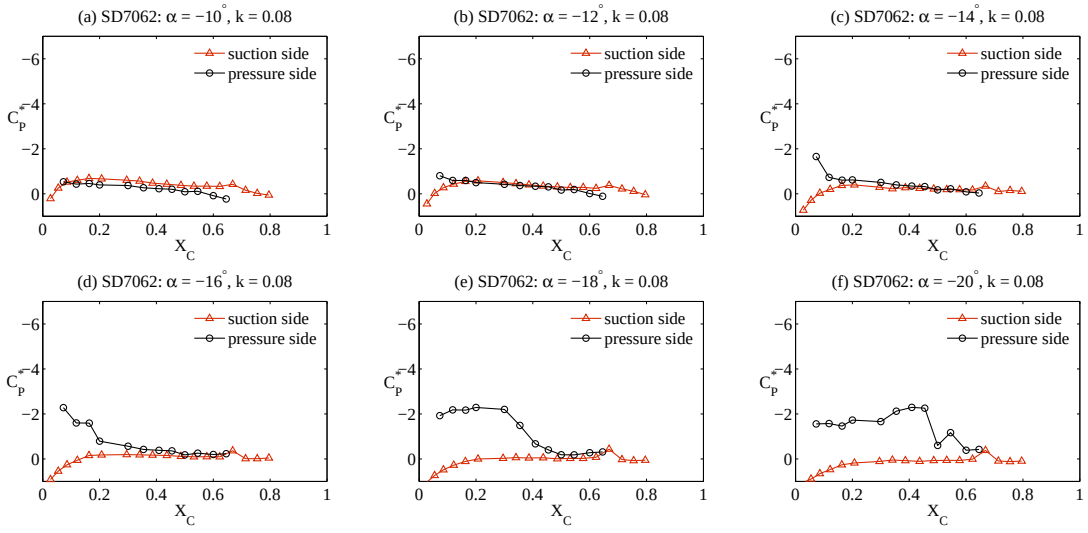

Figure 7.51: Unsteady C_P^* at a reduced frequency of 0.08: SD7062 - reversed-down.

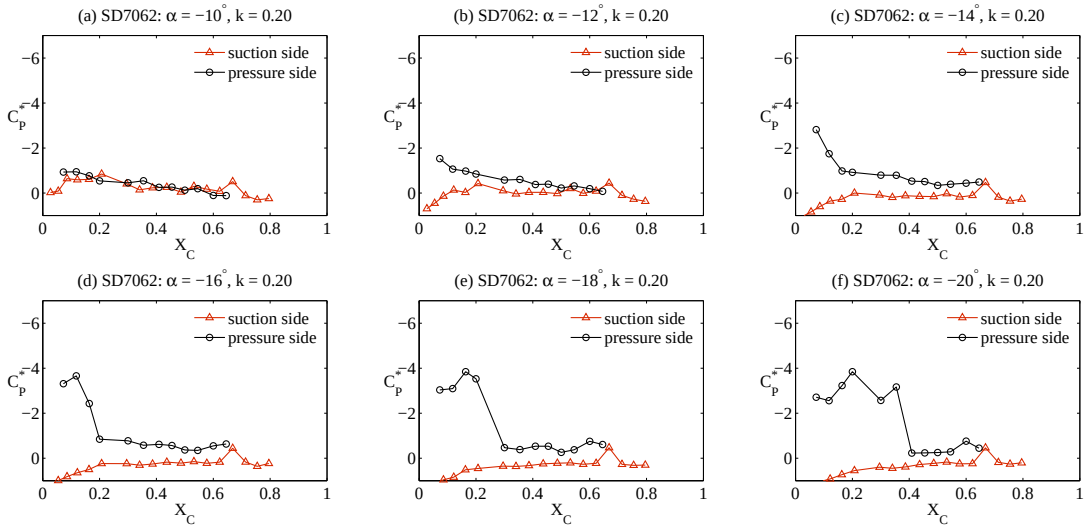

Figure 7.52: Unsteady C_P^* at a reduced frequency of 0.20: SD7062 - reversed-down.

It is apparent that, a dynamic-stall vortex has formed on the pressure side (solid lines with circles). The presence of the vortex increases the pressure peak to -2 and -4 at reduced frequencies of 0.08 and 0.20, respectively. It is also observed that the vortex grows in strength and stays attached on the surface longer when reduced frequency is increased (compare Fig. 7.51e with Fig. 7.52e). Dynamic-stall angles are $-22°$ and $-26°$ at reduced frequencies of 0.08 and 0.20, respectively.

Reversed camber mode with increasing incidence angle

Figures 7.53 and 7.54 are plots of unsteady C_P^* variations of this aerofoil section when operating in reversed camber mode and the incidence angle is increasing. The plots again present C_P^*s at some selected angles of $-20°$ to $-10°$ and they are expected to show the regain of suction pressure on the suction side.

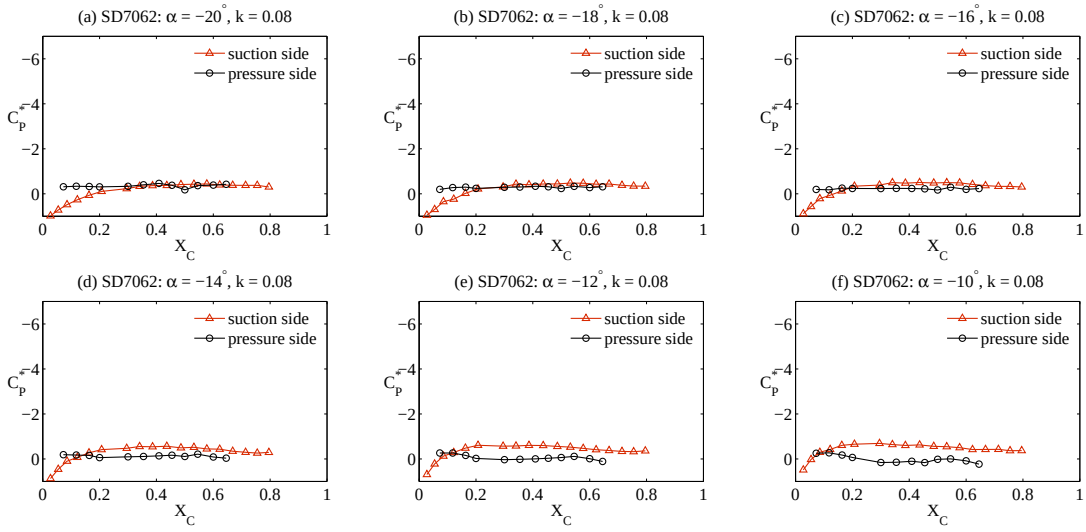

Figure 7.53: Unsteady C_P^* at a reduced frequency of 0.08: SD7062 - reversed-up.

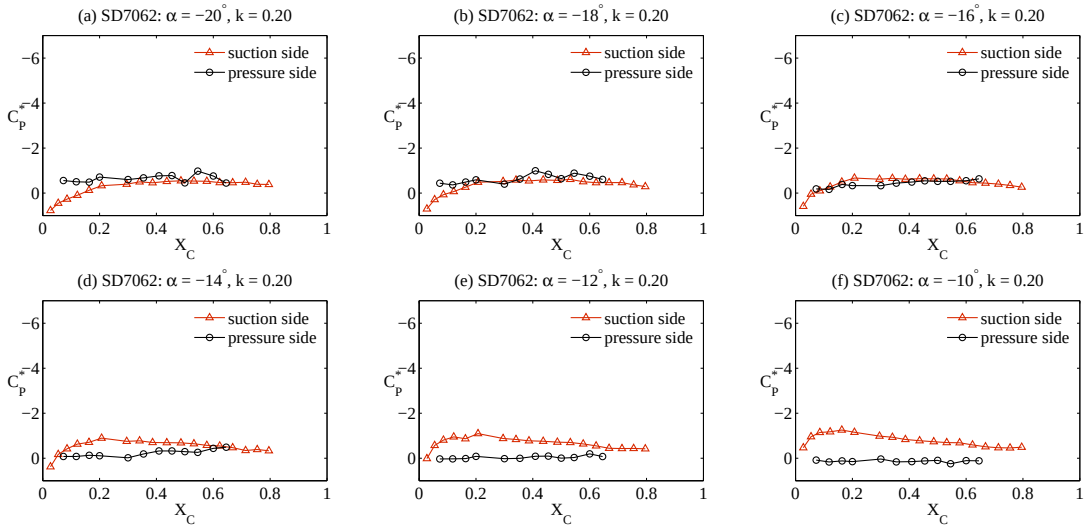

Figure 7.54: Unsteady C_P^* at a reduced frequency of 0.20: SD7062 - reversed-up.

The C_P^* on the pressure side is typically flat as the vortex formed has been shed (solid line with circle in Fig. 7.53a). The C_P^* on suction side (solid line with triangles) continuously regains its suction pressure which occurs at around $-10°$ at the reduced frequency of 0.08 (Fig. 7.53f). With increasing reduced frequency, the rate of regain in suction peak increases (7.54d).

Normal force coefficient

Based upon the C_P^* variations, dynamic airload generated by this aerofoil section can be obtained. C_N-α curves of the SD7062 aerofoil at the two reduced frequencies are presented in Figures 7.55 and 7.56, respectively.

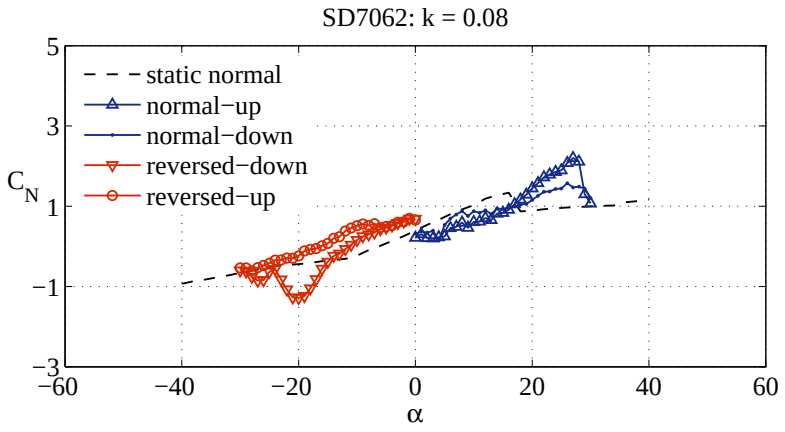

Figure 7.55: Unsteady C_N at a reduced frequency of 0.08: SD7062.

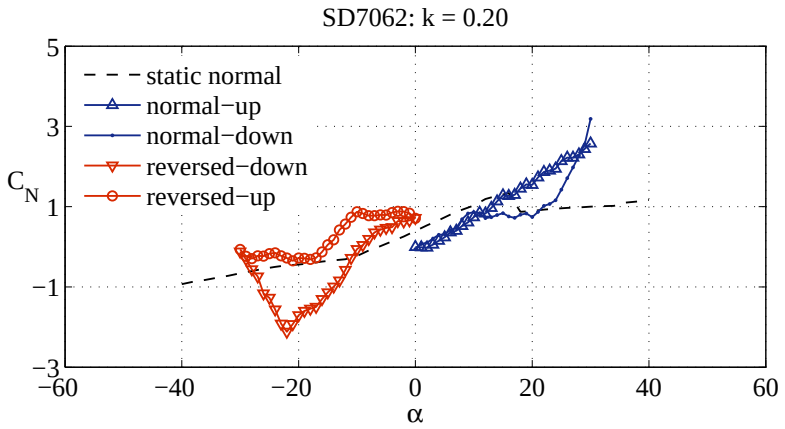

Figure 7.56: Unsteady C_N at a reduced frequency of 0.20: SD7062.

It can be seen that, although the hysteresis in C_N is comparable to the two previous cases, this aerofoil section exhibits a different behaviour and there exists a delay in flow development (lower C_N value) below stall angles. It is also observed that the hysteresis shape is significantly narrower in the normal mode. C_N variations of this aerofoil during the reversed camber mode closely resemble that of the SG6043 aerofoil section (see Fig. 7.45 and 7.46).

7.2.4 DU06-W-200 aerofoil

Normal mode with increasing incidence angle

Again, unsteady C_P^* distributions of the DU06-W-200 aerofoil at different incidence angles during its normal mode with pitch-up motion are presented in Figures 7.57 and 7.58.

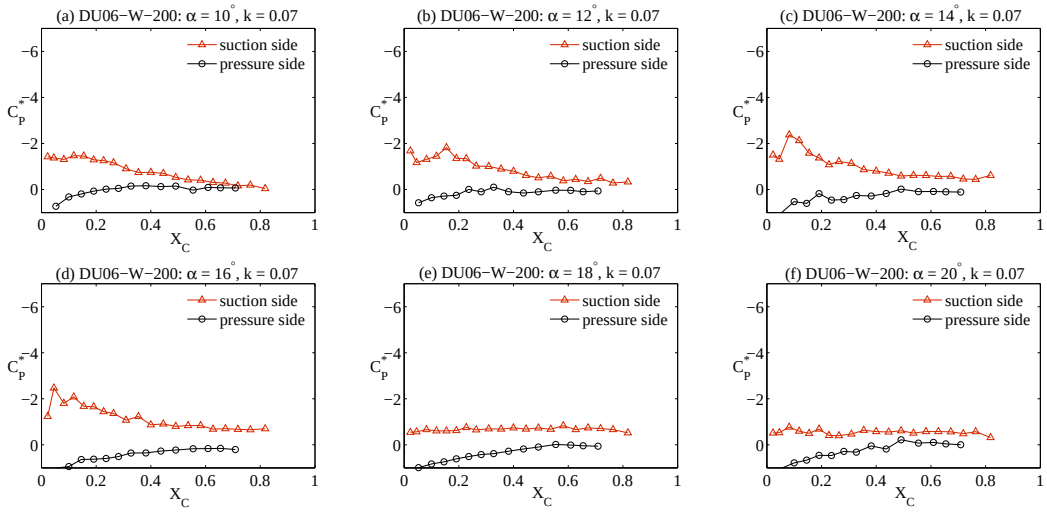

Figure 7.57: Unsteady C_P^* at a reduced frequency of 0.07: DU06-W-200 - normal-up.

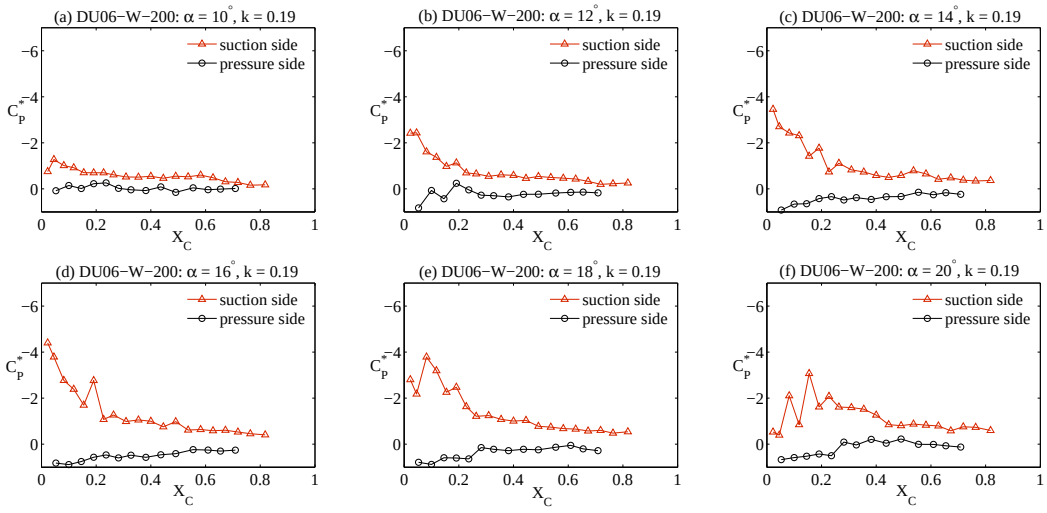

Figure 7.58: Unsteady C_P^* at a reduced frequency of 0.20: DU06-W-200 - normal-up.

It is observed that, at the reduced frequency of 0.07, the unsteadiness does not have a profound effect on the C_P^* development (Fig. 7.57a to 7.57d). The dynamic stall angle is 18° and is not significantly different from that was found under static conditions (Fig. 7.11). This transient effect is more pronounced with increasing reduced frequency. At the reduced frequency of 0.20, the maximum suction peak is increased to around -4 (Fig. 7.58d).

Normal mode with decreasing incidence angle

Figures 7.59 and 7.60 show unsteady C_P^*s at descending incidence angles, showing reattachment process of the DU06-W-200 aerofoil. As expected, the reattachment process will not take place until the incidence angle is sufficiently low (Fig. 7.59e and 7.60e).

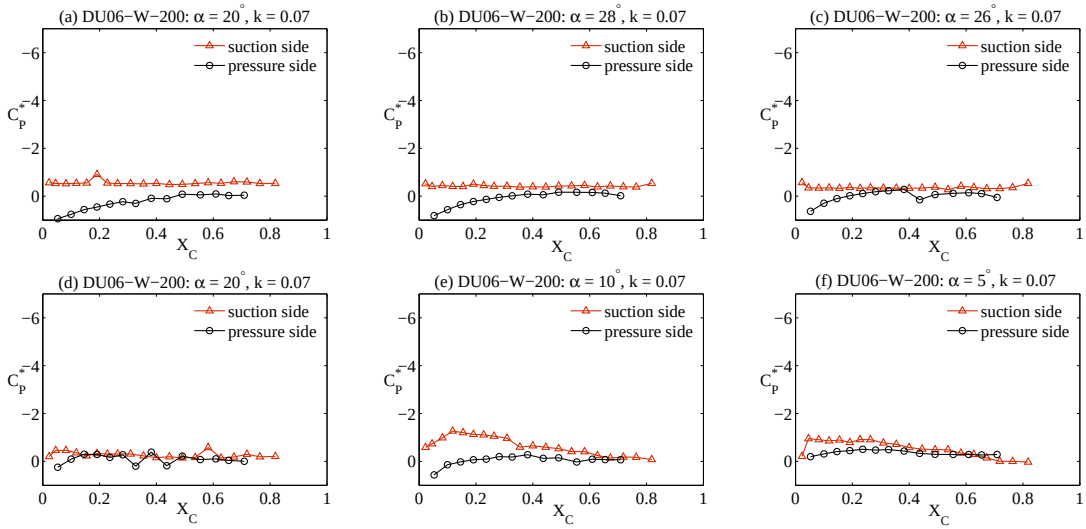

Figure 7.59: Unsteady C_P^* at a reduced frequency of 0.07: DU06-W-200 - normal-down.

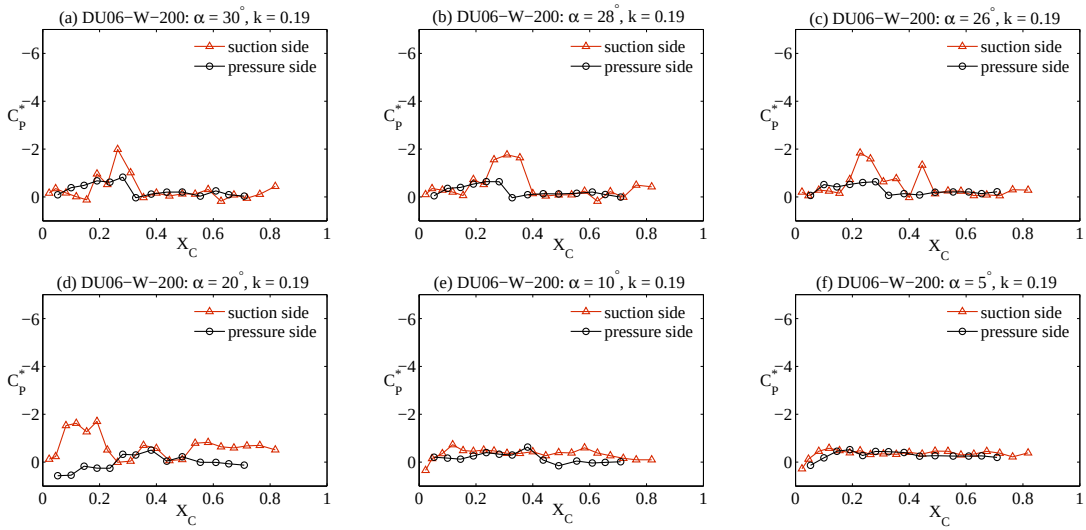

Figure 7.60: Unsteady C_P^* at a reduced frequency of 0.19: DU06-W-200 - normal-down.

Reversed camber mode with decreasing incidence angle

Figures 7.61 and 7.62 present unsteady pressure coefficients of the DU06-W-200 section at selected, descending incidence angles at reduced frequencies of 0.07 and 0.19, respectively. It is observed that the transient effect is relatively small at the reduced frequency of 0.07, similar to that found in the normal mode (Fig. 7.57).

The effect increases with increasing reduced frequency and the suction peak is increased to around -4 when the reduced frequency is increased to 0.19 (Fig. 7.61e and 7.62e). Comparison between the NACA0012 and the DU06-W-200 suggests that a thick aerofoil typically requires a higher reduced frequency to generate transient effects.

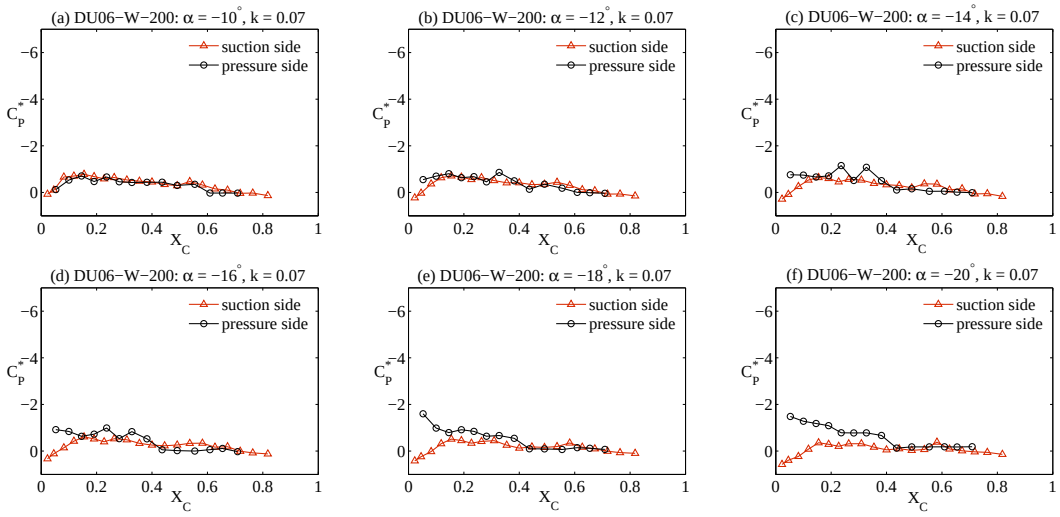

Figure 7.61: Unsteady C_P^* at a reduced frequency of 0.07: DU06-W-200 - reversed-down.

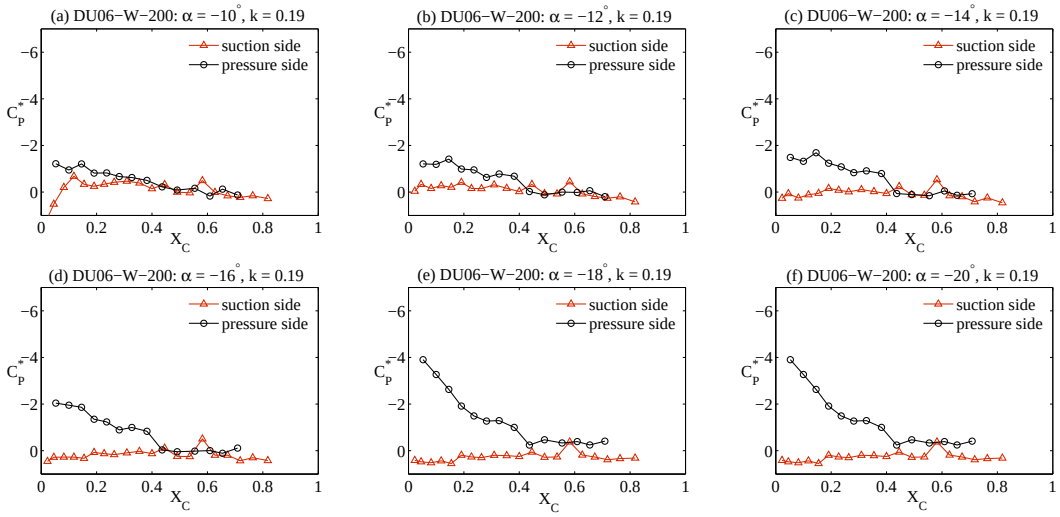

Figure 7.62: Unsteady C_P^* at a reduced frequency of 0.19: DU06-W-200 - reversed-down.

Reversed camber mode with increasing incidence angle

Figures 7.63 and 7.64 show C_P^* variations in this mode with increasing incidence angle which can be seen that the unsteady effect is small at the reduced frequency of 0.07. The regain of suction peak of the suction surface increases with increasing reduced frequency (see Fig. 7.63e and 7.64e, for example)

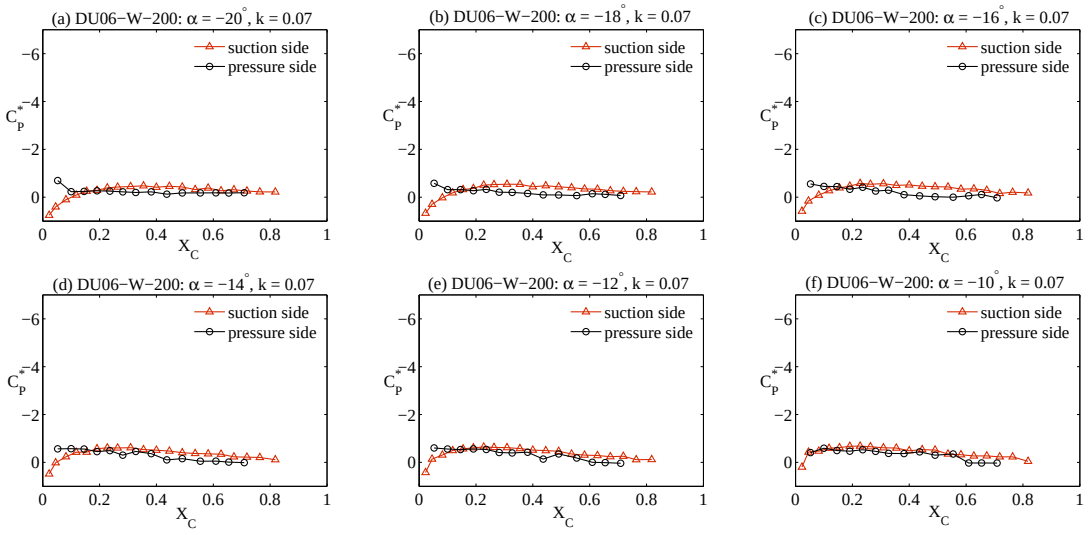

Figure 7.63: Unsteady C_P^* at a reduced frequency of 0.07: DU06-W-200 - reversed-up.

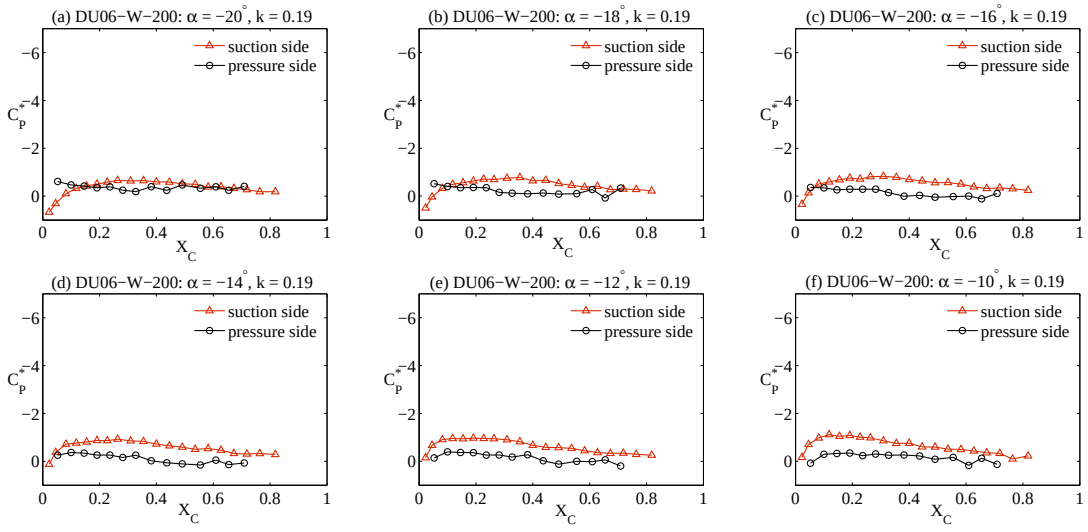

Figure 7.64: Unsteady C_P^* at a reduced frequency of 0.19: DU06-W-200 - reversed-up.

Normal force coefficient

Corresponding C_N curves of the DU06-W-200 aerofoil at the two reduced frequencies are presented in Figures 7.65 and 7.66, respectively. One characteristic that can be observed is that the effect of unsteadiness is relatively small on this section at the reduced frequency of 0.08 and the C_N curve is not significantly different from the static case. This performance characteristic strongly suggests that, in order to easily promote the unsteady thrust, the aerofoil should have a moderate thickness as it poses less inertia (for the same rotor configuration and material) and requires a smaller value of reduced frequency for the transient effect to be effective.

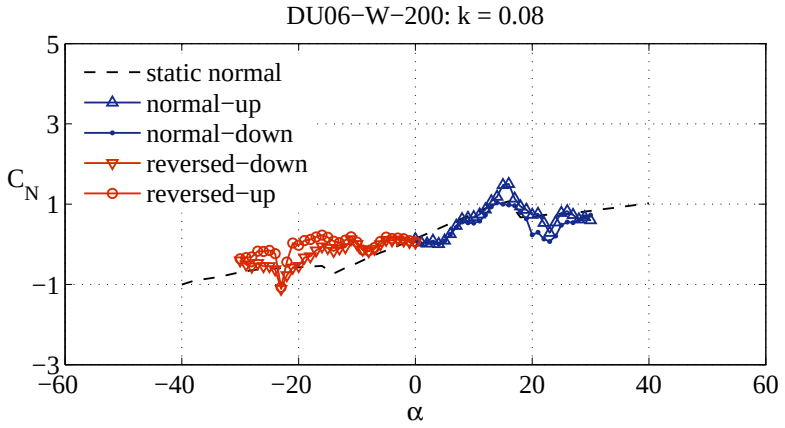

Figure 7.65: Unsteady C_N at a reduced frequency of 0.08: DU06-W-200.

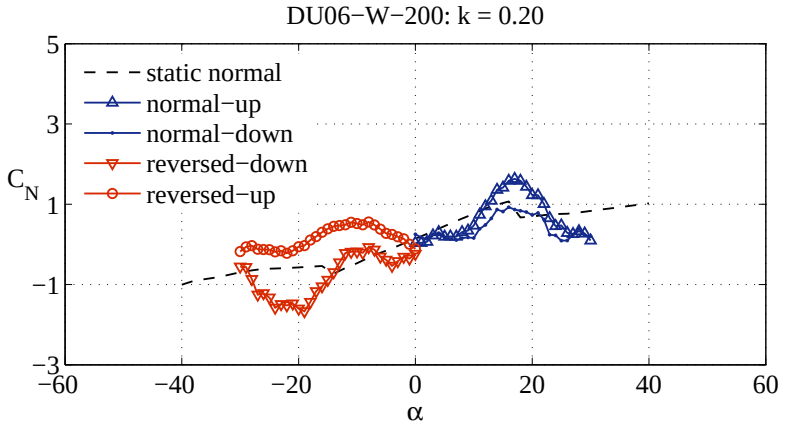

Figure 7.66: Unsteady C_N at a reduced frequency of 0.20: DU06-W-200.

7.3 Conclusions

Static and dynamic performance characteristics of NACA0012, SG6043, SD7062, and DU06-W-200 aerofoils had been presented in this chapter. At these Reynolds numbers (nominal 65,000 to 150,000), all four aerofoils demonstrate the formation

of a leading-edge separation bubble that ultimately bursts, leading to sudden stall. The most highly cambered aerofoil exhibits a simultaneous trailing-edge separation that advances upstream with increasing incidence, resulting in a more progressive stall characteristic, but it is always the bursting of the upstream bubble that leads to a fully stalled flow. After stall, the lift drops to a sustained but lower value, the magnitude of which is dependent upon aerofoil geometry. For the symmetrical and low camber aerofoils, the lift then rises gradually to a second peak at about 50° incidence, but this increase is less apparent for the higher camber sections.

The benefits of increased lift and more progressive stall from the cambered aerofoils are partly negated by a loss of performance arising from their reversed camber when they operate in an incidence angle of 180° to 360°. The drag characteristics of all four geometries are comparable.

A comparison between these new data and the widely used Sheldahl and Klimas data [141] for the NACA section shows good agreement for the pre-stall region but discrepancies are observed in the deep-stall region that are consistent with Rainbirds hypothesis [58] regarding the influence of wind tunnel test section geometry; a result that is confirmed by CFD modelling. In light of this, previous test data obtained from closed test sections should be viewed with caution, especially at high incidence angles. Comparisons of post-stall characteristics demonstrate discrepancies between wind tunnel data and AERODAS predictions. The discrepancies confirm the need for more high-quality, low-Reynolds number, and high-angle-of-attack data and the need for model improvements.

The unsteady surface pressure measurements have clearly shown that the effects of unsteadiness cannot be neglected. Experimental results presented in this chapter indicate that the unsteady effects are strongly influenced by incidence range, reduced frequency, and the aerofoil shape itself.

Under normal mode of operation (positive incidence angle), all aerofoils exhibit an increase in pressure on the suction peak, producing significant increments in airloads. The effect of aerofoil shape on dynamic-stall formation is clearly seen when the aerofoils operate with negative mean incidence angles at which their pressure sides play a role as suction sides. High cambered aerofoils such as SG6043 aerofoil is less effective in promoting dynamic-stall formation under these conditions. The effect of unsteadiness is more pronounced with increasing reduced frequency.

Although the dynamic stall process was found to be similar in all cases, the magnitude of aerodynamic loadings are different and this is directly related its static performance which is governed by the aerofoil shape. The aerofoil's static lift and stall characteristics are, to some extent, carried over into dynamic stall regime.

In summary, it is experimentally evident that, under the same incidence range and reduced frequency, the effects of unsteadiness on airloads are significantly influenced by the aerofoil shape. This suggests that the exploitation of the energetic, unsteady flow can be made through a suitable selection of an aerofoil profile.

Chapter 8

Aerodynamic Characteristics of Bird-like Aerofoils

The analogy between an aerofoil in Darrieus motion and the flapping-wing mechanism drawn in Chapter 4 suggests that the use of special aerofoils might lead to a significant performance improvement, particularly aerofoils that are similar to avian wings. An additional wind-tunnel test of a seagull-like aerofoil was therefore conducted, together with its blunt trailing edge version, under static and dynamic conditions. Their performance characteristics are presented in this chapter.

8.1 Aerofoils

Avian wing measurements by Liu et al [160] have revealed that the seagull wing profile is very similar to the S1223 aerofoil (Fig. 8.1) and this profile was therefore selected to represent the gull's wing. It is worth noting, however, that bird wing profiles are not constant over their wing spans and the seagull profile measured by Liu et al is an average profile over the wing span from 0.166 to 0.772 (where zero represents the wing root and one represents the tip). In addition, their wings are also flexible and can be adapted over wing-beat cycles to maximise force production. Despite that, the work described in this chapter gives fundamental insight into how bird's wings work.

Figure 8.1: Seagull wing profile, the S1223 and the S1223B.

The S1223 is a high-lift low-Reynolds-number section. It is thin and highly cambered (its maximum thickness and camber are 12.1% and 8.7%, respectively). Previous wind-tunnel measurements have shown that this aerofoil exhibits 30% higher lift

coefficient than the FX63-137 aerofoil and its high lift property is in part achieved through an exploitation of concave pressure recovery [154].

However, as is evident from previous investigations [44], aerofoils with this type of pressure recovery exhibit more severe adverse pressure gradient than the others and their aerodynamic performance is expected to degrade when operating at lower Reynolds numbers.

In order to explore an opportunity to improve its aerodynamic performance at lower Reynolds numbers and to increase its strength at the same time (it has a sharp and thin trailing edge (Fig. 8.1), the blunt trailing-edge modification, proposed by Standish and Van Dam [161], is adopted. Experimental measurements by Baker et al [162] had shown that the blunt trailing-edge modification can increase maximum lift coefficient of the aerofoil (In their work, the modification was made on a flatback aerofoil (called FB series) which was generated by combining a suction side of the thick, high lift inboard NREL aerofoils, and a structurally efficient high-pressure side drawn from the LS-1 series aerofoils [162]). However, one of the disadvantages of this modification is the increment in base drag which is caused by vortex shedding at the blunt trailing edge. So, the thickness of the blunt trailing edge (defined in terms of chord as thickness-to-chord ratio (t/c)) should not be too large.

Experimental investigations on an aerofoil having different thickness-to-chord ratios of 0.5%, 8.75%, and 17.5% have shown that the 8.75% offers highest lift-to-drag ratio at tested Reynolds numbers of 333,000 and 666,000 [162]. For this work, the ratio was decided to be 5% chord as Reynolds number range is lower (from 65,000 to 150,000, compared to 333,000 to 666,000). Coordinates of this blunt trailing edge aerofoil were generated by the method described by Baker et al [162] (to be found in appendix B). It is denoted as S1223B (Fig. 8.1).

8.2 Static performance

8.2.1 S1223 aerofoil

Figure 8.2 shows the lift and drag coefficient curves for the S1223 aerofoil at three tested Reynolds numbers. It is seen that this aerofoil exhibited high-lift properties and achieved a maximum lift coefficient of 1.644 at the highest Reynolds number of 133,000. However, as expected, it suffered performance degradation at the lowest Reynolds number at which the peak lift is reduced to 1.2 and the stall occurs at a much lower incidence angle (12°). The maximum values of lift are 1.23, 1.579, and 1.644 at respective incidence angles of 12°, 20°, and 22°.

With further small incidence increase, the flow separates and the aerofoil stalls. Here, the lift drops to a sustained value of around 0.97 at all Reynolds numbers. This post-stall lift is relatively high and this is due to the effect of camber which produces a large pressure difference between the suction and pressure surfaces even when fully stalled. The lift remains relatively constant with further incidence increase up to about 50°. After this, the lift decreases rapidly to around zero at 90° incidence angle.

A similar but reversed characteristic is mirrored beyond 90°. It was also observed that its lift characteristic does not produce a clear lift peak at the incidence angle of around 350° (or −10°). This characteristic is often seen for aerofoils with a high percent of camber [13].

In terms of drag, although the drag curve is comparable to those of other aerofoils, this aerofoil exhibits a relatively high drag at a zero incidence angle (approximately 0.07).

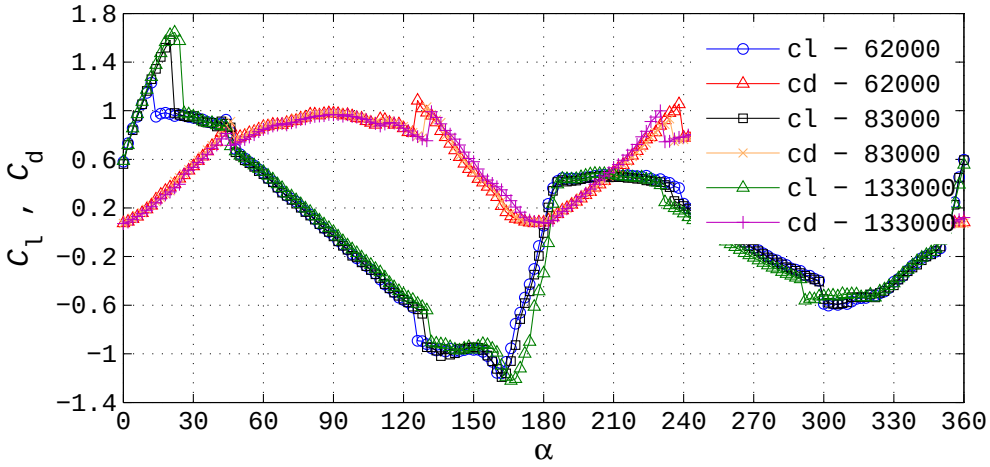

Figure 8.2: Lift and drag coefficients: S1223.

Surface pressure measurements reveal that this aerofoil demonstrates the presence of the laminar separation bubble (Fig. 8.3). It should be noted that although measurements were not possible close to the trailing edge because of insufficient blade thickness to accommodate the instrumentation, the trend of the pressure change on both sides gives confidence that the variation is well-captured. The bubble progresses upstream with increasing incidence angle and the stall is caused by bubble bursting, leading to an abrupt stall and a sharp lift peak (Fig. 8.2).

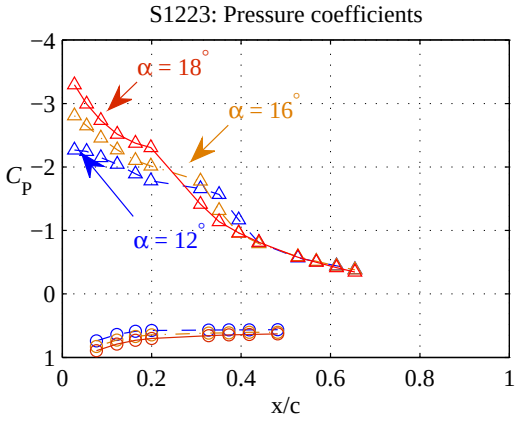

Figure 8.3: Pressure coefficients: S1223.

8.2.2 S1223B aerofoil

The lift and drag characteristics of the S1223B are presented in Figure 8.4 and it can be seen that the maximum lift is less sensitive to Reynolds number change. This property is a result of its thickness at the trailing edge which effectively reduces adverse pressure gradient along the suction surface. The maximum values of lift are 1.663, 1.755, 1.756 at respective incidence angles of 20°, 22°, 22°

With further incidence increase, the aerofoil suddenly stalls and the lift coefficient drops to a sustained value of approximately one. This remains relatively constant up to around 50° before rapidly decreasing to zero at a 90° incidence angle. Above 90°, the trend is reversed. Force measurements show that the datum drag coefficient is increased to around 0.1, compared to 0.07 of the S1223 section.

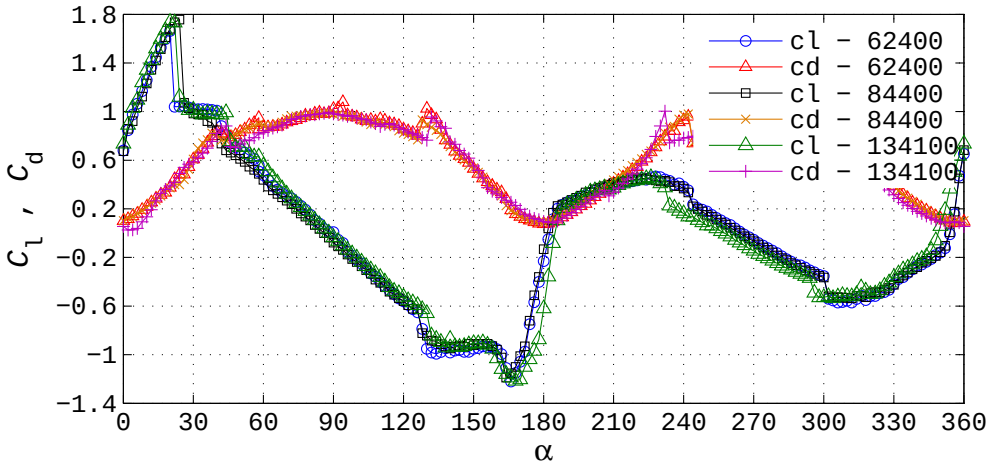

Figure 8.4: Lift and drag coefficients: S1223B.

Surface pressure measurements on this aerofoil section reveal that this modification alters the flow on both suction and pressure surfaces (Fig. 8.5). The underlying flow physics of this blunt modification is anticipated to be similar to that which is observed for a Gurney flap and on an inverted strip (Fig. 8.6). The Gurney flap is a short flat plate attached to the trailing edge on the pressure side of the aerofoil. The inverted strip is basically the Gurney flap that is attached on the suction side.

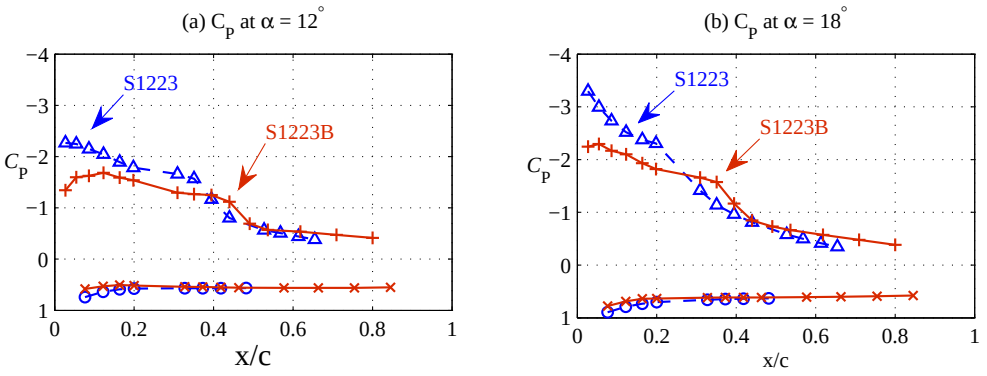

Figure 8.5: Comparison of pressure coefficients.

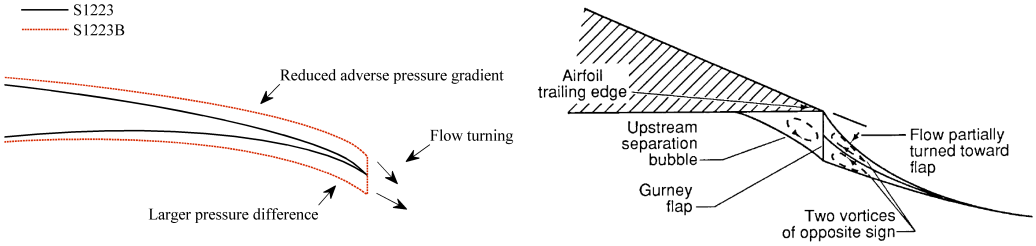

Figure 8.6: Flow over a Gurney flap [163].

Basically, the addition of the Gurney flap will induce the flow to accelerate over the suction surface and to decelerate on the pressure surface, causing an downward deflection (flow turning) at the trailing edge (it is also viewed as an effective camber as it shifts wake deficit to lie downward) (Fig. 8.6). The addition of an inverted strip on the suction side will result in an opposite effect and will produce an upward deflection.

The blunt trailing edge modification which adds thickness symmetrically to the camber line can then be viewed as an addition of both the Gurney flap and the strip on both surfaces and this effectively decelerates the flow on both sides (as indicated by the reduction of pressure peak on the both surfaces (at around 0.1c, Fig. 8.5a)).

The addition of the thickness also reduces the adverse pressure gradient that the flow has to overcome on the suction side. The flow then separates further downstream (0.3c in comparison to 0.2c for the S1223 case at the incidence angle of 12°, Fig. 8.5a). This modification also produces a larger pressure difference between suction and pressure surfaces near the trailing edge (from 0.5c to 1c). The presence of a separation bubble and its movement towards the leading edge when the incidence is increased indicates that the stall is caused by bubble bursting.

8.3 Dynamic performance

Presentation of dynamic performance is made in terms of unsteady C_P^* and C_N. Discussion of this performance is made aerofoil by aerofoil and case by case (Fig. 8.7).

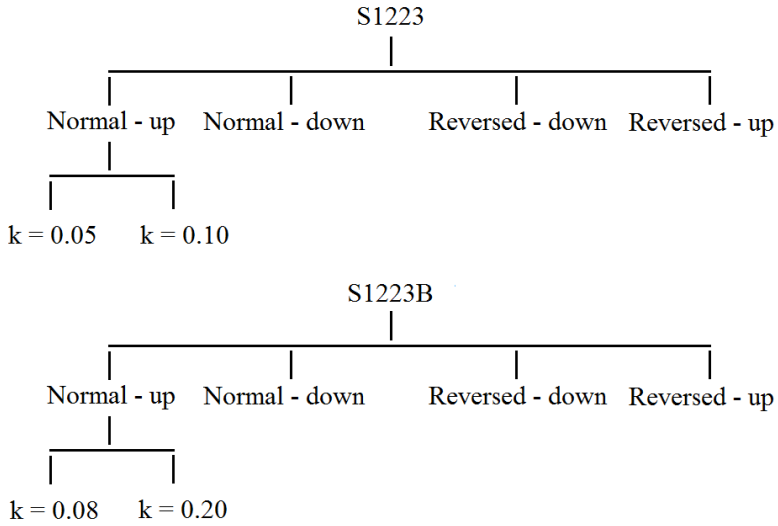

Figure 8.7: Order of presentation.

8.3.1 S1223 aerofoil

It is unfortunate that the potentiometer used for tracking incidence angle was broken during the tests of this section and dynamic performance is available only at the highest Reynolds number (150,000) which was tested up to a reduced frequency of around 0.1. Despite that, the data should be sufficient to give some insights on how this aerofoil behaves dynamically.

Normal mode with increasing incidence angle

Dynamic C_P^* variations of the S1223 aerofoil at reduced frequencies of 0.05 and 0.10 are presented in Figure 8.8 and 8.9, respectively. Both figures show unsteady C_P^* at selected, ascending angles of attack from 12° to 28° with a 2° increment (pitch-up motion).

It can be observed that, although the development of surface pressure is similar to that of static case, there exists a delay in flow development. For example, at an incidence angle of 12° (Fig. 8.8a), the suction peak under dynamic conditions is lower than that of static case (compare Fig. 8.8a and Fig. 8.3). Development of dynamic-stall vortex occurs at a comparatively high incidence angle (20°), compared to the conventional section like NACA0012 (10°) (see Fig. 7.24).

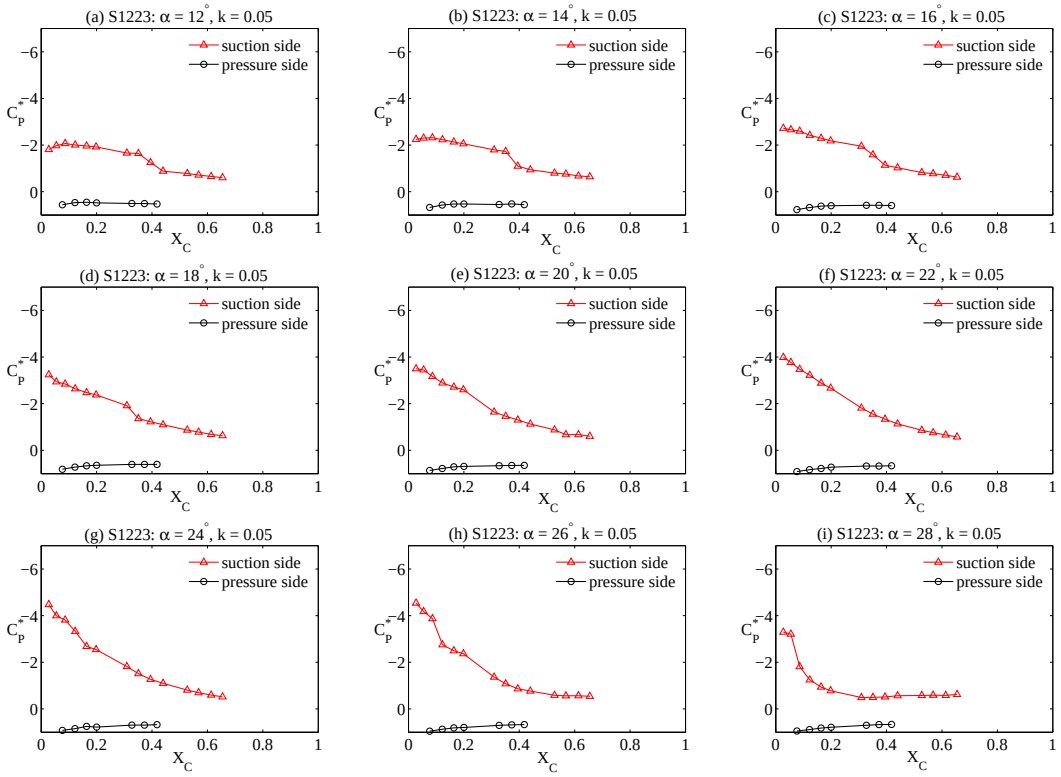

Figure 8.8: Unsteady C_P^* at a reduced frequency of 0.05: S1223 - normal-up.

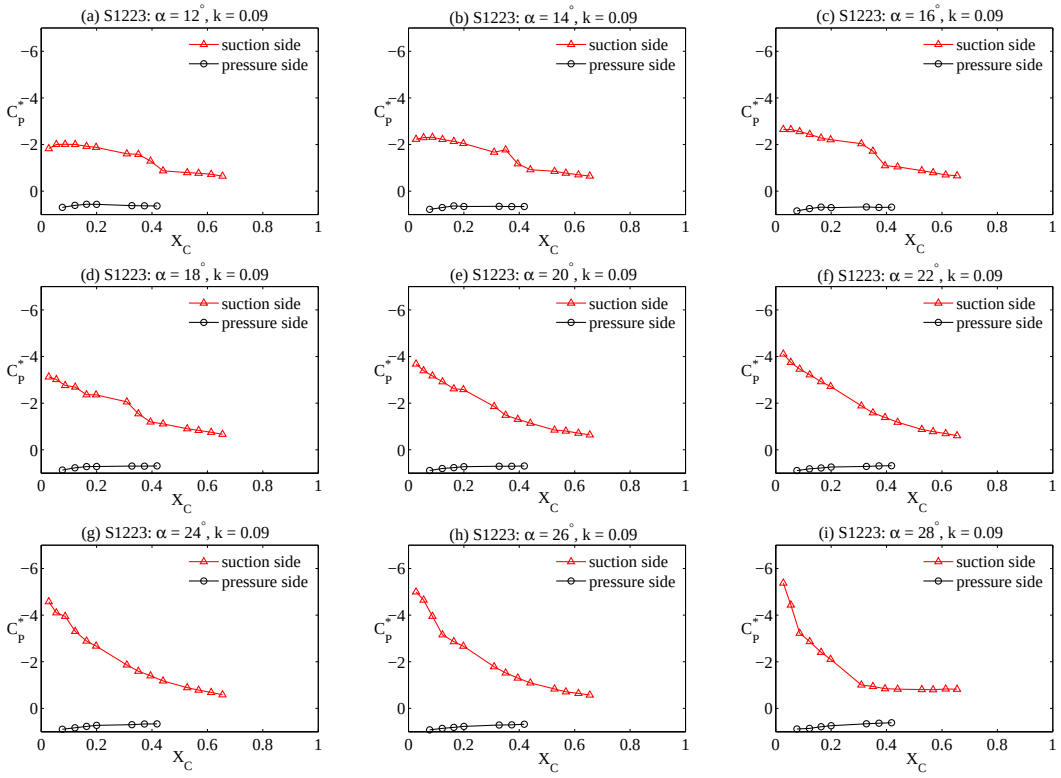

Figure 8.9: Unsteady C_P^* at a reduced frequency of 0.09: S1223 - normal-up.

This delay of flow development is thought to be a result of its camber line that has a high maximum camber located near the leading edge. This camber line effectively makes the leading edge to "droop" downward. This configuration will cause the flow to stay attached at the leading edge up to a higher incidence. Formation of dynamic-stall vortex then takes place at a higher incidence angle [164].

Formation of a laminar separation bubble is also observed under this dynamic condition (at around 0.25c at 0.30c at the reduced frequencies of 0.05 and 0.10, respectively) (Fig. 8.8a and 8.9a). The bubble progresses upstream with increasing incidence angle as found in static cases. As soon as it reaches the leading edge, it bursts and the aerofoil is fully stalled.

This sudden stalling behaviour is significantly different from that was found in the SD7062 case in which the progress of bubble to the leading edge will initiate the vortex to traverse over the aerofoil surface and the aerofoil will be fully stalled when the vortex is shed into the wake. This behaviour is due to its concave pressure recovery type that exhibits more severe adverse pressure gradient. With this severe pressure gradient, the separated flow cannot form transition in the free air and reattach the aerofoil as a turbulent boundary layer, leading to an abrupt stall.

Due to this sudden stall, the vortex convection is less visible and the nose-down pitching moment is smaller. As previously presented in Chapter 7, this nose-down pitching moment is of significance as it causes torsional damping on the rotor structure. In the helicopter application, the idea of drooped leading edge has been applied to helicopter rotor blade to alleviate torsional damping during retreating phase [165]. Birds seem to use this technique naturally to reduce torsional force on their wings.

The dynamic effect is more pronounced when the aerofoil pitches up at a higher reduced frequency of 0.09 (Fig. 8.9). At this reduced frequency, the vortex grows in strength and the suction peak is increased to around -5.4. The stall angle is postponed up to 30°.

Normal mode with decreasing incidence angle

Figures 8.10 and 8.11 present unsteady C_P^* with descending incidence angles of 30°, 28°, 26°, 20°, 10°, and 5° at reduced frequencies of 0.05 and 0.09 respectively, showing reattachment process.

It is seen that, at the reduced frequency of 0.05, the C_P^* variation is constant over the incidence range (Fig. 8.10a to Fig. 8.10d) and flow reattachment process seems to occur at an incidence angle of 10° at both reduced frequencies (Fig. 8.10e and 8.11e). Convection of a small vortex is observed at the reduced frequency of 0.09, suggesting that the aerofoil has not stall yet and the convection is initiated by the aerofoil movement.

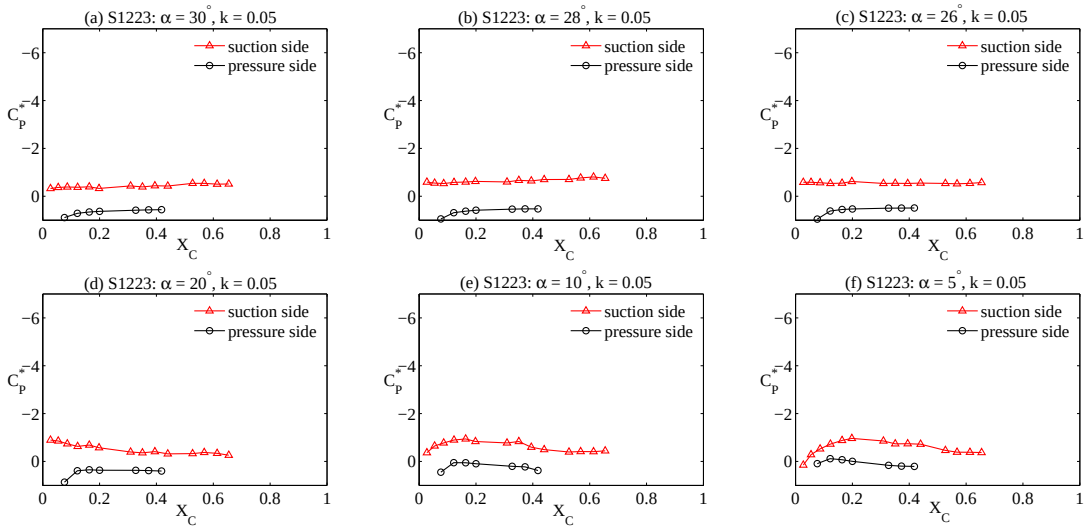

Figure 8.10: Unsteady C_P^* at a reduced frequency of 0.05: S1223 - normal-down.

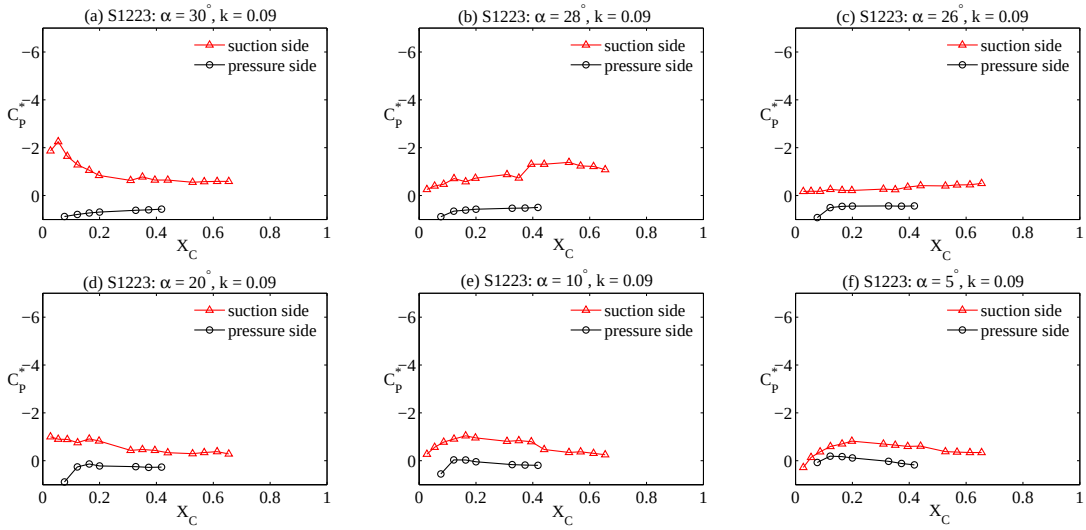

Figure 8.11: Unsteady C_P^* at a reduced frequency of 0.09: S1223 - normal-down.

Reversed camber mode with decreasing incidence angle

Figures 8.12 and 8.13 present unsteady pressure coefficients at selected incidence angles from $-10°$ to $-20°$. With this movement, the formation of dynamic-stall vortex takes place on the pressure side (solid line with circles).

However, pressure measurements had shown that the flow separates all over the pressure surface and there is no vortex formation at the tested reduced frequencies. This is thought to be a result of the leading edge shape that does not support flow attachment at the beginning of the reversed camber mode.

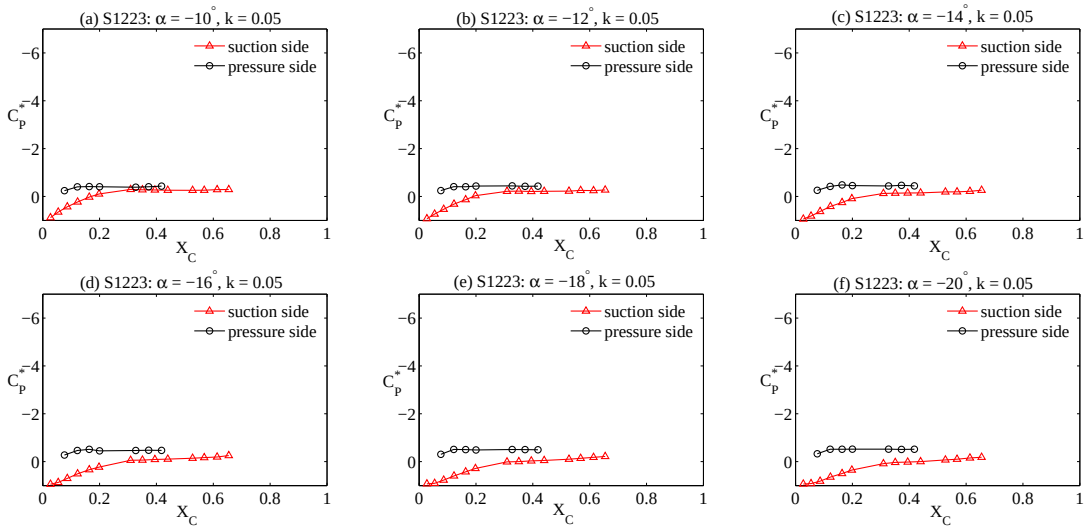

Figure 8.12: Unsteady C_P^* at a reduced frequency of 0.05: S1223 - reversed-down.

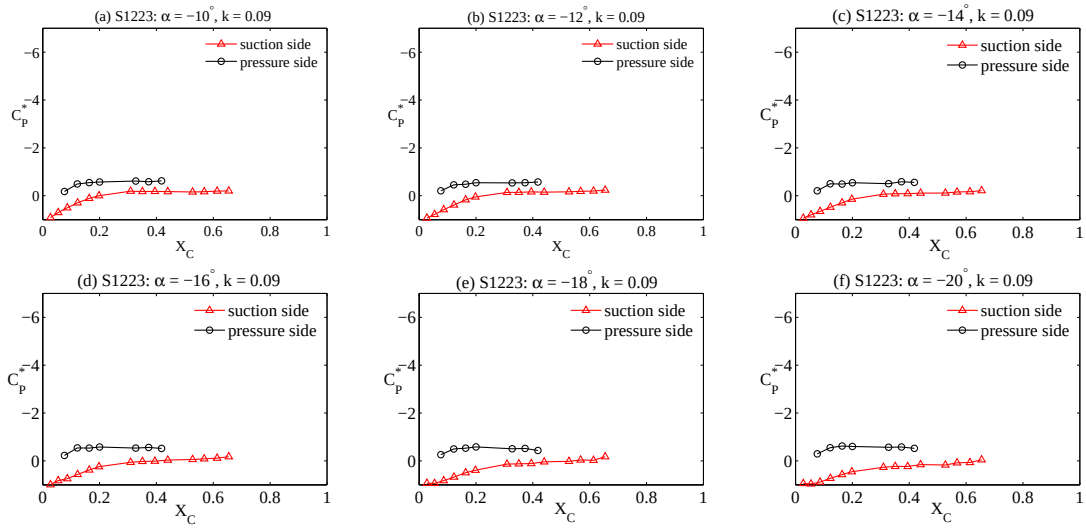

Figure 8.13: Unsteady C_P^* at a reduced frequency of 0.09: S1223 - reversed-down.

Reversed camber mode with increasing incidence angle

Figures 8.14 and 8.15 show unsteady C_P^* variations from incidence angle of $-20°$ to $-10°$ which represents the return of the aerofoil to the normal mode of operation.

It can be seen that suction pressure continues to develop. This regain of suction peak is closely related to the aerofoil leading edge shape. The leading edge shape of this aerofoil seems to cause the airflow to stay attached faster, resulting in a comparatively fast turning rate. The returning rate increases with increasing reduced frequency (compare Fig. 8.14d and 8.15d, for example).

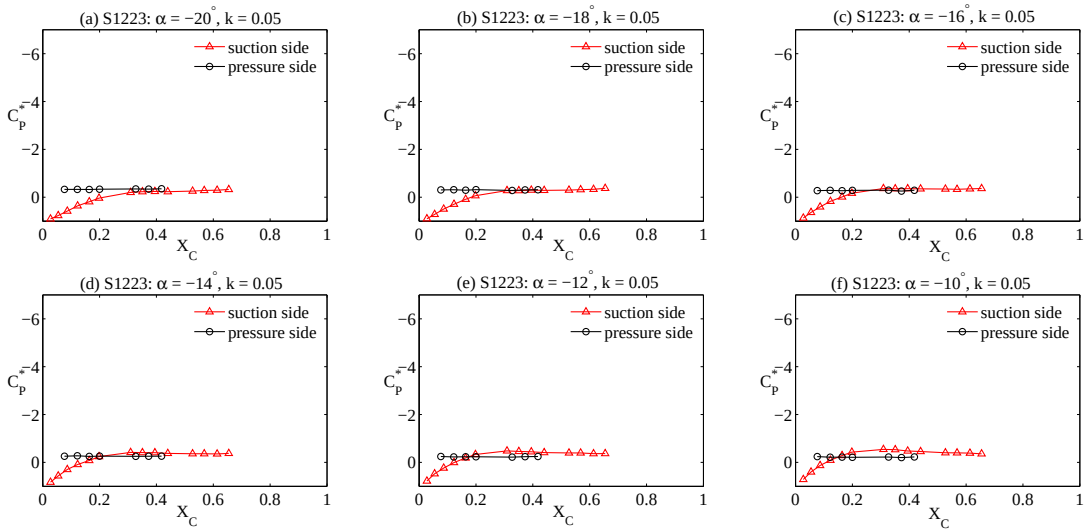

Figure 8.14: Unsteady C_P^* at a reduced frequency of 0.05: S1223 - reversed-up.

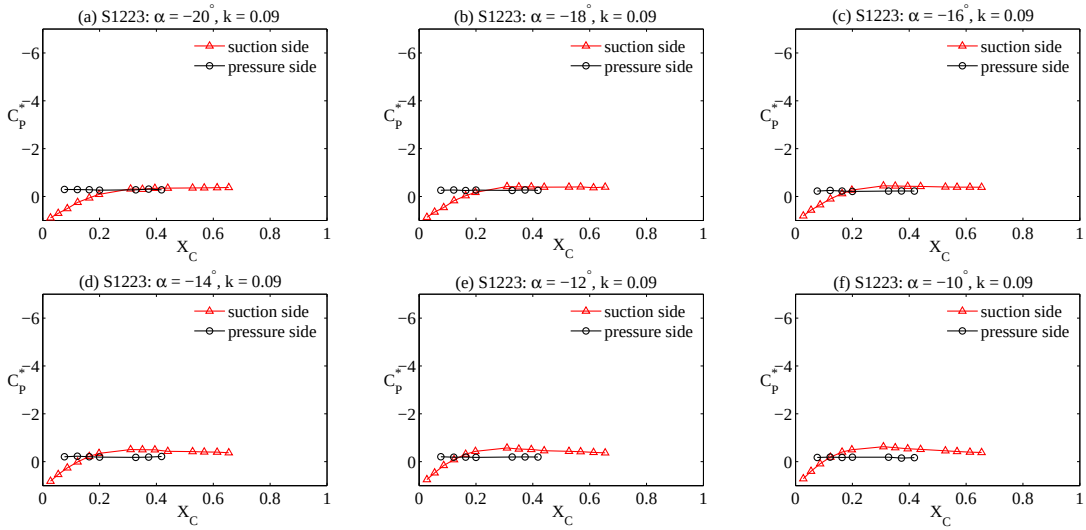

Figure 8.15: Unsteady C_P^* at a reduced frequency of 0.09: S1223 - reversed-up.

Unsteady normal force coefficient

Corresponding C_N curves of this S1223 aerofoil section are presented in Figures 8.16 and 8.17 together with its static normal force.

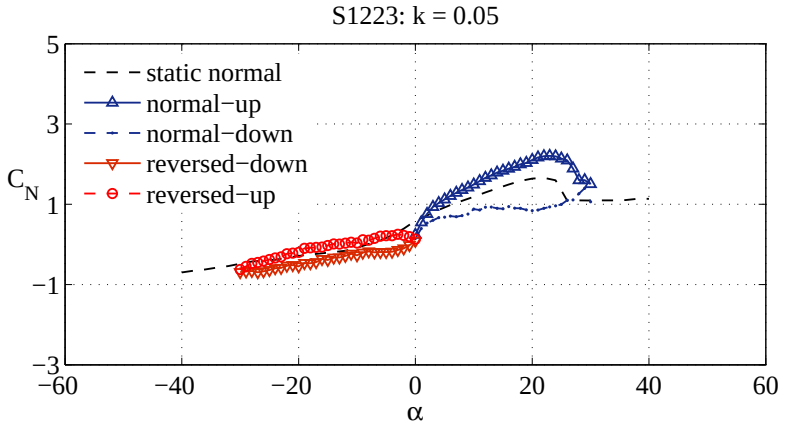

Figure 8.16: Unsteady C_N at a reduced frequency of 0.05: S1223.

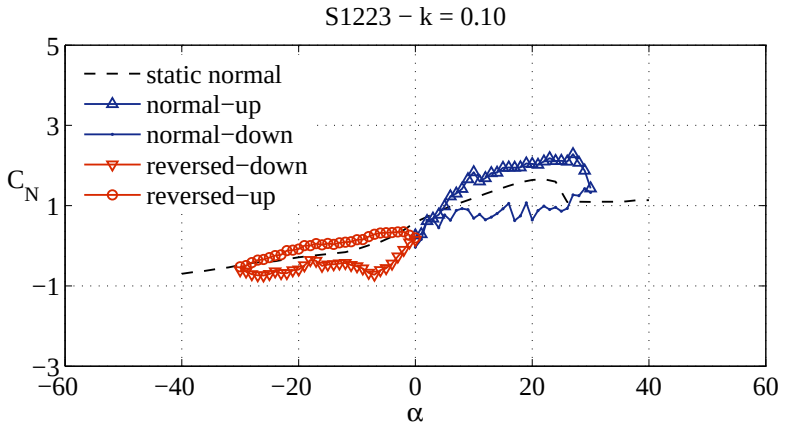

Figure 8.17: Unsteady C_N at a reduced frequency of 0.10: S1223.

It is observed that, in the normal mode, the normal force is continuously increasing with increasing incidence angle due to the formation of a dynamic-stall vortex. After that, the C_N will drop to around its static value and continues with this value until the flow reattaches, causing a hysteresis loop. The presence of unsteadiness overshoots the maximum C_N to around 2.2 at both reduced frequencies.

In contrast, in the reversed camber operation, the hysteresis loop is comparatively small at the reduced frequency of 0.05. The C_N behaviour is largely quasi-steady and roughly follows the static curve. Dynamic effects become more significant at a reduced frequency of 0.10 where there is a clear peak in normal force at around $-10°$ incidence angle. The hysteresis loop widens with increasing reduced frequency.

8.3.2 S1223B aerofoil

Normal mode with increasing incidence angle

Again, Figure 8.18 and 8.19 present unsteady surface pressure variations of the S1223B aerofoil at reduced frequencies of 0.08 and 0.22, respectively.

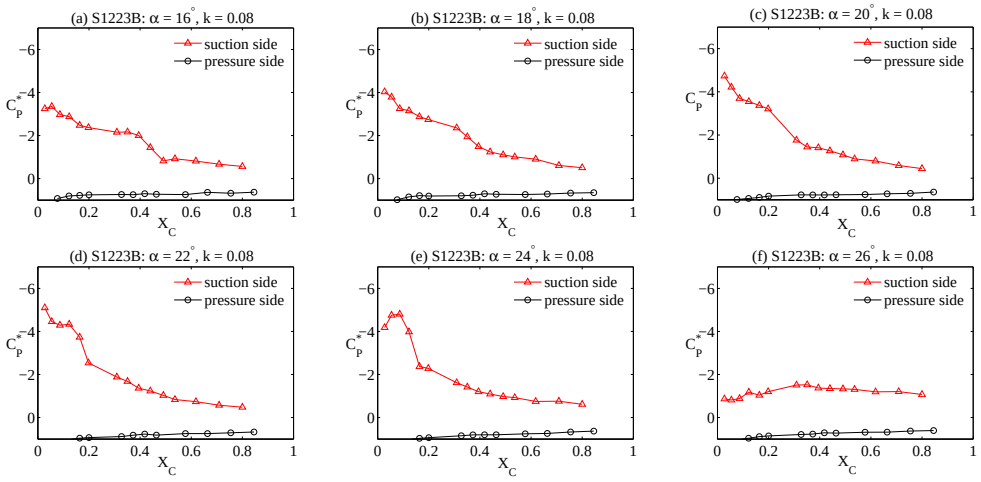

Figure 8.18: Unsteady C_P^* at a reduced frequency of 0.08: S1223B - normal-up.

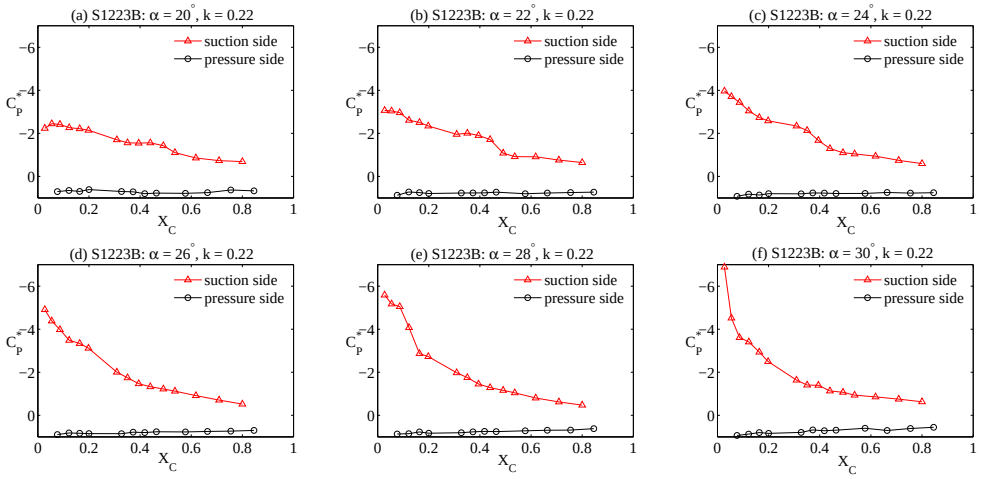

Figure 8.19: Unsteady C_P^* at a reduced frequency of 0.22: S1223B - normal-up.

It can be seen that the pressure variations are comparable to that of the S1223 case except the formation of bubble was found to take place further downstream (at around 0.2 at a reduced frequency of 0.08 (Fig. 8.18a). The maximum suction peak is approximate -5 and -7 at the reduced frequency of 0.08 and 0.22, respectively (double of that was found statically) (see Fig. 8.18d and 8.19f). The stall is postponed to higher 30° at the highest reduced frequency.

Normal mode with decreasing incidence angle

Figure 8.20 presents again unsteady C_P^* distributions during this pitch-down motion at a reduced frequency of 0.08 and it is seen that they are nearly constant over the incidence range (Fig. 8.20a to e). The flow reattachment is observed at an incidence angle of around 5° (fig. 8.21f). At the reduced frequency of 0.22, it is apparent that the aerofoil does not stall yet at the incidence angle of 30° and it is the pitch-down motion that forces the vortex to transverse along the aerofoil chord (Fig. 8.21a to 8.21d).

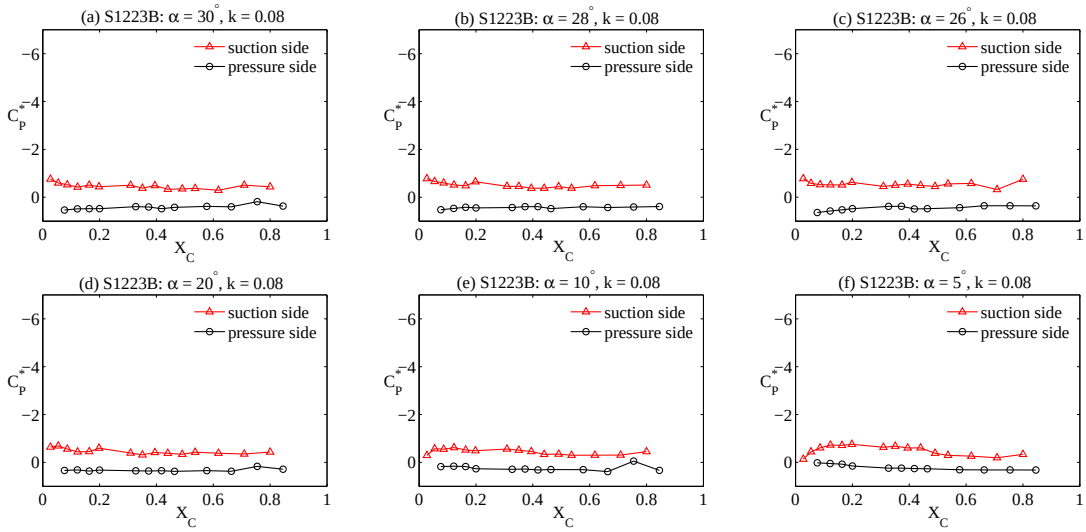

Figure 8.20: Unsteady C_P^* at a reduced frequency of 0.08: S1223B - normal-down.

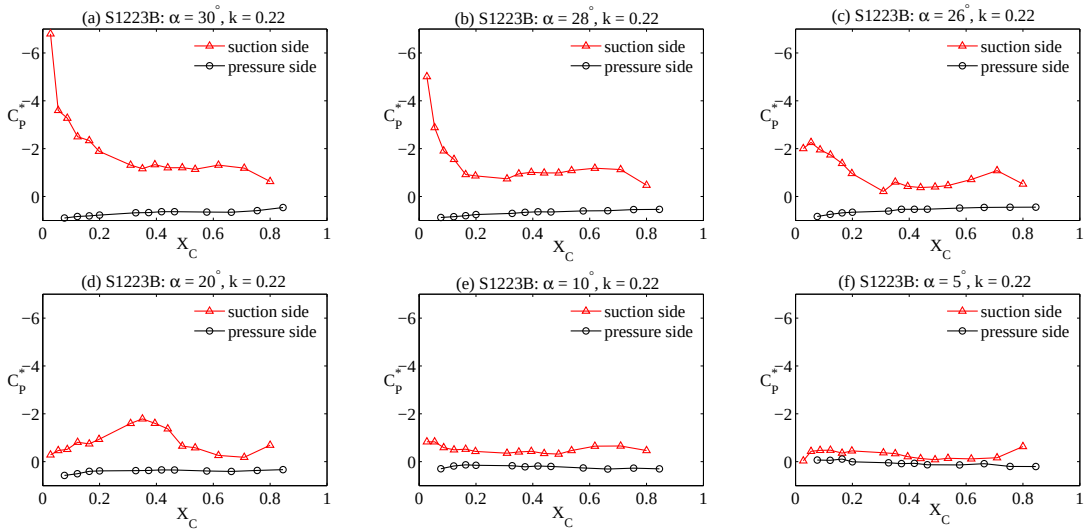

Figure 8.21: Unsteady C_P^* at a reduced frequency of 0.22: S1223B - normal-down.

Reversed camber mode with decreasing incidence angle

Pressure measurements during this mode of operation reveal that the formation of dynamic-stall vortex is greatly influenced by reduced frequency (Fig. 8.22 and 8.23). At the reduced frequency of 0.16, the formation and convection of dynamic-stall vortex is clearly seen. This characteristic effectively postpones stall angle and promotes more continuous production of lift and thrust. The generation of lift force continues up to an incidence angle of around $-28°$ before the vortex is shed into the wake. The aerofoil is fully stalled at about $-30°$.

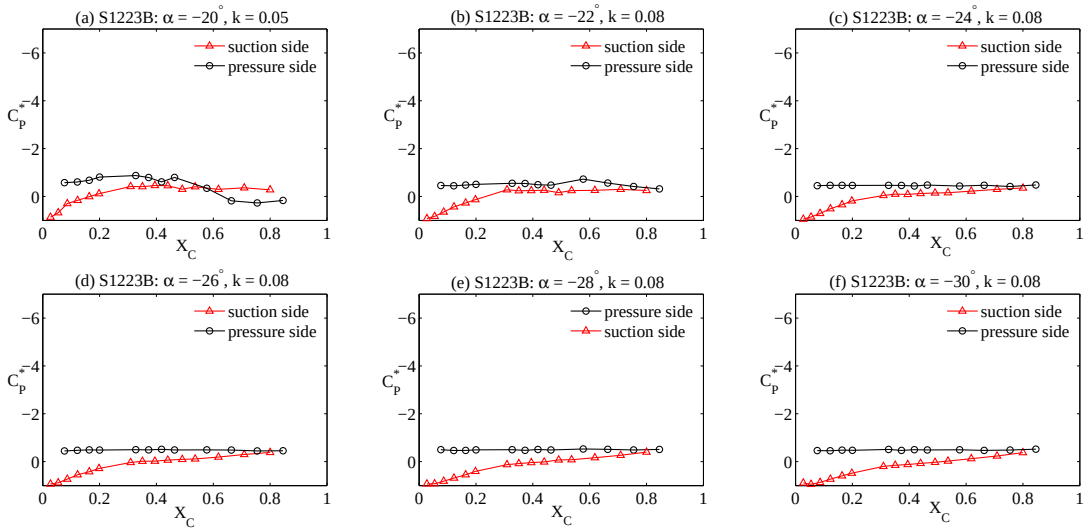

Figure 8.22: Unsteady C_P^* at a reduced frequency of 0.08: S1223B - reversed-down.

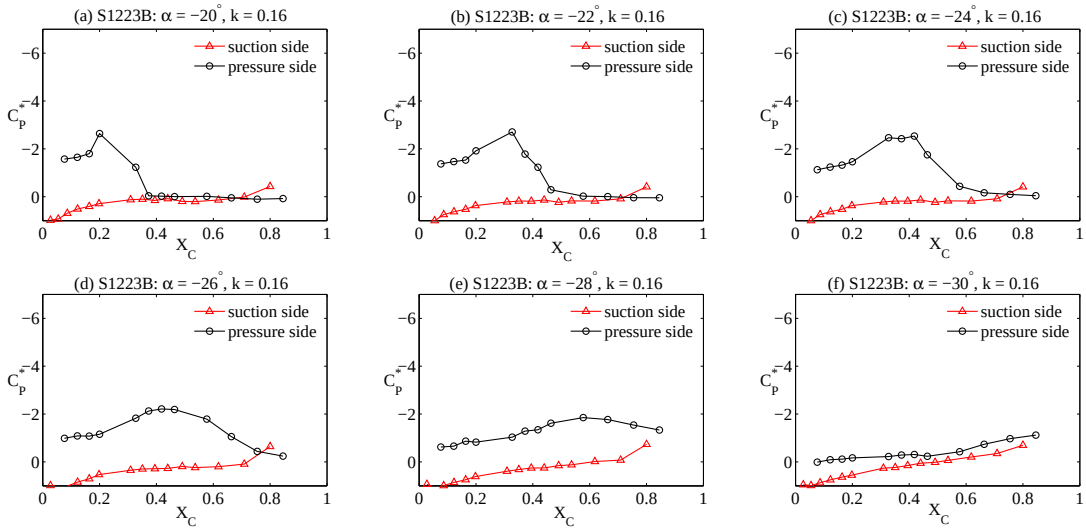

Figure 8.23: Unsteady C_P^* at a reduced frequency of 0.16: S1223B - reversed-down.

Reversed camber mode with increasing incidence angle

Unsteady C_P^* distributions of pitch-up motion during reversed camber mode are presented in Figures 8.24 and 8.25. It is seen that pressure coefficients on both sides are nearly the same at the incidence ranges from $-20°$ to $-16°$ and the difference only occurs near the leading edge, leading to a small negative thrust force. The regain of suction peak and its return to the normal mode of operation seems to occur at an incidence angle of $-14°$ at both reduced frequencies.

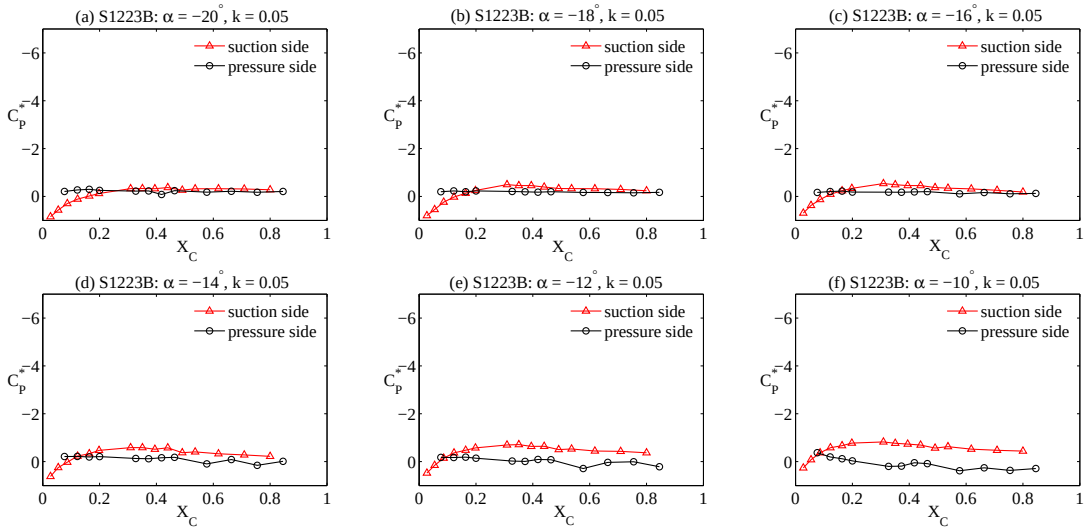

Figure 8.24: Unsteady C_P^* at a reduced frequency of 0.08: S1223B - reversed-up.

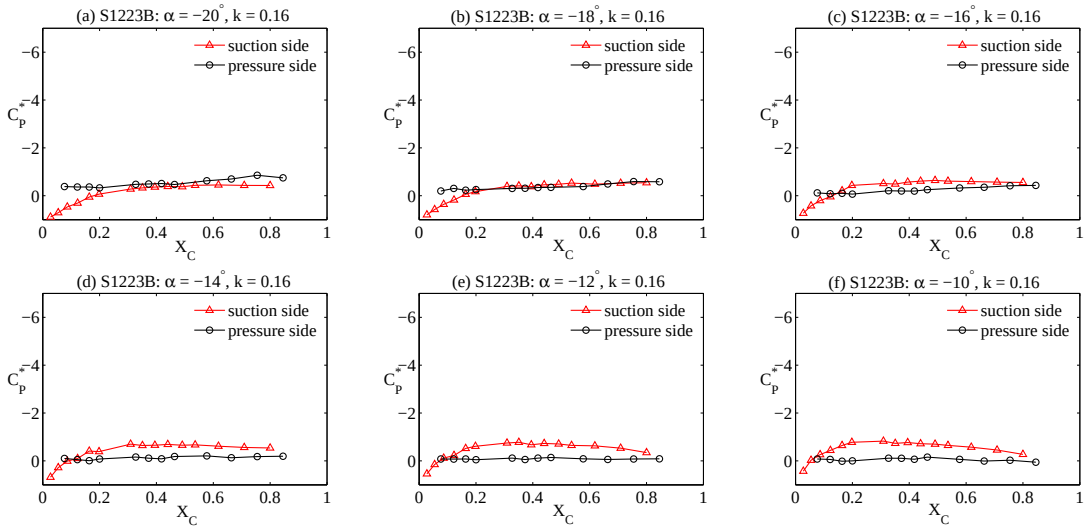

Figure 8.25: Unsteady C_P^* at a reduced frequency of 0.16: S1223B - reversed-up.

Normal force coefficient

Corresponding C_N curves under these conditions are presented in Figures 8.26 and 8.27 together with its static C_N curves. In general, its overall behaviour was found to be similar to that of the S1223 aerofoil. The performance characteristics of this aerofoil at a high reduced frequency of 0.16 have clearly shown that an overshoot of C_N in the reversed camber operation will occur only if the reduced frequency is sufficiently high.

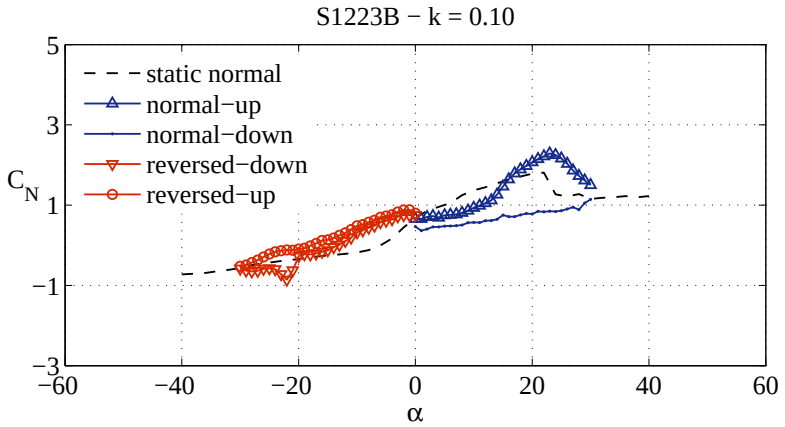

Figure 8.26: Unsteady C_N at a reduced frequency of 0.08: S1223B.

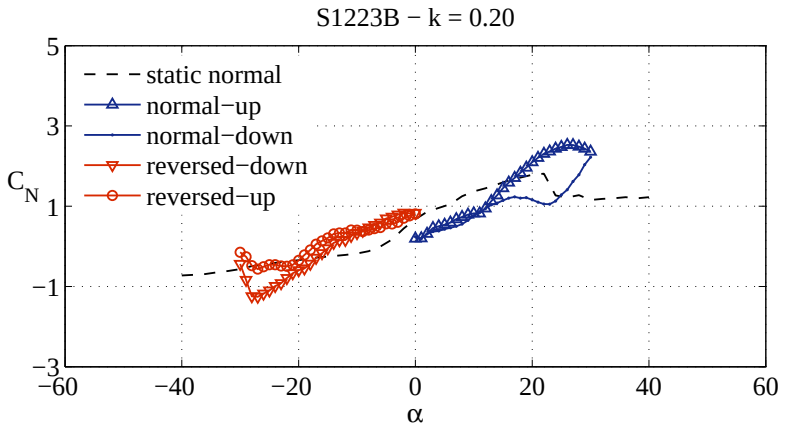

Figure 8.27: Unsteady C_N at a reduced frequency of 0.16: S1223B.

8.4 Conclusions

Performance characteristics of two bird-like aerofoils have been presented in this Chapter. Static wind-tunnel measurements of forces and surface pressure distributions revealed that both aerofoils exhibit high-lift properties. For the S1223, the highest lift coefficient is approximately 1.6 at the highest tested Reynolds number. The maximum lift decreases with reducing Reynolds number. The S1223B exhibits

better performance at low Reynolds numbers and the maximum lift produced is approximately 1.7 for all Reynolds numbers tested.

Both aerofoils exhibit abrupt stalling behaviour. Surface pressure measurements revealed that a laminar separation bubble exists on both aerofoils (the formation of bubble was found to occur further downstream for the S1223B). The bubble progresses upstream with increasing incidence angle and as soon as it reaches the leading edge, the aerofoils stall. The stalling mechanism was then caused by the process of bubble bursting.

Dynamic measurements have shown that the surface pressure is significantly altered by the unsteadiness. It was found that the suction pressure peak was increased when the aerofoils operate within the positive range (normal mode of operation). The suction peak C_P^* can be as high as -7 (approximately double of that was found statically). The formation of a separation bubble is also observed under dynamic conditions. With incidence increase, the bubble progresses upstream and the stall is initiated by the bubble, just like those found statically. The dynamic stall angle was found to be higher than 30° at the highest reduced frequency of 0.22.

By way of contrast, the effects of unsteadiness such as the increment in suction peak and the formation of the dynamic-stall vortex are less pronounced when the aerofoils operate with reversed camber operation (negative incidence range). During this mode, the suction and pressure sides are reversed and the pressure side which is not intended to promote attached flow is then not so effective in generating a suction peak. This causes the flow to separate, resulting in ineffectiveness in promoting unsteady force. The formation of the dynamic-stall vortex will be seen only if the reduced frequency is sufficiently high.

This high reduced frequency requirement during reversed camber operation is consistent with the strategy that birds employ to generate lift and thrust during the downstroke. They typically flap their wings at a faster rate and spread their wings as much as possible (increasing chord length and reducing wing's effective camber) to increase the level of unsteadiness.

In summary, the bird-like aerofoil sections which are highly cambered provide two aerodynamic characteristics for flying: high forward thrust during the upstroke and high lift force for normal crusing flight. The high percent of camber, which is needed to generate lift force to support their bodies, makes their wings ineffective in generating forward thrust during the downstroke (critical during take-off). This drawback is tackled by other techniques such as wing spreading to maximise thrust production during take-off.

This performance characteristic will be compared with those of other sections to get an idea of how the aerofoil for the Darrieus rotor can be improved. This comparison is presented in the next chapter together with Darrieus turbine performance modelling.

Chapter 9

H-Darrieus Turbine Self-starting Behaviour

This chapter models and investigates H-Darriues turbine self-starting behaviour. It first discusses the aerofoil in Darrieus motion and its expected performance when moving along the flight path with the assistance of aerofoil wind-tunnel data and consideration of bird flying. Performance modelling and investigations are presented at the end of the chapter.

9.1 The aerofoil in Darrieus motion

9.1.1 Bird flying

In flapping flight, birds perform a specific technique to generate lift and thrust. Studies on bird locomotion have shown that birds generate different wake structures when flying at low and high speeds [136]. The wakes are caused by different wingbeat patterns: figure-of-eight and elliptical (Fig. 9.1).

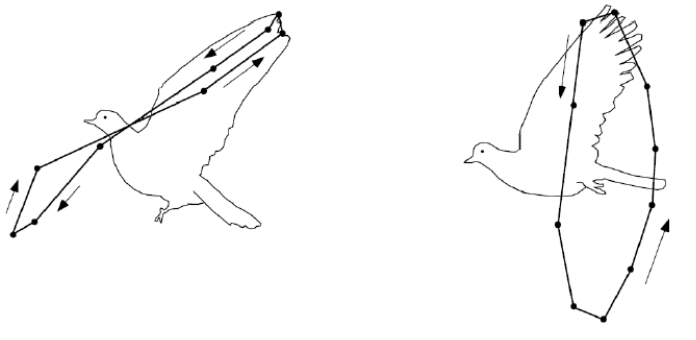

(a) Figure-of-eight pattern (b) Elliptical pattern

Figure 9.1: Wingbeat patterns at low- and high-flying speeds (adapted from [166]).

One of the main differences between these two patterns is the driving force generated throughout the stroke. While lift and thrust are continuously generated in the elliptical pattern, the forces are 'discrete' in the figure-of-eight pattern and only produced during downstroke. In general, the figure-of-eight pattern has a longer downstroke (about two thirds of the total cycle [167, 168]). The relative timing and the pattern change with increasing flying speed. If the speed is sufficiently high, wings during upstroke will become effective in producing lift and thrust. The wingbeat then becomes an elliptical pattern in which each stroke lasts approximately the same (Fig. 9.1b).

The figure-of-eight pattern is used at low flying speeds, in particular during take-off. In order to maximise the driving force during the downstroke, birds typically flap their wings very fast (increasing reduced frequency), spread their wings as much as possible (increasing effective chord length), and sweep their wings forward (increasing the duration of force production). They also fold and retract their wings during the upstroke to reduce air resistance and shorten recovery period.

This flapping technique suggests that, in order to improve the turbine's ability to self-start, the Darrieus blade should:-

1. be effective in generating thrust during downstroke
2. produce less drag (or less negative thrust) during upstroke
3. have a short recovery period in order to promote more continuous thrust generation
4. exhibit a long downstroke phase at low tip speed ratios in order that a significant amount of thrust can be generated

It is interesting to note that the aerofoil in Darrieus motion exhibits an asymmetry of the relative timing of the upstroke and the downstroke and inherently provides a longer downstroke phase at low tip speed ratios (the peak of Darrieus incidence angle occurs before the azimuth angle of 90° and the negative peak occurs after the azimuth angle of 270° (see Fig. 4.2 in chapter 4)). The fourth requirement is then automatically satisfied.

Since the Darrieus blade is fixed and can not be adapted over the cycle, the first three requirements can be satisfied by suitably selecting an aerofoil profile and by properly sizing rotor geometry.

9.1.2 Aerofoil performance comparisons

It is noted that the aerofoils tested in this course of study can be broadly divided into three groups: symmetrical (NACA0012 and DU06-W-200), moderately cambered (SD7062 and SG6043), and highly cambered (S1223 and S1223B). Three aerofoils

are then selected to be representatives in this discussion and they are the NACA0012, the SD7062, and the S1223B.

Unsteady thrust (C_t) of the three aerofoils at a reduced frequency of 0.2 are presented in Figure 9.2. The C_t behaviour is also marked as state 1 to 4 to represent different motions during the wing-beat cycle (Fig. 9.2 and 9.3).

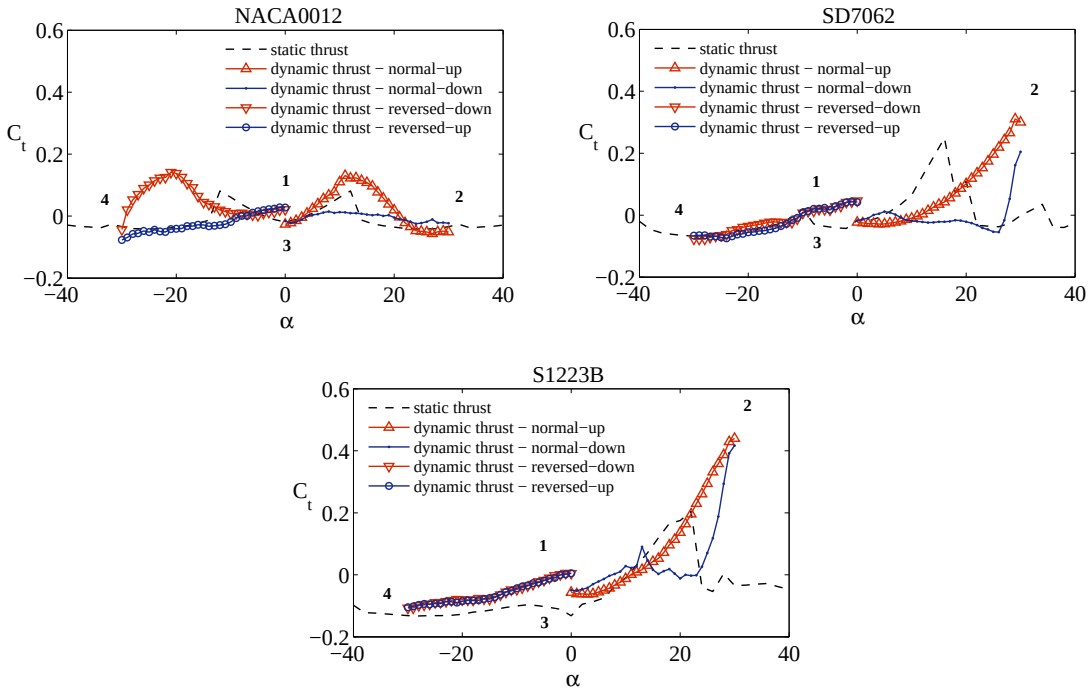

Figure 9.2: Thrust coefficients.

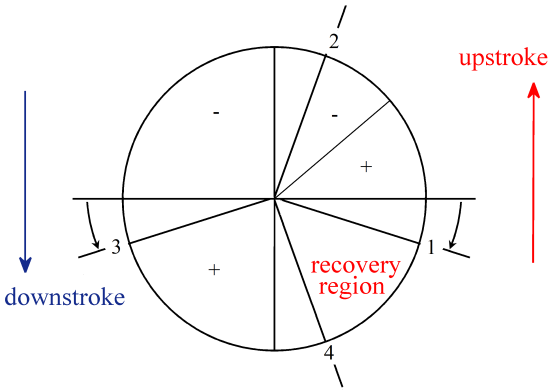

Figure 9.3: The shift of midstroke due to cambered aerofoil section.

The motions in the Darrieus flight path are:-

1. The second half of the up-stroke (from 1 to 2), represented by a solid line with a triangle marking.

2. The first half of the down-stroke (from 2 to 3), represented by a solid line.

3. The second half of the down-stroke (from 3 to 4), represented by a solid line with upside down triangles.

4. The first half of the up-stroke or recovery region (from 4 to 1), represented by a solid line with open circles.

It can be seen that the use of cambered sections (having an asymmetric property) will shift the zero-lift angle of attack to the negative range, leading to a shift of the neutral point (or midstroke (states 1 and 3)) to the lower half circle. This effectively shortens the recovery region (the third requirement).

In terms of unsteady thrust, it is observed that the three aerofoil generate different C_t characteristics. The symmetrical section can generate a positive thrust coefficient of around 0.15 in both modes of operation. Dynamic-stall angles of attack are about 20° and −30° for normal and reversed mode, respectively.

Superior performance of the cambered sections is observed during stage 1 to 2 (Fig. 9.2). The positive thrust coefficient is significantly higher (about 0.3 and 0.45 for the SD7062 and the S1223B, respectively) and the stall angles are postponed to approximate 30° for both sections. In addition, the use of these cambered sections, which exhibit higher post-stall lift, also leads to less negative thrust during state 2 to 3 (the second requirement). This, together with the shorten recovery period (Fig. 9.3), makes the use of cambered aerofoils beneficial over the symmetrical aerofoil during the upstroke.

However, the cambered sections do not exhibit a clear positive thrust during state 3 to 4 (downstroke) which is the main thrust contributor at low tip speed ratios. A close examination of pressure distribution has revealed that its leading edge shape has lost its 'propulsive effect' during this mode of operation (Fig. 9.4).

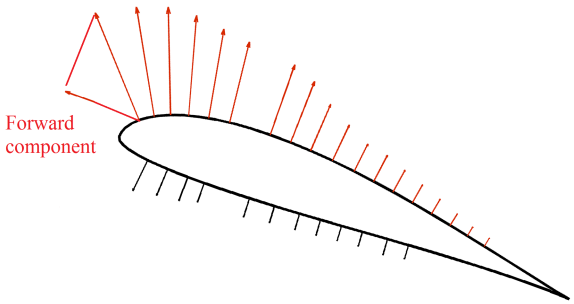

Figure 9.4: Example of pressure distribution over the aerofoil surface: SD7062.

The propulsive effect is greatly influenced by the leading edge shape of the aerofoil and can be easily generated in normal operation (propulsive effect is caused by the suction peak that has a forward thrust component) (Fig. 9.4). This forward component is lost when operating with reversed camber mode since the leading edge shape is comparatively flat (for the SD7062 section). This can be worse on the

high cambered section as the pressure surface is 'concave' and any pressure difference caused by the vortex formation will not promote propulsion.

It is worth noting that this effect is further amplified by vortex formation under dynamic conditions. The presence of the dynamic-stall vortex induces higher suction peak which results in an additional forward thrust component. Additionally, its presence also delays stall up to a higher incidence angle, effectively increasing the range that the propulsive effect is present. This characteristic is one of the reasons why an additional propulsive force is created when operating under dynamic conditions. This unsteady propulsive force will be continuously generated if the aerofoil oscillates within the dynamic-stall angle range.

It is apparent from this performance comparison that the leading edge shape of the aerofoil is critical. In order to promote unsteady thrust in both modes of operation, the aerofoil should be able to generate suction peaks in both modes of operation.

The requirement of being able to generate a forward thrust component during both modes of operation makes the symmetrical aerofoil sections (i.e. the NACA0015 and NACA0018) a simple and attractive choice for Darrieus rotors. However, there is still room for improvement. It is likely that a small percent of camber can be added to improve the aerofoil performance during upstroke but the maximum camber should be located further down to the trailing edge in order that the leading edge shape is still active in generating the forward thrust component when operating with reversed cambered operation.

To sum up, based upon the aerodynamic data presented, the performance comparison has indicated that:-

- The leading edge shape of the aerofoil is critical and must be in the shape that it can produce propulsive effects when operating in both modes of operation.
- A small percent of camber can be added to increase performance during upstroke.
- The pressure recovery type is also of importance. A well-designed recovery type can lead to an efficient production of propulsion and an decrease in vortex convection that poses extra load to the rotor structure.

Performance modelling presented in this work is restricted to the conventional NACA section.

9.2 Performance modelling

9.2.1 Mathematical models

A numerical model was developed under assumptions that:-

- wind speed is *steady* and *uniform* across the rotor swept area.

- the turbine spins slowly during start-up and the effect of induced velocity is *negligible*.
- there is *no* blade/wake interaction within the turbine and each blade is aerodynamically *independent*.
- effects of unsteadiness caused by a combined pitch and plunge motion can be represented by those caused by pure pitch motion.

Based upon these assumptions, the calculation of flow conditions that the blade experiences can be obtained through velocity triangle analysis. The sign convention used in this analysis has been already presented in Chapter 4 (Fig. 4.1).

Flow conditions (resultant wind speed, incidence angle, and reduced frequency) that the blade experiences depends upon the blade azimuth angle and its speed relative to the wind (Fig. 9.5).

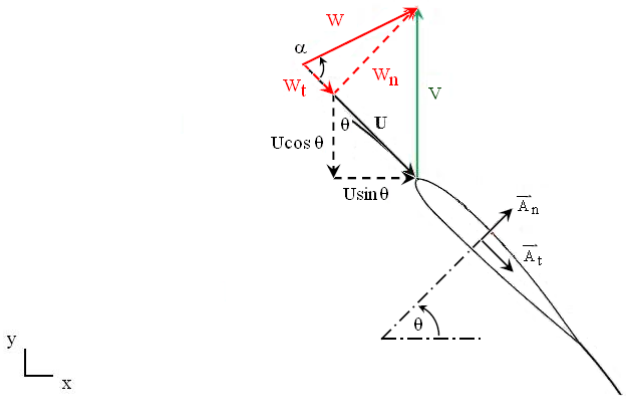

Figure 9.5: Vectorial description of aerofoil position and velocities.

As seen from Figure 9.5, the aerofoil position can be determined by two unit vectors; namely unit normal and tangential vectors ($\vec{A}_n$ and $\vec{A}_t$) which can be written in cartesian coordinate as

$$\vec{A}_n = (\cos\theta)\hat{\imath} + (\sin\theta)\hat{\jmath} \tag{9.1}$$

$$\vec{A}_t = (\sin\theta)\hat{\imath} - (\cos\theta)\hat{\jmath} \tag{9.2}$$

Similarly, free-stream velocity and headwind velocity caused by the blade movement can be written in vector forms as

$$\vec{V} = V\hat{\jmath} \tag{9.3}$$

$$\vec{U} = (U\sin\theta)\hat{\imath} - (U\cos\theta)\hat{\jmath} \tag{9.4}$$

Resultant velocity perceived by the blade is simply a summation of free-stream wind speed and headwind speed

$$\vec{W} = (U\sin\theta)\hat{\imath} + (V - U\cos\theta)\hat{\jmath} \tag{9.5}$$

Resultant wind speed in normal and tangential components are obtained by projecting this wind speed into normal and tangential directions, respectively.

$$\vec{W}_n = \vec{W}\cdot\vec{A}_n = (U\sin\theta)(\cos\theta) + (V - U\cos\theta)(\sin\theta) \tag{9.6}$$

$$\vec{W}_t = \vec{W}\cdot\vec{A}_t = (U\sin\theta)(\sin\theta) - (V - U\cos\theta)(\cos\theta) \tag{9.7}$$

The arctangent of $\vec{W}_n/\vec{W}_t$ is the Darrieus incidence angle that the blade experiences

$$\alpha_D = \arctan\left[\frac{\vec{W}_n}{\vec{W}_t}\right] = \arctan\left[\frac{(U\sin\theta)(\cos\theta) + (V - U\cos\theta)(\sin\theta)}{(U\sin\theta)(\sin\theta) - (V - U\cos\theta)(\cos\theta)}\right] \tag{9.8}$$

Dividing the numerator and denominator at the right hand side by V, the following expression is obtained:

$$\alpha_D = \arctan\left[\frac{(\lambda\sin\theta)(\cos\theta) + (1 - \lambda\cos\theta)(\sin\theta)}{(\lambda\sin\theta)(\sin\theta) - (1 - \lambda\cos\theta)(\cos\theta)}\right] \tag{9.9}$$

Rearranging,

$$\alpha_D = \arctan\left[\frac{\sin\theta}{\lambda - \cos\theta}\right] \tag{9.10}$$

The magnitude of the resultant wind speed and Reynolds number are

$$W^2 = (U\sin\theta)^2 + (V - U\cos\theta)^2 = U^2 + V^2 - 2UV\cos\theta \tag{9.11}$$

$$Re = \frac{\rho W c}{\mu} \tag{9.12}$$

Or in terms of tip speed ratio as

$$W = V \times \sqrt{\lambda - 2\lambda\cos\theta + 1} \tag{9.13}$$

$$Re = \left[\frac{\rho V c}{\mu}\right] \times \sqrt{\lambda - 2\lambda\cos\theta + 1} \tag{9.14}$$

The level of unsteadiness is typically expressed in terms of reduced frequency which is defined as

$$k = \frac{\omega c}{2W} \tag{9.15}$$

where ω is rotational speed, c is aerofoil chord, and W is relative speed. It can be expressed in terms of tip speed ratio as

$$k = \left[\frac{c}{D}\right] \times \left[\frac{\lambda}{\sqrt{\lambda^2 - 2\lambda\cos\theta + 1}}\right] \tag{9.16}$$

Knowing the incidence angle, Reynolds number, and reduced frequency, lift and drag coefficients can be calculated. Thrust coefficient is found by resolving the forces into a circumferential direction.

$$C_t = C_l(\alpha_D, Re, k)\sin\alpha_D - C_d(\alpha_D, Re, k)\cos\alpha_D \tag{9.17}$$

A tangential force and driving torque generated by each blade is then

$$F_i = (\frac{1}{2}\rho c S W^2) \times C_t \tag{9.18}$$

$$T_i = F_i(\theta) \times R \tag{9.19}$$

Net driving torque produced by the rotor is a summation of all torques and torque coefficient are

$$T = \sum_{i=1}^{n} T_i \tag{9.20}$$

$$C_q = \frac{T}{1/2\rho c S W^2 R} \tag{9.21}$$

9.2.2 Time stepping

Modelling of the starting behaviour is based upon the approach of Dominy et al [24] which is carried out by stepping the time and tracking the blades over the flight path (Fig. 9.6). A computational sequence is summarised in Figure 9.7.

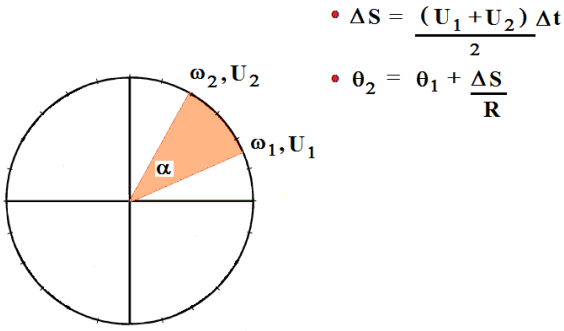

Figure 9.6: Time stepping.

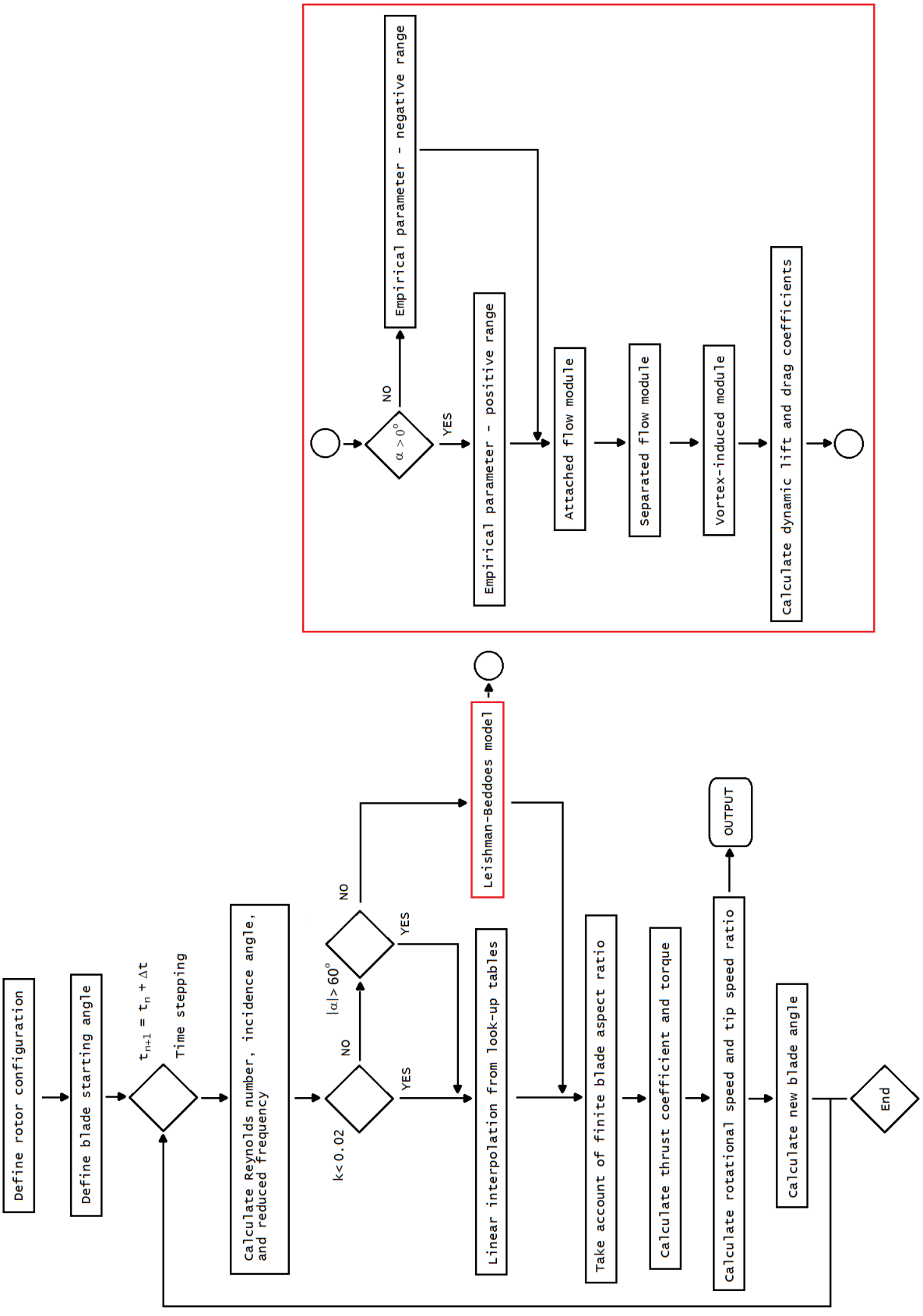

Figure 9.7: Computational sequence.

From a predefined rotor configuration, blade starting position, and free-stream wind speed, flow conditions that each blade experiences are calculated.

The flow conditions determine lift and drag forces at each time step. The forces are resolved in a circumferential direction to obtain thrust coefficient which will be used to calculate torque. Knowing torque and rotor inertia, the new rotational speed at the next time step is

$$\omega_{n+1} = \omega_n + \Big(\frac{\sum_{i=1}^{B} T_i}{J}\Big)\Delta t \tag{9.22}$$

The new headwind velocity that the blade experiences is then

$$U_{n+1} = \omega_{n+1} \times R \tag{9.23}$$

The circular path that the blade travels is calculated from an average headwind velocity over the segment.

$$\Delta S = \frac{(U_{n+1} + U_n)}{2} \times \Delta t \tag{9.24}$$

The new blade position is then

$$\theta_{n+1} = \theta_n + \frac{\Delta S}{R} \tag{9.25}$$

This angle change is updated over the Darrieus circle and, whenever the blade completes the full circle (azimuth angle is larger than 360°), it will be reset to comply with the sign convention (Fig. 4.1).

The calculation of torque at each time step depends on the reduced frequency that the blade experiences. As long as the reduced frequency is lower than 0.02, C_l and C_d are interpolated from look-up tables which contain static wind-tunnel data at nominal Reynolds numbers of 65000, 90000, and 150,000 through 360°. If the Reynolds number is out of the range, the low (or high) end values are used instead of extrapolation.

If the reduced frequency is higher than 0.02 and the magnitude of the incidence angle is lower than 60° (experimental results from the previous chapters have shown that the effect of unsteadiness is negligible when the flow is fully separated (a quasi-steady assumption is assumed if $|\alpha| \geq 60°$)), unsteady effects are incorporated into the model by the use of the Leishman-Beddoes dynamic-stall model (Fig. 9.7).

A general LB module is used to calculate C_l and C_d for both normal and reversed camber modes of operation. The model basically provides transient forces which are obtained from the integration of unsteady pressure coefficients presented in the previous chapters. The mode change is detected by checking the product of present and previous incidence angles (the incidence angle is in the range of $-180°$ and 180°):

$$(\alpha_{new} - \alpha_0) \times (\alpha_{old} - \alpha_0) \tag{9.26}$$

where α_0 is zero-lift incidence angle.

If the product is negative, the mode of operation has changed and a flag is set. The flag will be used to reset time-history calculation and local vortex time. The vortex time is allowed to increase as long as the product $(\alpha_{new} - \alpha_0) \times (\alpha_{old} - \alpha_0)$ is positive to track vortex movement in each mode of operation. Calculations of the three submodules are made sequentially to get dynamic lift and drag. The resultant C_l and C_d are resolved into circumferential direction to obtain C_t and torque. A summary of the dynamic-stall model and parameters used in simulations can be found in Appendix D.

Three dimensional effects such as blade tip loss have also been taken into account [22]. In this modelling, the circulation loss near the tip are taken into consideration by applying Prandtl' tip loss function to both ends of the blades (Fig. 9.8). The following equations are applied:-

$$F_{eff} = F_1 \times F_2 \tag{9.27}$$

$$F_1 = \frac{2}{\pi} \arccos(e^{-f}) \quad \text{and} \quad f = \frac{B}{2} \frac{r - R_1}{R \sin \alpha_D} \tag{9.28}$$

$$F_2 = \frac{2}{\pi} \arccos(e^{-f}) \quad \text{and} \quad f = \frac{B}{2} \frac{R_2 - r}{R \sin \alpha_D} \tag{9.29}$$

where B is number of blade and α_D is the incidence angle.

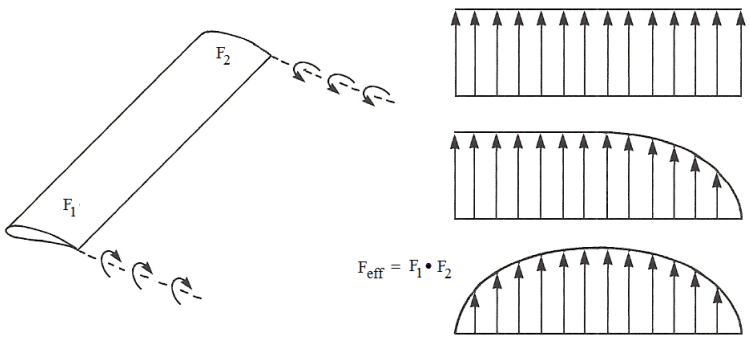

Figure 9.8: Tip effect modelling.

It is important to note however that, although the application of this tip function is sensible, the validity of this approach to Darrieus blades is of question. Further experimental research and verification is needed in this area.

The corrected torque is then used to calculate new rotational speed and blade position from which the same process is repeated.

9.3 Validation

Validation of the model was performed by simulating the turbines tested by Hill et al [10], Rainbird [58], and Chua [8]. A time increment of 0.001s was used in all simulations. Table 9.1 summarises turbine geometric parameters. Figures 9.9 and 9.10 show validation results. It is noted that the prediction of Chua's result was made using static lift and drag coefficients of a NACA0015, provided by Rainbird [58]. Dynamic parameters such as dynamic-stall angle were kept unchanged in all predictions.

Table 9.1: Turbine configurations.

Configuration	Hill et al and Rainbird	Chua
Number of blades	3	3
Aerofoil	NACA0018	NACA0015
Chord (m)	0.083	0.070
Span (m)	0.6	0.5
Radius (m)	0.375	0.25
Inertia ($kg - m^2$)	0.018	0.015
Solidity (σ_r) (-)	0.664	0.84
Chord-to-diameter ratio (-)	0.11	0.14
Blade aspect ratio (-)	7.229	7.143

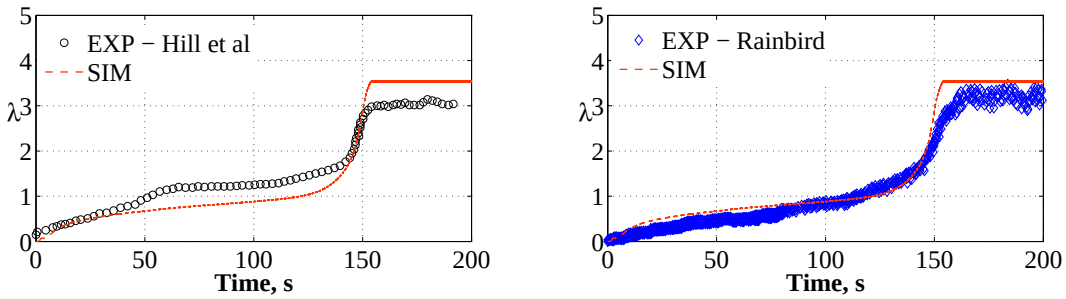

Figure 9.9: Starting behaviour validation: Hill et al and Rainbird cases.

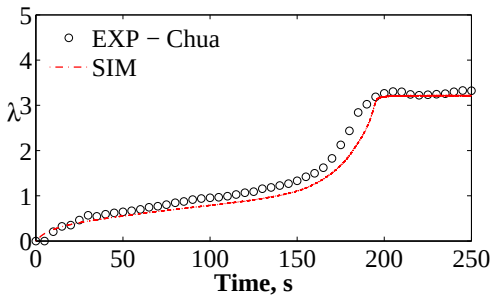

Figure 9.10: Starting behaviour validation: Chua case.

Overall, the experimental and predicted results are is qualitative agreement and the overall behaviour of the starting is well-captured. In the first validation, dis-

crepancies are observed in two areas: the plateau (between 40s to 140s) and the final, operating tip speed ratio that the rotor reaches (between 160s to 200s). The discrepancy in the plateau area is comparatively large and the model predicts that the rotor accelerates to a tip speed ratio of around 0.7 before decelerating, causing a TSR plateau. This difference is less seen in the second validation. The plateau is less evident in the Rainbird test and the rotor seems to accelerate continuously, though with a decreasing acceleration rate between 50s and 100s before reaching the second acceleration zone.

Over-prediction of the final, operating tip speed ratio is seen in both validation cases. The over-prediction is anticipated to be a result of bearing friction of the real machine and windage of the blade support arms which are assumed to be zero in the predictions. Another might be the effect of blade/wake interaction. The wake generated by the upstream blade might alter the flow that the downstream blade experiences and the assumption that each blade is aerodynamically independent might be invalid under this condition.

In Chua's case, it can be seen that the result is in good agreement for the entire starting process, particulary in the second zone; a region where the tip speed ratio increases with a decreasing acceleration rate (referred to as a plateau in Hill et al experiment). It is noted that over-prediction of the steady, operating region is small in this prediction and this is expected to be a result of wind-tunnel data provided by Rainbird in which drag is relatively high (around 0.03 for the NACA0015 in comparison to 0.0228 for the NACA0018 at a comparable Reynolds number). This is anticipated to be a result of manufacturing process [58]. Since the NACA0015 section is expected to exhibit lower drag than that of the NACA0018, an over-prediction will be present if other wind tunnel data is used.

All in all, the model developed can predict the Darrieus rotor starting behaviour reasonably well and can be used to understand flow conditions and its fundamental starting behaviour. Discrepancies between the experiments and the model prediction also suggests that extensive wind tunnel testing of the turbine at various conditions is required.

9.4 Results

9.4.1 Rotor performance

Figure 9.11 presents Darrieus turbine starting behaviour together with variations of flow conditions that the blade experiences during the starting process.

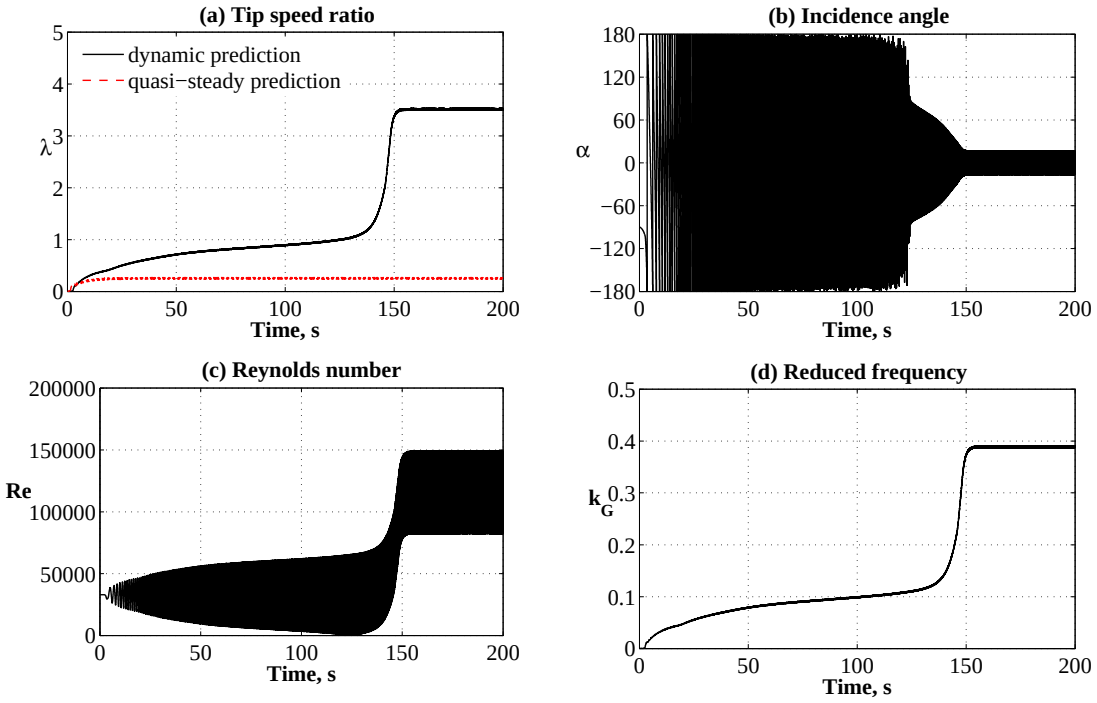

Figure 9.11: Darrieus turbine starting behaviour and flow conditions that the blade experiences.

During the first acceleration, the Reynolds number that the blade experiences is around 33,000 when stationary before varying over the flight path when the rotor rotates; minimum and maximum values occur at azimuth angles of 0° and 180°, respectively (see Fig. 4.2a). Since the tip speed ratio is lower than one, incidence angle variation in this region is still large and the blade experiences all possible angles of attack (±180) (Fig. 9.11b). The rate of incidence change gradually increases with increasing tip speed ratio. It is worth noting that the driving thrust generated by the blade is alternately driven by drag and lift (drag-driven state occurs in quadrant 4 and 1 due to an extremely large incidence angle. The lift-driven state occurs in quadrant 2 and 3). Quasi-steady and transient predictions are in good agreement up to a tip speed ratio of around 0.3.

Beyond the tip speed ratio of 0.3, the transient effect is present and plays a role in driving the rotor. As discussed in the previous chapters, this transient effect is significant when the aerofoil is not fully stalled (normally in the incidence range of ±45). Consideration of incidence variation indicates that this occurs in quadrant 3 (see Fig. 4.2b) and it is, therefore, the blade in quadrant 3 that provides an

additional thrust to drive the rotor in this region. It is also observed that the Reynolds number variation is getting large with increasing tip speed ratio and will be periodically approaching zero at the unity tip speed ratio (taking place at the azimuth angle of 0° and the low Reynolds number will cover a significant part in quadrant 4 and 1). The blade in these two quadrants is therefore less effective in producing thrust, causing the tip speed ratio to increase with a reducing acceleration rate (Fig. 9.11a).

The rotor will enter full lift-driven state (flapping-wing analogy) at the unity tip speed ratio. The driving force in quadrants 1 and 4 which was previously generated by drag has now reversed to be generated by lift. With an incidence range that is still large (for example, ±64° at $\lambda = 1.1$) and low Reynolds number in quadrants 4 and 1, the blade in these quadrants is still not effective in driving the rotor and it is the blade in quadrant 3 that provides most of the drive, leading to a 'discrete' thrust generation and a comparatively low driving force. With the slowly increasing tip speed ratio, the incidence range slowly reduces and the Reynolds number range slowly increases (Fig. 9.11b and c).

The discrete thrust-producing state continues until the rotor reaches a significantly higher tip speed ratio (around 1.5 to 2). At this tip speed ratio, the lowest Reynolds number at the azimuth angle of 0° is increased to around 33,000 and the incidence range becomes small (±30). The blade in quadrant 1 becomes active again in generating thrust. The rotor then takes off to a steady, operating tip speed ratio of around 3.4 where Reynolds number variation has jumped to lie in the range from 66,000 to 131,000 and the incidence angle variation is between ±20.

Torque characteristic of the Darrieus rotor is predicted and presented in Figure 9.12. It can be seen that the torque generated by the rotor is comparatively high when stationary before decreasing with increasing tip speed ratio. The C_q reduces with increasing tip speed ratio and will be very low at the tip speed ratio of one. With further TSR increase, C_q gradually increases until it reaches its peak of about 0.3 at a tip speed ratio of 2.5 before decreasing again.

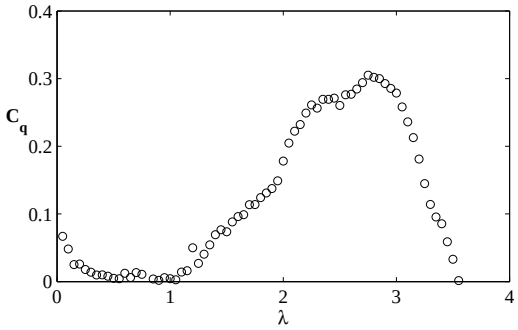

Figure 9.12: Torque coefficient.

A complete summary of the rotor behaviour is presented in Figure 9.13.

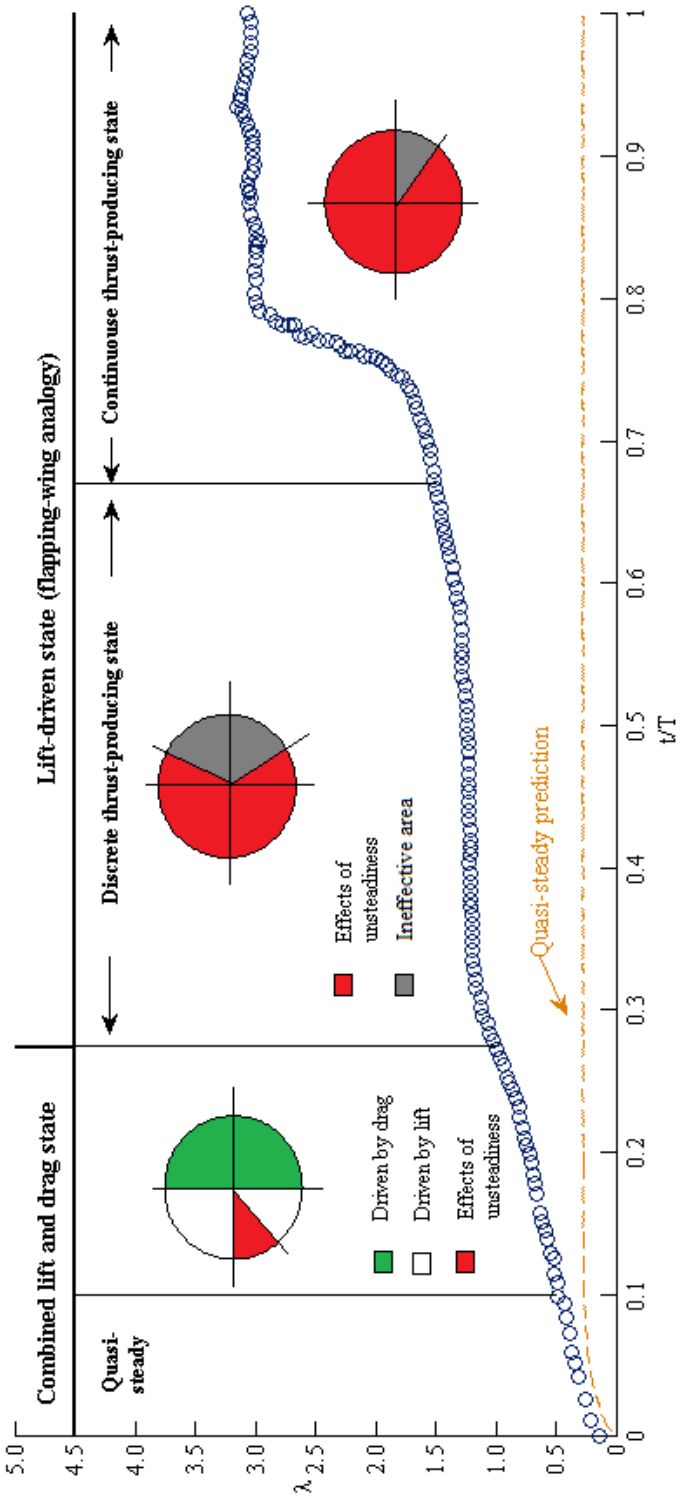

Figure 9.13: A summary of Darrieus turbine starting behaviour.

Rotor morphology

As suggested by the analogy that rotor geometry such as chord-to-diameter ratio (c/D) and blade aspect ratio (AR) seems to have an influence on the turbine ability to start, a parametric study was conducted in this section to explore this in detail.

The investigation was made by defining rotors to have diameters of 0.5, 0.75, and 1.0m and spans of 0.3 to 1.2 (Fig. 9.14). The blade chord length (c) will be changed to obtain c/D ratios of 0.05, 0.10, 0.12, and 0.14. It is noted that, for a specific diameter and span, the c/D and AR are connected and a modification of one parameter will affect the value of another. For example, for a diameter of 0.5 and a span of 1.0, a chord length of 0.025 gives a c/D ratio of 0.05 and a AR of 40. If the chord length is modified to be 0.05, the c/D ratio will be increased to 0.10 and the AR will be decreased to 20. Different span lengths were simulated to cover a wider range of blade aspect ratio (between 4.29 to 40).

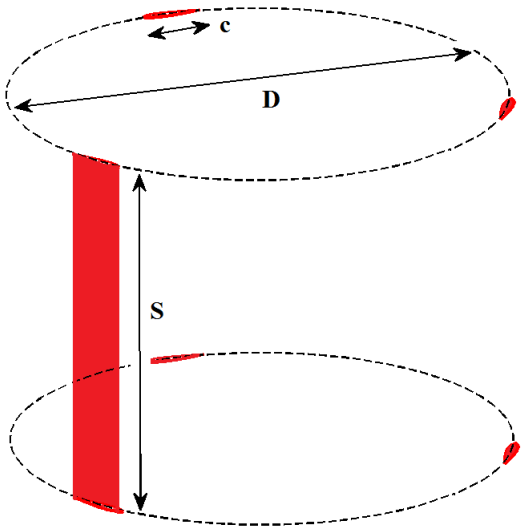

Figure 9.14: Rotor geometry.

All simulations were performed at a wind speed of 6 m/s. Blade material is assumed to be the same as that of Hill et al rotor [10]. Table 9.2 lists c/D and AR ratios from the predefined rotor geometry. It also presents calculated rotor inertia (J), steady tip speed ratios that the rotors reach (λ), and time that the rotors take (T_S). The maximum simulation time is 200 second and any rotor that can accelerate out of the plateau within this simulation time is marked as self-starting.

Table 9.2: Effects of rotor geometry on self-starting capability.

Case	c **(m)**	D **(m)**	S **(m)**	c/D	AR	S/D	J	λ	T_S **(s)**	**Self-starting**
1	0.025	0.50	0.30	0.05	12.0	0.60	0.0024	0.00	≥ 200	×
2	0.050	0.50	0.30	0.10	6.00	0.60	0.0024	0.50	≥ 200	×
3	0.060	0.50	0.30	0.12	5.00	0.60	0.0029	0.00	≥ 200	×
4	0.070	0.50	0.30	0.14	4.29	0.60	0.0034	0.00	≥ 200	×
5	0.025	0.50	0.40	0.05	16.0	0.80	0.0024	0.00	≥ 200	×
6	0.050	0.50	0.40	0.10	8.00	0.80	0.0032	0.50	≥ 200	×
7	0.060	0.50	0.40	0.12	6.67	0.80	0.0039	3.22	100	✓
8	0.070	0.50	0.40	0.14	5.71	0.80	0.0045	3.47	50	✓
9	0.025	0.50	0.50	0.05	20.0	1.00	0.0024	0.00	≥ 200	×
10	0.050	0.50	0.50	0.10	10.0	1.00	0.0040	0.50	≥ 200	×
11	0.060	0.50	0.50	0.12	8.33	1.00	0.0048	3.27	95	✓
12	0.070	0.50	0.50	0.14	7.14	1.00	0.0056	3.46	50	✓
13	0.025	0.50	0.80	0.05	32.0	1.60	0.0032	0.00	≥ 200	×
14	0.050	0.50	0.80	0.10	16.0	1.60	0.0064	0.52	≥ 200	×
15	0.060	0.50	0.80	0.12	13.3	1.60	0.0077	3.35	80	✓
16	0.070	0.50	0.80	0.14	11.4	1.60	0.0090	3.60	40	✓
17	0.025	0.50	1.00	0.05	40.0	2.00	0.0040	0.00	≥ 200	×
18	0.050	0.50	1.00	0.10	20.0	2.00	0.0080	0.52	≥ 200	×
19	0.060	0.50	1.00	0.12	16.7	2.00	0.0096	3.35	80	✓
20	0.070	0.50	1.00	0.14	14.3	2.00	0.0112	3.50	40	✓
21	0.025	0.75	0.50	0.05	20.0	0.67	0.0045	0.00	≥ 200	×
22	0.075	0.75	0.50	0.10	6.67	0.67	0.0136	0.57	≥ 200	×
23	0.090	0.75	0.50	0.12	5.56	0.67	0.0163	0.00	≥ 200	×
24	0.105	0.75	0.50	0.14	4.76	0.67	0.0902	0.00	≥ 200	×
25	0.025	0.75	0.60	0.05	24.0	0.80	0.0054	0.00	≥ 200	×
26	0.075	0.75	0.60	0.10	8.00	0.80	0.0163	0.57	≥ 200	×
27	0.090	0.75	0.60	0.12	6.67	0.80	0.0195	3.28	85	✓
28	0.105	0.75	0.60	0.14	5.71	0.80	0.0228	1.86	60	✓
29	0.025	0.75	0.75	0.05	30.0	1.00	0.0068	0.00	≥ 200	×
30	0.075	0.75	0.75	0.10	10.0	1.00	0.0203	0.57	≥ 200	×
31	0.090	0.75	0.75	0.12	8.33	1.00	0.0244	3.28	85	✓
32	0.105	0.75	0.75	0.14	7.14	1.00	0.0285	1.86	80	✓
33	0.025	0.75	0.90	0.05	36.0	1.20	0.0081	0.00	≥ 200	×
34	0.075	0.75	0.90	0.10	12.0	1.20	0.0244	0.57	≥ 200	×
35	0.090	0.75	0.90	0.12	10.0	1.20	0.0293	3.28	85	✓
36	0.105	0.75	0.90	0.14	8.57	1.20	0.0342	1.87	70	✓
37	0.050	1.00	0.60	0.05	12.0	0.60	0.0193	0.00	≥ 200	×
38	0.100	1.00	0.60	0.10	6.00	0.60	0.0386	0.45	≥ 200	×
39	0.120	1.00	0.60	0.12	5.00	0.60	0.0463	0.00	≥ 200	×
40	0.140	1.00	0.60	0.14	4.29	0.60	0.0540	0.00	≥ 200	×
41	0.050	1.00	0.80	0.05	16.0	0.80	0.0257	0.00	≥ 200	×
42	0.100	1.00	0.80	0.10	8.00	0.80	0.0514	0.45	≥ 200	×
43	0.120	1.00	0.80	0.12	6.67	0.80	0.0617	1.11	≥ 200	×
44	0.140	1.00	0.80	0.14	5.71	0.80	0.0720	0.81	≥ 200	×
45	0.050	1.00	1.00	0.05	20.0	1.00	0.0321	0.00	≥ 200	×
46	0.100	1.00	1.00	0.10	10.0	1.00	0.0643	0.43	≥ 200	×
47	0.120	1.00	1.00	0.12	8.33	1.00	0.0771	1.11	≥ 200	×
48	0.140	1.00	1.00	0.14	7.14	1.00	0.0900	0.81	≥ 200	×
49	0.050	1.00	1.20	0.05	24.0	1.20	0.0386	0.00	≥ 200	×
50	0.100	1.00	1.20	0.10	12.0	1.20	0.0771	0.43	≥ 200	×
51	0.120	1.00	1.20	0.12	10.0	1.20	0.0925	1.11	≥ 200	×
52	0.140	1.00	1.20	0.14	8.57	1.20	0.1080	0.81	≥ 200	×

It can be seen from the Table that the rotor geometry has an impact on the rotor ability to start. In general, any rotor that has a small c/D ratio of 0.05 will not start whatever the value of blade aspect ratio is; a direct result of the small chord

length that leads to a small Reynolds number when stationary. With an increment of the c/D ratio from 0.05 to 0.10, the Reynolds number is sufficiently high and the rotor will be able to generate an amount of torque and manages to start spinning. This sufficiently high Reynolds is critical since if the Reynolds number is too low, the aerofoil will suffer performance degradation (for example, lift curve slope will be significantly reduced in comparison to a high Reynolds number [44], leading to a very small amount of torque). The rotor, however, cannot take off to its final tip speed ratio (see case 2, for example) as the level of unsteadiness created by this c/D ratio is still low (around 0.033) and the additional, unsteady thrust is not effectively generated.

With a sufficiently high c/D ratio of 0.12, the reduced frequency increases and unsteady thrust is generated. This unsteady thrust drives the rotor through the startup period and the rotor manages to take off to its steady, operating tip speed ratio of around 3. A further increase of c/D ratios to 0.14 shortens the blade aspect ratio and the time that the rotor takes to take off is decreased (compare cases 11 and 12, for example). It is also observed that rotors that have too small span length will not start although the c/D ratio is high (cases 3 and 4).

With increasing diameter, the rotor tends to have a difficulty to start. This increase poses two effects to the rotor. Firstly, it increases the rotor inertia (recall that $J = \frac{mD^2}{4}$) and, at a certain value of diameter, rotors will fail to start (cases 37 to 52). Secondly, in the view of flapping, the large diameter causes a large stroke amplitude which leads to a slow rate of flapping.

The distance that the blade has to travel to begin a new stroke can be calculated from

$$D_f = \frac{\pi D}{B} - c \tag{9.30}$$

where D is diameter, B is number of blade, and c is the aerofoil chord.

Rotors in cases 7 and 39, which have the same c/D ratio of 0.12, have D_f values of 0.473m and 0.927m, respectively. This indicates that the blade in the latter case has to travel at a longer distance to enter the area where thrust is generated.

Based upon the simulation results, self-starting rotors are in the following ranges:-

$$0.5 \leq D \leq 0.75 \tag{9.31}$$

$$0.12 \leq c/D \leq 0.14 \tag{9.32}$$

$$5.71 \leq AR \leq 16.7 \tag{9.33}$$

It is worth noting however that all of the simulated rotors have a comparatively low inertia and this undoubtedly promotes the ability to start. For a given amount of thrust, a rotor with the low inertia can be easier sped up (a faster increase in the

rotational speed and reduced frequency ($\omega c/2V$)), leading to a further generation of unsteady thrust. With the diverse use of material, the rotor configuration that has the ability to start can be significantly changed.

9.4.2 System performance

The starting performance of the entire system (or the effect of the generator and the load on the turbine starting capability) can be easily observed by plotting the Darrieus torque characteristic together with resistive torque posed by the generator and the load. (Fig. 9.15). As seen, if the cogging torque is high, the net torque can be negative in the first two regions (first acceleration and plateau) and the turbine will be locked. Reduction of this cogging torque will undoubtedly promote the turbine ability to start. Development of a special generator is extremely useful, particulary the generator that has no cogging torque [4].

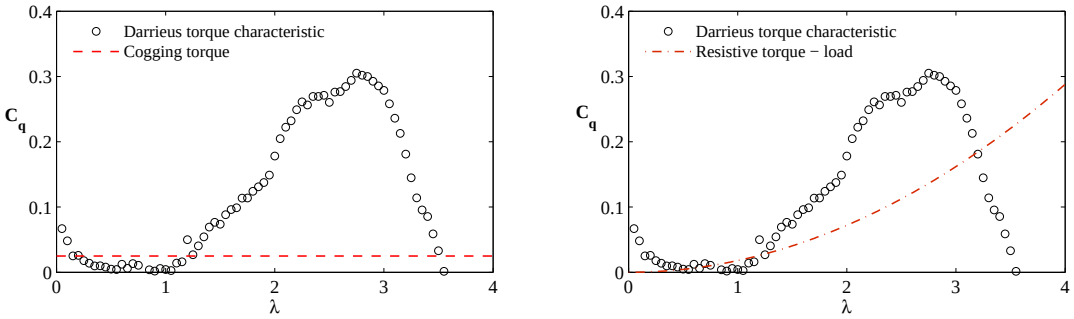

Figure 9.15: Cogging and resistive torques.

In addition to the cogging torque, the resistive torque created by the load is also of importance. As already seen in Chapter 3, different loads pose different resistive torque characteristics and if the resistive torque is increased too quickly (this resistive torque is often found in resistive heating; the magnitude depends on its resistive value) the net torque will be negative. Careful matching between the turbine and the load undoubtedly helps to promote the turbine's ability to self-start.

9.5 Self-starting definition

The investigations conducted so far also raises a question of how the self-starting should be defined. Previous researchers had defined that the turbine is self-starting when it can accelerate from rest to the point that a significant power has been produced [6,170]. This definition is load-dependent and the term 'significant power' is imprecise.

There exist circumstances that power can be generated while the machine has not reached its 'real' operation yet. One of the clearest case is resistive heating cases in which heat will be generated as soon as the machine spins. With the resistive

torque that increases continuously with increasing tip speed ratio, it is likely that the net torque will be small or even negative at the tip speed ratio of around 1 and the turbine will not further accelerate (Fig. 9.15). Under this condition, the turbine has not reached its real operation but can produce some power. As a consequence, the self-starting should not be defined in terms of power.

Another specific definition had been proposed in terms of tip speed ratio. Lunt [171] defined that the machine is deemed to have started if it has accelerated from rest to a condition where the blade operates at a steady speed that exceeds the wind speed (tip speed ratio of 1) as he believed that the machine will further accelerate once the machine has been driven by lift. However, this present investigation has shown that, although the blade operation has shifted from the combined lift- and drag-driven to fully lift-driven at this tip speed ratio, the torque coefficient is the 'lowest' and the machine is prone to be locked in the deadband. The change from combined to full lift-driven state is then not a guarantee that the machine will continue to accelerate.

One of the possible definitions is to cover the whole process and the turbine is said to be self-starting when it can accelerate from the rest to its final operating tip speed ratio. The final operating tip speed ratio, however, depends on a number of parameters such as free-stream wind speed, rotor configuration, aerofoil employed, and the load that the machine is connected to. Wind tunnel investigations by Reynolds [172] has shown that, for a specific rotor configuration (the rotor tested is the same as that tested by Hill et al [10]), the final tip speed ratio increases with increasing free-stream wind speed (increased aerodynamic torque). It also decreases with increasing resistive load as it poses more resistive torque for the turbine to overcome and the new equilibrium occurs at a lower tip speed ratio. In essence, the resistive load will make the turbine reach a lower tip speed ratio where the incidence range is higher (Fig. 9.16). With increasing resistive torque, the operating tip speed ratio decreases and, if the resistive torque is too high, the machine will fall into the deadband; the region where thrust is discrete and is not the real operation of the turbine.

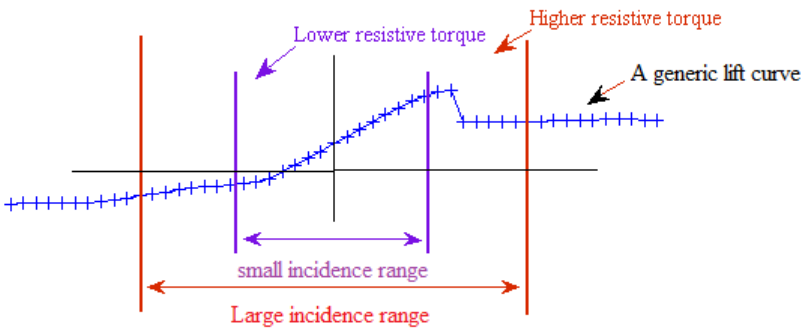

Figure 9.16: Effect of resistive load on the steady-state, operating tip speed ratio.

In the light of this information, an H-Darrieus turbine is said be self-starting if:-

"The turbine can accelerate from rest to the tip speed ratio that thrust is continuously generated over the Darrieus flight path. Its final operating tip speed ratio will be an equilibrium point where aerodynamic and resistive torques match."

9.6 Conclusions

Self-staring behaviour of the H-Darrieus turbine had been investigated in this chapter through the simple pitch-heave concept. A consideration of bird flight has also made to identify required performance of the Darrieus blade over the Darrieus flight path. The consideration suggests that the aerofoil blade must be able to produce thrust during downstroke operation (or reversed camber operation). It should also exhibits less negative thrust during upstroke in order to promote more continuous generation of thrust.

Performance comparison of different aerofoils has been made and it was found that the aerofoil shape is vitally important, particularly the leading edge shape. It was also found that aerofoils with high percent of camber will lose its effectiveness in producing forward thrust when operating in the reversed camber operation and the conventional, symmetrical aerofoil sections such as the NACA0015 and NACA0018 are still a simple and attractive choice.

Incorporation of dynamic performance into the performance modelling has improved the prediction of Darrieus turbine self-starting behaviour, stressing the importance of transient behaviour which cannot be neglected. The difference between the predictions using quasi-steady and transient approximations has also indicated that the unsteadiness associated with the rotor can be exploited to promote the turbine ability to self-start. The analogy suggests that the level of unsteadiness is governed by the rotor geometry.

The investigations presented here strongly indicate that the H-Darrieus turbine has a potential to self-start. However, it depends upon a number of issues including the understanding of rotor aerodynamics, the development of strong and lightweight materials, the development of generator technology, and the suitable matching between the rotor and the load. It is therefore understandable why it is commonly believed that this type of turbine cannot self-start.

Chapter 10

Conclusions and Recommendations

The ultimate aim of this thesis is to get insight into how small wind turbines (both horizontal- and vertical-axis) behave during start-up and what benefits that can be obtained from the improved starting. In order to achieve this, a series of measurements and simulations have been carried out. This chapter concludes the main findings and give recommendations for future work.

10.1 Conclusions

10.1.1 Effects of Improved starting capability on energy yield

A complete study on the entire horizontal-axis wind turbine generation system has been undertaken to estimate potential benefits of improved starting. Comparisons of three different blade configurations reveal that the use of mixed-aerofoil blades leads to a significant increase in starting capability. Generally, the improved starting capability reduces the time that the turbine takes to reach its power-extraction period and, hence, an increase in overall energy yield. The increase can be as high as 40%.

10.1.2 Starting behaviour of small horizontal-axis wind turbines

The starting behaviour of the horizontal axis wind turbine consists of two processes: idling and rapid acceleration. The rotational speed slowly increases in the first region as the blade experiences low Reynolds number and high incidence angle. This process continues until the Reynolds number is sufficiently high and the incidence angle is low. Here, the turbine accelerates rapidly to a steady, operating tip speed ratio.

10.1.3 Starting behaviour of small H-Darrieus wind turbines

Careful consideration of flow conditions that the Darrieus blade experiences when moving along its axis has shown that there is analogy between the aerofoil in Darrieus motion and flapping-wing mechanism. This analogy, together with a consideration of flapping creatures, suggests that the unsteadiness (or transient behaviour) associated with the blade motion is the key to resolve discrepancy between experiments and quasi-steady based theory. This present work has shown that the accurate prediction of the starting behaviour can be made only if the transient aerofoil behaviour is incorporated into the model.

Darrieus turbine starting behaviour consists of three processes: first acceleration, plateau, and second acceleration.

In the first acceleration period, the rotor is alternately driven by lift and drag; drag-driven is generated when the blade is in quadrant 4 and 1. This period can also be divided into quasi-steady approximation and transient states. The discrepancy between quasi-steady and transient predictions also suggests that the unsteadiness associated with the rotor can be exploited to generate additional thrust.

In the last two periods (flapping-wing analogy), the rotor is solely driven by lift. However, at the beginning of this period, the driving force is mainly generated by the blade in quadrant 3 where Reynolds number is comparatively high and incidence angle is small. The blade in quadrant 4 and 1 is ineffective in generating the driving force as it perceives very low Reynolds number and a large area of high incidence angle. This process continues until the Reynolds number is sufficiently high and the incidence angle is sufficiently low. Here, the rotor accelerates rapidly to a steady, operating tip speed ratio.

A parametric study on the effects of rotor geometry on the self-starting behaviour revealed that the chord-to-diameter ratio, and blade aspect ratio is an important factor to promote the generation of unsteady thrust. This ratio should be sufficiently high. Rotor diameter and number of blade are important as they determine how frequent that the unsteady thrust will be generated. The study also shows that the blade aspect ratio and rotor inertia is also of importance.

10.1.4 Aerofoil performance characteristics at low Reynolds numbers and high angles of attack

All of the investigations of turbine starting behaviour are based upon a new set of aerofoil performance data which were obtained at specific conditions. One of the main concerns in obtaining this kind of data is the effect of wall proximity which had been numerically investigated in this present work. The investigation confirms the existence of wall proximity.

Six aerofoils have been tested in this course of study at low Reynolds numbers (nominal 65,000, 90,000, and 150,000) through 360°. It was found that all aero-

foils demonstrate the formation of a leading-edge separation bubble that ultimately bursts leading to sudden stall. After stall, the lift drops to a sustained but lower value, the magnitude of which is dependent upon aerofoil geometry. For the symmetrical and low camber aerofoils, the lift then rises gradually to a second peak at about 50° incidence, but this increase is less apparent for the higher camber sections. The benefits of increased lift and more progressive stall from the cambered aerofoils are partly negated by a loss of performance arising from their reversed camber when they operate in an incidence angle of 180° to 360°. The drag characteristics of all geometries are comparable.

A comparison between these new data and the widely used Sheldahl and Klimas data [141] for the NACA section shows good agreement for the pre-stall region but discrepancies are observed in the deep-stall region that are consistent with Rainbirds hypothesis regarding the influence of wind tunnel test section geometry.

10.1.5 Unsteady aerofoil performance characteristics

Aerofoil performance characteristics were found to be significantly changed under dynamic conditions. The change depends on a number of parameters including aerofoil shape, mode of operation, incidence change, and reduced frequency. This change in transient flow characteristics is significant near stall and is negligible at very high incidence angles when the aerofoil is fully stalled.

A comparison of unsteady thrust of different aerofoils indicated that the increase in suction peak (and unsteady thrust) is greatly dependent on the leading edge shape of the aerofoil. The bird-like aerofoils which are highly cambered will lose this property when operating in the reversed mode of operation. It therefore cannot be used directly on Darrieus blades to improve the turbine starting capability.

10.1.6 Significant and original contributions

All in all, this thesis has furthered our understanding of wind turbine starting behaviour. This thesis has shown that starting capability is important and has a significant impact on the turbine performance and the overall energy output. This capability is normally ignored in wind turbine design and the benefits of improved starting performance has never been quantified.

This thesis proposes a new perspective on the analysis of Darrieus turbine self-starting capability by raising the idea of analogy between the aerofoil in Darrieus motion and flapping-wing mechanism. The idea had been applied to understand the complex starting behaviour of Darrieus turbines and has shed light on how the rotor configuration affects the turbine ability to start and how the aerofoil for Darrieus rotors can be improved. This information has never presented by previous research work.

All of the above contributions are supported by a great amount of aerofoil aerodynamic performance data which was tested at low Reynolds numbers, high incidence

angles, and high reduced frequencies. This kind of data is scarce in the literature.

10.2 Recommendations

10.2.1 Model improvement

Although the model developed can predict the H-Darrieus turbine starting behaviour reasonably well, there is still room for further improvement. One of the key assumptions of this present model is that each blade is aerodynamically independent. In reality, there exists an interaction between the wake generated by the blade upstream on the blade downstream. Incorporation of this effect will further improve the accuracy of the model.

10.2.2 Optimisation of aerofoil profile for Darrieus rotors

Optimisation of aerofoil geometry for the Darrieus rotor is also worth investigation. This optimisation is challenging as the aerofoil has to operate well for a wide range of flow conditions. Optimisation of an aerofoil for different flow conditions is complex in itself and normally made through a conformal-mapping method [173]. This is further complicated by unsteady flows as the aerofoil shape should be effective in exploiting the unsteadiness. CFD-based optimisation seems to be ideal for this complex task.

10.2.3 Experiments on tip effects

Further work can be conducted to investigate the effect of blade aspect ratio. Although the tip correction method used in this work gives reasonable results, it is likely that there might be a significant difference in tip loss, particularly when the blade aspect ratio becomes small. The incorporation of this aspect into the model will allow a more complete of parametric studies. The tip loss caused by different blade tips and the addition of aerodynamic devices such as flap are also worth investigation.

10.2.4 Rotor morphology

Since the Darrieus rotor configuration has an influence on the turbine ability to start and the final tip speed ratio that the turbine can reach, it would be useful to examine a rotor configuration that provide a good compromise between self-starting and energy-production performance.

10.2.5 Effects of atmospheric turbulence on H-Darrieus turbine performance

Wind tunnel and CFD investigations could be made to further explore the starting behaviour under real, turbulent environments.

References

[1] Global Wind Energy Council (2010), *Global Wind Power Boom Continues Despite Economic Woes*, [Online], Available from: http://www.gwec.net [Accessed: 04 June 2012].

[2] Wolrd Wind Energy Association (2008), *Wind Turbine Generates More than 1% of the Global Electricity*, Press release World Wind Energy Association.

[3] British Wind Energy Association (2012), *UKWED Statistics*, [Online], Available from: http://www.bwea.com/statistics/ [Accessed: 19 July 2012].

[4] Bumby, J., Stannard N., and Martin, R. (2006), *A Permanent Magnet Generator for Small Scale Wind Turbines*, Proceedings of the 17th International Conference on Electrical Machines, Chania, Crete, Greece.

[5] MacDonald, M. (2003), *The Carbon Trust & DTI Renewable Energy Network Impact Study Annex 1: Capacity Mapping & Market Scenarios for 2010 and 2020*, The Carbon Trust & DTI .

[6] Ebert, P.R., and Wood, D.H. (1999), *Observations of the Starting Behaviour of a Small Horizontal-axis Wind Turbine*, Journal of Renewable Energy, **12**, pp 245–257.

[7] Mayer, C., Bechly, M.E., Hampsey, M., and Wood, D.H. (1999), *The Starting Behaviour of a Small Horizontal-axis Wind Turbine*, Journal of Renewable Energy, **22**, pp 411–417.

[8] Chua, K.L. (2002), http://www.wind-turbineanalysis.netfirm.com [Accessed: 29 December 2010].

[9] Wright, A.K., and Wood, D.H. (2004), *The Starting and Low Wind Speed Behaviour of a Small Horizontal Axis Wind Turbine*, Journal of Wind Engineering and Industrial Aerodynamics, **92**, pp 1265–1279.

[10] Hill, N., Dominy, R., Ingram, G., and Dominy, J. (2008), *Darrieus Turbines: the Physics of Self-starting*, Proceedings of the Institution of Mechanical Engineers, Part A: Journal of Power and Energy, **223**, pp 21–29.

[11] Wood, D.H. (2001), *A Blade Element Estimation of the Cut-in Wind Speed of a Small Turbine*, Journal of Wind Engineering, **25(2)**, pp 125–130.

[12] Abbott, I.H., and Von Doenhoff, A.E. (1959), **Theory of Wing Sections: Including a Summary of Airfoil Data**, Dover Publications, New York.

[13] Selig, M.S., and McGranahan, B.D. (2004), *Wind Tunnel Aerodynamic Tests of Six Airfoils for Use on Small Wind Turbine Blades*, ASME Journal of Solar Energy Engineering, **126**, pp 986–1001.

[14] Timmer, W., and van Rooij, R. (2001), *Some Aspects of High Angle-of-attack Flow on Airfoils for Wind Turbine Application*, In the Proceedings of European wind energy conference "wind energy for new millennium", held in Copenhagen, Denmark, 2-6 July.

[15] Leishman, J.G. (2006), **Principles of Helicopter Aeodynamics**, Cambridge Aerospace Series.

[16] Ramsey R.R., and G.M. Gregorek (1999), *Effects of Grid Roughness and Pitch Oscillations on the S824 Airfoil*, National Renewable Energy Laboratory, The Ohio State University, NREL/TP-442-7817.

[17] Jones, G. (2010), *Global Warming, Sea Level Change and the Impact on Estuaries*, Marine Pollution Bulletin, **28(1)**, pp 7–14.

[18] United Nations (2003), *Kyoto Protocal to the United Nations Framework Convention on Climate Change*, United Nations.

[19] Darrieus, G.J.M. (1931), *Turbines Having Its Rotation Shaft Transverse to the Flow of the Current*, US. patent, No. 1835081.

[20] Worstell, M.H. (1982), *Aerodynamic Performance of the 17-Meter-Diameter Darrieus Wind Turbine in the Three-Bladed Configuration: An Addendum*, Sandia Laboratories, SAND79-1753

[21] Kooiman, S.J., and Tullis, S.W. (2010), *Response of a Vertical Axis Wind Turbine to Time Varying Wind Conditions Found within the Urban Environment*, Journal of Wind Engineering **34(4)**, pp 389–401.

[22] Howell, R., Qin, N., Edwards, J., and Durrani, N. (2010), *Wind Tunnel and Numerical Study of a Small Vertical Axis Wind Turbine*, Journal of Renewable Energy **35(2)**, pp 412–422.

[23] Martens, S., van Kuik, G., and van Bussel, G. (2003), *Performance of an H-Darrieus in the Skewed Flow on a Roof*, Journal of Solar Energy Engineering, **125(4)**, pp 433–440.

[24] Dominy, R., Lunt, P., Bickerdyke, A., and Dominy, J. (2007), *The Self-starting Capability of a Darrieus Turbine*, Proceedings of the Institution of Mechanical Engineers, Part A: Journal of Power and Energy, **221**, pp 111–120.

[25] Tangler, J.L., and Somers, D.M. (1995), *NREL Airfoil Families for HAWTs*, National Renewable Energy Laboratory, NREL/TP-442-7109.

[26] Manwell, J.F., McGowan, J.G., and Rogers, A.L. (2002), **Wind Energy Explained: Theory, Design and Application**, John Wiley & Son Ltd. Hopkins University Press Series.

[27] Hansen, A.D., Lov, F., Blaabjerg, F., and Hansen, L.H. (2004), *Review of Contemporary Wind Turbine Concepts and Their Market Penetration*, Journal of Wind Engineering, **28(3)**, pp 247–263.

[28] Giguere, P., Selig, M.S., and Tangler, J.L. (2004), *Blade design Trade-Offs Using Low-Lift Airfoils for Stall-Regulated HAWTs*, Journal of Solar Energy Engineering, **121**, pp 217–223.

[29] Giguere, P. and Selig, M.S. (2004), *New Airfoils for Small Horizontal Axis Wind Turbines*, ASME Journal of Solar Energy Engineering, **120**, pp 108–114.

[30] Migliore, P.G. and Fritschen, J.R. (1982), *Darrieus Wind Turbine Airfoil Configurations*, A subcontract report, Solar Energy Research Institute, SERU/TR-11045-1.

[31] Klimas, P.C. (1984), *Tailored Airfoils for Vertical Axis Wind Turbines*, Sandia National Laboratories, SAND84-1062.

[32] Berg, D.E. (1990), *Customised Airfoils and Their Impact on VAWT Cost of Energy*, Sandia National Laboratories, SAND90-1148C.

[33] Somers, D.M. (1994), http://www.airfoils.com/pubs1, [Accessed: 4 May 2012].

[34] Classens, M. (2006), *The Design and Testing of Airfoils for Application in Small Vertical Axis Wind Turbines*, Master Thesis, Faculty of Aerospace Engineering, Delft University of Technology.

[35] Islam, M., Ting, D.S.K., and Fartaj, A. (2007), *Design of a Special-Purpose Airfoil for Smaller-Capacity Straight-Bladed VAWT*, Journal of Wind Engineering, **31(6)**, pp 401–424.

[36] Dahl, K.S. and Fuglsang, P. (1998), *Design of the Wind Turbine Airfoil Family RISO-A-XX*, Riso National Laboratory, Riso-R-1024.

[37] Timmer, W.A. and van Rooij, R.P.J.O.M. (2003), *Summary of the Delft Universiy Wind Turbine Dedicated Airfoils*, The American Institute of Aeronautics and Astronautics, AIAA 2003-0352.

[38] Kelly, B., Tangler, J.L., Smith and Jager, D. (1992), *Measured and Predicted Rotor Performance for the SERI Advanced Wind Turbine Blades*, National Renewable Energy Laboratory, NREL/CP-500-28410.

[39] Thies, W. (1986), *Eppler-Profile*, Modell-Technik-berator, **120**, pp 108–114.

[40] Althaus, D. and Wortmann, F.X. (1981), *Stuttgarter Profilkatalog I*, Friedr. Vieweg & Sohn (Braunschweig).

[41] Selig, M.S., Donovan, J.F., and Fraser, D.B. (1989), *Airfoils at Low Speeds*, SoarTech 8, Technical Report.

[42] Somers, D.M. (1998), *The S822 and S823*, National Renewable Energy Laboratory, Riso-R-1024.

[43] UIUC Applied Aerodynamic Group (2010), http://www.ae.illinois.edu/m-selig/ads.html [Accessed: 4 June 2012].

[44] Selig, M.S., Guglielmo, J.J., Broeren, A.P., and Giguere, P. (1996), *Experiments on Airfoils at Low Reynolds Numbers*, 34th Aerospace Sciences Meeting & Exhibit, January 15-18, 1996, Reno, NV.

[45] Selig, M.S. (2003), *Low Reynolds Number Airfoil Design*, Low Reynolds Number Aerodynamics on Aircraft Including Applications in Emerging UAV Technology (VKI Lectures Series, RTO/AVT-KVI-104), von Karman Institute for Fluid Dynamics, Rhode-St-Gene‘se, Belgium.

[46] Selig, M.S., Guglielmo, J.J., Broeren, A.P., and Giguere, P. (1995), **Summary of Low-Speed Airfoil Data**, Vol. 1, SoarTech Publications, Virginia Beach, VA.

[47] Selig, M.S., Lyon, C.A., Giguere, P., Ninham, C.N., and Guglielmo, J.J. (1996), **Summary of Low-Speed Airfoil Data**, Vol. 2, SoarTech Publications, Virginia Beach, VA.

[48] Lyon, C.A., Broeren, A.P., Giguere, P., Gopalarathnam, A., and Selig M.S. (1998), **Summary of Low-Speed Airfoil Data**, Vol. 3, SoarTech Publications, Virginia Beach, VA.

[49] Loftin, L.K. (1954), *Airfoil Section Characteristics at High Angles of Attack*, National Advisory Committee for Aeronautics, NACA-TN-3241.

[50] Critzos, C.C., Heyson, H.H., Boswinkle, R.W. (1955), *Aerodynamic Characteristics of NACA 0012 Airfoil Section at Angles of Attack from* 0° *to* 180° , National Advisory Committee for Aeronautics, NACA-TN-3361.

[51] Sheldahl, R.E. and Klimas, P.C. (1981), *Aerodynamic Characteristics of Seven Symmetrical Airfoil Sections through 180-degree Angle of Attack for Use in Aerodynamic Analysis of Vertical Axis Wind Turbines*, National Renewable Energy Laboratory, SAND80-2114.

[52] Ostowari, C., and Naik, D. (1984), *Post-stall Studies of Untwisted Varying Aspect Ratio Blades with an NACA 4415 Airfoil Section - Part I*, Journal of Wind Engineering, **8(3)**, pp 176–194.

[53] Ostowari, C., and Naik, D. (1985a), *Post-stall Studies of Untwisted Varying Aspect Ratio Blades with an NACA 44XX Airfoil Section - Part II*, Journal of Wind Engineering, **9(3)**, pp 149–164.

[54] Ostowari, C., and Naik, D. (1985b), *Post-stall Wind Tunnel Data for NACA 44XX Series Airfoil Sections*, Texas A&M University.

[55] Mallon, K.J. (1992), *The NACA0018-64 Aerofoil at Low Reynolds Numbers with Application to Vertical Axis Wind Turbins - Including Turbulence Stimulation*, 11th Australasian Fluid Mechanics Conference, University of Tasmania, Hobart, Australia, 14-18 December.

[56] Timmer, W.A. (2010), *Aerodynamic Characteristics of Wind Turbine Blade Airfoils at High Angles-of-Attack*, In the Proceedings of Conference Torque 2010, The Science of Making Torque from the Wind, June 28-30, Crete, Greece.

[57] Bickerdyke, A. (2005), *The Aerodynamic Development of a Vertical Axis Wind Turbine*, M.Eng Thesis, School of Engineering, University of Durham.

[58] Rainbird, J. (2007), *The Aerodynamic Development of a Vertical Axis Wind Turbine*, M.Eng Thesis, School of Engineering, University of Durham.

[59] Crone, B. (2009), *The Aerodynamic Development of a Vertical Axis Wind Turbine*, M.Eng Thesis, School of Engineering, University of Durham.

[60] Viterna, L. and Corrigan, R. (1982), *Fixed Pitch Rotor Performance of Large Horizontal Axis Wind Turbines*, DOE/NASA Workshop on Large Horizontal Axis Wind Turbines, Cleaveland, Ohio.

[61] Lindenberg, C. (2001), *Stall Coefficients: Aerodynamic airfoil coefficients at large angles of attack*, ECN-RX- 01-004, ECN.

[62] Laino, D. (2005), *Foilcheck: A utility for creating aerodynamic input files for AeroDyn-based program*, National Renewable Energy Laboratory.

[63] Spera, D. (2008), *Models of Lift and Drag Coefficients of Stalled and Unstalled Airfoils in Wind Turbines and Wind Tunnels*, National Aeronautics and Space Administration, NASA/CR- 2008-215434.

[64] Timmer, W. and van Rooij, R. (2001), *The Performance of New Wind Turbine Blade Tip and Root Airfoils up to High Angles-of-attack*, Delft University of Technology, In Proceedings of the 2001 European wind energy conference, July 2001, Copenhagen. pp. 26.

[65] Webster, B.T. (1978), *An Experimental Study of An Airfoil Undergoing Cycloidal Motion*, MSc. Thesis, Mechanical Engineering Department, Texas Tech University.

[66] Graham, G.M. (1982), *Measurement of Instantaneous Pressure Distributions and Blade Forces on An Airfoil Undergoing Cycloidal Motion*, MSc. Thesis, Mechanical Engineering Department, Texas Tech University.

[67] Vittecoq, A. and Laneville, P. (1983), *The Aerodynamic Forces for a Darrieus Rotor with Straight Blades: Wind tunnel measurements*, Journal of Wind Engineering and Industrial Aerodynamics, **15**, pp 381–388.

[68] Fujisawa, N., and Takeuchi, M. (1998), *Flow Visualization and PIV Measurement of Flow Field around a Darrieus Rotor in Dynamic Stall*, Journal of Visualization, **1(4)**, pp 379–386.

[69] Shibuya, S., Fujisawa, N, and Takano, T. (1999), *Visualization and PIV Measurement of Unsteady Flow Around a Darrieus Wind Turbine in Dynamic Stall*, 7th International Conference on Nuclear Engineering, Tokyo, Japan, April, 19-13.

[70] Fujisawa, N., and Shibuya, S. (2001), *Observations of Dynamic Stall on Darrieus Wind Turbine Blades*, Journal of Wind Engineering and Industrial Aerodynamics, **89(2)**, pp 201–204.

[71] Ferreira, C.S., Bussel, G., Scarano, F., and Kuik, G. (2008), *PIV Visualization of Dynamic Stall VAWT and Blade Load Determination*, 46th AIAA Aerospace Sciences Meeting and Exhibit, 7-10 January 2008, Reno, Nevada, AIAA-2008-1317.

[72] Ferreira, C.S., Bussel, G., Kuik, G., and Scarano, F. (2008), *Visualization by PIV of Dynamic Stall on a Vertical Axis Wind Turbine*, Journal of Experiments in Fluids, **46(1)**, pp 97–108.

[73] Migliore, P.G., Wolfe, W.P., and Fanucci, J.B. (1980), *Flow Curvature Effects on Darrieus Turbine Blade Aerodynamics*, Journal of Energy, **40(2)**, pp 49–55.

[74] Ham, N.D. (1968), *Aerodynamic Loading on a Two-dimensional Airfoil during Dynamic Stall*, AIAA journal, **6**, pp 1927–1934.

[75] Carr, L.W., McAlister, K.W., and McCroskey, W.J. (1977), *Analysis of the Development of Dynamic Stall Based on Oscillating Airfoil Experiments*, National Aeronautics and Space Administration, NASA TN D-8382.

[76] McAlister, K.W., Carr, L.W., and McCroskey, W.J. (1977), *Dynamic Stall Experiments on the NACA 0012 Airfoil*, National Aeronautics and Space Administration, NASA TN D-8382.

[77] McCroskey, W.J., McAlister, K.W., Carr, L.W., and Pucci, S.L. (1982), *An Experimental Study of Dynamic Stall on Advanced Airfoil Sections-Volume 1 - Summary of the Experiment*, National Aeronautics and Space Administration, NASA-TM-84252.

[78] Lieshman, J.G. (1999), *Dynamic Stall Experiments of the NACA 23012 Aerofoil*, Journal of Experiments in Fluids, **9**, pp 49–58.

[79] Reuss, R.L., Hoffman M.J., and Gregorek, G.M. (1995), *Effects of Grid Roughness and Pitch Oscillations on the LS(1)-0421MOD Airfoil*, National Renewable Energy Laboratory, NREL/TP-442-6473.

[80] Janiszewska, J.M., Ramsay, R.R., and Hoffman, M.J., and Gregorek, G.M. (1996a), *Effects of Grid Roughness and Pitch Oscillations on the LS(1)-0417MOD Airfoil*, National Renewable Energy Laboratory, NREL/TP-442-7819.

[81] Hoffman, M.J., Reuss, R.L., and Gregorek, G.M. (1996), *Effects of Grid Roughness and Pitch Oscillations on the NACA 4415 Airfoil*, National Renewable Energy Laboratory, NREL/TP-442-7815.

[82] Ramsey, R.R., Hoffman, M.J., and Gregorek, G.M. (1996), *Effects of Grid Roughness and Pitch Oscillations on the S801 Airfoil*, National Renewable Energy Laboratory, NREL/TP-442-7818.

[83] Ramsey, R.R., Hoffman, M.J., and Gregorek, G.M. (1995), *Effects of Grid Roughness and Pitch Oscillations on the S809 Airfoil*, National Renewable Energy Laboratory, NREL/TP-442-7817.

[84] Ramsey R.R., Hoffman M.J., and Gregorek, G.M. (1999), *Effects of Grid Roughness and Pitch Oscillations on the S810 Airfoil*, National Renewable Energy Laboratory, The Ohio State University, NREL/TP-442-7816.

[85] Ramsey R.R., Hoffman M.J., and Gregorek, G.M. (1999), *Effects of Grid Roughness and Pitch Oscillations on the S812 Airfoil*, National Renewable Energy Laboratory, The Ohio State University, NREL/SR-440-8167.

[86] Ramsey R.R., and Gregorek, G.M. (1999), *Effects of Grid Roughness and Pitch Oscillations on the S813 Airfoil*, National Renewable Energy Laboratory, The Ohio State University, NREL/TP-442-8168.

[87] Janiszewska, J.M., Ramsay, R.R., Hoffman, M.J., and Gregorek, G.M. (1996b), *Effects of Grid Roughness and Pitch Oscillations on the S814 Airfoil*, National Renewable Energy Laboratory, NREL/TP-442-8161.

[88] Ramsey R.R., Hoffman M.J., and Gregorek, G.M. (1999), *Effects of Grid Roughness and Pitch Oscillations on the S815 Airfoil*, National Renewable Energy Laboratory, The Ohio State University, NREL/TP-442-7820.

[89] Ramsey R.R., Janiszewska M.G., and Gregorek, G.M. (1999), *Effects of Grid Roughness and Pitch Oscillations on the S825 Airfoil*, National Renewable Energy Laboratory, The Ohio State University.

[90] Fuglsang, P., Antonio, I., Bak, C., and Madsen, H.A. (1996b), *Wind Tunnel Tests of the Riso-1 Airfoil*, Riso National Laboratory, Riso-R-999.

[91] Fuglsang, P., Antonio, I., Dahl, K.S., and Madsen, H.A. (1998), *Wind tunnel tests of the FFA-W3-241, FFA-W3-301, and NACA 63-430 Airfoils*, Riso National Laboratory, Riso-R-041.

[92] Bak, C., Fuglsang, P., Johansen, J., and Antonio, I. (2000), *Wind tunnel tests of the NACA 63-415 and a Modified NACA 63-415 Airfoil*, Riso National Laboratory, Riso-R-1193.

[93] Fuglsang, P., Antonio, I., Sorensen, N., and Madsen, H.A. (1998), *Validation of a Wind Tunnel Testing Facility for Blade Surface Pressure Measurements*, Riso National Laboratory, Riso-R-981.

[94] Fuglsang, P., Dahl, K.S., and Antoniou, I. (1999), *P. Wind Tunnel Tests of the Riso-A1-18, Riso-A1-21, and Riso-A1-24 Airfoils*, Riso National Laboratory, Riso-R-1112(EN).

[95] Fuglsang, P., Bak, C., Gaunaa, M., and Antonio, I. (2003), *Wind Tunnel Tests of the Riso-B1-18 and Riso-B1-24*, Riso National Laboratory, Riso-R-1375.

[96] Gerontakos, P. (2004), *An Experimental Investigation of Flow Over an Oscillating Airfoil*, M.Eng Thesis, Department of Mechanical Engineering, McGill University.

[97] Gormont, R.E. (1973), *A Mathematical Model of Unsteady Aerodynamics and Radial Flow for Application to Helicopter Rotors*, USAAMRDL.

[98] Johnson, W. (1974), *Comparison of Three Methods for Calculation of Helicopter Rotor Blade Loading and Stress due to Stall*, National Aeronautics and Space Administration, NASA TN D-7833.

[99] Beddoes, T.S. (1976), *A Synthesis of Unsteady Aerodynamic Effects Including Stall Hysteresis*, Vertica, **1**, pp 113–123.

[100] Tran, C.T., and Petot, D. (1981), *Semi-empirical Model for the Dynamic Stall of Airfoil in View of the Application to the Calculation of Response of a Helicopter Blade in Forward Flight*, Vertica, **5**, pp 35–53.

[101] Gangwani, S.T. (1983), *Synthesized Airfoil Data Method for Prediction of Dynamic Stall and Unsteady Airloads*, National Aeronautics and Space Administration, NASA Contractor Report 3672.

[102] Leishman, J.G. and Beddoes, T.S. (1989), *A Semi-Empirical Model for Dynamic Stall*, Journal of the American Helicopter Society, **34(3)**, pp 3–17.

[103] Pierce, K.G. (1996), *Wind Turbine Load Prediction Using the Beddoes-Leishman Model for Unsteady Aerodynamics and Dynamic Stall*, MSc Thesis, Department of Mechanical Engineering, The University of Utah.

[104] Hansen, M.H., Gaunaa, M., and Hansen, H.A. (2004), *A Beddoes-Leishman type Dynamic Stall Model in State-space and Indicial Formulations*, Riso National Laboratory, Riso-R-1354.

[105] Gupta, S. and Leishman, J.G. (2006), *Dynamic Stall Modelling of the S809 Aerofoil and Comparison with Experiments*, Journal of Wind Energy, **9**, pp 521–547.

[106] Sheng, W., Galbraith, R.A. McD., and Coton, F.N. (2006), *A New Stall-Onset Criterion for Low Speed Dynamic Stall*, ASME Journal of Solar Energy Engineering, **128(4)**, pp 461–471.

[107] Sheng, W., Galbraith, R.A. McD., and Coton, F.N. (2008), *A Modified Dynamic Stall Model for Low Mach Numbers*, ASME Journal of Solar Energy Engineering, **130(3)**, pp 461–471.

[108] Sheng, W., Galbraith, R.A. McD., and Coton, F.N. (2010), *Applications of Low-Speed Dynamic-Stall Model to the NREL Airfoils*, ASME Journal of Solar Energy Engineering, **132**, pp 461–471.

[109] Worasinchai, S., Ingram, G.L., and Dominy, R.G. (2012), *Effects of Wind Turbine Starting Capability on Energy Yield*, ASME Journal of Engineering for Gas Turbines and Power, **134(4)**, 9 pages.

[110] Burton, T., Sharpe, D., Jenkins, N., and Bossanyi, E. (2001), **Wind Energy Handbook**, John Wiley & Sons Ltd.

[111] National Wind Technology Center (2003), *Wind Turbine Generator System Power Performance Test Report for the Bergey Excel-S/60 Wind Turbine with*

BW03 Airfoil Blades, National Renewable Energy Laboratory, NREL/EL-500-33450.

[112] National Wind Technology Center (2003), *Wind Turbine Generator System Power Performance Test Report for the Bergey Excel-S/60 Wind Turbine with SH3052 Airfoil Blades*, National Renewable Energy Laboratory, NREL/EL-500-33452.

[113] Selig, M.S. (2003), *Low Reynolds Number Airfoil Design*, Low Reynolds Number Aerodynamics on Aircraft Including Applications in Emerging UAV Technology (VKI Lectures Series, RTO/AVT-KVI-104), von Karman Institute for Fluid Dynamics, Rhode-St-Gene'se, Belgium.

[114] Muljadi, E. and Green, J. (2002), *Cogging Torque Reduction in a Permanent Magnet Wind Turbine Generator*, National Renewable Energy Laboratory, NREL/CP-500-30768.

[115] Lu, K., Rasmussen, P.O., and Ritchie, E. (2006), *An Analytical Equation for Cogging Torque Calculation in Permanent Magnet Motors*, Proceedings of the 17th International Conference on Electrical Machines, Chania, Crete, Greece.

[116] Miwa,M., and Dibben, D. (2004), *High Accuracy Torque Calculation for a Rotating Machine Using Adaptive Meshing*, IEEE Transactions on Magnetic, **120**, pp 108–114.

[117] Berges, B. (2007), *Development of Small Wind Turbines*, M.Sc. Thesis, Department of Mechanical Engineering, Technical University of Denmark.

[118] Stannard, N. (2008), *Generator Design for, and Modelling of, Small-scale Wind Turbines*, Ph.D. Thesis, School of Engineering, University of Durham.

[119] Hails, D. (2011), *Private communication.*

[120] Bumby, J. (2010), *Lecture Notes: Small Scale Wind Turbines*, School of Engineering and Computing Sciences, University of Durham, UK.

[121] Seguro, J.V. and Lambert, T.W. (2000), *Modern Estimations of the Parameters of the Weibull Wind Speed Distribution for Wind Energy Analysis*, Journal of Wind Engineering and Industrial Aerodynamics, **85(1)**, pp 75–84.

[122] Worasinchai, S., Ingram, G.L., and Dominy, R.G. (2012), *The Physics of H-Darrieus Turbine Self-starting Capability: Flapping-wing perspective*, GT2012-69075: ASME Turbo Expo 2012, June 11-15, 2012, Copenhagen, Denmark.

[123] Dickinson, M.H., Lehmann, F., and Sane S.P. (1999), *Wing Rotation and the Aerodynamic Basis of Insect Flight*, Journal of Science., **284**, pp 1954–1960.

[124] Anderson, J.M., Streitlien, K., Barrett, D.S. and Triantafyllou, M.S. (1998), *Oscillating Foils of High Propulsive Efficiency*, Journal of Fluid Mechanic, **360**, pp 41–72.

[125] Ellington, C. (1984), *The Aerodynamics of Flapping Animal Flight*, Journal of American Zoology, **24**, pp 95–105.

[126] Videler, J., and Kamermans, P. (1985), *Differnce between Upstroke and Downstroke in Swimming Dolphins*, Journal of Experimental Biology, **19**, pp 265–274.

[127] Crandell, K., and Tobalske, B. (2011), *The Aerodynamics of Tip-reversal Upstroke in a Revolving Pigeon Wing*, Journal of Experimental Biology, **214**, pp 1867–1873.

[128] Fish, F.E. (1993), *Power Output and Propulsive Efficiency of Swimming Bottlenose Dolphins (Tursiops Truncatus)*, Journal of Experimental Biology., **185**, pp 179–193.

[129] Dickinson, M., and Gotz, K. (1993), *Unsteady Aerodynamic Performance of Model Wings at Low Reynolds Numbers*, Journal of Experimental Biology, **174**, pp 45–64.

[130] Lau, T.C.W., Kelso, R.M., and Hassen, E.R. (2004), *Flow Visualisation of a Pitching and Heaving Hydrofoil*, Proceedings of the 15th Australasian Fluid Mechanics Conference, The University of Sydney, Sydney, Australia, 13-17 December.

[131] Godoy-Diana, R., Aider, J., and Wesfreid, J.E. (2008), *Transitions in the Wake of a Flapping Foil*, Journal of Physical Review E, **77**, 5 pages.

[132] Nakamura, Y. (1996), *Vortex Shedding from Bluff Bodies and a Universal Strouhal Number*, Journal of Fluids and Structures, **10**, pp 159–171.

[133] Taylor, G.K., Nudds, R.L., and Thomas, A.L.R. (2003), *Flying and Swimming Animals Cruise at a Srouhal Number Tuned for High Power Efficiency*, Journal of Nature, **425**, pp 707–711.

[134] Tullis, S., Fiedler, A., McLaren, K., and Ziada, S. (1998), *Medium-solidity Vertical Axis Wind Turbines for Use in Urban Environments*, VII World Wind Energy Association Conference, Kingston, Ontario, Canada.

[135] Hsieh, K. (2009), *Experimental and Numerical Studies of Torque and Power Generation in a Vertical Axis Wind Turbine*, Master Thesis, Department of Aeronautics and Astronautics, National Cheng-Kung University, Taiwan.

[136] Tobalske, B.W. (2000), *Biomechanics and Physiology of Gait Selection in Flying Birds*, Journal of Physiological and Biochemical Zoology, **73(60)**, pp 736750.

[137] Muraca, R.J. and Guiliotte, R.J. (1976), *Wind Tunnel Investigation of a 14' Vertical Axis Windmill*, NASA Technical Memorandum, NASA TM X-72663.

[138] Chasteau, V.A.L. (1977), *Operational Experience with a 5m Darrieus Wind Turbine*, 6th Australasian Hydraulic and Fluid Mechanics Conference, Adelaide, Australia, 5-9 December.

[139] Sheldahl, R.E., and Blackwell, B.F. (1977), *Free-Air Performance Tests of a 5-Meter-Diameter Darrieus Turbine*, Sandia Laboratories, SAND77-1063.

[140] Sheldahl, R.E., Klimas, P.C., and Feltz, L.V. (1980), *Aerodynamic Performance of the 5-Meter-Diameter Darrieus Turbine with Extruded Aluminum NACA0015-Blades*, Sandia Laboratories, SAND80-0179.

[141] Sheldahl, R.E. (1981), *Comparison of Field and Wind Tunnel Darrieus Wind Turbine Data*, Sandia Laboratories, SAND80-2469.

[142] Templin, R.J. and Rangi, R.S. (1983), *Vertical-axis Wind Turbine Development in Canada*, IEE proceeding, **130(9)**, Part A.

[143] Bergeles, G., Michos, A., and Athanassiadis, N. (1991), *Velocity Vector and Turbulence in the Symmetry Plane of a Darrieus Wind Generator*, Journal of Wind Engineering and Industrial Aerodynamics, **37**, pp 87–101.

[144] Ashwill, T.D. (1991), *Measured Data for the Sandia 34-Meter Vertical Axis Wind Turbine*, National Renewable Energy Laboratory, SAND91-2228.

[145] Moran, W.A. (1977), *Giromill Wind Tunnel Test and Analysis*, Mcdonnel Aircraft Company, COO/2617-4/1.

[146] Price, T.J. (2006), *UK Large-Scale Wind Power Programme From 1970 to 1990: The Carmarthen Bay Experiments and the Musgrove Vertical-Axis Turbines*, Journal of Wind Engineering, **30(3)**, pp 225-242.

[147] Bulow, F. (2011), *Extreme Load Conditions for Wind Powered Direct Drive PM Generator*, Licentiate Thesis, Division of Electricity, Department of Engineering sciences, Uppsala University, Sweden.

[148] Richardson, P.L. (2011), *How Do albatrosses Fly Around the World Without Flapping Their Wings?*, Progress In Oceanography, **88**, pp 46-58.

[149] Pennycuick, C.J., Fuller, M.R., Oar, J.J., and S.J. Kirkpatrick (1994), *Falcon versus Grouse: flight adaptation of a predator and its prey*, Journal of Avian Biology, **25**, pp 39-49.

[150] Worasinchai,S., and Ingram, G. and Dominy, R. (2011), *A Low-Reynolds-number, High-Angle-of-Attack Investigation of Wind Turbine Aerofoils*, Proceedings of the Institution of Mechanical Engineers, Part A: Journal of Power and Energy, **225(6)**, pp 748-763.

[151] Lissaman, P.B.S. (1983), *Low-Reynolds-Number Airfoils*, Annual Review Fluid Mechanics, **15**, pp 223–239.

[152] Swift, K.M. (2009), *An Experimental Analysis of the Laminar Separation Bubble At Low Reynolds Numbers*, MSc Thesis, Department of Mechanical, Aerospace and Biomedical Engineering, University of Tennessee - Knoxville, USA.

[153] Smith, A.M.O. (1975), *High-Lift Aerodynamics*, Journal of Aircraft, **12(6)**, pp 501–530.

[154] Selig, M.S., and Guglielmo, J.J. (1997), *High-Lift Low Reynolds Number Airfoil Design*, Journal of Aircraft, **34(1)**, pp 72–79.

[155] Turby (2011), http://www.turby.nl/ [Accessed: 11 Febuary 2011].

[156] Heffley, D. and Van Treuren, K.W. (2007), *Aerodynamic Characteristics of a NACA 4412 Airfoil*, School of Engineering and Computer Science, Baylor University, USA.

[157] Mueller, T.J., and DeLaurier, J.D. (2003), *Aerodynamics of Small Vehicles*, Annual Review Fluid Mechanics, **35**, pp 89–111.

[158] Worasinchai, S., Ingram, G., and Dominy, R. (2011), *The Effects of Improved Starting Capability on Energy Yield for Small HAWTs*, GT2011-45674: ASME Turbo Expo 2011. June 6-10, 2011, Vancouver, Canada.

[159] Sims-Williams, D. (2001), *Self-excited Aerodynamic Unsteadiness Associated with Passenger Cars*, PhD Thesis, School of Engineering, University of Durham.

[160] Liu, T., Kuykendall, K., Rhew, R., and Jones, S. (2004), *Avian Wings*, Proceedings of the 24th AIAA Aerodynamic Mesurement Technology and Ground Testing Conference, Portland, Oregon, 28 June - 1 July 2004.

[161] Standish, K.J., and Van Dam, C.P. (2003), *Aerodynamic Analysis of Blunt Trailing Edge Airfoils*, ASME Journal of Solar Energy Engineering, **125**, pp 479–487.

[162] Baker, J.P., and Mayda, E.A., and Van Dam, C.P. (2006), *Experimental Analysis of Thick Blunt Trailing-Edge Wind Turbine Airfoils*, ASME Journal of Solar Energy Engineering, **34(1)**, pp 72–79.

[163] Leibeck, R.H. (1978), *Design of Subsonic Airfoils for High Lift*, Journal of Aircraft, **15(9)**, pp 547–561.

[164] Sankar, L.N. (2000), *Dynamic Stall Characteristics of Drooped Leading Edge Airfoils*, Final report, NASA Ames Research Center.

[165] Martin, P.B., McAlister, K.W., and Chandrasekhara, M.S. (2003), *Dynamic Stall Measurements and Computations for a VR-12 Airfoil with a Variable Droop Leading Edge*, the American Helicopter Socity 59th, Annual Forum, Phoenix, Arizona, 6 - 8 May 2003.

[166] Tobalske, B.W., and Dial, K.P. (1996), *Flight Kinematics of Black-billed Magpies and Pigeons over a Wide Range of Speeds*, Journal of Experimental Biology, **199**, pp 263–280.

[167] Alexander, D.E. (2002), **Nature's Flyers: Birds, Insects, and the Biomechanics of Flight**, The Johns Hopkins University Press Series.

[168] Biewener, A.A. (2003), **Animal Locomotion**, Oxford Animal Biology Series, OUP Oxford.

[169] Platzer, M.F. and Jones, K.D. and Young, J. and Lai, C.S. (2008), *Flapping-Wing Aerodynamics: Progress and Challenges*, AIAA Journal, **46(9)**, pp 2136–2149.

[170] Kirke, B.K. (1998), *Evaluation of Self-starting Vertical Axis Wind Turbines for Stand-alone Applications*, Ph.D. Thesis, School of Engineering, Griffith University, Australia.

[171] Lunt, P.A.V. (2005), *An Aerodynamic Model for a Vertical-axis Wind Turbine*, M.Eng Thesis, School of Engineering, University of Durham, England.

[172] Reynolds, K. (2010), *VAWT Start up Characteristics*, M.Eng Thesis, School of Engineering and Computing Science, Durham University.

[173] Eppler, R. and Somers, D. (1980), *A Computer Program for the Design and Analysis of Low-speed Airfoils*, NASA-TM-81862, National Aeronautics and Space Administration.

[174] Leishman, J.G. (2002), *Challenges in Modeling the Unsteady Aerodynamics of Wind Turbines*, AIAA 2002-0037, 21st ASME Wind Energy Symposium and the 40th AIAA Aerospace Sciences Meeting, Reno, NV.

[175] Beddoes, T.S. (1984), *Practical Computation of Unsteady Lift*, Vertica, **8(1)**, pp 55–71.

[176] Chantharasenawong, C. (2007), *Nonlinear Aeroelastic Behaviour of Aerofoils Under Dynamic Stall*, Ph.D. Thesis, Department of Aeronautics, Imperial College, London, UK.

[177] Bauchau, O.A. (2007), *DYMORE USER'S MANUAL*, School of Aerospace Engineering, Georgia Institute of Technology.

[178] Mert, M. (1999), *Optimization of Semi-Empirical Parameters in the FFA-Beddoes Dynamic Stall Model*, FFA TN 1999-37, The Aeronautical Research Institute of Sweden.

Appendix A

Pressure tapping coordinates

Pressure tapping coordinates of all aerofoils for steady and unsteady tests are tabulated in table A.1 to A.10, respectively.

Table A.1: NACA0012 pressure tap coordinates for steady tests.

Suction	**surface**	**Pressure**	**surface**
x/c	y/c	x/c	y/c
0.0272	0.0000	0.0818	-0.0200
0.0636	0.0181	0.1272	-0.0254
0.1090	0.0254	0.1818	-0.0300
0.1545	0.0281	0.2363	-0.0318
0.2090	0.0318	0.2909	-0.0336
0.2636	0.0363	0.3454	-0.0318
0.3181	0.0354	0.4000	-0.0300
0.3727	0.0318	0.5727	-0.0209
0.4272	0.0300	0.6272	-0.0163
0.5909	0.0227	0.6909	-0.0109
0.6545	0.0172	0.7909	0.0000
0.7363	0.0100		
0.8545	0.0000		

Table A.2: NACA0012 pressure tap coordinates for unsteady tests.

Suction	**surface**	**Pressure**	**surface**
x/c	y/c	x/c	y/c
0.0273	0.0000	0.0568	-0.0127
0.0591	0.0164	0.1000	-0.0218
0.0955	0.0236	0.1409	-0.0264
0.1364	0.0282	0.1818	-0.0291
0.1773	0.0309	0.3182	-0.0327
0.3091	0.0345	0.3636	-0.0309
0.3545	0.0336	0.4091	-0.0291
0.4000	0.0318	0.4545	-0.0291
0.4455	0.0309	0.5000	-0.0255
0.4909	0.0282	0.5455	-0.0236
0.5364	0.0255	0.5909	-0.0173
0.5818	0.0218	0.6545	-0.0136
0.6273	0.0155		
0.6727	0.0127		
0.7273	0.0045		
0.7818	0.0000		

Table A.3: SG6043 pressure tap coordinates for steady tests.

Suction	**surface**	**Pressure**	**surface**
x/c	y/c	x/c	y/c
0.0272	0.0090	0.1000	0.0090
0.0727	0.0318	0.1545	0.0118
0.1272	0.0490	0.2090	0.0145
0.1818	0.0613	0.2636	0.0209
0.2363	0.0700	0.3181	0.0245
0.2909	0.0763	0.3727	0.0254
0.3454	0.0781	0.4272	0.0309
0.4000	0.0790	0.6090	0.0345
0.5818	0.0709	0.6636	0.0381
0.6363	0.0627	0.7272	0.0454
0.6909	0.0563		
0.7636	0.0409		

Table A.4: SG6043 pressure tap coordinates for unsteady tests.

Suction	**surface**	**Pressure**	**surface**
x/c	y/c	x/c	y/c
0.0273	0.0091	0.0864	0.0068
0.0591	0.0255	0.1273	0.0091
0.0955	0.0382	0.1727	0.0136
0.1364	0.0491	0.3182	0.0236
0.1818	0.0609	0.3636	0.0255
0.3045	0.0755	0.4182	0.0300
0.3500	0.0782	0.4636	0.0336
0.4000	0.0791	0.5091	0.0355
0.4409	0.0791	0.5636	0.0391
0.4909	0.0782	0.6136	0.0400
0.5455	0.0750	0.7273	0.0455
0.5909	0.0691		
0.6364	0.0636		
0.6818	0.0573		
0.7727	0.0400		
0.8182	0.0345		

Table A.5: SD7062 pressure tap coordinates for steady tests.

Suction	**surface**	**Pressure**	**surface**
x/c	y/c	x/c	y/c
0.0273	0.0091	0.0727	-0.0064
0.0545	0.0391	0.1182	-0.0100
0.0855	0.0545	0.1636	-0.0109
0.1218	0.0664	0.2273	-0.0109
0.1627	0.0773	0.2818	-0.0109
0.2073	0.0827	0.3545	-0.0045
0.2500	0.0855	0.4727	0.0000
0.2955	0.0882	0.5273	0.0045
0.3409	0.0882	0.5727	0.0055
0.3864	0.0864	0.6182	0.0073
0.4545	0.0791	0.7000	0.0155
0.5000	0.0750		
0.5455	0.0664		
0.5909	0.0609		
0.6364	0.0518		
0.6818	0.0418		
0.7273	0.0355		
0.7727	0.0236		
0.8273	0.0182		

Table A.6: SD7062 pressure tap coordinates for unsteady tests.

Suction	**surface**	**Pressure**	**surface**
x/c	y/c	x/c	y/c
0.0273	0.0091	0.0727	-0.0064
0.0545	0.0391	0.1182	-0.0100
0.0855	0.0545	0.1636	-0.0109
0.1218	0.0664	0.2000	-0.0100
0.1627	0.0773	0.3000	-0.0073
0.2073	0.0818	0.3545	-0.0045
0.2955	0.0845	0.4091	0.0000
0.3409	0.0845	0.4545	0.0000
0.3864	0.0836	0.5000	0.0045
0.4364	0.0782	0.5455	0.0064
0.4864	0.0745	0.6000	0.0073
0.5318	0.0673	0.6455	0.0100
0.5773	0.0591		
0.6227	0.0536		
0.6682	0.0427		
0.7136	0.0355		
0.7545	0.0245		
0.7955	0.0209		

Table A.7: DU06-W-200 pressure tap coordinates for steady tests.

Suction	**surface**	**Pressure**	**surface**
x/c	y/c	x/c	y/c
0.0227	0.0000	0.0527	-0.0255
0.0455	0.0291	0.1000	-0.0409
0.0818	0.0491	0.1455	-0.0500
0.1182	0.0618	0.1909	-0.0591
0.1545	0.0709	0.2364	-0.0618
0.1909	0.0764	0.2818	-0.0636
0.2273	0.0800	0.3273	-0.0645
0.2636	0.0818	0.3818	-0.0636
0.3091	0.0809	0.4364	-0.0591
0.3545	0.0791	0.4909	-0.0536
0.4000	0.0727	0.5545	-0.0455
0.4455	0.0664	0.6091	-0.0336
0.4909	0.0600	0.6545	-0.0227
0.5364	0.0518	0.7091	-0.0145
0.5818	0.0436		
0.6273	0.0355		
0.6727	0.0273		
0.7182	0.0209		
0.7636	0.0127		
0.8182	0.0045		

Table A.8: DU06-W-200 pressure tap coordinates for unsteady tests.

Suction	**surface**	**Pressure**	**surface**
x/c	y/c	x/c	y/c
0.0227	0.0000	0.0527	-0.0255
0.0455	0.0291	0.1000	-0.0409
0.0818	0.0491	0.1455	-0.0500
0.1182	0.0618	0.1909	-0.0591
0.1545	0.0709	0.2364	-0.0618
0.1909	0.0764	0.2818	-0.0636
0.2273	0.0800	0.3273	-0.0645
0.2636	0.0818	0.3818	-0.0636
0.3091	0.0809	0.4364	-0.0591
0.3545	0.0791	0.4909	-0.0536
0.4000	0.0727	0.5545	-0.0455
0.4455	0.0664	0.6091	-0.0336
0.4909	0.0600	0.6545	-0.0227
0.5364	0.0518	0.7091	-0.0145
0.5818	0.0436		
0.6273	0.0355		
0.6727	0.0273		
0.7182	0.0209		
0.7636	0.0127		
0.8182	0.0045		

Table A.9: S1223 pressure tap coordinates for steady and unsteady tests.

Suction	**surface**	**Pressure**	**surface**
x/c	y/c	x/c	y/c
0.0273	0.0145	0.0764	0.0145
0.0545	0.0436	0.1218	0.0191
0.0864	0.0600	0.1636	0.0273
0.1227	0.0727	0.2000	0.0345
0.1636	0.0864	0.3273	0.0582
0.1982	0.0955	0.3727	0.0636
0.3091	0.1045	0.4182	0.0682
0.3509	0.1036	0.4818	0.0891
0.3945	0.1000		
0.4400	0.0964		
0.5273	0.0891		
0.5682	0.0855		
0.6136	0.0818		
0.6545	0.0805		

Table A.10: S1223B pressure tap coordinates for steady and unsteady tests.

Suction	**surface**	**Pressure**	**surface**
x/c	y/c	x/c	y/c
0.0273	0.0145	0.0764	0.0145
0.0545	0.0436	0.1218	0.0200
0.0864	0.0600	0.1636	0.0273
0.1227	0.0727	0.2000	0.0345
0.1636	0.0864	0.3273	0.0564
0.1982	0.0955	0.3727	0.0600
0.3091	0.1045	0.4182	0.0682
0.3509	0.1036	0.4636	0.0709
0.3945	0.1091	0.5773	0.0773
0.4400	0.1073	0.6636	0.0745
0.4909	0.1000	0.7545	0.0700
0.5364	0.0973	0.8455	0.0573
0.6182	0.0909		
0.7091	0.0773		
0.8000	0.0673		

Appendix B

Aerofoil coordinates: S1223B aerofoil

Table B.1: S1223B coordinates.

Suction	**surface**	**Pressure**	**surface**
x/c	y/c	x/c	y/c
0.0000	0.0000	0.0000	0.0000
0.0002	0.0029	0.0001	-0.0014
0.0008	0.0075	0.0008	-0.0059
0.0022	0.0137	0.0014	-0.0069
0.0048	0.0210	0.0031	-0.0087
0.0071	0.0259	0.0079	-0.0107
0.0108	0.0326	0.0145	-0.0115
0.0150	0.0388	0.0214	-0.0119
0.0199	0.0449	0.0333	-0.0120
0.0285	0.0537	0.0463	-0.0115
0.0357	0.0600	0.0639	-0.0104
0.0490	0.0700	0.0812	-0.0089
0.0680	0.0820	0.1035	-0.0066
0.0802	0.0886	0.1295	-0.0037
0.0955	0.0961	0.1640	0.0013
0.1101	0.1025	0.2010	0.0078
0.1250	0.1082	0.2512	0.0159
0.1403	0.1135	0.2961	0.0228
0.1573	0.1187	0.3339	0.0281
0.1747	0.1234	0.3816	0.0342
0.1956	0.1280	0.4301	0.0393
0.2128	0.1313	0.4794	0.0435
0.2326	0.1345	0.5265	0.0465
0.2636	0.1381	0.5768	0.0482
0.2965	0.1399	0.6317	0.0484
0.3285	0.1404	0.6765	0.0474
0.3596	0.1401	0.7156	0.0455
0.3875	0.1392	0.7368	0.0440
0.4161	0.1379	0.7633	0.0416
0.4464	0.1360	0.7894	0.0387
0.4786	0.1337	0.8095	0.0360
0.5058	0.1314	0.8303	0.0327
0.5354	0.1288	0.8699	0.0250
0.5641	0.1261	0.8992	0.0177
0.5907	0.1234	0.9215	0.0112
0.6107	0.1212	0.9448	0.0031
0.6504	0.1164	0.9571	-0.0019
0.6815	0.1123	0.9718	-0.0088
0.7187	0.1071	0.9890	-0.0188
0.7480	0.1026	0.9923	-0.0210
0.7833	0.0967	0.9980	-0.0250
0.8174	0.0905	1.0000	-0.0250
0.8450	0.0848		
0.8718	0.0788		
0.8897	0.0742		
0.9105	0.0684		
0.9255	0.0638		
0.9418	0.0582		
0.9537	0.0537		
0.9629	0.0499		
0.9734	0.0451		
0.9808	0.0411		
0.9869	0.0370		
0.9919	0.0330		
0.9972	0.0282		
1.0000	0.0250		

Appendix C

The AERODAS model

The AERODAS is a correlated model developed by Spera [63] to predict lift and drag coefficients at high incidence angles. It consists of two curves intended to cover unstalled and stalled regimes (Fig. C.1). As seen from the figure, the model requires a number of parameters to define aerodynamic coefficient variations in both regimes (referred to as 1 and 2, respectively).

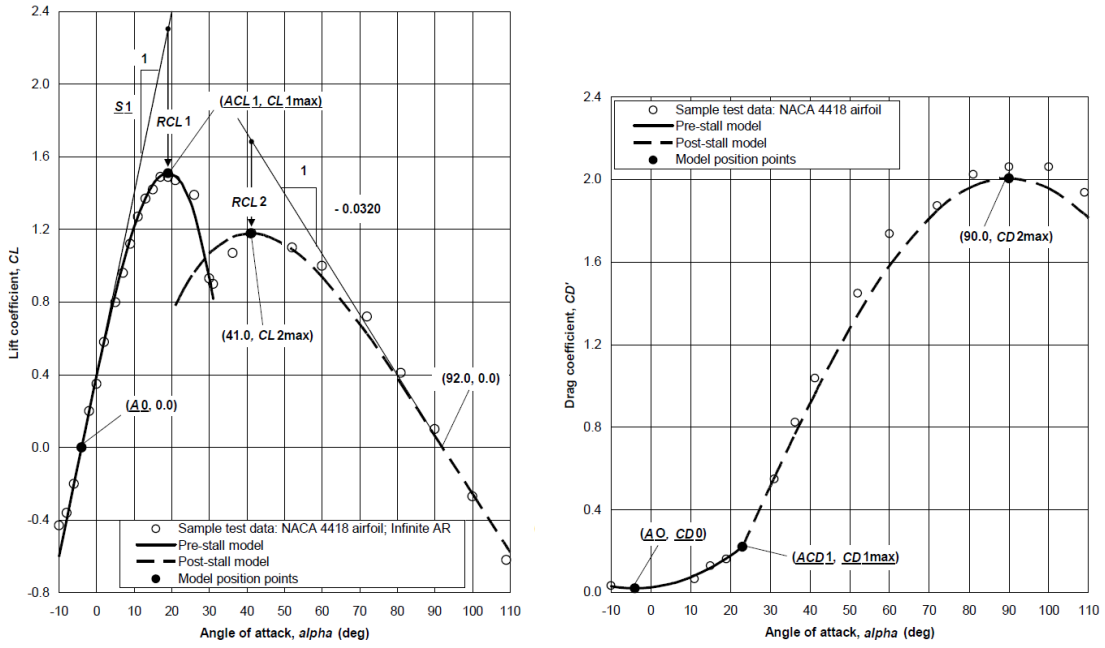

Figure C.1: AERODAS modelling.

C.1 Variations in unstalled regime

Parameters required in the unstalled regime are: zero-lift angle of attack ($A0$), linear curve slope ($S1$), maximum lift coefficient ($CL1max$), angle of attack that maximum lift occurs ($ACL1$). Similarly, drag calculation requires minimum drag coefficient ($CD0$), angle of attack that minimum drag occurs ($A0$), maximum drag coefficient

(or stalled drag coefficient) ($CD1max$), and angle of attack that maximum drag occurs ($ACD1$)

The following equations are applied to calculate lift and drag coefficients in pre-stall regime.

$$CL1 = S1 * (\alpha - A0) - RCL1\Big(\frac{\alpha - A0}{ACL1 - A0}\Big)^{N1} \tag{C.1.1}$$

$$CD1 = CD0 + (CD1max - CD0)((\alpha - A0)/(90^\circ - ACD1) \times 90^\circ)^2 \tag{C.1.2}$$

where

$$RCL1 = S1 \times (ACL1 - A0) - CL1max \tag{C.1.3}$$

$$N1 = 1 + CL1MAX/RCL1 \tag{C.1.4}$$

C.2 Variations in stalled regime

Since experiential data from different tests indicated that lift and drag coefficients are strongly affected by blade aspect ratio and aerofoil thickness, a superposition technique has been applied to calculate maximum values which are needed to define the variations. The maximum lift and drag in this regime are expressed as:

$$CL2max = F1[t/c] \times F2[AR] \tag{C.2.5}$$

$$CD2max = G1[t/c] \times G2[AR] \tag{C.2.6}$$

where $F1$, $F2$, $G1$, and $G2$ are empirical functions for thickness and aspect ratio (F and G are for lift and drag calculations, respectively). The following equations are applied to calculate the functions:

$$F1 = 1.190\ [1.0 - (t/c)2] \tag{C.2.7}$$

$$F2 = 0.65 + 0.35\ \exp[-(9.0/AR)^{2.3}] \tag{C.2.8}$$

$$G1 = 2.300\ \exp(-[0.65(t/c)]^{0.90}) \tag{C.2.9}$$

$$G2 = 0.52 + 0.48\ \exp[-(6.5/AR)^{1.1}] \tag{C.2.10}$$

Finally, variations of lift and drag coefficients in the post-stall regime are calculated from

$$CL2 = -0.032\,(\alpha - 92^\circ) - RCL2\Big(\frac{92^\circ - \alpha}{51^\circ}\Big)^{N2} \tag{C.2.11}$$

$$CD2 = CD1MAX + (CD2MAX - CD1MAX)\sin\Big(\frac{90^\circ - \alpha}{\alpha - ACD1} \times 90^\circ\Big) \tag{C.2.12}$$

where

$$RCL2 = -0.032\,(41^\circ - 92^\circ) - CL2max = 1.632 - CL2max \tag{C.2.13}$$

$$N2 = 1 + CL2max/RCL2 \tag{C.2.14}$$

Appendix D

The Leishman-Beddoes model

D.1 An overview

The LB model is a semi-empirical model. It consists of linear and non-linear equations which are based on both classical unsteady thin-aerofoil theory and parameters deduced from wind-tunnel measurements. It divides important flow phenomena into three modules: attached-flow, separated-flow, and vortex-induced flow modules (Fig. D.1). A very brief overview is presented here and more details will follow in subsequent sections.

D.1.1 Input

A time history of incidence angle is input to the model together with variables that define flow conditions.

D.1.2 The attached flow

This module comprises of circulatory and impulsive submodules. The incidence angle history is input to this module to calculate normal force due to attached flow (C_N^P) which is a superposition of circulatory normal force (C_N^C) and impulsive normal force (C_N^I). If the maximum incidence angle is lower than the static stall angle, this value will be directly used to calculate lift and drag coefficients. If not, the C_N^P is sent to the separated flow module for further calculations. Empirical parameters (A_1, A_2, b_1, and b_2) which determine aerofoil response are needed.

D.1.3 The separated flow

This module consists of two submodules accounting for pressure and boundary-layer lags. The normal and chordwise force due to separated flow (C_N^f) is computed by sequentially taking account of these two lags into the normal force due to attached flow (C_N^P). In order to implement this module, static separation point (f) and time parameters that determine lagging effects (T_P and T_f) have to be known.

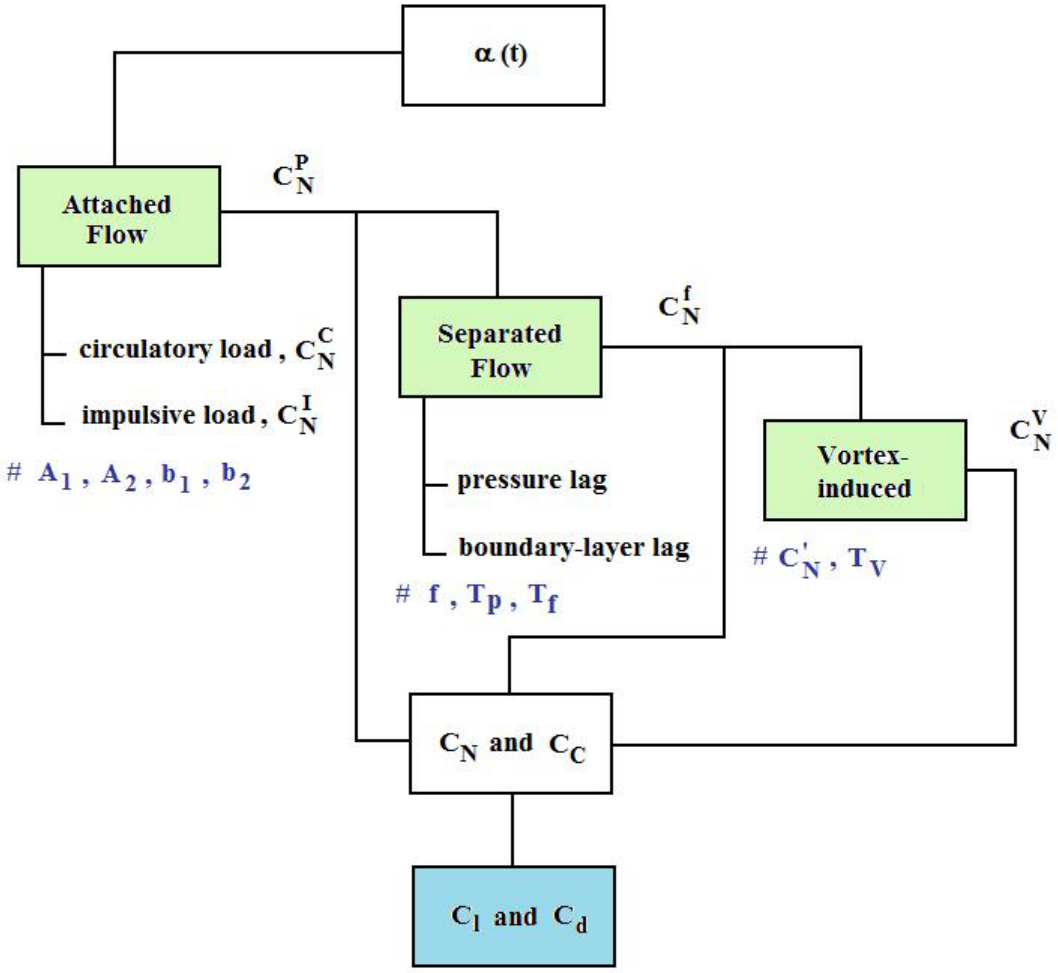

Figure D.1: The Leishman-Beddoes model submodules.

D.1.4 The vortex-induced flow

If the normal force coefficient due to separated flow (C'_N) is higher than a critical normal force coefficient (C_{N1}), the so-called dynamic-stall vortex forms, leading to the normal force coefficient due to vortex formation (C_N^v). This value is then combined with C_N^f to obtain total normal force coefficient (C_N^T). Empirical parameters needed for the calculations are the critical normal force coefficient (C_{N1}) and time parameter (T_v).

D.1.5 Output

Since the LB model was originally derived based on normal and chord coefficients (Fig. D.2), the following equations are used to calculate lift and drag coefficients:

$$C_l = C_N \cos\alpha - C_C \sin\alpha \tag{D.1.1}$$

$$C_d = C_N \sin\alpha + C_C \cos\alpha + C_{d0} \tag{D.1.2}$$

where C_{d0} is drag coefficient at zero angle of attack.

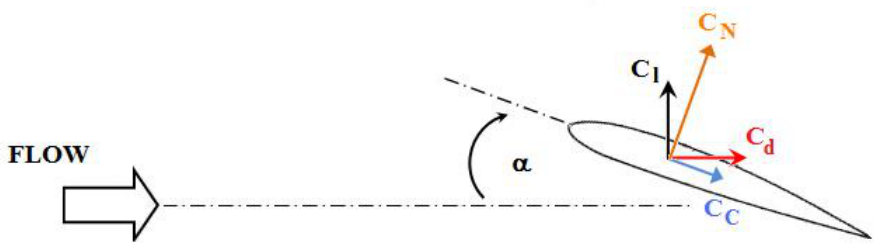

Figure D.2: Frame of reference.

D.2 The attached flow

According to Beddoes [175], the response of an aerofoil due to a step change of incidence angle can be broken into two parts: impulsive and circulatory responses. The former represents the response to an instantaneous load (impulse) which is large at first and then rapidly reduces with time. The latter represents a response to the impulsive load as the flow needs some time to establish itself to the new state caused by the load. This is small at first and then gradually increases to the equilibrium. The total response is a superposition of these two.

The two responses are modelled using two indicial functions. Leishman states that: "*By definition, an indicial function is the response to a disturbance that is applied instantaneously at time zero and held constant thereafter, that is, a disturbance given by a step function.*" [15]. Circulatory and impulsive responses due to a step change in angle of attack are denoted as ϕ_α^c and ϕ_α^I, respectively.

With the two responsive functions, the resulting normal force due to a step change in incidence angle is

$$\Delta C_{N\alpha} = (C_{N\alpha}\phi_\alpha^C + \frac{4}{M}\phi_\alpha^I)\Delta\alpha \tag{D.2.3}$$

where $C_{N\alpha}$ is the linear slope of normal force coefficient, M is a Mach number, and $\Delta\alpha$ is a step change in incidence angle.

Integration of this small step change gives a cumulative effect of a time history of incidence angle (only the circulatory is presented as an example here).

$$C_{N\alpha}^c = \int_{t0}^{t} C_{N\alpha}\phi_\alpha^C d\alpha \tag{D.2.4}$$

The circulatory indicial function can be approximated using an exponential function as [15]

$$\phi_\alpha^C = 1.0 - A_1 \exp(-b_1\beta S) - A_2 \exp(-b_2\beta S) \tag{D.2.5}$$

where A_1, A_2, b_1, and b_2 are parameters determine the aerofoil response.
Eq. D.2.4 then becomes:

$$C^c_{N\alpha} = C_{N\alpha} \times \Big[\alpha(t) - \int_{t0}^{t} A_1 \exp(-b_1\beta S)\, d\alpha - \int_{t0}^{t} A_2 \exp(-b_2\beta S)\, d\alpha\Big] \quad \text{(D.2.6)}$$

The second and third terms in the bracket are defined as deficiency functions. The circulatory normal force can then be written in a recursive form as

$$C^C_{N\alpha,n} = C_{N\alpha}\,[\alpha_n - X^1_n - Y^1_n] \quad \text{(D.2.7)}$$

In conclusion, the circulatory normal force at a time step n is a combined effect and depends on the angle of attack at this present time and accumulating effects from the previous time steps.

The impulsive normal force can be derived in a similar way. A summary of equations used for both calculations are given below.

D.2.1 Circulatory load due to a step change in incidence angle

As seen from the previous discussion, this is equivalent to the static case in that its is proportional to lift slope $C_{N\alpha}$ but an equivalent angle of attack which includes time lags is used (represented by deficiency functions (X_n and Y_n)).

$$C^C_{N\alpha,n} = C_{N\alpha}\,\alpha_{eq,n} = C_{N\alpha}\,[\alpha_n - X^1_n - Y^1_n] \quad \text{(D.2.8)}$$

The deficiency functions at a time depends on many factors such as the value of previous step (X_{n-1} and Y_{n-1}), a change in angle of attack at present time ($\Delta\alpha_n$), and aerofoil characteristics (A_1, A_2, b_1, b_1). These expressions are used to calculate the deficiency functions at time step n:

$$X^1_n = X^1_{n-1} \exp(-b_1\beta^2\Delta S_n) + A_1\Delta_n \exp\Big(\frac{-b_1\beta^2\Delta S_n}{2}\Big) \quad \text{(D.2.9)}$$

$$Y^1_n = Y^1_{n-1} \exp(-b_2\beta^2\Delta S_n) + A_2\Delta_n \exp\Big(\frac{-b_2\beta^2\Delta S_n}{2}\Big) \quad \text{(D.2.10)}$$

where V is the velocity , c is the aerofoil chord, β is the Prandtl-Glauert compressibility factor ($\beta = \sqrt{1 - Ma^2}$), and ΔS_n is the dimensionless time step at time n.

D.2.2 Impulsive load due to a step change in incidence angle

The impulsive load caused by instantaneous change in angle of attack is

$$C^I_{N\alpha,n} = \frac{4K_\alpha T_I}{M}\Big(\frac{\Delta\alpha_n}{\Delta t_n} - D_n\Big) \tag{D.2.11}$$

where D_n is the deficiency function for impulsive load. It is calculated from

$$D_n = D_{n-1}\exp\Big(\frac{-\Delta t_n}{K_\alpha T_I}\Big) + \Big(\frac{\Delta\alpha_n - \Delta\alpha_{n-1}}{\Delta t_n}\Big)\exp\Big(\frac{-\Delta t_n}{2K_\alpha T_I}\Big) \tag{D.2.12}$$

where

$$K_\alpha = \frac{0.75}{(1-Ma) + \pi\beta^2 Ma^2(A_1 b_1 + A_2 b_2)} \tag{D.2.13}$$

and

$$T_I = \frac{c}{a} \tag{D.2.14}$$

where c is the aerofoil chord and a is a speed of sound.

D.3 The separated flow

Before considering the airload caused by an aerofoil under unsteady separated flow, it is useful to understand how the normal force caused by the trailing-edge separated flow is modelled in "static" cases.

For the static case, when the incidence angle increases, flow separation occurs at the trailing edge. This separation reduces the overall circulation generated by the aerofoil and, hence, the normal force. Beddoes devised the Kirchhoff and Helmholtz solution for the lift on a flatplate with a fixed separation point [15] as

$$C_N = C_{N\alpha}\Big(\frac{1+\sqrt{f}}{2}\Big)^2(\alpha - \alpha_0) \tag{D.3.15}$$

where $C_{N\alpha}$ is the linear curve slope in the attached flow, α is the angle of attack, α_0 is the zero-lift angle of attack, and f is a static separation point which is defined to be 1 if the flow is fully attached and 0 if the flow is fully separated (Fig. D.3).

With this equation, the calculation of the normal force at any angle of attack is reduced to the separation point calculation which can be directly deduced from static wind-tunnel test by resolving lift and drag coefficients in terms of normal force. By considering a set of tests, Leishman suggested that the static separation point can be modelled using two exponential functions and three empirical parameters are needed to define the separation curve: α_1, S_1, and S_2.

For the dynamic case, this separation point is altered. When the aerofoil is suddenly pitched to a new angle of attack at which separated flow occurs, a dynamic-stall vortex forms, introducing a more attached flow at the leading edge and a suppression of the trailing-edge separation movement. These two phenomena are modelled sequentially using two lags: pressure and boundary-layer lags.

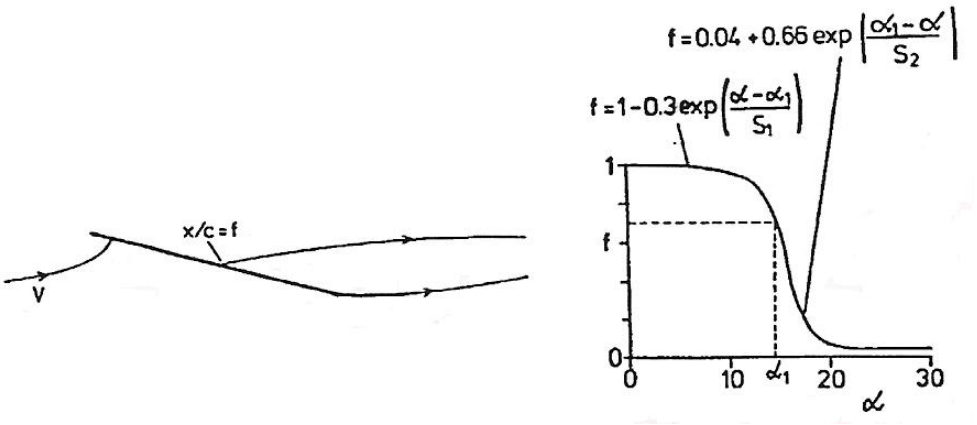

Figure D.3: Definition and modelling of separation point [102].

The lag of pressure reduces the normal force that the aerofoil perceives. It can be expressed as a function of deficiency function as

$$C'_{N,n} = C^P_{N,n} - D_{P,n} \tag{D.3.16}$$

where the deficiency function is as follows:

$$D_{P,n} = D_{P,n-1} \exp\Big(\frac{-\Delta S_n}{T_P}\Big) + (C^P_{N,n} - C^P_{N,n-1}) \exp\Big(\frac{-\Delta S_n}{2T_P}\Big) \tag{D.3.17}$$

where T_P is a time constant for pressure lag. Physically, the higher value means the slower response. It is reported that this value is independent of aerofoil shape [15].

Due to the lag in pressure response at the leading edge, the effective angle of attack perceived by the aerofoil is changed.

$$\alpha_{f,n} = \frac{C'_{N,n}}{C^S_{N\alpha}} + \alpha_0 \tag{D.3.18}$$

This effective angle of attack is then used to calculate an effective separation point.

$$f'_n = f(\alpha_{f,n}) \tag{D.3.19}$$

The delay of boundary-layer effects at the trailing edge is taken into account by adding a deficiency function to this effective separation point.

$$f''_n = f'_n - D_{f,n} f'' = f'_n - D_{f,n} \tag{D.3.20}$$

The deficiency function for this temporal effect is:

$$D_{f,n} = D_{f,n-1} \exp\Big(\frac{-\Delta S_n}{T_f}\Big) + (f'_n - f'_{n-1}) \exp\Big(\frac{-\Delta S_n}{2T_f}\Big) \tag{D.3.21}$$

where T_f is a time constant for boundary-layer response. This parameter is greatly influenced by the vortex movement and how the incidence angle changes (increasing or decreasing). The following equation is applied [176].

$$T_f = \begin{cases} T_{f0} & \text{if } \alpha\alpha' > 0 \text{ and } 0 \leq \tau_v \leq T_{vl} \\ \frac{1}{3}T_{f0} & \text{if } \alpha\alpha' > 0 \text{ and } T_{vl} \leq \tau_v \leq 2T_{vl} \\ 4T_{f0} & \text{if } \alpha\alpha' > 0 \text{ and } \tau_v \geq 2T_{vl} \\ 0.5T_{f0} & \text{if } \alpha\alpha' < 0 \text{ and } 0 \leq \tau_v \leq 2T_{vl} \\ 4T_{f0} & \text{if } \alpha\alpha' > 0 \text{ and } \tau_v \geq 2T_{vl} \end{cases} \tag{D.3.22}$$

where τ_v is vortex time used to identify vortex position, T_{vl} is the time that the vortex takes to reach the trailing edge.

At the first instant of the onset of vortex formation, the τ_v is calculated from [177].

$$\tau_v = \Delta t\Big(\frac{W}{b}\Big)\left(\frac{|C'_{N,n}| - C_{N1}}{|C'_{N,n}| - |C'_{N,n-1}|}\right) \tag{D.3.23}$$

The progress of the vortex over the aerofoil chord is calculated from

$$\tau_{v,n} = \tau_{v,n-1} + \Delta t\Big(\frac{W}{b}\Big) \tag{D.3.24}$$

where Δt is the time step used in the computation, c is the aerofoil chord, W is the resultant wind speed perceived by the aerofoil. The vortex is said to be shed when $\tau_v \geq T_{vl}$ and the effect of vortex on the airload is expected to be reduced.

Finally, the instantaneous normal force coefficient including both pressure and boundary-layer lags is [105]:

$$C^f_{N,n} = C_{N\alpha}\Big(\frac{1+\sqrt{f''_n}}{2}\Big)^2 \sin(\alpha - \alpha_0) \tag{D.3.25}$$

The instantaneous chord force coefficient is calculated from

$$C^f_{C,n} = \eta\, C_{N\alpha}(\alpha - \alpha_0)\tan\alpha\sqrt{f''_n} \tag{D.3.26}$$

In conclusion, the following steps are applied to obtain the instantaneous force coefficients due to separated flow:

1. Knowing 'static' separation point, T_P, T_f, and normal force coefficient from the attached flow.
2. Calculate the lagged normal force coefficient from Eq. (D.3.17).
3. Calculate the effective angle of attack from Eq. (D.3.18).
4. Calculate the effective separation point from Eq. (D.3.19).
5. Calculate the dynamic separation point from Eq. (D.3.20).

6. Calculate the instantaneous normal and axial force coefficient from Eqs. (D.3.25) and (D.3.26).

D.4 The vortex-induced flow

The increment in normal force coefficient during vortex-induced flow ($C^v_{N,n}$) is modelled as an excessive circulation in the vicinity of the aerofoil.

The increment is determined by vortex strength ($C_{v,n}$) which is a difference between normal force coefficient generated by the attached flow (C^C_N) and the normal force coefficient generated by the separated flow (C^f_N). The basic underlying of this idea is that when the vortex is build up it promotes more attached flow at the leading edge and suppresses the trailing-edge separation and the flow behaves, to some extent, like attached flow (Fig. D.4).

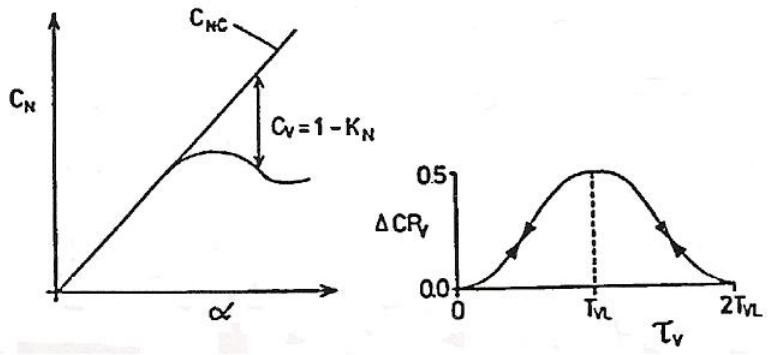

Figure D.4: Vortex-induced airload [102].

The vortex strength is

$$C_{v,n} = C^C_{N,n} - C^f_{N,n} \tag{D.4.27}$$

This vortex strength contributes to the increase in normal force ($C^v_{N,n}$) when the aerofoil pitches up. This equation is applied.

$$C^v_{N,n} = \begin{cases} C^v_{N,n-1} \exp(\frac{-\sigma_v \Delta S_n}{T_v}) + (C_{v,n} - C_{v,n-1}) \exp(\frac{-\sigma_v \Delta S_n}{2T_v}) & \text{if } \alpha \leq \alpha_1 \\ C^v_{N,n-1} \exp(\frac{-\sigma_v \Delta S_n}{T_v}) & \text{otherwise} \end{cases} \tag{D.4.28}$$

where T_v is a time parameter for vortex.

This time parameter is influenced by vortex movement and the following equation is used:

$$T_v = \begin{cases} T_{v0} & \text{if } \alpha\alpha' > 0 \text{ and } 0 \le \tau_v \le T_{vl} \\ 0.25T_{v0} & \text{if } \alpha\alpha' > 0 \text{ and } T_{vl} \le \tau_v \le 2T_{vl} \\ 0.9T_{v0} & \text{if } \alpha\alpha' > 0 \text{ and } \tau_v \ge 2T_{vl} \\ 0.5T_{v0} & \text{if } \alpha\alpha' < 0 \text{ and } 0 \le \tau_v \le 2T_{vl} \\ 0.9T_{v0} & \text{if } \alpha\alpha' > 0 \text{ and } \tau_v \ge 2T_{vl} \end{cases} \tag{D.4.29}$$

The instantaneous total normal force coefficient is calculated from

$$C_{N,n} = f_n'' \cdot C_{N,n}^p + (1 - f_n'') \cdot C_{N,n}^f + C_{N,n}^v \tag{D.4.30}$$

D.5 Parameters used in the LB Model

D.5.1 Parameters from static data

A number of parameters have to be deduced from static data and they are:-

- Normal curve slope ($C_{N\alpha}$)
- zero-normal-force angle of attack (α_0)
- Critical normal force coefficient (C_{N1})
- Effective separation point (f)

The first three parameters can be obtained by performing a linear regression of C_N curves (Fig. D.5). From the regression, the α_0 is obtained by setting normal force coefficient to be zero. The C_{N1} is the maximum C_N before stall.

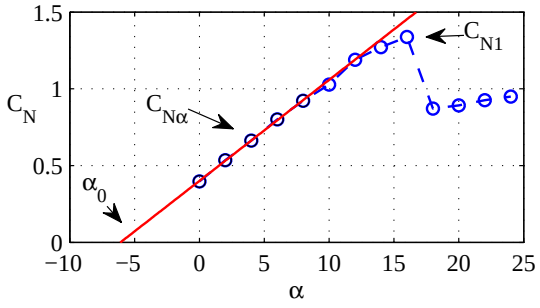

Figure D.5: Normal force curve slope.

These values are: $C_{N\alpha} = 4.6595$, $\alpha_0 = -0.209$, and $C_{N1} = 1.0781$.

In the original LB model, the effective separation point is modelled using two exponential functions and three parameters are needed to define the curve: α_1, S_1, and S_2.

However, Pierce [103] and Sheng et al. [107] had shown that this modelling is not general and does not work well for all aerofoils. They suggested that, instead

of using the functions, separation points can be provided to the model in a form of look-up table and a separation point at any angle of attack can be obtained from linear interpolation. The parameters that define the separation curve are then not required.

The effective separation point can be calculated from

$$f = \left[2\sqrt{\frac{C_N}{C_{N\alpha}(\alpha - \alpha_0)}} - 1\right]^2 \tag{D.5.31}$$

where C_N is normal force coefficient calculated from static wind-tunnel data, $C_{N\alpha}$ is the linear curve slope of normal force in attached flow region and α_0 is angle of attack with zero normal force coefficient. An example of the separation point is shown in Fig. D.6.

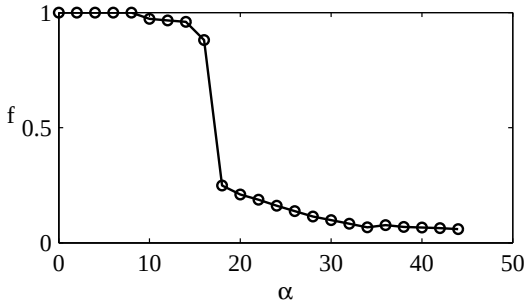

Figure D.6: Separation curves.

D.5.2 Parameters from dynamic data

The parameters required are indicial coefficients (A_1, A_2, b_1, and b_2) and time constants (T_P, T_{f0}, T_{v0}, and T_{vl}). The indicial coefficients are used to determine how the aerofoil responds when the incidence variation is within attached flow regime. Derivation of indicial coefficients involves optimisation process which is conducted to minimise difference between experimental and predicted results [15, 178].

However, detailed optimisation is out of the scope of this study. Since a variation of airload in the attached flow is small in comparison to that of separated and vortex flow regimes (typically leads to a small elliptical loop), it is assumed that the variation of this transient airload is small and the original indicial coefficients proposed by Leishman and beddoes [102] ($A_1 = 0.3$, $A_2 = 0.7$, $b_1 = 0.14$, and $b_2 = 0.53$) are used throughout this present study.

The second set of parameters is time constants which is used to determine flow development in separated and vortex-induced modules. Physically, the higher time constant value, the lower rate of flow development as defined in terms of deficiency function (for example, $D_{P,n} = D_{P,n-1}\exp\left(\frac{-\Delta S_n}{T_P}\right) + (C^P_{N,n} - C^P_{N,n-1})\exp\left(\frac{-\Delta S_n}{2T_P}\right)$).

Original values of time constants are used in this study except the response in normal mode where the stall is sudden ($T_{f0} = 0.5$ instead of 3). In addition,

dynamic stall angles, which are obtained from experiments, are also provided to the program to further control the airload calculation. Tables D.1 and D.2 summarise time constants and dynamic-stall angles used in this present work.

Table D.1: Time constants.

Time constant	Mode of operation	
	Normal	Reversed
T_P	1.7	1.7
T_{f0}	0.5	3.0
T_{v0}	6.0	6.0
T_{vl}	11.	11

Table D.2: Dynamic-stall angles.

Reduced frequency	**Normal**			**Reversed**		
	Re = 65,000	Re = 90,000	Re = 150,000	Re = 65,000	Re = 90,000	Re = 150,000
k = 0.02	12°	12°	12°	17°	12°	12°
k = 0.05	12°	12°	12°	27°	22°	12°
k = 0.10	15°	15°	15°	29°	22°	15°
k = 0.15	15°	15°	15°	30°	22°	15°
k = 0.20	18°	18°	18°	30°	22°	18°